Exploring graphitic carbon nitrides for (opto)electronic applications

Dissertation

zur Erlangung des akademischen Grades

Doctor rerum naturalium

-Dr. rer. nat.-

im Fach: Chemie

Spezialisierung: Organische und Bioorganische Chemie

eingereicht an der

Mathematisch-Naturwissenschaftliche Fakultät der

Humboldt-Universität zu Berlin

von

Burmeister, David

Präsidentin der Humboldt-Universität zu Berlin

Prof. Dr. Julia von Blumenthal

Dekanin der Mathematisch-Naturwissenschaftlichen Fakultät

Prof. Dr. Caren Tischendorf

Gutachter : 1. Prof. Dr. Michael J. Bojdys

2. Prof. Dr. Emil J.W. List-Kratochvil

3. Prof. Dr. Arne Thomas

Datum der mündlichen Prüfung: 17.10.2023

EIGENSTÄNDIGKEITSERKLÄRUNG

Ich erkläre, dass ich die Dissertation selbständig und nur unter Verwendung der von mir gemäß § 7 Abs. 3 der Promotionsordnung der Mathematisch-Naturwissenschaftlichen Fakultät, veröffentlicht im Amtlichen Mitteilungsblatt der Humboldt-Universität zu Berlin Nr. 42/2018 am 11.07.2018 angegebenen Hilfsmittel angefertigt habe.

Datum Unterschrift

Acknowledgements

I would first like to thank my thesis advisor Prof. Dr. Michael Janus Bojdys of the Chemistry department at Kings College London and affiliate of the Humboldt-Universität zu Berlin. He, together with Prof. Dr. Emil List Kratochvil was always available to discuss the challenges I faced within the elaboration of experiments and the thesis in general.

Also I want to thank Prof. Dr. Hans Gerhard Börner, Prof. Dr. Christoph T. Koch, Prof. Dr. Gudrun Scholz, Prof. Dr. Phillip Adelhelm, Prof. Dr. Norbert Esser, Prof. Dr. Norbert Koch, Dr. Michael Tovar, Prof. Dr. Franziska Emmerling, Dipl.-Chem. Kerstin Scheurell, Stefanie Markstein, Dr. Manfred Weiss, Paul Zybarth and Bodo Kranz for providing crucial access to instruments, laboratories and service measurements.

I am deeply grateful for the computational chemistry results provided in the collaboration with Prof. Dr. Catherina Cocchi and Dr. Michele Guerrini underpinning most of the experimental results.

I pay a particular vote of gratitude to my colleagues Dr. Matthias Trunk, Dr. Jieyang Huang, Dr. Ranjit Kulkarni, Dr. Julian Plaickner, Johannes Müller, Dr. Felix Hermerschmidt, Dr. Giovanni Ligorio, Dr. Sarah Vogl, Dr. Beatrice Cula, Ha Ahn Tran, Max Heyl, Fabian Gärisch, Josefine Sprachmann, Niklas Grabicki, Vincent Schröder, Nicholas Zorn Morales and Michael Hengge. They supported my path by teaching me new techniques and discussing experiments along my exploration of carbon nitride materials.

In addition I would like to acknowledge the referees of this thesis and their valuable comments.

Finally, I express my very profound gratitude to my parents Angela Axhausen and Stefan Burmeister for providing me with unfailing support and continuous encouragement throughout my years of study. Also I would like to thank my grandmother Helga Axhausen for always being a great supportive force in my life.

Abstract

Graphitic carbon nitrides are organic covalently-bonded, layered, and crystalline semiconductors with high thermal and oxidative stability. These properties make 2D layers of graphitic carbon nitrides potentially useful in overcoming the limitations of 0D molecular and 1D polymer semiconductors. However, only few reports have shown them being employed in optoelectronic applications. With the goal to find better reaction conditions that enable higher product quality from the ionothermal synthesis the size effect of anions is studied by using an iodide eutectic instead of bromide or chloride eutectic. The highest crystalline condensation product obtained is melem, revealing that the large iodide anion is not capable of stabilizing a graphitic structure. Studying the synthesis conditions of poly(triazine imide) (PTI), the best characterized graphitic carbon nitride in literature, it is revealed that the brown discoloration of the product is due to a carbon rich side product. Reduction of reaction temperature and increase of reaction time allows omittance of carbonisation. Analyzing the electronic structure with *ab initio* calculations one finds that the lowest energy electronic transition in PTI is forbidden due to a non-bonding uppermost valence band. A uppermost non-bonding valence band is most reminiscent of lone-pair semiconductors and unknown in the world of organic semiconductors making PTI the first organic lone-pair semiconductor. The low electrical conductivity of PTI derivatives of 10^{-7}-10^{-10} S cm^{-1} is compared to nanoscale conductivity values obtained by THz-TDS spectroscopy revealing a conductivity of up to 0.26 S cm^{-1}. This indicates that macroscopic conductivity is hampered by the nano-crystalline character due to charge carrier trapping at crystal interfaces. The effective mobility is in the range of amorphous organic semiconductors 10^{-3}-10^{-4} cm^2 V^{-1} s^{-1}. The charge carrier density of 10^{20} cm^{-3} in the PTI derivatives is unexpectedly high. Ultraviolet photoelectron spectroscopy was used in combination with the electronic structure and the optical gaps to derive energy level diagrams revealing an electron affinity of 4.2 eV in PTI-LiBr enabling potentially environmentally stable n-transport. Application of PTI-LiBr in a single layer organic light emitting diode revealed that the electroluminescence maximum is red-shifted by 0.5 eV in regard to the photoluminescence.

Zusammenfassung

Graphitische Karbonitride sind organische, kovalent gebundene, geschichtete und kristalline Halbleiter mit einer hohen thermischen und chemischen Stabilität. Diese Eigenschaften machen 2D Schichten der graphitischen Kristalle potentiell nützlich für das Ziel, Limitationen von organischen 0D Molekularen und 1D polymerischen Halbleitern zu überwinden. Trotz dieser interessanten Eigenschaften haben nur wenige Publikationen erfolgreich graphitische Karbonitride in optoelektronischen Bauteilen eingesetzt. Um die Vorteile dieser Materialien nutzbar zu machen, wurden bessere Synthesebedingungen gesucht. Die Verwendung von einem Iod-Eutektikum zeigt, dass Anionen mit einem größeren Radius als Bromid nicht für die Stabilisation von graphitischen Karbonitriden geeignet sind. Das Optimieren der Synthesebedingungen von Poly(triazin-imid)-LiBr resultiert in der Reduzierung von einem kohlenstoffreichen Zersetzungsprodukt bei vollständiger Kondensation. Das Untersuchen der elektronischen Struktur mit *ab initio* Berechnungen ergibt, dass der elektronische VB-CB-Übergang verboten ist. Dies resultiert daraus, dass die Zustände des obersten Valenzbandes nichtbindender Natur sind. Ein Band aus nichtbindenden Elektronen als oberstes Valenzband ist vor allem aus „lone-pair semiconductors“ aus der sechsten Hauptgruppe bekannt. In der Welt organischer Halbleiter wurde dieses Phänomen bisher nicht beobachtet. Die geringe makroskopische elektrische Leitfähigkeit der PTI-Filme von 10^{-7}-10^{-10} S cm^{-1} wurde mit der Leitfähigkeit auf Nanoebene von 0.26 S cm^{-1} verglichen, woraus gefolgert werden kann, dass der Ladungsträgertransport durch den nanokristallinen Charakter an den Kristall-Kristall Übergängen gestört wird. Die Mobilität von 10^{-3}-10^{-4} cm^2 V^{-1} s^{-1} ähnelt der von amorphen organischen Halbleitern, während die Ladungsträgerdichte von 10^{20} cm^{-3} unerwartet hoch ist. Ultraviolett-Photoelektronenspektroskopie in Verbindung mit der berechneten elektronischen Struktur und den optischen Übergängen resultierte in Energieniveaudiagrammen die eine Elektronenaffinität von bis zu 4.2 eV nahelegen. Dies erlaubt stabilen Elektronentransport in der Präsenz von Sauerstoff. Die Applikation von PTI-LiBr in einer organischen lichtemittierenden Diode zeigte, dass das Elektroluminezenz Maximum verglichen mit der Photomlumineszenz um 0,5 eV rotverschoben ist.

List of Publications

Parts of this dissertation have been published:

[1] "Development of metal-free layered semiconductors for 2D organic field-effect transistors", D. Burmeister, M. G. Trunk, M. J. Bojdys, *Chem. Soc. Rev.* **2021**, *50*, 11559–11576. DOI 10.1039/d1cs00497b

[2] "Optimized Synthesis of Solution-Processable Crystalline Poly(Triazine Imide) with Minimized Defects for OLED Application", D. Burmeister, H. A. Tran, J. Müller, M. Guerrini, C. Cocchi, J. Plaickner, Z. Kochovski, E. J. W. List-Kratochvil, M. J. Bojdys, *Angew. Chemie Int. Ed.* **2022**, *61*, 2–10. DOI 10.1002/anie.202111749

[3] "Size Effects of the Anions in the Ionothermal Synthesis of Carbon Nitride Materials", D. Burmeister, J. Müller, J. Plaickner, Z. Kochovski, E. J. W. List-Kratochvil, M. J. Bojdys, *Chem. – A Eur. J.* **2022**, *28*, DOI 10.1002/chem.202200705.

[4] "On the non-bonding valence band and the electronic properties of poly(triazine imide), a graphitic carbon nitride", David Burmeister, Alberto Eljarrat, Michele Guerrini, Eva Röck, Julian Plaickner, Christoph T. Koch, Natalie Banerji, Caterina Cocchi, Emil J. W. List-Kratochvil, Michael J. Bojdys, Chem. Sci. 2023, 14, 6269–6277, DOI 10.1039/D3SC00667K

Further scientific contributions of the author:

[5] "Antiaromatic Covalent Organic Frameworks Based on Dibenzopentalenes", Josefine Sprachmann, Tommy Wachsmuth, Manik Bhosale, David Burmeister, Glen J. Smales, Maximilian Schmidt, Zdravko Kochovski, Niklas Grabicki, Robin Wessling, Birgit Esser, Emil J. W. List-Kratochvil and Oliver Dumele, J. Am. Chem. Soc., **2023**, 145, 5, 2840–2851, DOI 10.1021/jacs.2c10501

[6] "One-pot synthesis of high-capacity silicon anodes via on-copper growth of a semiconducting, porous polymer", J. Huang, A. Martin, A. Urbanski, R. Kulkarni, P. Amsalem, M. Exner, G. Li, J. Müller, D. Burmeister, N. Koch, T. Brezesinski, N. Pinna, P. Uhlmann, *Nat. Sci.* **2022**, *2*, 1–19. DOI 10.1002/ntls.20210105

[7] "Direct growth of crystalline triazine-based graphdiyne using surface-assisted deprotection-polymerisation", R. Kulkarni, J. Huang, M. Trunk, D.

Burmeister, P. Amsalem, J. Müller, A. Martin, N. Koch, D. Kass, M. J. Bojdys, *Chem. Sci.* **2021**, *12*, 12661–12666. DOI 10.1039/d1sc03390e

[8] "Thermally Activated Gold-Mediated Transition Metal Dichalcogenide Exfoliation and a Unique Gold-Mediated Transfer ", M. Heyl, D. Burmeister, T. Schultz, S. Pallasch, G. Ligorio, N. Koch, E. J. W. List-Kratochvil, *Phys. Status Solidi - Rapid Res. Lett.* **2020**, *14*, 1–5. DOI 10.1002/pssr.202000408

[9] "Sulfur-and boron-containing porous donor-acceptor polymers for photocatalytic hydrogen evolution", M. G. Trunk, G. Li, H. Küçükkeçeci, D. Burmeister, M. Obermeier, B. T. Bonkano, A. Thomas, M. Schwalbe, M. J. Bojdys. DOI 10.26434/chemrxiv-2021-q1b4b-v2, in review.

Table of contents

Chapter 1. Introduction and motivation 1
Chapter 2. Theoretical background 5
2.1. Carbon nitrides –first steps– 6
2.2. From 1D to 2D band gaps in organic semiconductors 12
2.3. Charge transport regimes in crystalline organic semiconductors 16
2.4. Current description of transport in carbon nitride materials 22
2.5. (Organic) thin film transistors 23
2.6. Organic- light emitting diode 26
2.7. An attempt to classify research materials on the basis of literature 27
2.8. Theory of applied material science: Improving semiconducting crystalline organic frameworks towards application 30
2.9. Context and definition for the “graphitic carbon nitride” material 32
Chapter 3. Experimental procedures for condensed carbon nitrides 35
3.1. Synthesis of carbon nitrides in eutectic salt melts 36
3.2. Characterisation methods and sample requirements 40
Chapter 4. Size effects of the anions in the ionothermal synthesis of carbon nitride materials 55
4.1. Results and discussion 58
4.2. Conclusion 77
Chapter 5. Poly(triazine imide)-from synthesis to device 79
5.1. Introduction 81
5.2. Results and discussion 82
5.3. Conclusion 119
Chapter 6. Summary and conclusion 121
References 127
Appendix 138

List of abbreviations

BET	*Brunauer-Emmett-Teller*
CB	*conduction band*
CN	carbon nitride
COF	*covalent organic framework*
CP-MAS	*cross-polarisation magic-angle spinning*
DCDA	*dicyandiamide*
DFT	*density functional theory*
DSM	*Drude–Smith Model*
EA	*elemental analysis*
EDX	*Energy-dispersive x-ray spectroscopy*
EELS	*Electron energy loss spectroscopy*
FT-IR	*Fourier transform-infrared spectroscopy*
gCN	*graphitic carbon nitride*
hBN	*hexagonal boron nitride*
HGCN	*heptazine-based graphitic carbon nitride*
HIB	*hole injection barrier*
HOMO	*highest occupied molecular orbital*
HRTEM	*high resolution transmission electron microscopy*
ICP-OES	*inductively coupled plasma optical emission spectroscopy*
IP	*ionisation potential*
ITO	*indium tin oxide*
LUMO	*lowest unoccupied molecular orbital*
MOF	*metal organic frameworks*
OFET	organic thin film transistor
OLED	*organic light emitting diode*
OSC	*organic semiconductor*
OTFT	organic thin film transistor
PEDOT:PSS	*poly(3,4-ethylenedioxythiophene) polystyrene sulfonate*
PES	*photoelectron spectroscopy*
PL	*photoluminescence*
PLE	*photoluminescence excitation*
PTI	*poly(triazin imide)*
PTI-IF	*poly(triazine imide)-intercalation free*
PTI-LiBr	*poly(triazine imide)-lithium bromide*
PTI-LiCl	*poly(triazine imide)-lithium chloride*
PXRD	*powder x-ray diffraction*

QY	*quantum yield*
SEM	*scanning electron microscopy*
scXRD	*single crystal x-ray diffraction*
SFM	*scanning force microscopy*
ssNMR	*solid state nuclear magnetic resonance spectroscopy*
ssUV-Vis	*solid state absorption spectroscopy*
TEM	*transmission electron microscope*
TGCN	*triazine-based graphitic carbon nitride*
THz-TDS	*time-domain-THz spectroscopy*
TLM	*transfer length method*
UPS	*ultroviolet photoelectron spectroscopy*
UV-Vis	*absorption spectroscopy*
VB	*valence band*
WF	*work function*
XRD	*x-ray diffraction*

Chapter 1. Introduction and motivation

Die nachfolgende Abhandlung umfaßt eine Reihe von neuen Verbindungen, deren Entstehen eben so sonderbar und merkwürdig ist, als ihr Verhalten und ihre Eigenschaften.
(The following treatise comprises a number of compounds, whose formation is as strange and peculiar as its behaviour and its properties.)
Justus Liebig, Über einige Stickstoffverbindungen, Annalen der Physik, 1835, translated by David Burmeister.

The global society is facing health (COVID19), energy (fossil fuels) and ecological (climate change) crises in a degree unknown in the past fifty years.[1,2] Behind some of these crises technological problems lie in wait of being challenged with new materials or concepts. A material class central to our technological advancement in the last 70 years is the semiconductor. Semiconductors fulfil different key functions with high efficiency. They can convert photons into electrical potentials (photovoltaic cells), electrical potentials into photons (light emitting diodes), photons into chemical potential (e.g. photocatalytic water splitting) and electrical potential into bits of information (transistors, sensors). The semiconductor is the link between these different energy forms which is why one can also refer to them as energy conversion materials. Efficient conversion of these energy forms with semiconductors produced from earth-abundant materials at low energetic cost is advancement worth aiming for.

With the continuous evolution of ever smaller and ever faster electronics the fundamental field enabling the flourishing technology is often overlooked in day-to-day life: material science. The amalgamation of physics, chemistry, and engineering into the interdisciplinary profession provides us with an evolving tool set required to manipulate ever smaller electronic devices and understand and utilize new materials and phenomena down to atomic scales.

The state-of-the-art devices available today are based on single-crystalline silicon with ultra-high purity of up to 99,999999999% (11 N) for electronic grade silicon or 99.9999 (6 N) for solar cell grade silicon.[3] The high purity enables precise geometrical structuring as well as manipulation of charge carrier transport in the material. The technology used to build the successively smaller-sized transistors is arguably the most sophisticated ever developed.

Silicon technology can currently produce feature sizes down to 5 nm with one central processing unit comprising three billion transistors (i7-8086K). However, short channel effects, no further increase in clock frequency, high energy consumption during production (up to 2% of US energy consumption in the manufacturing sector), usage of critical raw materials, and costly photolithography tools become increasingly deterrent.[4,5] According to the International Technology Roadmap for Semiconductors (ITRS) further miniaturisation of silicon technology is economically unfeasible.[6] This realisation renewed interest into researching material classes that could rival if not outperform silicon at short channel lengths.

Only in 2004 with the discovery of graphene, atomically thick, covalently bonded carbon films, it became apparent that atomically thin crystals – 2D crystals – can be exfoliated from graphitic parent materials. Prior to that, scientific consensus was that such layers would be unstable and could not exist.[7,8]

The 2D material class was discovered, constituting the physical limit of thickness, atomic thickness. Semiconducting members from the class of 2D materials are thought to be the best candidates to compete with silicon at under 5 nm thickness in semiconducting electrical devices. The confinement of the electronic structure to an atomic layer unveiled interesting phenomena, for example massless electrons in graphene and indirect-to-direct band gap transition in MoS_2.[9,10] Exciting observations like these energized the material science community to search for new 2D, layered and graphitic materials with the potential to be exfoliated to monolayers.

Today the main classes of established two-dimensional materials are divided into the Graphene family, 2D chalcogenides and 2D oxides.[11] In addition to these subclasses organic chemistry enabled the synthesis of 2D covalent conjugated organic frameworks (2D COFs). The material class that this work evolves around

can be thought of as part of this family: “graphitic carbon nitrides”. Graphitic carbon nitrides promise a unique set of highly sought-after properties: high environmental stability, low toxicity for biological tissues, low opacity, low density, consisting of elements with high earth abundance, 2D crystals, blue photoluminescence, and semiconducting behaviour due to their π-conjugation.[12–15] However, graphitic carbon nitrides as well as covalent organic frameworks in general have seen little to no application in optoelectronic devices up to this point.

Goal of this work is to access the suitability of graphitic carbon nitride materials such as poly(triazine imide) (PTI) for optoelectronic applications. To achieve this objective, new synthesis conditions are researched in order to increase product quality as well as to identify potentially evolving new carbon nitride phases.

Central scientific questions that are addressed in this work are:

(i) Is it possible to improve the quality or generate new phases of graphitic carbon nitrides by increasing the anion size in the ionothermal synthesis?

(ii) What is the reason for the lack of applications of PTI in optoelectronic devices?

(iii) What are the intrinsic semiconductor properties of PTI-intercalation free (PTI-IF) and PTI-lithium bromide (PTI-LiBr), e.g. charge carrier density, mobility, conductivity and energy levels?

(iv) Is it possible to build a PTI-LiBr organic light-emitting diode with blue electroluminescence?

To ease the reader into the terms and concepts used in the field of condensed carbon nitrides, which can be confusing if not misleading at times, I want to give a short summary of the history of graphitic carbon nitrides in the following part.

Chapter 2. Theoretical background

We learn wisdom from failure much more than from success.
We often discover what will do, by finding out what will not do;
and probably he who never made a mistake never made a discovery.
Samuel Smiles, 1812-1904.

Partial content of this chapter is based on work that has been published in: D. Burmeister, M. G. Trunk, M. J. Bojdys, *Chem. Soc. Rev.* **2021**, *50*, 11559–11576.

Author contributions: D. B. and M. G. T. drafted the review article. D. B. prepared the figure items. M. J. B. revised the draft.

2.1. Carbon nitrides –first steps–

In 1835 Justus Liebig published his work on the decomposition reaction of potassium thiocyanate, with the goal to learn about the relationships of heteroatom-containing organic compounds.[16] The substances he synthesised, isolated, analysed, described and labeled are today still called by the trivial names he assigned to them (melon, melamin, melam). When synthesising melon, Liebig thought he had obtained a free radical, which was an inaccurate conclusion.[17] Melon is a one-dimensional chain of melem units. In later studies the goal to obtain fully condesed carbon nitride was formulated.[18] The first claim of a synthesis approaching a C_3N_4 compound was postulated in 1912 by Franklin.[19] Since these initiating steps in the field of condensed carbon nitrides huge progress has been made in understanding the structure and electronic properties of this material class due to the plethora of new characterisation methods available.

The first wave of interest –the prediction of low crompressibility–

In 1985 Marvin L. Cohen published a formula detailing the simplification of the calculation of bulk moduli of covalent solids. He concluded that the bulk moduli can be described for a certain class of material, e.g. group III-V semiconductors in dependence of just the nearest neighbour distance (bond length) and ionicity. This formula predicted that for a tetrahedral CN compound the bulk modulus was significantly higher than that of diamond. This prediction induced the first wave of interest in the synthesis of CN solids for tribological applications.[20]

First reports of successful syntheses of CN crystallites typically accompanied by an amorphous CN phase were reasoned to be polycrystalline β-C_3N_4.[21–23] A theoretical paper by Teter and Hemley suggested that the material of lesser hardness, α-C_3N_4 was energetically favoured and fits the crystallography data better than β-C_3N_4.[24] Nesting and Badding noticed the co-evolution of a crystalline pure carbon phase that could not be assigned.[25]

Most synthesis strategies to this point were based on high-pressure decomposition of C-N-H precursors,[26,27] ion and vapour deposition of nitrogen ions and carbon vapour,[28] plasma decomposition of methane and N_2,[29] shock wave compression,[30] sputtering experiments,[31,32] and pulsed laser ablation of graphite in combination with an atomic nitrogen source.[21]

The conducted synthesis approaches for materials approaching C_3N_4 stoichiometry with high energies at non-equilibrium conditions like sputtering typically impeded structural formation by displacing atoms via knock-on collisions.[33]

Kouvetakis et al. synthesized C_3N_4 films by chemical vapour deposition (CVD) of C_3N_4 precursors and introduced the idea of a triazine-based layered structure, today crystals of this compound are denoted as triazine-based graphitic carbon nitride (TGCN).[34] The nitrogen concentration of the CN product obtained was the highest achieved in a condensed CN structure to that day. However, the deposited films did not show diffraction signals besides a d-spacing of 3.6 Å similar to that of amorphous carbon.

The standard analytical method used to determine the structure of the synthesized mostly amorphous nano-crystallite containing CN materials was electron diffraction. However, diffraction methods proved to be insufficient as analytical standalone technique for carbon nitride materials since *lonsdaleite* (hexagonal diamond) and FeO(OH) which can form during synthesis and transmission electron microscopy (TEM) specimen preparation respectively match the predicted diffraction pattern of the hypothetical β-C_3N_4.[35,36] Elemental analysis of these studies were sometimes not reported or did not consider impurities like oxygen and hydrogen. These early studies emphasised the necessity of complementary analysis methods of the product phases. Typically, the crystallite sizes do not exceed ten to a few hundred nanometers and are predominantly accompanied by other amorphous or crystalline non-CN phases. It is crucial to employ analysis of the structures as thoroughly as possible with microscopic as well as macroscopic methods to not be misled.

Furthermore it was realised that the shear modulus is reflecting the hardness of materials better. A theoretical revision of carbon nitrides showed that they are only about 60% as hard as diamond.[37] With the motivation of finding a material harder than diamond and therefore a great material for tribological applications lost, and the harsh criticism of existing literature because of the lack of complementary analysis, the excitement about the material class was dampened.[36,38]

Kroke et al. proposed a graphitic tri-*s*-triazine-based graphitic carbon nitride, today typically referred to as HGCN (heptazine-based graphitic carbon nitride), and

synthesized polymers based on heptazine. HGCN was readily adopted in literature as a possible structure of g-C_3N_4.[39,40] Even though Lotsch et al. demonstrated that the structure of the so called g-C_3N_4 consists of 1D chains of heptazine units stacked and fixed in place by hydrogen bridge bonds this misconception prevails even in recent literature.[18]

Crystalline or not, due to the exceptional chemical stability, the HOMO-LUMO gap of the conjugated building blocks, and simple, cost-effective preparation as well as catalytic activity the interest shifted towards application as (photo)catalyst.[41–44]

The second wave of interest –C_3N_4 2D materials–

With the rapid increase in interest in graphitic materials around the year 2004, caused by the observation of drastic changes in the physical material properties when reduced from three to two dimensions, e. g. graphite to graphene, interest in graphitic carbon nitrides was renewed and new synthesis strategies evolved.[8,45] A new synthetic approach was the use of solvothermal conditions often successfully applied in inorganic synthesis.[46]

Different solvents like benzene and hydrazine were applied, however, the products typically still had residual NH/NH_2 groups as can be deduced from the 3200-3300 cm^{-1} IR bands.[47,48] More synthesis approaches in this period are reviewed by Thomas et al. who reasoned in his work that the most stable CN phase would be HGCN.[49] This claim was supported by density functional theory (DFT) calculations. For complete condensation higher temperatures and absence of reducing agents were necessary. A medium-pressure (27 G Pa), high-temperature (1700 °C) synthesis showed for the first time a crystalline C_2N_2(NH) material.[50] The reasoning of high temperature and closed-vessel synthesis to enable reversibility was also investigated by Michael Bojdys et al. who used a eutectic salt melt of lithium and potassium chloride for polycondensation at ionothermal conditions of dicyandiamide. The structural analysis of the crystalline product led him to the conclusion that the observed product is HGCN.[51]

The crystalline product was later identified as poly(triazine imide) (PTI) with intercalated lithium and chloride ions.[52] This product constitutes the first truly graphitic carbon nitride for which the structure was fully resolved. Hence, we want

to direct our attention to the synthesis, structure, morphology, and recent results regarding this material in more detail.

Poly(triazine imide) –the first graphitic carbon nitride–

The synthesis of PTI is based on an ionothermal polycondensation reaction in a eutectic salt melt of lithium and potassium chloride. The high temperature of 600 °C, presence of ammonia and the closed vessel enables reversible reactions.[53] The product morphology is characterised as hollow tubes consisting of hexagonal prisms with single crystallites on the order of 50 nm and of a brown colour.[52]

The structure is composed of a 2D network of planar layers of nitrogen-bridged triazine units with intercalated Li^+ and Cl^- ions. The layers are stacked in an AA* manner (alternating layers with each second layer mirrored through the triazine units) so that pore channels run orthogonally to the covalently bonded 2D planes of the crystals.

The optical gap of PTI-LiCl was determined to be 2.2 eV. This is 0.5 eV smaller when compared to the optical gap of polymeric melon.[54] The halide and metal ions can be exchanged post synthesis to tune the gallery height.[55,56] Due to relatively high order it was possible for the first time to resolve the triazine breathing modes via Raman in a graphitic CN material at 1000 cm^{-1} and 680 cm^{-1} with a laser wavelength of 325 nm.[57] This is a great achievement since it addresses the criticism stated earlier to use complementary analysis approaches and optical methods as well as diffraction. Furthermore, it opens the door to secondary experiments investigating the vibrations of the material in dependence of temperature or dopants. Another complementary approach applying NMR and electron diffraction pinned down the positions of hydrogen and chloride ions.[58]

An extensive study on the formation processes of PTI-LiCl from different precursors was published by Kessler et al..[59] This study suggests that the first step of PTI-LiCl formation is always the formation of melem. Melem then has to fragment via a ring-opening reaction, and 1D triazine strands are assembled under elimination of ammonia.

While the existence of the crystalline graphitic-CNH material showed that it is not impossible to form such, the complete condensation to a binary CN material had still to be achieved.

The first fully condensed C_3N_4 material – triazin-based graphitic carbon nitride–

Synthesis and characterisation of triazine-based graphitic carbon nitride (TGCN) was first reported by Siller et al..[60] The structure of TGCN consists of 2D networks of triazine units bridged by nitrogen atoms. In contrast to PTI-LiCl, no NH bonds are left. This phase constitutes the first report of a crystalline, graphitic material from just carbon and nitrogen to this day.

The synthesis employs again the advantages of ionothermal synthesis in a eutectic salt melt. Overall, the synthesis conditions are extremely similar to the synthesis of PTI-LiCl. Dicyandiamide (DCDA) is ground into a eutectic salt mixture and heated to 600 °C. The differences to the synthesis of (PTI) is the eutectic salt lithium bromide, potassium bromide, the heat is applied in two successive steps, starting at 400 °C, and the reaction time is increased to 3 days.

These changes are sufficient to observe a new carbon nitride phase evolve at the walls of the quartz ampules and the melt-gas interface. The macroscopic appearance is described as flake-like with colours ranging from transparent red for short reaction times to shiny opaque for long reaction times.

The structural assignment is conducted by a combination of high resolution TEM (HRTEM) and PXRD measurements. The observed HRTEM images with a hexagonal periodicity of 2.6 nm were matched to HRTEM simulations of ABC-stacked TGCN. The synchrotron PXRD measurements further reinforced the PXRD results in showing the (100) a = 0.504 nm reflection. The best fit for the PXRD data is found to be an ABA stacking. The conflicting observations of TEM and PXRD were interpreted as low interplanar forces that enable the possibility of different stacking orders.

On the basis of solid-state UV-Vis spectra it was reasoned that the optical gap of the structure is less than 1.6 eV. However, it should be noted that the presented DFT calculation of single-layer TGCN indicates a band gap of 2.5 eV, and that DFT typically underestimates the band gap.

Suter et al. tried to reproduce the synthesis of TGCN reported by Siller et al.[57] but the product he obtained did not show the same PXRD reflections. The elemental composition showed additional carbon when compared to the ideal C_3N_4 composition and the Raman spectrum did not show triazine breathing modes.

Nevertheless he received a similar HRTEM image with the same periodicity observed by Siller et al. Small area electron diffraction (SAED) patterns recorded at the crystalline spots of the sample showed reflection spots at d = 2.6 Å which were reasoned to indicate graphite. Graphite could evolve from carbonisation and would also explain the carbon rich product. However, the HRTEM pattern did not match the pattern of graphite, as few-layer graphite typically has a hexagonal periodicity of 2.1 Å.[61]

The variation from the work conducted by Siller et al. is likely due to slight differences, for example in the geometry and heating curve of the furnace. This might be the reason for the different product quality.

In conclusion, two major challenges appear to be present in most of the synthesis products obtained: Potentially highly condensed carbon nitride crystals were always obtained only in the nano-crystalline range. These have been challenging to characterise by other methods than electron microscopy and in some cases proposed structures had to be refuted. Secondly, decomposition into carbon-rich co-phases as well as evolution of amorphous co-phases were observed. The structurally best-described graphitic carbon nitride is PTI obtained from ionothermal synthesis in eutectic salt melts.

2.2. From 1D to 2D band gaps in organic semiconductors

Organic materials are typically considered to consist mainly of carbon, hydrogen, oxygen, nitrogen, and sulfur. Carbon, with four valence electrons, a medium electronegativity of 2.55 (Pauling) and three different hybridisation states (sp, sp^2, sp^3) can form a plethora of different bonds with different bonding partners as well as itself. This versatility is already apparent in the allotropes of carbon, e.g. diamond, graphite, lonsdaleite, Buckminster fullerene, carbon nanotubes, amorphous carbon, graphdiyne, and the over about 280 more unique periodic structures.[62]

To obtain a semiconducting organic material the hybridisation of the carbon atoms is key. If all four valence electrons are involved in single bonds (σ-bonds) the material property will be insulating as the highest occupied molecular orbital (HOMO)- lowest occupied molecular orbital (LUMO) energy gap is exceeding the semiconducting range (0.15 eV equals a narrow band gap semiconductor, >2 eV equals a wide band gap semiconductor, >6 eV equals insulators, e.g. ethane HOMO-LUMO gap 13 eV, as obtained from DFT: DMOL3, B3LYP, 631g).[63] This property also explains the absence of light absorption of ethane in the visible range.

Such materials are widely employed as translucent packaging materials (polyethylene PE), transparent plexiglass (poly(methyl methacrylate), PMMA) or insulators, but are not suited to be semiconductors. 1D-carbon chains based on sp^3 bonds are also referred to as saturated hydrocarbons as they are saturated with hydrogen.

To gain access to the semiconducting properties of carbon, unsaturated bonds are needed (diamond is a wide-band semiconductor and an exception to the rule).[64] Instead of hybridizing the 2s and all 2p atomic orbitals of the ground state electronic structure ($1s^2 2s^2 2p^2$) to give four degenerate sp^3 orbitals, only one or two 2p orbitals are hybridized to yield sp or sp^2 hybridisation, respectively. Following this reasoning we can increase the length of the conjugated carbon chains as shown in Figure 1 and observe the effect on the π-frontier orbitals. In a 1D crystal like polyacetylene (sp^2) or polyine (sp) the conjugation along the chain may even be expected to result in metallic behaviour, however it has been observed that symmetry breaking is energetically favourable for the system, resulting in a persistent energy gap between the bonding π- and antibonding π^*-orbitals.[65] This

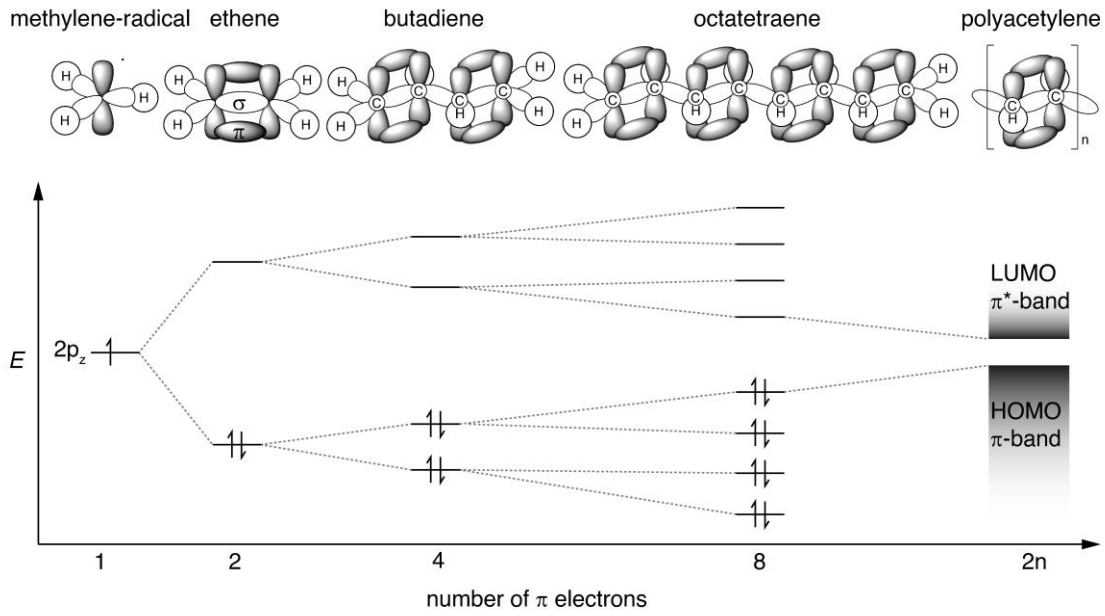

Figure 1. Top: Simplified depiction of π– and σ–bonding patterns in a methylene- radical, unsaturated carbohydrates, and polyacetylene. Bottom: Corresponding occupied and unoccupied energy levels. (Figure adapted from Griffith et al..)[185]

phenomenon is referred to as Peierls instability, Peierls distortion or dimerisation.[66] The symmetry breaking is apparent in the electronic structure as well as in the physical structure resulting in a bond length alteration in the chain of R_{CC} = 1.44-1.36 Å. One can now follow along this Gedankenexperiment of growing the 1D crystal further by utilizing the C-H bonds, which are already in plane with the C-C bonds, to expand the structure slowly into the second dimension. As we find in Figure 2, the effect of Peierls distortion dominates the characteristics of the electronic structure from polyacetylene to four-stranded graphene nanoribbons. More conjugated carbon strands than four lead to degeneration of the HOMO and LUMO state, resulting in semi metallic character of the material.

This is most famously known for graphene. The otherwise extraordinary charge transport characteristics are dulled by the absence of a band gap, not allowing the application of graphene as an efficient semiconductor in a field effect transistor. Large efforts were undertaken in the last decades to “open up” the band gap of graphene.[67,68] Many new graphene derivatives like fluorographene and graphane have been synthesized and analysed.[69–71] However, obtaining a homogeneous

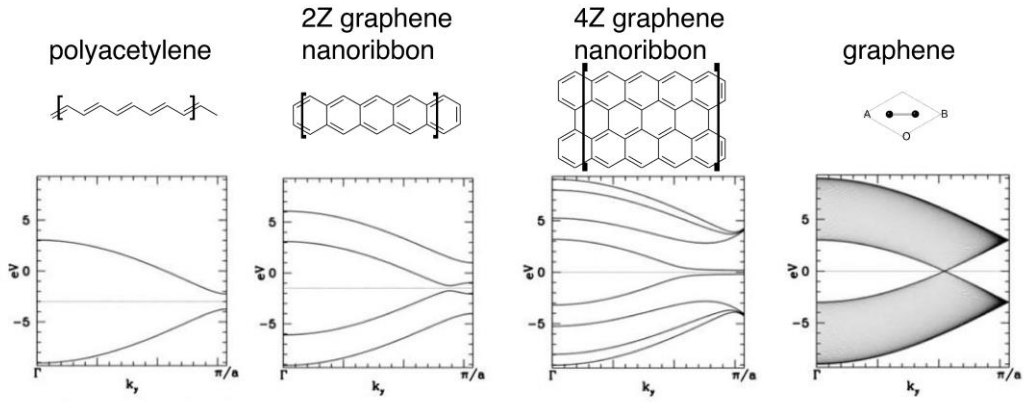

Figure 2. From polyacetylene to four-stranded (one strand corresponds to one carbon chain in longitudinal direction) graphene nanoribbons the dominating factor is still Peierls distortion opening a gap in the electronic structure. Further extension as shown in graphene leads to a metallic character. (Figure adapted from Tozzini et al.)[186]

material with similar charge transport characteristics as graphene and a band gap, allowing to negate the off-state current is not achieved yet.[72]

The second approach to attain organic 2D semiconductors utilizes the intrinsic property that is Peierls distortion to the "thin" conjugated carbon strands in building 2D networks with them. These materials are considered a subfamily of crystalline organic frameworks (COFs) with the important additional requirement of being conjugated. Instead of reducing the crystallinity of graphene by introducing defects this approach allows to synthesize graphitic materials in a bottom-up approach.

Polymerisation of such structures results typically in "single carbon strands" like imine-linkers connecting neighbouring aromatic building blocks like benzene or triazine. As we can see in Figure 2, strong Peierls distortion leads to significant band gaps. A potential path to counteract large band gaps is known from synthesis of narrow band gap organic semiconductors: introduction of donor-acceptor systems. Such donor-acceptor interactions are expected to result in lower band gaps due to the relative position of the LUMO of the acceptor to the HOMO of the donor in molecular subunits (Figure 3).

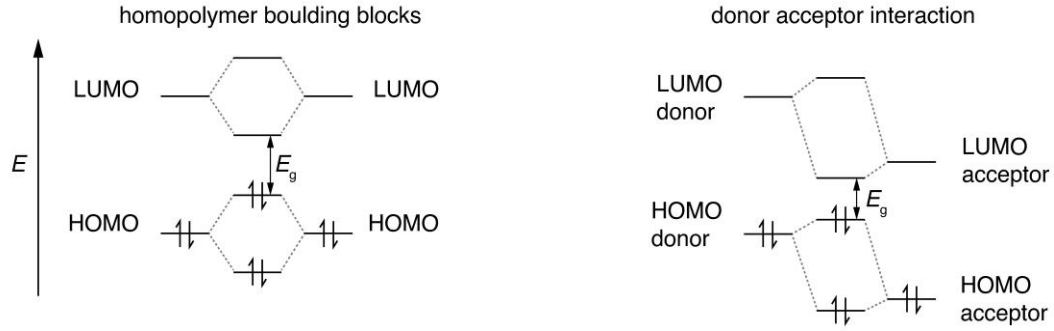

Figure 3. Representative depiction of hybridization of frontier molecular orbitals of homopolymer building blocks and donor-acceptor building blocks. The relative position of the acceptor LUMO and the donor HOMO results in a smaller HOMO-LUMO gap E_g in donor-acceptor systems. (Figure adapted from Bakhshi et al..)[187]

A reduction in the HOMO-LUMO gap is also observed when alternating carbon and nitrogen atoms in a conjugated system (e.g. benzene ~6.6 eV > 1,3,5-Triazine ~6 eV (DFT)).[73] In addition, due to the high electronegativity of nitrogen which is the fourth most electronegative element (3.04 Pauling) when compared to carbon (2.55 Pauling) the energy of the LUMO is lowered. An electron affinity of -4 eV or more negative is of advantage for stable electron transport.[74]

While potentially highly performant structures have been predicted, no viable candidates with high field effect mobility have been found experimentally yet.[75] One main reason for this lack of encouraging experimental data is that not many conjugated 2D COFs have been experimentally obtained in a quality high enough (large crystal domains, low defects) to study the electronic structure reliably. The second reason is that, unlike in 1D organic semiconductors where high symmetry is considered to be helping mobility, some 2D structures have been found lately to lead to topological flat bands or in other words complete charge carrier localisation in the 2D plane.[76]

Only by increasing the crystal domain size experimentally and being informed by the theoretical electronic structure and topological effects, significant improvements in the performance of 2D COFs can be obtained.

2.3. Charge transport regimes in crystalline organic semiconductors

The injection of a charge carrier in an organic semiconductor is typically argued to result in the formation of a polaron. Polarons are positively or negatively charged particles that displace the surrounding atoms from their equilibrium lattice positions to screen the charge. If the relaxation energy is larger than the energy gained through delocalisation in the periodic lattice, localisation is favoured and the polaron forms.[77] Polaron formation results in an increase in the effective mass of the carrier and hence a reduction of the mobility.[78] Polarons are located on polaron energy levels above the HOMO and below the LUMO and are transported via a hopping mechanism from site to site. Since each hop must overcome an activation barrier proportional to the relaxation energy, the mobility increases exponentially with temperature.

For band-like transport, as observed in inorganic semiconductors, a reduction of the mobility is expected as carriers are scattered by phonons. For intrinsic silicon the mobility in the phonon-dominated transport region is proportional to the temperature

$$\mu_{Si} \propto T^{-\frac{3}{2}}$$

where μ_{Si} is the band mobility and T the temperature.[79]

In high-mobility organic semiconductors, a decrease of the mobility with temperature was observed, contradicting the polaron picture. Also, the calculated relaxation energies of the electrons to form polarons in these molecular materials are insufficient to favour polaron formation.[80] However, the mobility values observed for these systems are still not in the Drude band regime requiring at least $\mu \gtrsim 50$ cm^2 V^{-1}s^{-1} at room temperature.[81]

These observations gave rise to the formulation of a new theory, the transient localisation theory for high mobility organic semiconductors. It describes a transport regime where charge carriers, instead of being weakly scattered, move through a slowly varying, strongly disordered environment. This dynamic disorder is caused by thermal fluctuations. For this reason, unlike in materials with Anderson localisation (also called strong localisation, a quantum process leading to localisation of a wave due to static disorder) caused by static, structural disorder,

dynamic disorder does not lead to the occurrence of thermally excited carriers, and decreases the mobility at higher temperatures, correctly predicting the experimentally observed behaviour. The transient localisation mobility can be described by

$$\mu = \frac{e}{k_B T} \frac{L^2}{2\tau_{vib}}$$

where μ is the charge carrier mobility, e is the elementary charge, L is the transient localisation length, k_B is the Boltzmann constant, T is the temperature and τ_{vib} is the timescale of intermolecular motion.[81]

If energetic disorder is too strong, charge carriers become localised on one molecular unit whereby the transient localisation theory becomes invalid and a description by thermally activated hopping has to be applied as detailed at the beginning of the section. The breakdown of the transient localisation regime can be simulated in the equation for the transient localisation mobility by setting $L \approx a \approx$ 6 Å or one molecular unit, k_BT = 25 meV and $\tau_{vib} = \omega_0^{-1}$ with $\hbar\omega_0 \approx 5$ meV, the time scale of an intermolecular motion where ħ is the reduced Planck constant and ω_0 the frequency resulting in $\mu \lesssim 0.5$ cm^2 V^{-1} s^{-1}.[81] Hence, reducing the dynamic disorder for example by increasing the covalent character and thus reducing intermolecular interactions is a promising strategy to increase the mobility in an organic semiconductor.

Exploring today's commercially employed organic semiconductors for opto-electronic devices with this theory gives a better understanding of the processes at hand. We can subdivide them into firstly small molecular semiconductors such as Rubrene or tri-isopropylsilyly-ethynyl-pentacene and secondly polymeric semiconductors such as polyfluorenes or polythiophenes.

Small molecular semiconductors can be altered at the atomic scale to obtain different crystallisation behaviour and charge transport behaviours as well as different emission energies (Figure 4, top). Purification is typically possible by preparative chromatography. The highest transistor mobility of 18 cm^2 V^{-1} s^{-1} is observed in small molecular single crystals of Rubrene, which still does not fall into the band transport regime.[82]

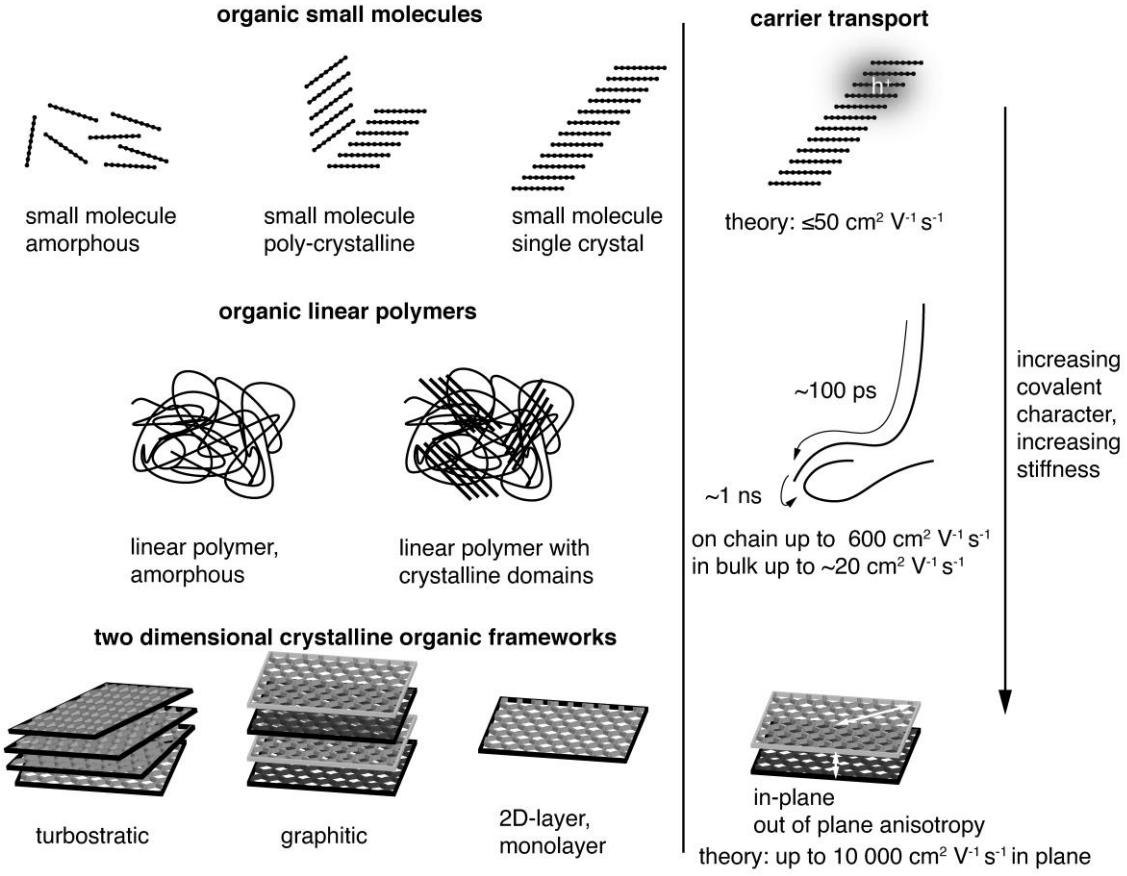

Figure 4. Three different stages of covalent character in organic semiconductors: 0D small molecules, 1D polymers and 2D conjugated covalent organic frameworks.

The mobility observed in the small molecular crystals is governed, as elucidated above, by transient localisation physics. Increased mobility can be obtained by molecular design, reducing coupling between carriers and molecular vibrations and hence decrease the localisation. For actual materials and devices the upper limit can be estimated from band theory to be 50 $cm^2 V^{-1}s^{-1}$ at room temperature, in the presence of intramolecular vibrations only, without consideration of defects and intermolecular vibrations.[81]

To allow even higher mobility, the second class - stiff macromolecular conjugated backbones of ladder-type polymers - have been researched extensively (Figure 4, center).[83] Modern low-disorder donor-acceptor copolymers allow charge transport along the conjugated backbone of the linear polymer. Purification is typically achieved by gel permeation chromatography. The low energetic disorder in these materials is believed to be due to less backbone conformations present. The gain in mobility due to increased chain length typically tails off at a molecular weight

of around 100 kDa. Charge carrier transport along these single chains is correlated with time frames of about 10 ps and mobilities of up to 600 $cm^2 V^{-1} s^{-1}$. However, eventually charges will have to move between neighbouring chains. These structural defects (chain-ends) are acting as traps. These processes are in the nanosecond range and reduce the overall mobility drastically – typically to well under 20 $cm^2 V^{-1} s^{-1}$.

The promise of layered systems, such as covalent organic frameworks (COFs), is to overcome challenges of the molecular and polymeric systems and yield structures with higher mobility, theoretically up to 10 000 $cm^2 V^{-1} s^{-1}$ (Figure 4, bottom).[75] Polymers as well as small molecules are mostly van-der-Waals-cohered solids which allow aforementioned intra- and intermolecular vibrations as well as many different conformations causing (transient-)disorder induced localisation of charge carriers which is expected to be inherently less pronounced in the covalent crystals. The covalent scaffold also allows to diminish drift and diffusion of large atoms or molecular dopants through the material.[84] This could allow addressing different interfaces in multilayer devices and heterostructures separately from each other. Increasing the number of charge carriers by doping increases the conductivity of the material since organic materials have typically only few charge carriers at room temperature ($\sim 10^0$ cm^{-1}).[85]

The conductivity, σ, of a semiconductor can be expressed as

$$\sigma = e\ (\mu_h n_h + \mu_e n_e)$$

with elemental charge e, μ the mobility of the holes and electrons respectively and n the charge carrier density of holes and electrons respectively.[79] This expression clearly demonstrates the importance of a thorough understanding of the density and origin of charge carriers and the charge carrier mobility in a research material to be able to interpret conductivity values accurately.

Isolation of monolayers of the layered covalent materials would allow further miniaturisation of organic semiconducting devices, potentially reducing short-channel effects in field effect transistors and allowing to study the effects of confinement of an electronic system into 2D organic materials. Further, preparation

of van der Waals heterostructures with other 2D materials is of high interest, as it allows to study hybrid inorganic-organic van der Waals heterostructures.[86]
Whereas the charge transport characteristics of small molecular semiconductors and linear polymers are characterized well at this point, the exploration of charge transport and electronic structures of 2D COFs is still at its beginning.
The question arises: If 2D COFs have superior mobility and can be obtained by organic synthesis, what is holding them back? The experimentally obtained mobility values cannot achieve the high mobility values predicted by theory yet. Table 1 shows experimentally obtained mobility values from different 2D COF materials. Whereas performant small molecular organic semiconductors and polymers can exhibit higher mobility than in amorphous silicon (up to 6 $cm^2\ V^{-1}\ s^{-1}$) 2D COFs barely reach this goal yet.[87,88] The performance lack has several reasons. Condensation of conjugated covalent organic crystals has some major obstacles. One obstacle is that in contrast to small molecular semiconductors and polymers there are no post-synthesis purification steps possible. This induced large interest in reversible linking reactions like imine-condensations, or in the case of carbon nitrides polycondensation in a closed reaction chamber, allowing reversible reactions with NH_3 and other intermediates.[89]
Another obstacle is crystallite size. To garner the advantages of the 2D organic materials it is necessary to obtain single crystallites on the order of at least ~100 μm for example for mechanical exfoliation of monolayers (dimension in plane with covalent layers). At the moment mostly nano-crystallites (~200-300 nm) are synthetically accessible.
A major challenge that has not yet been mentioned is acquiring high crystal quality without structural defects. The upper mobility limits that were established in the last paragraphs were only accounting for dynamic disorder by vibrations and slow charge transfer between π-systems connected via van der Waals interaction. However, in real crystals defects like point defects and grain boundaries have to be expected but are hard to study in the nano-crystalline realm as methods that could resolve point defects like scanning force microscopy are not suitable. Additionally, not all materials have the topology allowing high mobility of charge carriers in their electronic system. An interesting topology study by Thomas et al. indicated that

three-armed cores with high symmetry are expected to show flat bands. The study found that four-armed cores are topologically superior for charge transport with higher band dispersion.[90]

In summary, one can conclude that to achieve high mobility 2D COFs, one has to increase crystal size, decrease defects and aim for a suited symmetry.

Table 1. Experimentally obtained mobility values from 2D COF materials. Table reproduced from Burmeister et al..[106]

Material	**Material class**	**Vertical dimension (method)**	**Mobility (charge carrier, method)**	**Ref.**
Graphene	2D semimetal	0.4±0.3 nm (Peak force tapping SFM)	200,000 $cm^2 V^{-1} s^{-1}$ (electron, suspended, 5 K)	[188–190]
Graphdiyne	2D semiconductor		10,000 $cm^2 V^{-1} s^{-1}$ (electron, theory)	[75]
Porphyrin-imine COF	bulk semiconductor	-	8.1 $cm^2 V^{-1} s^{-1}$ (hole, TOF)	[191]
Benzodithiophene -imine COF	bulk semiconductor	1.8 nm (SFM)	3 x 10^{-6} $cm^2 V^{-1} s^{-1}$ (hole, FET)	[192]
Porphyrin-imine COF on hBN (COF-366@hBN)	bulk semiconductor	2.34-4.56 nm (SFM)	0.015 x 10^{-6} $cm^2 V^{-1} s^{-1}$ (hole, FET)	[193]
Porphyrin-dihydroxyphenylene COF	bulk semiconductor	0.7 nm (SFM)	1.3 x 10^{-6} $cm^2 V^{-1} s^{-1}$; 1.6 x 10^{-4} $cm^2 V^{-1} s^{-1}$ (I_2-doped)	[194]
Benzodithiophene -boronate ester COF	bulk semiconductor	80 nm (cross-section SEM)	3 x 10^{-7} $cm^2 V^{-1} s^{-1}$ (hole-only device)	[195]
Graphdiyne	bulk semiconductor	2.9 nm	6.25 $cm^2 V^{-1} s^{-1}$ (FET)	[196]
Poly-1,3,5-benzene Suzuki polymer	bulk semiconductor	-	3.2 $cm^2 V^{-1} s^{-1}$ (FET)	[197]
Triazatruxene Suzuki polymer	bulk semiconductor	2.5-46 nm (SFM)	1.37 $cm^2 V^{-1} s^{-1}$ (hole, FET)	[198]

2.4. Current description of transport in carbon nitride materials

As discussed, heteronuclear 2D covalent materials and, as such, graphitic carbon nitrides, bear the hope to supply high mobility, 2D semiconductors. The physically existent and studied carbon nitride structures however, as of today, do not fall into the "high mobility", "transient localisation regime" category but rather in the hopping regime. In this paragraph we will lay out why, looking at three aspects of charge transport in the materials: firstly, in-plane transport; secondly, out of plane transport; and lastly, transport in polycrystalline films.

The goal in organic 2D materials is to obtain high in-plane transport, a major reason why this is difficult in graphitic carbon nitrides is that the electronic structure of TGCN as well as PTI shows low dispersion (band curvature) of the valence and conduction band around the Γ-point, implicating high effective masses of respective charge carriers.[12]

The major reason for the high degree of localisation in materials bridged by secondary amine units like PTI is the sp^3 hybridisation. Even though PXRD measurements suggest that the nitrogen bridge is in plane with the rings in intercalated structures, DFT simulations typically predict buckled structures with the hydrogen at the nitrogen not completely in plane in bulk materials, pointing toward remaining sp^3 character.

An experimental study comparing in-plane and out-of-plane conductivity in nano-crystalline TGCN samples found that indeed the out-of-plane conductivity is about 65 times higher compared to in-plane measurements. The experimental efforts were compared to theoretical random walk simulations, showing that hopping transport would be favoured out-of-plane.[91] These findings are a first indication that indeed the localisation of carriers in-plane is so high that out-of-plane hopping between the stacked conjugated rings is more effective than in-plane transport.

Since no graphitic carbon nitride single crystals large enough for individual electric characterisation and band structure characterisation with elaborate photoelectron emission methods are available as of today, all experimental electronic measurements rely on polycrystalline samples with domain sizes on the order of 200 nm supported by calculated band structures.

Next to in-plane and out-of-plane transport an important aspect is the morphology of the material. In materials like PTI, crystallites are loosely packed, impeding effective charge transport between the crystallites due to “crystal boundaries” that have to be overcome. Similar to the polymer case, where charge carriers can move vastly better on-chain than between chains, this leads to an increased resistivity over relevant film dimensions for electric characterisation.

To experimentally study the electronic properties of these materials, higher quality and larger crystallites need to be obtained. The obtained materials can be utilized depending on morphology and properties in different electrical devices which will be elucidated in the following sections.

2.5. (Organic) thin film transistors

One of the most common organic field effect transistor (OFET) architectures used to characterize the electronic properties and performance of organic semiconductors is the organic thin film transistor (OTFT). The OTFT is a device comprising three terminals, namely source, drain, and gate. (Figure 5 a). A thin film (20-200 nm) of an organic semiconductor, called the active layer, is either spincoated or evaporated by physical vapour deposition onto what is referred to as the “gate insulator” (typically silicon dioxide). The gate insulator electrically separates the “gate” (typically doped and conductive silicon) from the active layer as well as source and drain electrodes. COF films can either be grown from solution directly on a substrate; alternatively, a thin film can be transferred onto a substrate. For a top contact device the source and drain contacts are evaporated on top of the active layer. Bottom contact devices have the source and drain contacts prefabricated directly on the gate insulator, and the active layer is deposited on top.

Typically, organic semiconducting materials show similar electron and hole mobilities. However, the surface groups of commonly used gate insulator materials

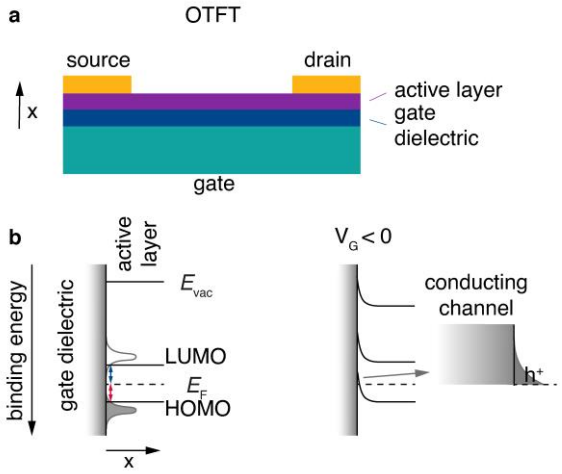

Figure 5. a) Schematic of a top contact bottom gate organic thin film transistor. b) Electronic levels at a semiconductor gate interface, relevant for the operation of the transistor in hole accumulation mode. (Figure reproduced from Burmeister et al..)[106]

– such as silicon dioxide – negatively affect the electron conduction by trapping electrons.[92,93] Ambient water and oxygen have the same effect. For this reason, simple OTFT architectures are most often only used in p-type operation (i.e., hole conduction). To enable stable n-type conduction in an organic semiconductor under ambient conditions, the onset lowest unoccupied molecular orbital energy has to be more negative than -4 eV. To reach this threshold, electron-withdrawing groups or heteroatoms have to be introduced into the structure of the semiconductor.[74,94]

Charge transport in organic small molecules and conjugated one-dimensional polymers is predominantly hopping between adjacent π-orbitals, therefore it is expedient to think of the energy levels as a Gaussian-shaped distribution of localised highest occupied molecular orbital (HOMO) and lowest unoccupied molecular orbital (LUMO) states.[85] Even "band-like" transport characteristics in small molecule single crystals cannot be equated with band transport in inorganic materials.[95] The energy level alignment of a typical OTFT architecture without applied voltage is depicted (Figure 5 b, left). To simplify the concept, the onsets of the LUMO and HOMO are denoted as lines.

An ideal semiconducting organic material has close to no charge carriers at room temperature, and typically injection barriers are present between the organic active layer and the metal contacts (Fermi level pinning).[85] This results in hole and electron injection barriers (Figure 5 b, red and blue arrow, respectively) which are

the energetic differences between the Fermi level and the onsets of HOMO and LUMO, respectively.

For an applied voltage between drain and source (V_{DS}) the corresponding current (I_{DS}) is therefore low; this is called the "off-state". To switch to the "on-state", negative gate voltage (V_G) is applied between source and gate electrode resulting in an electric field arising between gate and active layer. The electric field and therefore the field effect can be maximised by decreasing the gate insulator thickness with a 2D insulator, for example with hBN or by using a high k dielectric. A 2D example is using highly crystalline hBN to increase the performance of 2D transistors by providing a trap-free as well as thin dielectric.[96] Its main task is however to inhibit current flow between gate and active layer and the result is what can be thought of as a capacitor. Positive charge carriers start to accumulate in the active material at the insulator interface (Figure 5, b, right). This local positive "charging" of the active material induces a reduction of the local Fermi level of the active layer at the insulator interface, resulting in an alignment of the transport states (HOMO) of the active layer and the electrode Fermi level. The now established energy level alignment constitutes a conductive channel for holes which can be injected from the source electrode. The described effect is synonymous to the "field effect" in organic materials and "switches" the previously non-conductive active material into a conducting channel for holes. For an applied voltage V_{DS} the corresponding current I_{DS} should be increased by orders of magnitudes compared to the off-state. Due to the necessary accumulation of charges at the interface between insulator and active layer, this mode of operation is known as "accumulation" or "enhancement".[97] An electron conduction mode can be established if the device architecture (no Si-OH/active layer interface) and the material (no charge traps for electrons) allow it. Transistors that function in electron as well as hole conduction mode are called ambipolar. The extraction of the field-effect mobility from the obtained I-V curves (output characteristics and transfer curves) is discussed in great detail elsewhere.[98]

Replacing the active layer of a field effect transistor with a 2D crystal has two major advantages. 3D materials like silicon stripped down to less than 3 nm thickness are strongly affected by dangling bonds. The dangling bonds constitute scattering sites

which decrease the mobility of the material at these small dimensions. 2D crystals on the other hand are atomically thin without dangling bonds, therefore the problem is non-existent for this material class. The second merit of 2D crystals lies in their electrostatic properties. In short-channel field effect transistors with 3D active layers current leakage is typically induced due to poorly controllable electrostatics between electrons in the channel and the electric field applied by the gate. Whereas the channel in 3D active layers has a physical extension, in 2D crystals all carriers are confined to the atomically thin channel and the electric field can take effect more evenly.

2.6. Organic- light emitting diode

One of the overarching goals is to explore the applicability of graphitic carbon nitrides in optoelectronic devices. Organic light emitting diodes (OLEDs) can be produced from various organic semiconductors (OSCs) and are less reliant on high structural order and mobility as for example field effect transistors.

Figure 6 summarizes the most important processes in an OLED.[97] The emission layer, the organic semiconductor is sandwiched between two electrodes. The cathode has a low work function (here exemplified by calcium) and the anode has a high work function (here denoted as PEDOT:PSS). The goal is to line up the highest occupied molecular orbital (HOMO) level of the emitter with the Fermi level of the anode, or hole transport layer, and the lowest unoccupied molecular orbital (LUMO) with the Fermi level of the cathode to enable effective charge carrier injection without large injection barriers. If an external voltage is applied holes are injected from the anode and electrons are injected from the cathode. In most emitter materials the injected charges can be considered negative and positive polarons

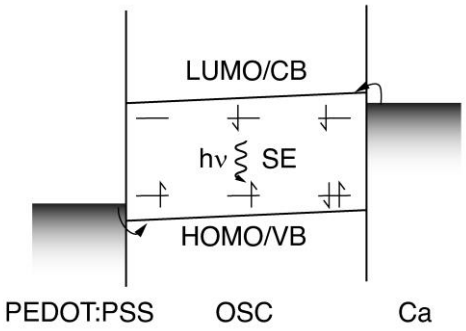

Figure 6. Schematic depiction of the energy levels and fundamental processes in a single layer organic light emitting device. (Figure adapted from Koch.[97])

(Figure 6, denoted by unpaired electrons in polaron states above the HOMO and below the LUMO). If two polarons of opposite charge meet, they can form a bound neutral quasiparticle, an exciton. Typical lifetimes of excitons in organic semiconductors are in the nano-second regime whereupon they radiatively decay.[99]

Due to the lack of heavy elements in organic semiconductors, spin statistics lead to a 25:75 singlet to triplet exciton ratio. Triplet states are long-lived and tend to recombine non-radiatively, reducing the efficiency of the device. It should be mentioned that current research has found processes to increase the singlet quantum yield (thermally activated delayed fluorescence), however in the scope of this work the fundamental process of singlet exciton (SE) (Figure 6) emission is sufficient to follow along.[100]

Typically, OLED emitters are small-molecules or polymers utilizing fluorescence, phosphorescence or thermally activated delayed fluorescence recombination pathways.[101] Until now there have been no reports of successful integration of covalent organic frameworks into OLEDs as processing into homogeneous films is challenging and the defect density of the structures is typically high.

2.7. An attempt to classify research materials on the basis of literature

Choosing research materials to work with in a project can be a daunting task as everyday a plethora of new papers is published and often it is difficult to reproduce highly optimized synthesis conditions in one's own lab. Especially starting a new project one finds oneself with little experience regarding the new material.

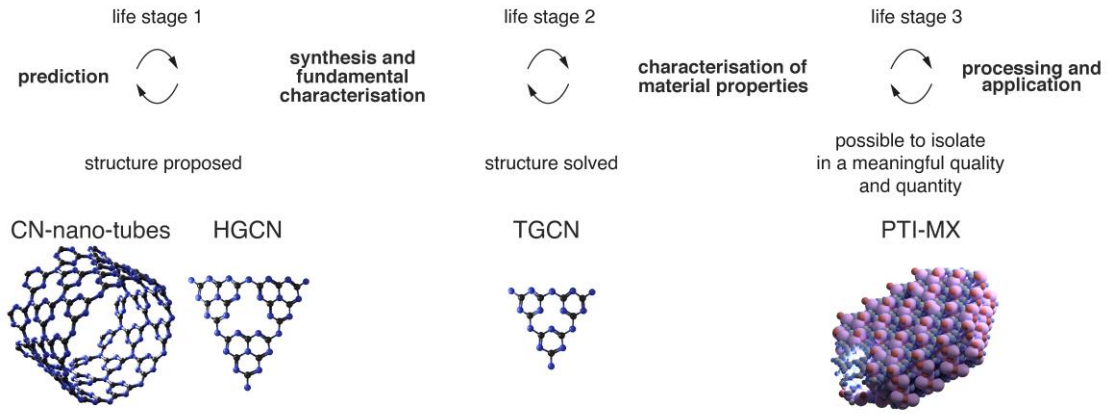

Figure 7. Assigning materials from literature to a "life stage" can help to understand current challenges that the material or material class faces and point towards useful goals the material has to meet to become viable for high value applications.

One of the most helpful distinctions one can try to make comparing different materials in current literature is trying to access their viability for certain use cases. For this one can subdivide them into "life stages" (Figure 7). Especially at the beginning of a project it is beneficial to have a thorough understanding of how established the new material or material class is in terms of structural characterisation as well as material properties.

Materials in life stage 1 are only predicted but have not been synthesized. Due to the drastic increase in computational power it is possible to create and study whole libraries of compounds theoretically via DFT. An example for a life stage one material in the world of carbon nitrides would be carbon nitride Bucky balls and nanotubes.[102,103] However, what can typically not be obtained, as of today, from these calculations are reasonable synthetic pathways for the experimental synthesis of these theoretical compounds. Another good example for a life stage one material is heptazine based graphitic carbon nitride (HGCN). While it is the structure most often associated with so called gCN materials in many pieces of recent literature, crystalline HGCN has yet to be synthezised. This life stage is therefore defined by the absence or disproven experimental characterisation of a material like HGCN.

The next life stage is defined by successful connection between a material (e.g. two dimensionally covalently interlinked heptazine units (HGCN)) and structural solution by experimental data obtained from crystallites. This is the stage where a material gets "discovered". It is not necessarily pure (mixed phases) nor defect-free

and it might be not possible to collect resilient data for material properties from electrical measurements as defects dominate the properties. Once the discovery of the material is made, and it has a certain level of interest for the community, typically many groups try to replicate the synthesis to use their established property manipulation pathways to obtain a better material. If it is not possible to increase the product quality and quantity from this life stage like observed for example for TGCN up to this point, processing and application are not possible.[57,104]

Once the material can be obtained in a high quality and quantity the material enters stage three. It is now possible to obtain resilient material properties which inform the scientist on which applications might be of interest. For example, if the material is structurally fully characterized and one does not find large disparities between the theoretic models and the experimental values the goalpost shifts to application. An example for a material from the class of carbon nitrides is PTI. To access the viability of PTI in e.g. an OLED, useful scientific questions are: Is there photoluminescence and at what energy? How large is the quantum yield? How long is the fluorescence lifetime? How do these values compare to known organic emitters? This enables the experimentalist to set the expectations for the experiment.

This classification is meant as part of an approach to protect early career scientists in the field of material science from submitting too early in the material life to advanced material characterisation methods and applications and lose precious time on gathering uninterpretable results. This is especially important if the goal is to use the material in high value applications like OLEDs or transistors as the charge transport and optical properties in the semiconductor is highly dependent on the defect amount and the electronic structure of the materials.

2.8. Theory of applied material science: Improving semiconducting crystalline organic frameworks towards application

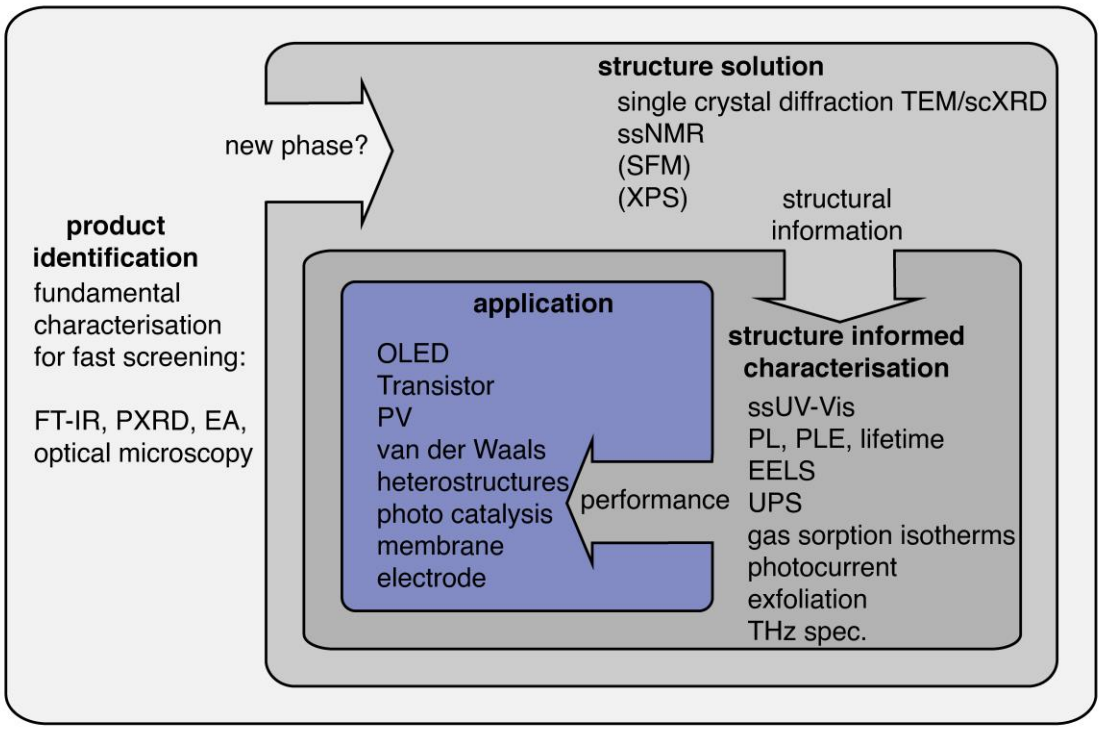

Figure 8. Towards application: Characterisation flow chart for complex products subdivided into four steps: Product identification or screening, structure solution, structure-informed characterisation and performance-informed application.

Repeating published procedures for the synthesis of new materials can be challenging, as sometimes small differences in experimental layout have been crucial to the success of the original work. Hence, synthesising and working with new materials requires monitoring as many material properties as possible for all obtained products.

A flow-chart-like method of characterisation can help to minimize time spend on elaborate characterisation methods when the material quality does not suffice to obtain resilient data from more sensitive characterisation methods, e.g. ultraviolet photoelectron spectroscopy (UPS), transmission electron microscopy (TEM), scanning force microscopy (SFM) etc.. It is important to gain an understanding at what point a material is suited for a certain method. While this understanding will also be gained with experience, it is worth to have a guideline to minimize frustration in the early parts of a material science project. The presented

characterisation flow chart can be generalised from carbon nitrides to other crystalline organic systems (Figure 8). While it will not be applicable in all cases and often it might be advisable to look at the here presented steps in parallel due to time pressure, the conceptualisation and visualisation of a material characterisation from start to application can be of great help.

The first step, product identification or screening consists of four fast typically highly accessible methods, Fourier transform-infrared spectroscopy (FT-IR), PXRD, elemental analysis (EA) and optical microscopy. The most important question at this foundation building step is if the obtained phase is known (if yes, how pure is it?)? If databank searches are inconclusive and comparison to other similar synthesis conditions does not yield an answer, the next step is structure solution. Obtaining a crystalline product that can be structurally solved often requires to optimise synthesis conditions. If the crystallinity cannot be increased to a degree where single crystal diffraction is possible, describing the building blocks obtained from vibrational analysis and solid state nuclear magnetic resonance spectroscopy (ssNMR) and preparation of a proposed structure should be conducted.

If the structure was solved successfully it is used to inform the scientist which direction of application might be interesting and, accordingly, the more time-consuming characterisation methods of step three would be chosen.

With the performance parameters or material properties at hand it is possible to decide whether or not the next large time investment should go into preparation and potentially optimisation of the application chosen.

For example, a typical line of thought following this flow chart would be: Does the structure have a conjugated system that can be used for charge transport? Does the conjugated system show visible photoluminescence and a low lifetime? Can the product be processed into thin films? Is there electroluminescence in an organic light emitting diode?

While this figure is obviously a simplification, it encapsulates the vast range of problem-solving skill that is required to move from one step to the next and the multitude of characterisation methods one has to be aware of to be able to make educated decisions. To successfully pursue such a project, strong interdisciplinary bonds as well as connections between institutions are valuable.

2.9. Context and definition for the “graphitic carbon nitride” material

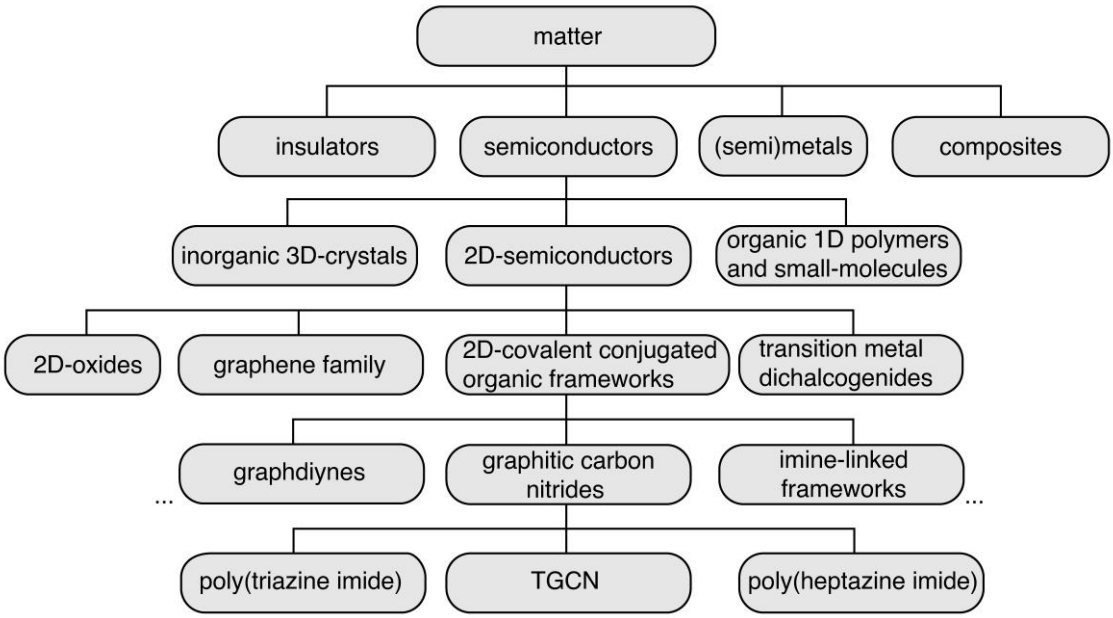

Figure 9. Contextualisation of graphitic carbon nitride materials in a material family tree.

Materials can be subdivided into various classes according to their properties. In Figure 9, a visualisation of the material classes linked with graphitic carbon nitrides is presented. In the context of electronic devices it is useful to first distinguish metals, insulators, and semiconductors. Semiconductors can be subdivided into inorganic, organic and 2D semiconductors. The subdivision of the 2D semiconductor material class is inspired by Geim et al. and extended with 2D covalent, conjugated, organic frameworks (2D COF).[11] In organic chemistry the term commonly used for organic covalent scaffolds is crystalline organic framework (COF). However, this umbrella term includes also 3D covalent structures and non-conjugated structures that are not interesting in the search for new organic semiconducting 2D materials. Throughout this work the term 2D COF is used to specify materials that are crystalline, covalent, organic, framework materials with conjugated subunits.

The subdivision of the 2D COF class is mostly determined by the linking chemistry such as diyne- or imine-linkers between conjugated subunits. Graphitic carbon nitrides are allocated an extra subclass as their synthesis and properties differ distinctively from the other organic 2D COFs.

Material science as part of applied sciences relies on conceptualisation of matter by finding the most appropriate descriptors. As we already found out revisiting the

history of carbon nitrides, the use of some descriptors as for example “graphitic” in gCN or HGCN were discovered to be misinterpretations. To avoid this confusion the definitions of the terms used to describe graphitic carbon nitrides will be laid out in this paragraph.

Graphitic is a term used for a crystalline material with covalent bonds in a two dimensional plane and a non-covalent interaction between these planes. Additionally, the material exhibits a stacking order (e.g. AB or AA). In contrast, turbostratic materials are materials exhibiting two dimensional layers as well, however the planes are rotationally faulted, without a stacking order.[105] This can be due to energy differences between stacking modes being small, allowing for different energetic minima and random lateral displacement of layers to each other. 2D materials are materials only consisting of one atomic layer of their graphitic parent material the most famous example being graphite as parent material of graphene. This distinction is important and one of the major reasons for the great scientific interest in this material class, as the confinement of the electronic system into the two dimensional material can lead to drastic changes of the material properties. In graphene the electronic structure exhibits Dirac cones that allow the existence of massless electrons while in MoS_2 one observes a transformation of an indirect to a direct band gap material.[9,10]

Synthesis of 2D materials can be persued in a bottom-up approach for example by synthesis at liquid-liquid phase borders or in a bottom-down approach using mechanical exfoliation of the parent crystal.[106]

Graphitic carbon nitrides that have been successfully synthezised in sizable quantities are poly(triazine imide) and poly(hepazine imide) (Figure 9, left row).[107] These structures, however, still contain stoichiometric amounts of hydrogen at the imine bonds. Hence, they could be also referred to as graphitic CNH materials which would be arguably more accurate. For the sake of simplicity in this work the term “graphitic carbon nitrides” encompasses graphitic CN as well as CNH materials. The first discovery of a graphitic material containing only carbon and nitrogen in a C_3N_4 stoichiometry was made 2014. The structural analysis indicated it to be triazine-based graphitic carbon nitride (TGCN) (Figure 10, top right). The tri-*s*-triazine analogue, heptazine based graphitic carbon nitride (HGCN), has not yet been

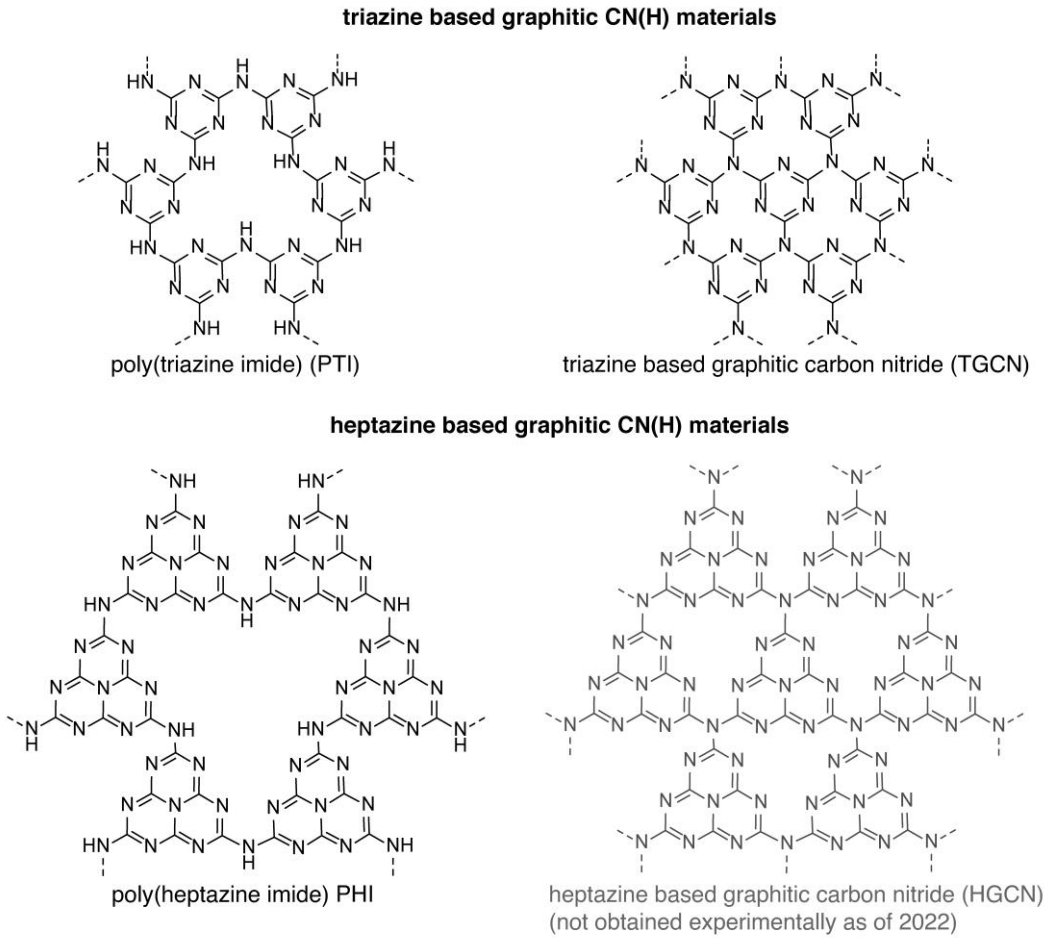

Figure 10. Cut outs of covalently bonded planes from graphitic CN(H) materials depicted without intercalated ions and defects. Top row: graphitic materials based on triazine buiding blocks. Bottom row: graphitic materials based on tri-*s*-triazine buiding blocks.

obtained (Figure 10, bottom right). The stacking distance in ion containing structures typically exceeds that of intercalation free products (PTI-LiBr 3.52 Å, PTI-IF water free 3.23 Å).[14,108] More exotic phases of carbon nitrides such as tubes and fullerene like structures are discussed in literature but will not be elaborated on since they have not been successfully synthesized yet.[102,109,110]

The high nitrogen content in the structures results in properties that are rarely found in organic semiconducting materials. The products are typically highly temperature-resistant and have high ionisation potentials as well as high electron affinities. Hence, high environmental stability and potentially stable n-type transport in the materials are projected.

Chapter 3. Experimental procedures for condensed carbon nitrides

Jack of all trades, master of none.
Geffray Minshull, 1618.

In the following chapter the particularities of synthesis and characterisation methods for carbon nitride phases are presented. Specific synthesis procedures for the different eutectics as well as the employed materials and instruments can be found in the appendix.

3.1. Synthesis of carbon nitrides in eutectic salt melts

The first attempts to obtain highly condensed carbon nitrides were made by heating carbon nitride precursors such as urea up to 600 °C in air and analysing the products. Today we know that the highest condensed product that can be obtained in this way is melon.[18] To obtain other phases many reaction conditions were researched such as: Synthesis in anvil cells, condensation directly at interfaces, sputtering, and electrochemical deposition.[106] However, these mostly resulted in disordered CNH materials instead of crystalline frameworks and often had low yields. The most successful approach discovered to date is synthesis in ionothermal conditions utilizing a eutectic salt melt. This synthesis allowed condensation of the first truly graphitic carbon nitride, poly(triazine imide) with lithium chloride intercalation (PTI-LiCl).[112] The success of obtaining nearly quantitative amounts of a highly condensed graphitic carbon nitride sparked widespread interest in the condensation of carbon nitrides in eutectic salt melts.

The following description of the synthesis and characterisation methods used in this work is meant to communicate a basic understanding of the tool set nessesary for ionothermal synthesis. The preparation of the eutectic requires dried salts. These can be either bought as anhydrous salt from suppliers and directly transferred into the glovebox, which is the least time consuming way or have to be obtained by drying the salt. To dry the salt it is necessary to weigh in about 20% more since hygroscopic salts like LiBr tend to have crystal water. To be as close as possible to the eutectic point it is also advisable not to dry the eutectic mixture of the salts but to dry the salts separately as they can have different amounts of crystal water. This can lead to significant errors in the salt ratio obtained after drying. Drying can be performed in a round bottom flask with greased hollow glass stopper and valve under reduced pressure ($<10^{-3}$ mbar) for 48-72 h at 200 °C.

Once the dry salts are obtained the round bottom flask is flushed with argon and evacuated for transfer into the glove box.

The quartz ampules (12 cm long, inner diameter 27 mm, outer diameter 27 mm, long neck inner diameter 8 mm with NS14 female joint) are prepared by being rinsed with Milli-Q water and acetone, dried in the drying cabinet, equipped with a greased hollow glass stopper, heatgun-dried, and evacuated.

The salt, ampules, a mortar with pistil, spatulas, weighing dishes and an ampule funnel are transferred into the glovebox and the eutectic salt mixture is prepared. The salts are ground in the mortar, weighed in and mixed with the pre-ground precursor (dicyandiamide). The finished reaction mixture of eutectic and precursor is then once more ground thoroughly to give a silica-like, fine powder. The freshly ground powder is transferred into the ampule. A standard amount of eutectic is either ~50 g for three ampules or 100 g for 6 ampules with each 15 g eutectic and 1 g dicyanamide.

It is crucial for being able to close the quarz ampule to use a funnel with a long stem to not contaminate the neck of the ampule. Carbon residues on the inside of the ampule negate the flow behaviour of quarz (melting point 1700 °C) due to formation of silicon carbide (2300 °C, decomposition).

The filled ampules are reequipped with the hollow glass stopper with valve and transferred out closed. The ampules are evacuated slowly as the powder is easily thrown up and pulled into the Schlenk line ($<10^{-3}$ mbar for 5 min).

The ampules are then transported to a quartz glass blower and closed in a hydrogen flame (Figure 11). The closed ampule is then placed in the furnace either at room temperature or in a pre-heated condition and the temperature program is run. An easily overlooked pitfall can be the furnace layout. In the case of the Nabertherm, L 5/11/B180 the heating coils are placed directly under the bottom plate. With an IR-thermometer temperature differences of up to 70 K are present during the heating phase between the temperature shown by the furnace display which are determined at the top of the oven and the actual temperature of the bottom plate. This can lead to fast degradation of organic samples at synthesis temperatures close to their decomposition

Figure 11. Mr. Müller from Glasbläserei Müller (Adlershof, Berlin) closing ampules with a hydrogen flame of a reaction mixture for graphitic carbon nitride synthesis.

temperature. To address this one can reduce the heating slope and protect the ampule from direct contact with the bottom plate (Figure 12).

The position of the Ampules should be held constant between experiments to subject all ampules to the same conditions. The two major variables for the heating program are reaction temperature and duration. The maximum temperature is set by the onset of carbonisation which is evident by a brown discolouration of the obtained product. Temperatures above 550 °C have shown to be non-expedient in this work for this very reason. With prolonged reaction times (seven days) complete condensation of DCDA to PTI-LiBr is possible at temperatures as low as 475 °C.

After natural cooling of the furnace, when the reaction is complete, the ampule is broken by making a predefined breaking point with a glass cutter and breaking the ampule inside a sheet of aluminium foil. This prevents glass shrapnel to a large extent but should still be done under a fume hood, as ammonia and other volatile reaction products are set free. The salt monolith is taken out, and glass shards are removed from it. If the top of the salt block is coloured brown it is likely that at the surface an unwanted carbonisation reaction took place. Depending on requirements for the product, it makes sense to discard the top part of the salt block by either sawing or scraping it off with a razor blade. This will reduce the yield but may further increase product homogeneity which is much more important if the goal is to use it for example in optoelectronic devices. The salt block is then transferred into a 50 mL falcon tube and filled to about 35 mL with hot Milli-Q water. The salt block is dissolved in about five minutes by shaking it on a shaker and the slurry is centrifuged, the supernatant is discarded and the pellet is washed three times with water and two times with methanol.

Figure 12. Additional porcelain spacers between bottom plate and ampule to reduce over-shooting the target temperature during heating slopes.

The product is then transferred into vacuum-safe glassware and the methanol is evaporated. The

product is then dried at 200 °C for 24 h and the yield is determined.

Crystalline compounds obtained from this synthesis are typically either intercalation compounds like PTI-LiBr or small molecules like Melem. The only discovery of a highly condensed C_3N_4 compound obtained from a synthesis like this is reported to be triazine-based graphitic carbon nitride (TGCN). Deintercalation of the obtained product can be performed via Soxhlet extraction with water for three to twenty days.

Advantages and disadvantages of polycondensation reactions in eutectic salt melts compared to conventional polymerisations

To understand the choice of the eutectic salt melt for the reactions presented in this work it is important to make a comparison with the approach that would be used in modern synthesis approaches for covalent organic frameworks like imine-COFs.[113] One of the biggest distinguishing factors is that the poly-condensation reaction does not require synthesis of monomer molecules. A low-cost CN-precursor like dicyandiamide or melamine can be used for the condensation reaction. The C_3N_3-rings, and subsequently the condensed structures are formed in situ.

This allows synthesis of the materials in gram scale and implies easy upscaling.

However, this comes also with a disadvantage: The obtained structures are determined by thermodynamics diminishing the opportunity to manipulate the structure with atomic precision by changing the monomer structure as would be possible in the synthesis of e.g. imine-COF monomer units.

An advantage of the ionothermal conditions is that they can stabilise phases that are not observed in absence of the salt melt e.g. PTI. Formation of these crystallites is enabled by the stabilisation of the graphitic structure by the ion intercalation almost like a three-dimensional epitaxy. Condensed crystalline structures without intercalation are only rarely found and are only present in extremely small quantities, e.g. TGCN. Salt intercalation can be removed from graphitic crystallites by Soxhlet extraction to obtain an intercalation free CNH compound.

As of writing this work, new synthesis approaches for mono crystalline COFs are successfully applied, for example synthesis in supercritical fluids.[114] While suited for 2D imine COFs these methods would likely not be applicable to condense pure

graphitic CN systems as the activation energy for the condensation reaction is too high.

A general feature seems to be the inhomogeneous crystal growth of the crystallites obtained, as the crystals appear to be elongated in the stacking direction rather than in the plane of the covalent bonds. For 2D electronics, crystals with large covalent planes instead of elongated stacked structures are necessary.

An additional challenge working with products from eutectic salt melts can be the presence of low-solubility salt crystals in the product. This underlines the necessity of characterisation with orthogonal methods and solid fundamental characterisation to avoid mistaking salt crystals for carbon nitride phases.

3.2. Characterisation methods and sample requirements

Elemental analysis

Elemental analysis of the bulk material is the first step to define a material as it provides crucial information about its elemental components. In this work the elemental composition of the powders was determined by using a combination of combustion EA and inductively coupled plasma optical emission spectroscopy (ICP-OES for metal ions of Li, Na, K). Proper drying is crucial as residual solvent (methanol, water) can cause large errors in the hydrogen amount and lead to misinterpretation of the condensation degree of the sample. Samples for combustion are dried at 200 °C for 24 h as described in Chapter 3 transferred into the glovebox and ~1 mg is weighed into a combustion boat. The combustion boat is closed and transferred in inert atmosphere to the measurement service. Samples for ICP-OES are dissolved in a mixture of sulfuric acid, nitric acid and hydrochloric acid in a ratio of 2:2:1. The carbon nitride samples were heated in the microwave in the acidic mixture to accomplish sample digestion before they were diluted with distilled water.

Sample requirements: powder, ~100 mg for multiple measurements.

Vibrational analysis

With information about the elemental composition being collected, fast and typically accessible methods to obtain information about present bond types and

structural building blocks in the material is vibrational analysis by attenuated total reflection Fourier transform-infrared spectroscopy (ATR FT-IR) and Raman spectroscopy. Especially FT-IR allows a fast answer to the amount of residual NH end groups (~3200-3300 cm^{-1}) and the presence of C_3N_3 ring stretches (~810 cm^{-1}) pointing towards the presence of triazine or heptazine.[115]

For distinction between heptazine and triazine and addressing single crystallites, UV-Raman microscopy can be a first indicator as heptazine has strong bands at 1155 and 545 cm^{-1}.[116]

To measure Raman spectra of graphitic carbon nitrides like PTI, it is necessary to use a UV-excitation source. It is argued that a UV-source is necessary to excite the ring modes, as the higher energy (i.e., lower wavelength) allows to excite spatially localized modes better.[57,117] Two reasons why the UV-excitation source enhances the Raman intensity obtained from these modes with UV-excitation can be added. The first point is that the Raman scattering intensity generally scales with $\sim\nu_0^4$, with ν_0 being the wavenumber of the excitation source. Hence, lasers with shorter wavelength result in higher Raman scattering intensity. The second point is the resonance effect. When the excitation source is close to the optical gap (3.2-3.5 eV) of the material the Raman scattering intensity is enhanced. Still, the scattering cross section of the triazine rings in (PTI) is severely reduced when compared to molecules like melamine that can be measured with excitation sources in the visible region e.g. 532 nm even though band gap as well as the triazine mode are very similar.[118] Another advantage of deep UV-Raman measurements, e.g. at 266 nm (4.6 eV) is that one can mostly avoid the fluorescence background of the semiconducting samples.

Sample requirements ATR FT-IR: powder, ~3mg, non-destructive

Sample requirements UV-Raman microscopy: crystallites or thin film on quarz-substrate.

Optical microscopy

Optical microscopy is a fast way to obtain information about the presence of macroscopic crystallites and the crystal morphology. In the case of nano-crystallites optical microscopy is only useful to determine the film morphology.

Confocal laser microscopy

Laser microscopy can be useful to gather quantitative depth information about micro-crystallites or thin films using a step-height measurement.

Solid state nuclear magnetic resonance

Solid state nuclear magnetic resonance (ssNMR) employing cross-polarisation magic angle spinning spectrometer (CPMAS) was utilised to obtain ^{13}C and ^{15}N spectra. The chemical shift allows assignment of carbon and nitrogen species to structural motives like C_3N_3 rings and NH end groups. Collecting spectra of Nitrogen is however time consuming as the isotope has a low natural occurrence of only 0.4%. Sample requirements: powder, ~300mg, non destructive.

Macroscopic diffraction methods, data collection and interpretation

X-ray diffraction is best performed with a Cu Kα source since products can have large unit cells. For powder samples of more than 200 mg a standard plastic sample holder is sufficient. For thin films and low sample amounts, a low-noise single-crystal Si sample holder is advisable. For unit cells under 10° 2θ it is necessary to use a Bruker D8 or equivalent as low-angle signals might not be resolved. Phases that do not exhibit reflections at low angles can be characterized with table-top instruments like the Bruker D2 Phaser.

Analysing different condensation properties, additional reflections hint towards other phases, e.g. carbonisation at 26° 2θ, peak position as the peak position is used to calculate the d-spacing according to Braggs law for constructive interference.[119]

$$n\lambda = 2d\sin(\theta)$$

n = diffraction order

λ = wavelength of the x-ray source

d = crystal-plane distance

θ = glancing angle

Also the full width at half maximum can be monitored as it can be used to estimate the crystallite size as obtained by the Scherrer equation.[120]

$$L = \frac{K\,\lambda}{\Delta(2\theta)\cos(\theta)}$$

L = size of the crystallite orthogonally to the lattice plane of the reflection

K = Scherrer factor, 0.93

λ = wavelength of x-ray radiation

$\Delta(2\theta)$ = full width at half maximum of observed reflection in radians

θ = Bragg angle of reflection or $(2\theta)/2$

Known structures can be fitted by e.g. Accelrys Material Studio 7.0 using a Pawley fit and should obtain a weighted profile R factor (Rwp) value of ∼12 or lower. Materials Studio and FullProf also allow to do Rietveld refinement for structures that have good Pawley fits. However, mixed phases and low crystallinity of the organic condensation products tend to render Rietveld refinement unusable.
For unknown products a data bank search can be conducted. If the structure cannot be assigned, and if eight or more peaks are available, and belong to one phase it is possible to close in on unit cell candidates by indexing algorithms like DICVOL91 and TREOR90 in Materials Studio.

Sample requirements PXRD: standard sample holder: powder ∼300 mg
single crystal Si sample holder: 5 mg powder/films, non destructive.

Single crystal x-ray diffraction

Single crystal x-ray diffraction (scXRD) can be performed for single crystals that can be mounted on 10 μm mounting loops. If the collected data set is integrable with XDSApp3, structure solution can be performed in Olex using ShellXT.[121,122] A main effort is to obtain single crystallites of condensed graphitic carbon nitride phases that can be structurally investigated with this method as it supplies the atomic positions in the unit cell directly. To this point no single crystallites of graphitic carbon nitride with sufficient size were isolated that could be structurally

investigated with scXRD. A valuable tool for mounting carbon nitride crystallites are IMINA piezo micro-actuators. The probe tips can be used for an oil-mediated pickup transfer of small crystallites.

Sample requirements scXRD: Single crystallite size of over 5 μm and enough structural integrity to be mechanically transferred.

Electron microscopy

Electron microscopy is becoming the most versatile analysis method existing as one can perform imaging, elemental analysis, structural analysis, vibrational analysis and analysis of the valence band in one instrument at nanometer scales. Particle size under 1 μm for scanning electron microscopy (SEM) images are better for less charging, especially for samples with low conductivity. Transmission electron microscopy is best conducted with thin sample sheets of sub 200 nm.

It is of utmost importance to have studied the fundamental characterisation of the sample and refined the synthesis conditions to the highest possible degree as one can spend weeks on inhomogeneous sample areas of mm^2 without gaining useful information about the target material. If the goal is to synthesize a "crystalline" material, a few "glassy" peaks in the PXRD with full width at half maximum of larger than 5° 2θ are typically not worth to investigate by electron microscopy. The time is better invested in trying to increase the crystallinity of the product if possible.

Electron diffraction methods like small area electron diffraction (SAED) and convergent beam electron diffraction (CB-ED) are used to collect spot pattern or ring pattern (depending on the nature of the crystallites) of the sample. The observed reflections should be in close agreement with the PXRD results. It can be challenging to find crystallites in zone axis with the incident beam depending on the morphology of the crystallites. Hence it can be useful to collect maps where each pixel is a diffraction image. This also allows observation of dominant orientations of nano-crystallites relative to a surface.

Energy dispersive x-ray spectroscopy (EDX) can be used to obtain informations about the elemental composition. Elements with $z<5$ cannot be monitored by this method, with z the atomic number.[123] Carbon quantification was usually in good

agreement with the expected values even though some carbon is also deposited during the measurement by the electron beam.
Electron energy loss spectroscopy (EELS) allows to obtain qualitative information about the presence of lithium. EELS also enables measurement of the band gap and vibrational spectra of single nano-crystallites.

Sample requirements electron microscopy: Sub mg samples can be analyzed, typically particles are rather to large instead of to small which can lead to severe charging. Organic samples tend to degrade rapidly in the electron beam and are best analyzed using cryo-TEM sample holders and low dose aquisition.

Scanning force microscopy

Scanning force microscopy (SFM) is reliant on clean crystal surfaces to unveil the periodic surface features of crystals. The inhomogeneity of the products obtained by the condensation reaction renders them unsuitable for SFM analysis.
Sample requirement: PTI nanocrystals are not readily imaged as they tend to be moved by the SFM tip on the substrate surface. Nano-crystals also tend to attach to the tip reducing the obtained resolution drastically making unit cell or atomic resolution unviable. Carbon nitride micro-crystals fixed on scotch tape that are larger than 5x5 μm can be successfully approached with modern systems like the Cypher-ES instrument (Asylum Research Oxford Instruments Inc.). The high optical magnification accessible and the possibility to obtain high resolution imaging in amplitude modulation mode (AM) in a nitrogen atmosphere without need for ultra high vacuum or contact mode measurements increase accessibility of this method for organic crystals. The challenge is to place the tip on the crystallite without driving it down the edges to avoid collision of the tip with the crystallite side.
The scanned periodic surface structure can be compared with Connolly surfaces of the crystal structure in Materials Studio.

Sample requirements SFM: Fixed micro-crystals (for example on scotch-tape) with clean surfaces. Surface cleaning can be achieved by sonication in isopropanol of the fixed crystal in some cases.

Nitrogen and carbon dioxide adsorption isotherms

Nitrogen sorption isotherms at low temperatures allow to study the surface area and pore volume of porous materials. Nitrogen is often utilized as its quadrupole moment allows formation of a monolayer on most surfaces.[124] The sample is weighed and transferred into a measurement cell. It is activated at elevated temperatures and reduced pressure to empty the pore volume. After activation nitrogen is slowly inserted into the measuring cell where it interacts with the surface of the sample and its pores. The amount of nitrogen inserted into the cell is monitored as a function of the change of the cell pressure relative to the saturation pressure of nitrogen at the cell temperature (p/p_0). Once the saturation pressure is reached at $p/p_0=1$ the desorption isotherm is collected. The shape of the obtained adsorption and desorption isotherms is indicative of the size and geometry of the pores.[125,126] The surface area can be deduced using the Brunauer-Emmett-Teller (BET) theory. Since liquid amines as well as solid amines with high surface area are interesting for carbon dioxide scrubbing, the heat of adsorption and uptake of CO_2 can be studied.[127,128] To calculate the heat of adsorption, isotherms at different temperatures have to be obtained. The isosteric heat of adsorption is then accessed using the Clausius Clapeyron equation as detailed in the appendix.

Sample requirements: ~50 mg dried sample is required, non destructive.

Absorption and luminescence characterisation

UV-Vis spectra of dispersions and films of nano-crystalline graphitic carbon nitrides are dominated by Rayleigh scattering. Since most electronic transitions are in the UV range where the scattering intensity is high since it is scaling with λ^{-4}, interpretation of the spectra to obtain absorption onsets is challenging.[129] Hence, in parts of this study absorbance maxima were used to describe the position of electronic transitions in the spectra.

For a better description of the optical gap the powder can be pressed into a sample holder for diffuse reflectance measurements in an integrating sphere. With the Kubelka-Munk expression the diffuse reflectance can be converted into absorbance spectra.[130] Using the Tauc expression allows to estimate the size of the optical gap.[131] The equations are detailed in the appendix. Photoluminescence (PL) and

photoluminescence excitation spectra (PLE), lifetime measurements and quantum yield measurements can be obtained from the same sample yielding information about the emissive state(s) corresponding to the chosen excitation energies.
Interactions of sample and acid or dopants can be studied best in dispersions as one can determine the concentrations accurately. Dispersions can be obtained by ultra-sonication in water and sedimentation of large particles by centrifugation.
Absorption spectroscopy (UV-Vis) in transmission geometry sample requirements: Characterisation of low sample amounts is possible, ~1 mg. Sample has to stay dispersed during the measurement.
ssUV-Vis sample requirements: Powders are best pressed into a sample holder and covered with a fitting quartz glass cover to avoid contamination of the integrating sphere.
Lifetime, PL, PLE and quantum yield (QY) sample requirements: These methods are able to study dispersions as well as films and pressed powders. For reflectance measurements, ca 1 cm by 1 cm opaque, flat films or pressed pellet surfaces are required.

Processing

For the following characterisation methods and application in thin-film devices it is necessary to be able to process the product into thin films covering substrate areas as homogeneously as possible. Spin-coating is often not suited due to the low concentration of the dispersions obtained, that are mostly “spun off” the surface during the spin-coating program. Dispersions of nanoparticles tend to cluster during drying after drop casting. This is caused by the “coffee stain effect”. This can be mitigated in some cases by slow drying of the drop-cast films at room temperature.

Electrical conductivity

Studying the electrical conductivity of graphitic carbon nitride nanocrystals can be achieved by electrical measurements of thin films and time-domain-THz spectroscopy of pressed pellets (THz-TDS). Determination of the resistivity of semiconducting samples typically relies on four-point techniques. This method allows to determine the resistance of a sample without the contact resistance (R_c). Common experimental set-ups require however reasonably good conductivity of the sample to be studied as well as a well-defined geometry of the sample and probe tips (~40x larger sample than probe spacing, sheets ~40% of probe spacing or thinner). Due to the low conductivity and the loosely packed nature of the films of graphitic carbon nitrides discussed in this work, four-point measurements with a Jandel four-point probe setup and an Imina-micro-actuator based set up were not viable. To nevertheless study the material properties in a thin film set-up, an interdigitated indium-tin-oxide substrate was used. The high surface area of the electrodes when compared to the probe tips of the four-point technique and the low channel width (50 μm) allowed to obtain IV-characterisation. However, the contact resistance is part of the device resistance unlike in four-point measurements (see schematic in Figure 13). The contact resistance of PTI-LiBr interdigitated devices is estimated by the transfer length method (TLM) to be $2R_c$ = 8.1 10^7± 7.7 10^7 Ω. The uncertainty is caused by the low film homogeneity over the substrate area (drop casting, coffee stain effect). The sheet resistance is R_S = 6.3 10^6±2.3 10^6 Ω □$^{-1}$. The specific contact resistance is ρ_c = 2.3 10^9 ± 0.8 10^9 Ω cm^2. The value is almost four orders of magnitude higher

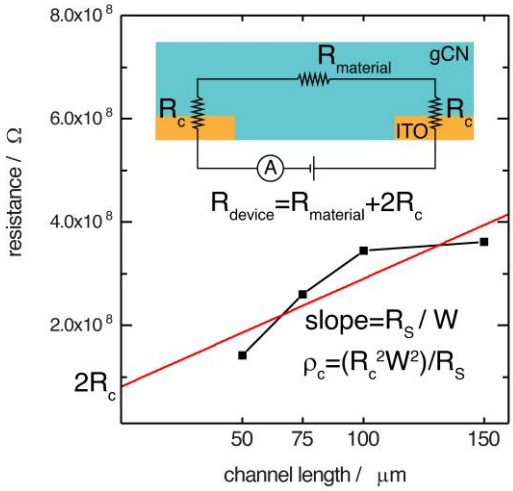

Figure 13. Approximation of the contact resistance in ITO/PTI-LiBr interdigitated devices by transfer length method (TLM). Interdigitated substrates with 50, 75, 100 and 150 μm channel length and 3 cm channel width (W) are produced and the resistance is plotted against the channel length. The y-axis intersection of the linear fit equals $2R_c$ and the slope equals the sheet resistance divided by the width of the channel.

when compared to a commonly used organic semiconductor such as pentacene. Pentacene exhibits a specific contact resistance of 6.58 10^5 $\Omega\,cm^2$ in ITO TLM measurements.[132] This indicates that contact engineering in future device generations will be necessary in order to reduce the contact resistance. In the mostly used 50 μm device set up, $2R_C$ is about half of the total device resistance R_{device}. The conductivity values were obtained neglecting the contact resistance and current crowding using the total device resistance as detailed in the appendix. To consolidate these results, more studies are needed as the uncertainty of the presented TLM measurement is significant.

Since the characterisation of electrical conductivity relies on the transport of charge carriers through a macroscopic distance of the material under investigation it is effected by the morphology of the material. Graphitic carbon nitrides are typically nano-crystalline, meaning that charge carriers have to cross many crystal-crystal interfaces to get from cathode to anode. This further deteriorates the conductivity as charge carriers can be trapped at these interfaces. To study the conductivity at the nano-scale, inside the nano-crystallites THz-TDS can be used. Together with the effective mass of the carriers that can be obtained from a band structure calculated with DFT and the modified Drude–Smith Model (DSM), the mobility and charge carrier density can be accessed. However, this is only possible if the material contains a significant charge carrier density. In intrinsic organic semiconductors this is typically not expected as the charge carrier density should be low $\sim 10^0$ cm^{-3}.[133] However, in metal organic frameworks (MOFs) and COFs there are multiple reported studies indicating that these materials can be studied also in an un-doped state likely due to significant amounts of defect-induced charge carriers.[134–136] THz-TDS results allow to access the conductivity that would be expected for large single crystallites even though at the moment only nano-crystallites are available. Comparison of the conductivity at the nanoscale with macroscopic measurements can be used to study the effect of the nano-crystalline character on charge transport.

Interdigitated substrate

The sample has to be dispersible in a solvent to yield thin films on a substrate. Low sample amounts of 10-20 mg can be sufficient, depending on the film thickness

needed and the thin-film processing method (sample wastage: spin coating>doctor blade> drop casting). Microporous and nano-crystalline samples can be effected by environmental conditions, hence, a study in reduced pressure can be insightful.

Terrahertz-time domain spectroscopy

About 300 mg sample are pressed into a pellet with a pellet press. Samples with low charge carrier density will show no shift in the THz-TDS pulse disallowing the extraction of conductivity and mobility values. For the determination of the charge carrier density and the effective mobility, the effective mass of the charge carrier has to be obtained from a calculated band structure.

Photoelectron spectroscopy

Photoelectron spectroscopy (PES) can be used to study the elemental composition and chemical states by x-ray photoelectron spectroscopy (XPS). The XPS experiment utilizes monochromatic x-rays from a x-ray source (e.g. Aluminium kα 1468 eV) to excite core electrons from the sample atoms. The information depth is limited by the inelastic mean free path of the emitted electron in the material, typically in the range of 5 nm. This fact makes the method “surface sensitive” as no bulk information is collected. The energy of the elastically scattered electrons is analysed in an energy discriminating detector. The obtained peak positions can then be correlated with the binding energy of core electrons of an element and its chemical state. To be able to discern the carbon species from the carbon nitride film from adventitious carbon it is advisable to use indium tin oxide substrates and cover them as homogeneously as possible. Thin films ~50 nm have less peak broadening and no spectrum shift but show substrate peaks from oxygen and indium. Thick films >200 nm should not show oxygen and indium peaks in pure carbon nitride samples but suffer from peak broadening and spectrum shift due to charging. Next to sample charging even on indium-tin-oxide due to the poor film formation properties of the pristine nano-crystallites, the quantitative analysis of carbon of only thinly covered samples can be altered by adventitious carbon due to bare ITO in the measurement area. It is hence more reliable to use elemental analysis by combustion to determine C:N ratios for the bulk material.

Ultraviolet photoelectron spectroscopy (UPS) uses UV light (e.g. Hydrogen Ly-α: 10.2 eV or Helium Iα: 21.23 eV) instead of x-rays exciting the valence band electrons instead of the core electrons of the sample surface. UPS can access the work function (WF) measuring a secondary electron cut-off and hole injection-barrier (HIB) from the valance band scan of thin films allowing to calculate the ionisation potential (IP) (IP = WF + HIB) which is the energetic distance between valence band onset and vacuum level. The energy level diagram can be constructed using these values allowing to determine injection barriers at metal-semiconductor interfaces and to study the effect of surface modifications and doping on the WF of the material. In combination with the optical gap and DFT the position of the conduction band minimum can be estimated allowing to determine the electron affinity which is the energetic difference between conduction band minimum and vacuum level.

The predominant challenge of PES methods is the low conductivity of the carbon nitride nano-crystalline phases ($\sim 10^{-10}$ S cm^{-1}) that was observed to drop further, about one to two orders of magnitude, under reduced pressure.

Sample requirements: Thin films of the sample on an ITO substrate have to be prepared. The thin films have to have sufficient conductivity in ultra-high vacuum (preferably $>> 10^{-10}$ S cm^{-1}) and contain no volatile constituents, e.g. I_2, solvents etc. Charging is typically present if multiple scans show an increased binding energy of the onset of photoelectron generation.

Application as organic light-emitting diode

Single-layer OLEDs consist of a transparent anode on a substrate, a hole transport layer like PEDOT:PSS, the active emission layer and a cathode typically consisting of a thin layer of calcium and a supporting layer of aluminium. To apply the CN layer on top of the hydrophilic PEDOT:PSS layer it is necessary to use a CN dispersion in an lipophilic solvent like chlorobenzene as the PEDOT:PSS layer is otherwise re-solubilised. It is useful to discard larger agglomerates in the dispersion by a centrifugation step and working with the supernatant. This reduces the concentration but allows to deposit more homogeneous films in multiple consecutive drop-casting steps.

Sample requirements: Solution processing onto a PEDOT:PSS film of a continuous film is required. The sample should show significant photoluminescence; advisable is a QY of 0.5% or higher for research materials. Photoluminescence lifetimes of the singlet state are preferably as short as possible, ~1-10 ns.[137]

Density functional theory

The density functional theory (DFT) is a computational quantum mechanical modelling method that one can utilise to investigate the electronic structure of atoms, molecules and condensed phases. DFT has developed into an important tool for chemists and physicists for theoretical description of physical properties of matter. Today, many experimental investigations in organic and inorganic chemistry are routinely accompanied by DFT. In this scope DFT was also used in this thesis to give access to theoretical vibrational analysis, the electronic structure, the effective mass of charge carriers, absorption spectra, geometry-optimized structures, formation energies and considerations regarding charge transfer between heterojunctions and ions in organic networks. Especially periodic boundary conditions turned out to be of great benefit to describe the electronic systems of the organic crystals accurately and connect the experimentally observed effects of e.g. protonation on the optical states with the according causes in the electronic structure. To evaluate the electronic structure of the crystals one needs to interpret the band structure. An example is shown in Figure 14. The band structure displays the electronic states in respect to their energy and wave vector k. In most use cases, studying well-known semiconductors such as silicon it is often sufficient to access the size of the band gap as well as its nature (indirect/direct) to give a reasonable interpretation of the material. However, working with organic research materials like 2D COFs for a valid interpretation of the band structure it is necessary to take also the nature of the CB and VB states (π-states/lone-pairs), anisotropy effects on charge carrier transport due to the graphitic character, as well as the density of states, allowed absorption processes and the band curvature into consideration to access the effective mass of charge carriers. The estimation of the charge carrier mass by evaluation of the band curvature is helpful, as it allows to access charge carrier density and mobility in cooperation with THz-TDS data.[138]

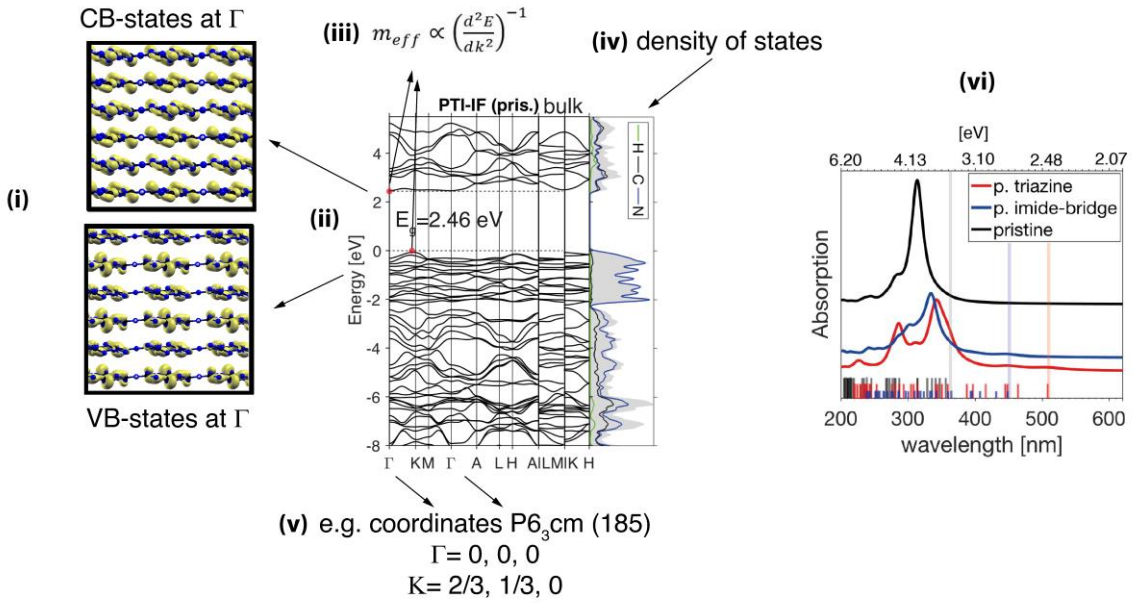

Figure 14. Example for the interpretation of a band structure of a graphitic carbon nitride together with optical and structural features. (i) Shape and localization of CB and VB states in real space, (ii) nature and size of band gap, (iii) evaluation of curvature of upper most VB and lowest CB gives an estimation of the effective carrier mass (m_{eff}) of electron and hole, (iv) density of states, (v) high symmetry points in reciprocal space and vectors corresponding to inplane (Γ–K) and out of plane (Γ–A) transport in the anisotropic direct lattice of the graphitic crystal, (vi) allowed (high intensity) and forbidden (no intensity) transitions identified with time dependent DFT calculations.

For the interpretation of the visualisation of the CB and VB states additional calculations for the monolayer are useful as they tend to be less convoluted, and the properties of the monolayer tend to be preserved in the bulk graphitic material.

Chapter 4. Size effects of the anions in the ionothermal synthesis of carbon nitride materials

I know that many will call this useless work.
Leonardo Da Vinci, The notebooks of Leonardo Da Vinci, 1883.

The presented results of this chapter have been published in:
D. Burmeister, J. Müller, J. Plaickner, Z. Kochovski, E. J. W. List-Kratochvil, M. J. Bojdys, *Chem. – A Eur. J.* **2022**, *28, e202200705*.

Author contributions: D. B. conceived the idea for the project. D.B. designed the experiments, conducted them, collected the experimental data and interpreted it. J. M. and Z. K. contributed electron microscopy results. J. P. contributed UV-Raman results. Theoretical analysis and interpretation was conducted by M. J. B.. D. B. drafted the article with inputs from all authors. M. J. B. and E. L. K. revised the manuscript.

Next to temperature and reaction time the composition of the eutectic salt melt is the most important reaction condition. The ions present in the eutectic control the solvatisation of the intermediates and the localisation of intercalations leading to a templating effect and can undergo redox reactions with the carbon nitride species.

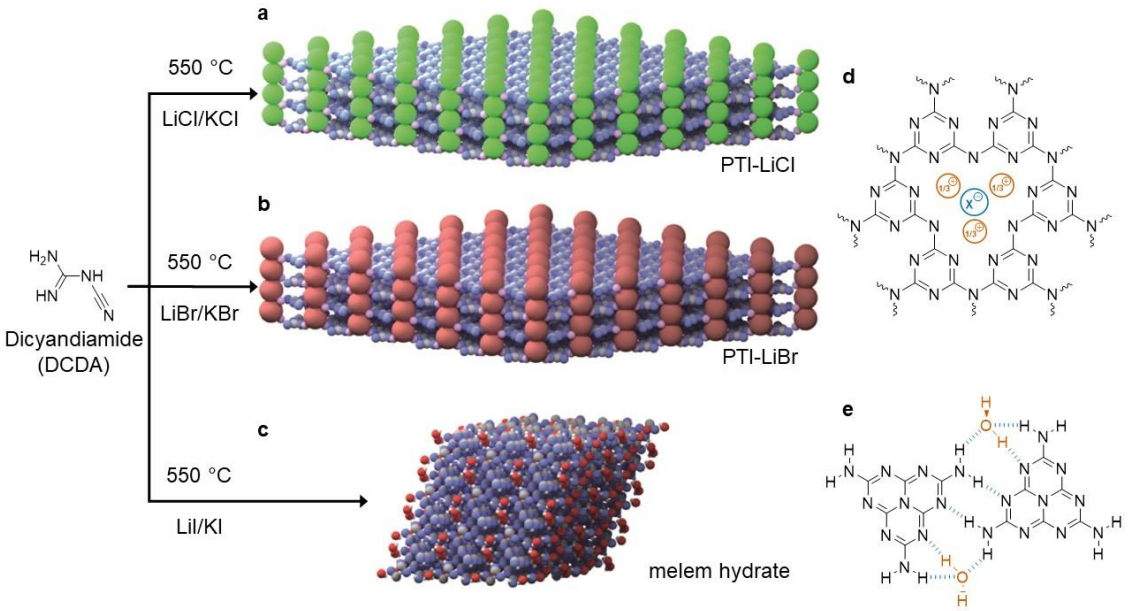

Figure 15. Condensation products of dicyandiamide (DCDA) in different eutectic salt melts: a) poly(triazine imide) with intercalated chloride (PTI-LiCl), b) poly(triazine imide) with intercalated bromide (PTI-LiBr), and c) melem hydrate ($C_6H_6N_{10} \cdot H_2O$). d) The poly(triazine imide) network forms triangular cavities with inclusion of halides (X^-, in blue) counterbalanced by lithium (in orange). e) Melem hydrate forms an extended hydrogen-bonded network (in blue) between melem ($C_6H_6N_{10}$) units and water (in orange) in three dimensions. Atom positions are depicted as spheres (nitrogen blue, carbon grey, hydrogen white, oxygen red, bromide red brown, lithium purple, chloride green) (Figure reproduced from Burmeister et al..[116])

The goal of this study is to identify the effect on the condensation reaction of the absence of "small" anions like chloride or bromine which demonstrably can intercalate into covalent product structures such as poly(triazine imide). The good fit of the halide anions into the pores of layered PTI suggests a strong interaction with the PTI backbone. Eutectic salt melts influence the structure of the carbon nitride materials formed in ionothermal synthesis as they act as polar solvents with high boiling points for organic mono- and oligomers.[139,140] To date, however, the role of the anions in the ionothermal formation of carbon nitrides has not been elucidated as the ions are treated in first approximation as inert solvents.

In this study, the influence of three eutectic salt melts with increasing anion sizes ($Cl^- < Br^- < I^-$) is studied systematically on the formation of carbon nitride materials during ionothermal synthesis, namely: (i) LiCl/KCl (45 wt%/55 wt%, m.p. 352 °C), (ii) LiBr/KBr (52 wt%/48 wt%, m.p. 348 °C), and (iii) LiI/KI (58 wt/42 wt%, m.p. 285 °C) (Figure 15 a-c, d).[141]

The lower melting point is thought to allow for faster solubilisation of the precursor in the beginning of the reaction and to diminish formation of carbon rich side products. The larger size of the anion could enable the formation of ion-free carbon nitrides like PTI-IF or even new phases stabilised by the bigger anion.

To contextualise the results the known chloride- and bromide-intercalates of poly(triazine imide) are considered and compared with the hitherto unidentified crystalline product from the iodide eutectic. The carbon nitride material from the LiI/KI salt melt is obtained as a powder from which one can isolate single crystallites for structural analysis using single crystal X-ray diffraction (sc-XRD). The isolated single crystals were identified as melem hydrate (Figure 15 c, e). Using the iodide eutectic as the medium for ionothermal synthesis, one does not observe the formation of a crystalline extended polymer with a higher degree of condensation. This finding strongly indicates that the smaller anions (Cl^- and Br^-) are stabilizing the formation of poly(triazine imide) layers and facilitate their π-π stacking, as confirmed by density functional theory (DFT) calculations.

4.1. Results and discussion

Experimental design

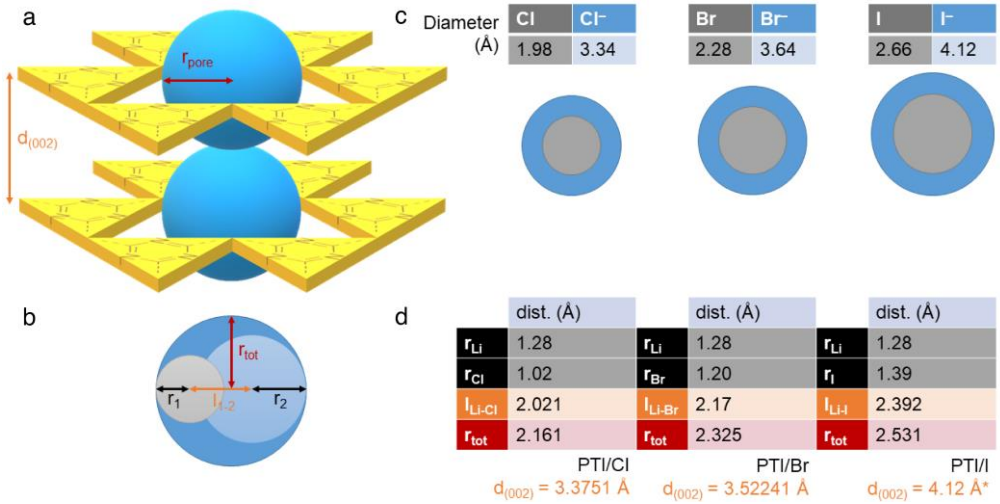

Figure 16. Considerations of available free volume for intercalation of lithium halide species in poly(triazine imide) frameworks. a) Principally available space in a PTI-based framework is confined by the pore diameter, r_{pore}, and the galley height, $d_{(002)}$. b) Representation of the dynamic covalent radius, r_{tot}, of a lithium halide. c) Diameters of halogen atoms and their respective halides. d) Calculation of the dynamic covalent radii of lithium chloride, lithium bromide, and lithium iodide. Below, gallery heights for poly(triazine imide) model structures with intercalated lithium halides, derived from experiment for PTI-LiCl and PTI-LiBr and, and estimated for PTI-LiI (denoted by *) on the basis of the iodide radius. (Figure adapted from Burmeister et al..[116])

The poly(triazine imide) (PTI) framework provides two types of potentially accessible volumes for lithium halide intercalates: (i) within the pores defined by the in-plane, covalent bonding pattern of covalently linked triazine (C_3N_3)-units (Figure 16, a; blue spheres with radius, r_{pore}), and (ii) in the galleries between π-π stacked PTI layers (Figure 16, a; with distance, $d_{(002)}$). Since the material is overall charge-neutral, one can assume intercalation of a lithium halide species with a total, dynamic radius, r_{tot}, that may not exceed the pore diameter, r_{pore} (Figure 16, b). The gallery height for stacked PTI sheets is known to be 3.3751 Å for PTI-Cl and 3.52241 Å for PTI-Br,[139,140] which correlates with the ionic diameters for chloride (3.34 Å) and for bromide (3.64 Å). Hence, for a hypothetical PTI-LiI one assumes that the gallery height does not exceed $d_{(002)}$ = 4.12 Å which is the radius of iodide (Figure 16, c). Using standard values from the Computational Chemistry Comparison and Benchmark Data Base (CCCBDB), one obtains dynamic radii of lithium halides as follows: 2.161 Å for LiCl, 2.325 Å for LiBr, and 2.531 Å for LiI (Figure 16 d). These will serve as probe radii for the generation of Connolly surfaces.

Further, one can consider the two extreme cases in which (i) the bridging NH-groups are fully deprotonated and become available for isoelectronic replacement by lithium cations (Figure 17 a, c, e, g, i, k) and (ii) the bridging NH-groups remain fully protonated (Figure 16 b, d, f, h, j, l). Examining the Connolly surfaces generated using these constraints (Figure 17, a-l), one can observe that lithium halides can in principle be intercalated into the interstitial spaces between the sheets above and below the pores of all PTI structures. In the case that bridging NH-groups are isoelectronically converted to NLi-groups, sufficiently large free volumes exist in the pores of PTI-LiCl and PTI-LiBr to allow in-plane incorporation. However, LiI is too large. In the case that bridging NH-groups remain unchanged, there appears to be no free volume within the pores, but all lithium halides could potentially be situated in the interstitial spaces above and below.

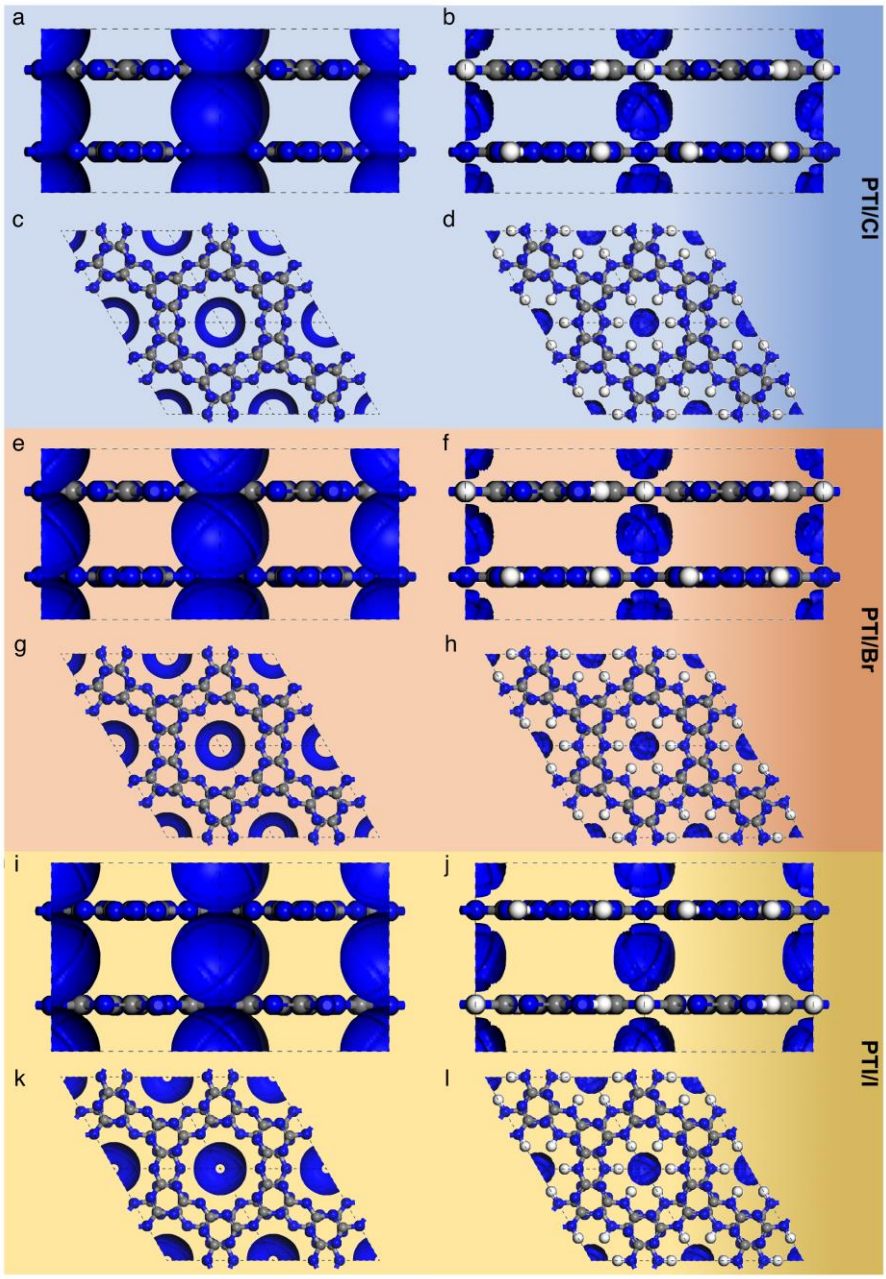

Figure 17. Connolly surface areas (in blue) generated for PTI frameworks with removed hydrogens (a, b) and without (c, d) using the dynamic covalent radius of LiCl as probe molecule. In analogy, Connolly surface areas generated for PTI frameworks using LiBr (e-h) and LiI (i-l) as probe molecules, respectively. (Figure adapted from Burmeister et al..[116])

The expected layer-stacking distance for PTI-LiI of ≥ 4.12 Å that is needed to accommodate a pillared arrangement of iodide species is exceptionally large for an aromatic, discotic system (*cf*. graphite 3.35 Å, PTI-LiCl 3.38 Å, PTI-LiBr 3.52 Å).[140] Hence, as a working-hypothesis, one can assume that a poly(triazine imide) with intercalated LiI will not form and that, instead, a synthesis in LiI/KI will conceivably

lead to (i) an intercalate-free PTI, (ii) a PTI with a stacking mode other than pore-on-pore, or (iii) a different material entirely.

Characterisation and identification of the crystalline product from the iodide eutectic

The ionothermal condensation of DCDA in LiI/KI eutectic is set up according to literature, in analogy to existing protocols for PTI-LiCl and PTI-LiBr,[60,115] and as outlined in the Experimental part. Reaction conditions with different temperatures between 450 °C and 550 °C and with reaction times from 12 h to 48 h have been screened. Products obtained at temperatures below 550 °C show broad peaks in the diffractogram (Figure 18 a), indicating that the condensation process is still incomplete. The color of the powders obtained in the range from 450-500 °C changes from white to bright yellow as temperature is increasing. FTIR spectra show the presence of NH_2 at 3460 and 3350 cm^{-1} signals and a peak at 796 cm^{-1} attributed to the out-of-plane breathing-mode of triazines (C_3N_3) and heptazines (C_6N_7) abbreviated as Tz and Hz in Figure 18 b.[142]

The elemental composition of products obtained at temperatures up to 500 °C for 24 h fits with the C:N ratio of melem (Table 2).

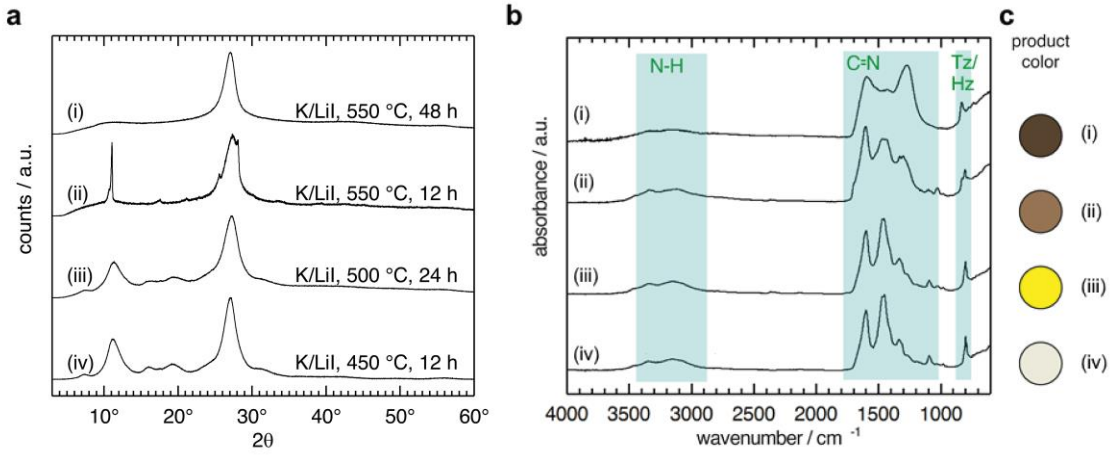

Figure 18. Powder x-ray diffraction (PXRD) data (a), Fourier transform-infrared (FT-IR) spectra (b), and product colors (c) of carbon nitride samples obtained at various conditions in a LiI/KI eutectic (i-iv). Figure reproduced from Burmeister et al..[116]

Table 2. Combustion elemental analysis of products obtained from the LiI/KI eutectic at various reaction conditions (i-v) compared to a LiBr/KBr sample. The C:N ratio of the products is compared to the theoretical C:N ratio of melem. (Table reproduced from Burmeister et al..[116])

Reaction conditions	C:N, combustion analysis
(i) LiI/KI, 550 °C, 48 h	0.55:0.45
(ii) LiBr/KBr, 550 °C, 48 h	0.41:0.59
(iii) LiI/KI, 550 °C, 12 h	0.46:0.54
(iv) LiI/KI, 500 °C, 24 h	0.38:0.62
(v) LiI/KI, 450 °C, 12 h	0.38:0.62
melem (theoretical)	0.38:0.62

Extended reaction times (*e.g.* 48 h) and higher temperatures (*e.g.* 550 °C) yield samples with drastically increased carbon content, leading to a darker coloration and an amorphisation of the product (Figure 18 a (i)). Compared to crystalline PTI-LiBr that is obtained as a beige powder after 48 h at 550 °C,[140] the early onset of carbonisation in LiI/KI eutectics indicates that the formation of a more temperature-stable, crystalline poly(triazine imide) structure is disfavored due to a lack of stabilising anions of appropriate size. Moreover, instead of the intercalation of alkali iodide and the appearance of a PTI-type diffraction pattern (Figure 18, a), one observes the formation of iodine vapors inside the quartz ampoule at temperatures above 480 °C. Applying bromide and chloride eutectics no gas of the according elemental halogenide is visible in the ampule up to 600 °C. This indicates that in the iodide eutectic DCDA reaction mix unidentified redox processes are ongoing at these temperatures (Figure 19).

Comparing the elemental compositions of products from bromide and iodide eutectics at the same reaction conditions implies faster carbonisation in iodine eutectics (Table 3). The C:N ratio at 550 °C is increased significantly from 41:59 to 55:45. Also, the hydrogen content is higher implying lower degree of condensation.

Table 3. Combustion elemental analysis of products obtained from the LiI/KI eutectic at various reaction conditions compared to a PTI-LiBr sample from a LiBr/KBr eutectic. (Table reproduced from Burmeister et al..[116])

sample	N wt%	C wt%	H wt%
LiBr/KBr, 550 °C, 48 h	43.118	25.958	1.059
LiI/KI, 550 °C, 48 h	38.100	40.009	2.688

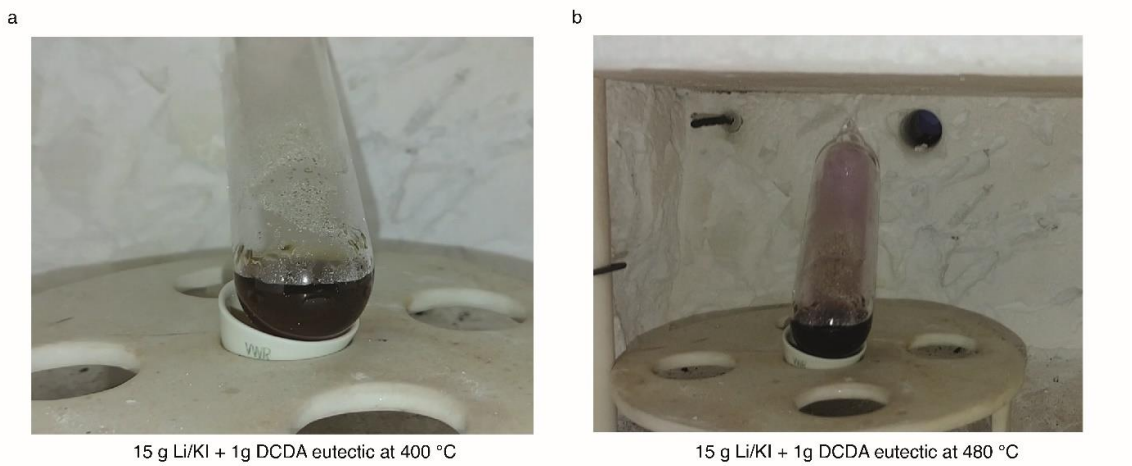

Figure 19. Images of reaction mixtures in a furnace at a 400 and b 480 °C. (Figure reproduced from Burmeister et al..[116])

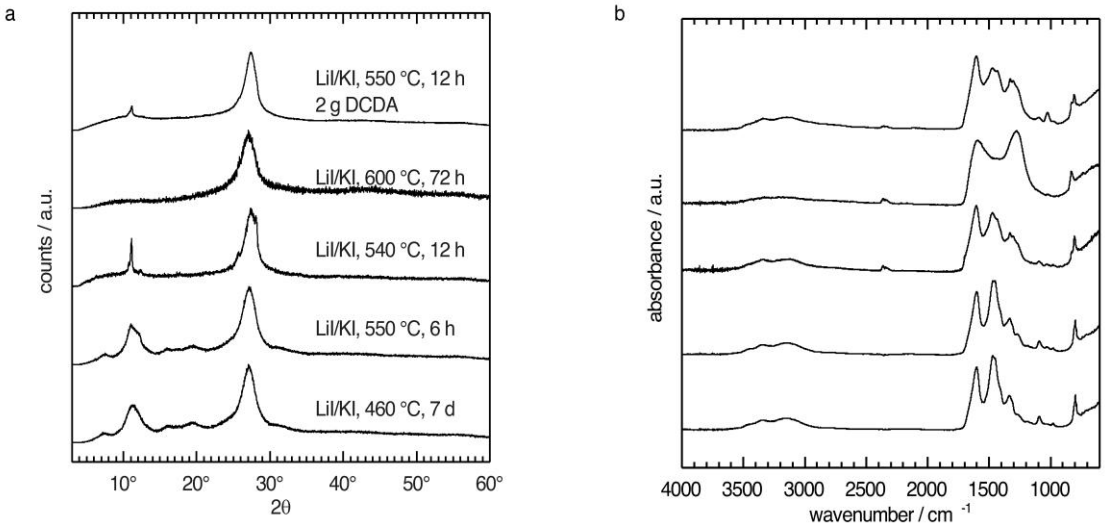

Figure 20. PXRD and FT-IR spectra of additional reaction conditions. (Figure reproduced from Burmeister et al..[116])

An overview of results of PXRD and FT-IR data for all additional products obtained at various reaction conditions is presented in Figure 20. ^{13}C cross-polarisation magic-angle-spinning (CP/MAS) solid-state NMR spectra of the products show bands at 154 ppm and 164 ppm in good agreement with the reported values for melem at 155 ppm and 164 ppm (Figure 21).[142]

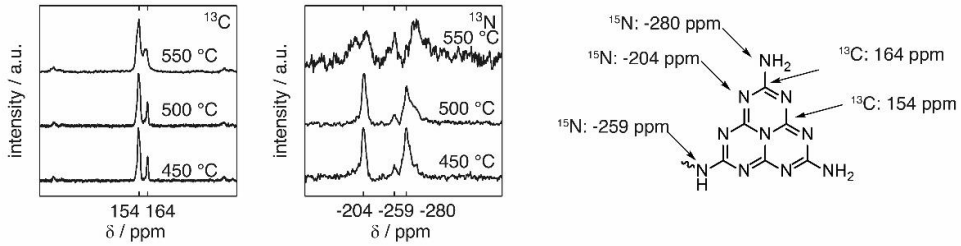

Figure 21. ^{13}C referenced to tetramethylsilane and ^{15}N referenced to nitromethane ssNMR spectra of carbon nitride condensation products from synthesis at 550 °C, 12 h (top line), 500 °C 24 h (middle line) and 450 °C 12 h (bottom line). The bands are assigned to a melem unit in a structural model on the right side of the spectra. (Figure reproduced from Burmeister et al..[116])

^{15}N solid-state NMR has two main features at -204 ppm and -280 ppm that one can assign to the pyridinic nitrogen and the amine nitrogen environments reported for melem (at -205 ppm and -281 ppm).[142] A weak band at -259 ppm is assigned to amorphous condensation products containing secondary amines that is structurally similar to short chains of condensed melem units (so-called "melon"). When compared to melon, the NH_2 (-265 ppm) and NH (-245 ppm) nitrogen bands are shifted towards higher ppm values.[18] The photoluminescence (PL) spectrum of the

product obtained at 450 °C has a maximum at 385 nm which coincides with the PL data obtained for pure melem (Figure 22).[142]

With increasing reaction temperature, the PL maximum shifts towards higher wavelengths. One can interpret this shift as an increasing contribution of the amorphous, brown phase that one can associate with disordered, partially carbonized melon-like structures.[18,49] In summary, samples obtained at temperatures up to 500 °C contain melem as the main phase product. At a temperature of approx. 550 °C, one observes the onset of carbonisation of the organic components.

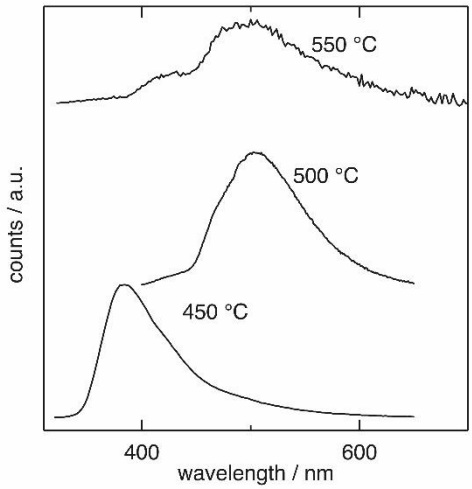

Figure 22. Photoluminescence spectra of CN condensation products from iodide eutectics. Product formed at 450 °C excited at 310 nm closely resembles the emission of melem with an emission maximum at 380 nm (bottom line). The emission of product formed at 500 °C excited at 370 nm is red-shifted with an emission maximum at 500 nm (middle line). The product formed at 550 °C excited at 310 nm follows the trend of the broadening emission at 500 nm. (Figure reproduced from Burmeister et al..[116])

The carbon nitride material with the highest apparent crystallinity (LiI/KI, 550 °C, 12 h; Figure 18, (ii)) is selected for detailed investigations. Light microscopy reveals two phases: a brown phase with no geometric order and a transparent phase with rectangular crystallites (Figure 27, a). The crystals were imaged by scanning electron microscopy (SEM) (Figure 27, b) showing characteristic, sharp edges and a rectangular shape.

Energy dispersive X-ray spectroscopy (EDX) of a crystallite corroborates the results of the combustion elemental analysis: the main elements are nitrogen (65 at%) and carbon

(35 at%). Contributions from salt residues and carbonisation are evident only in the amorphous, brown phase of the product (Figure 23).

Notably, one observes no evidence of iodide intercalation in the carbon nitride crystals. To prove that the sample is also free of alkali metals, ICP-OES and XPS is performed. The condensation product obtained at 550 °C, 12 h contains 0.38 wt% Lithium and 0.73 wt% potassium. These residual amounts of alkali metals are low and non-stoichiometric. They are most likely inclusions situated in the amorphous, brown phase

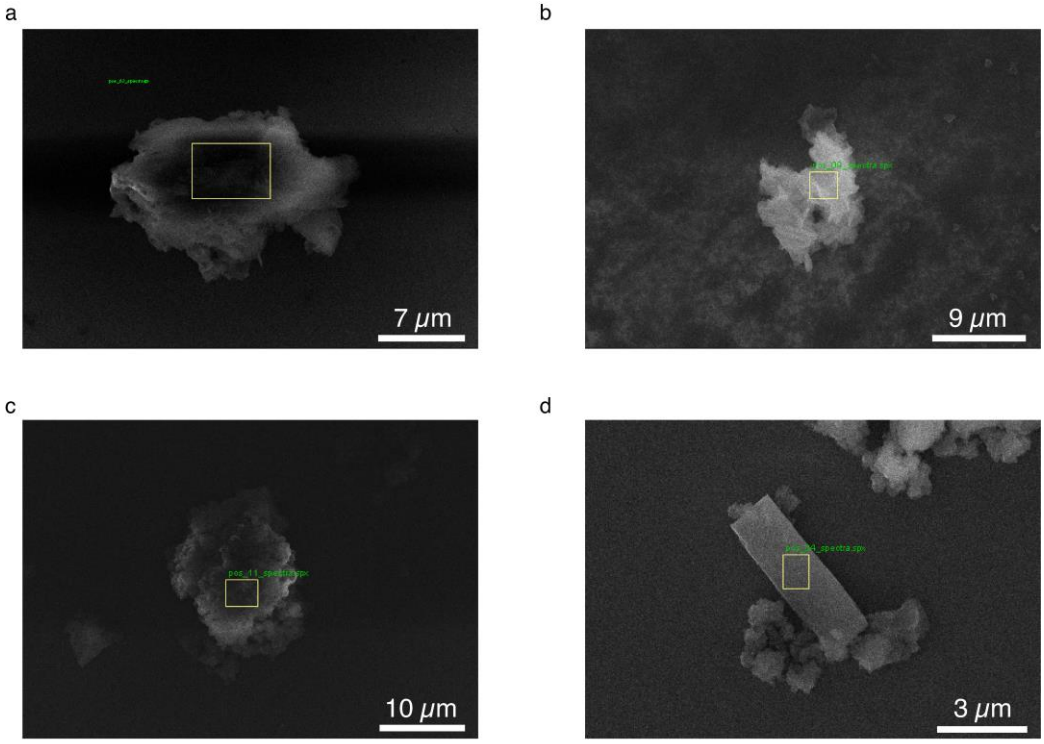

	nitrogen at%	carbon at%	potassium at%	iodine at%
a) 450 °C, 12 h	63±9	37±4	0±0	0±0
b) 500 °C, 12 h	62±8	38±4	0±0	0±0
c) 550 °C, 12 h, amorph	49±7	50±5	0.3±0.1	0±0
d) 550 °C, 12 h, crystal	65±10	35±4	0±0	0±0

Figure 23. Energy dispersive x-ray spectroscopy results obtained with an acceleration voltage of 15 kV of condensation products. Atomic percentages of nitrogen and carbon reflect the combustion analysis well. The increased carbon content of the 550 °C, 12 h can be attributed to the brownish amorphous phase. (Figure reproduced from Burmeister et al..[116])

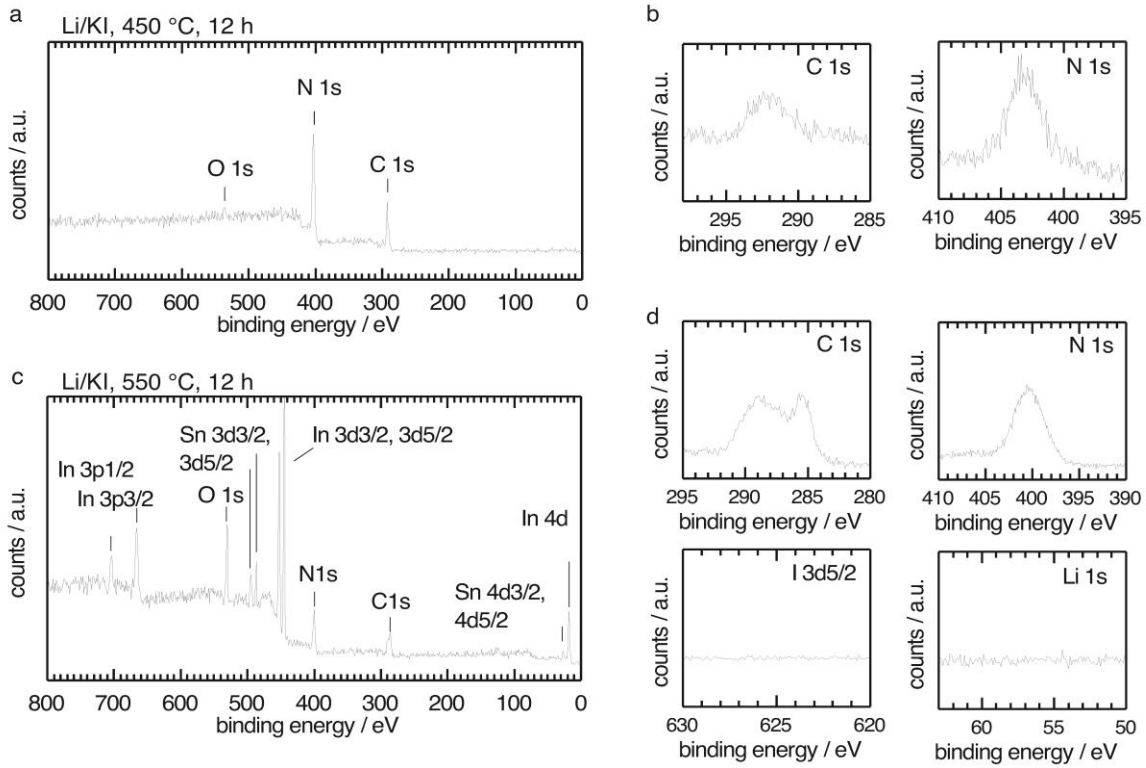

Figure 24. XPS spectra of condensation product from synthesis at 450 °C and 550 °C. The concentration of the salt melt ions in the sample surface of processed films on indium-tin oxide after workup is under the detection limit. a) XPS survey of CN condensation product from synthesis at 450 °C. Only carbon nitrogen and oxygen are present. b) XPS spectra of C 1s and N1s. The atomic percentages of carbon and nitrogen are in accordance with the values found by combustion analysis and EDX nitrogen (65 at% carbon 35 at%). Due to a film thickness of around 1-10 µm no indium and tin signals are obtained. However the absolute shift is most likely influenced by surface charging (compare e.g. the N 1s spectra). c) The XPS spectrum of the product obtained from synthesis at 550 °C has no ion contributions from the salt melt (LiI/KI) either. Due to reduced film thickness, in this sample, charging was successfully reduced (lower energy of peak maxima). However, full surface coverage was not achieved and hence contributions of elements of the indium tin oxide substrate are captured in the survey spectrum. d) The C 1s spectrum shows similar trends as observed for carbonisation in poly(triazine imide). A strong signal at 285 eV arises that can be interpreted as carbon rich environments. The carbon rich property is also reflected by comparison of the atomic percentages of nitrogen (47 at% and carbon 53 at%) to the condensation at lower temperature. Again these values are in good accordance with combustion analysis and EDX. (Figure reproduced from Burmeister et al..[116])

and cannot be washed out by hot water. XPS results confirm the CN-ratios observed in combustion elemental analysis and in EDX and show no salt contributions (Figure 24). UV-Raman spectra show indicative bands for heptazines at 1661 cm^{-1} (w), 1571 cm^{-1} (w), 1155 cm^{-1} (s) and 545 cm^{-1} (s) in the translucent crystals (Figure 25).[142] Strong bands at 980 cm^{-1} (s), 1401 cm^{-1} (s) and 1310 cm^{-1} (s) are unassigned. Raman bands in the amorphous, brown phase are weaker and broader compared to the spectra obtained for the crystals, as is anticipated for a highly disordered phase.

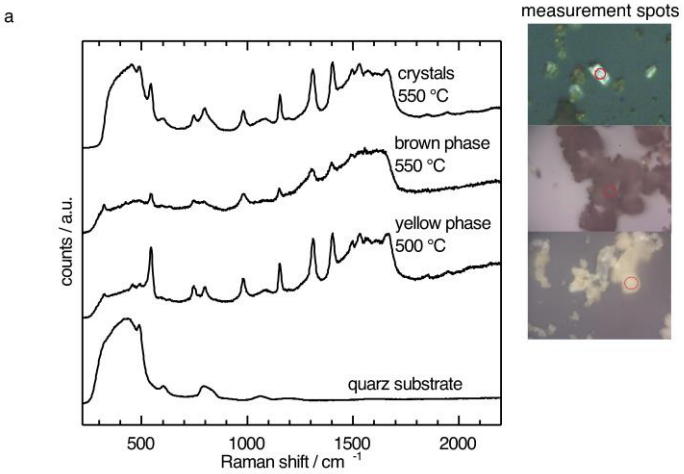

b

ν (observed this work)	ν reference	assignment
1661 (w)	1677 (w)	E′
1571 (w)	1581 (w)	E′
1530 (w)		
1494 (w)		
1401 (s)		
1310 (s)		
1197 (vw)		
1155 (s)	1155 (s)	A1′
980 (s)		
750 (w)		
545 (s)	545 (s)	A1′

Figure 25. UV-Raman spectrum with 255 nm excitation wavelength of DCDA condensation products in LiI/KI eutectics synthsised at 500 °C and 550 °C. a) rectangular crystals from 550 °C, 12 h reactions show well-resolved Raman bands on a quarz substrate (first line). The band positions of the coevolved brown phase are closely related to the bands observed in the crystalline phase. Product from synthesis at 500 °C, 12 shows the same dominant Raman bands as the product phases obtained from synthesis at 550 °C. The observed Raman bands are compared to literature values for melem. The high similarity of the spectra of the melem crystals obtained from 550 °C sample and the yellow phase from 500 °C further strengthens the hypothesis that the observed changes in the PXRD are due to phase changes of melem crystals. (Figure reproduced from Burmeister et al..[116])

One is able to solve the crystal structure of the crystalline phase using single-crystal x-ray diffraction. In this experiment, a micro actuator is used to pick up and transfer the micro-sized crystallites (Figure 26). The structure solution revealed the crystallites to be melem hydrate ($C_6N_7(NH_2)_3 \cdot H_2O$) (Figure 27, Table 4).

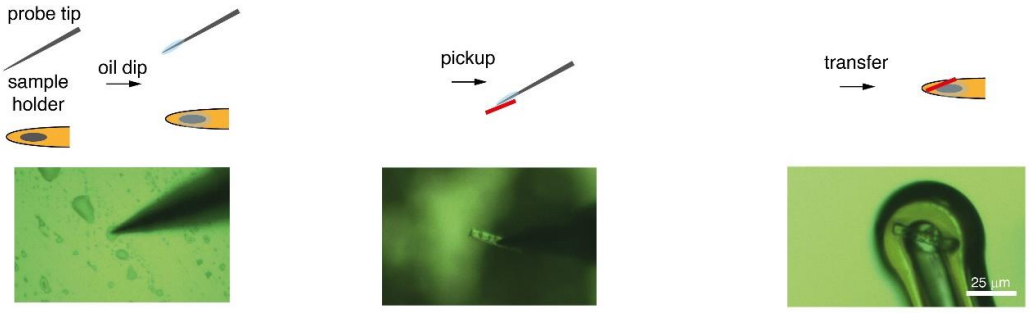

Figure 26. Single-crystal x-ray sample preparation. Summary of pick up transfer of microcrystals in presence of abundant amorphous phase. To be able to mount the crystals despite their small size and the presence of the second brown phase, a pickup transfer with micro-actuators is applied (IMINA technologies). A micro actuator tip is dipped into an oil-drop on a microscopy slide, resulting in better adhesion properties of the tip. The tip with the oil film is used to pick up the micro crystallites. A sample holder with a 10 µm loop is also dip-coated with oil. Then the crystallites are carefully transferred to the sample holder. (Figure reproduced from Burmeister et al..[116])

Table 4. Crystallographic data for melem hydrate ($C_6N_7(NH_2)_3 \cdot H_2O$) obtained from the ionothermal condensation of dicyandiamide in LiI/KI eutectic salt melt at 550 °C, 12 h. (Table reproduced from Burmeister et al..[116])

Identification code	melem hydrate
Empirical formula	$C_6H_8N_{10}O$
Formula weight	236.22
Temperature/K	100 K
Crystal system	monoclinic
Space group	$P2_1/c$
a/Å	8.6040(17)
b/Å	16.630(3)
c/Å	6.8840(14)
α/°	90
β/°	111.91(3)
γ/°	90
Volume/Å^3	913.8(4)
Z	4
ρ_{calc} g/cm^3	1.717
μ/mm^{-1}	0.132
F(000)	488.0
Crystal size/mm^3	0.1 × 0.04 × 0.01
Radiation	synchrotron (λ = 0.799897 Å)
2Θ range for data collection/°	4.898 to 59.504
Index ranges	$-11 \le h \le 11$, $-22 \le k \le 22$, $-8 \le l \le 8$
Reflections collected	15426
Independent reflections	2333 [R_{int} = 0.1298, R_{sigma} = 0.0782]
Data/restraints/parameters	2333/6/175
Goodness-of-fit on F^2	1.024
Final R indexes [I>=2σ (I)]	R_1 = 0.0797, wR_2 = 0.2012
Final R indexes [all data]	R_1 = 0.1656, wR_2 = 0.2574
Largest diff. peak/hole / e Å^{-3}	0.39/-0.37

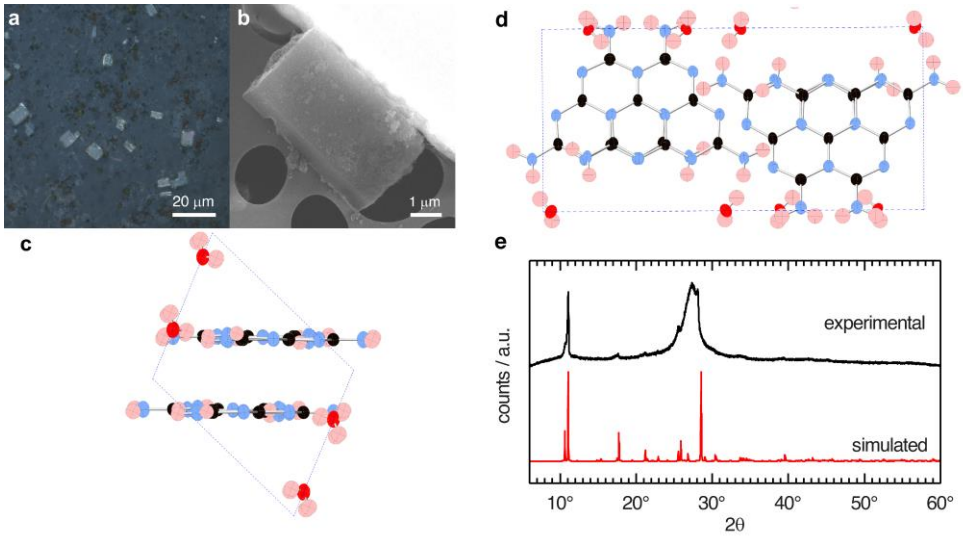

Figure 27. Structural characterisation of melem hydrate crystals obtained at 550 °C and 12 h in the LiI/KI eutectic salt melt. a) Light microscopy image of the bulk product on scotch tape shows two morphologies distinguishable as brown, amorphous particles and rectangular crystallites. b) Scanning electron microscopy (SEM) (20 kV accelerating voltage) image of a single crystallite. Ball-and-stick representation of the unit-cell of melem hydrate obtained from single-crystal x-ray diffraction projected along c) the b-axis and d) the c-axis, respectively. Atomic positions are marked as thermal ellipsoids, colored red for oxygen, blue for nitrogen, black for carbon and light red for hydrogen. Hydrogen positions are approximated. e) Comparison of the powder x-ray diffraction (PXRD) pattern of the bulk product (in black) and the simulated diffraction pattern of melem hydrate based on the structural data from single crystal x-ray diffraction data (in red). (Figure reproduced from Burmeister et al..[116])

The stacking distance of the melem units is 3.2 Å at slight offset to maximize polar interactions (Figure 27, c). Melem hydrate crystals are held together by a three-dimensional network of hydrogen bonds with lengths of ~2.2 Å between (i) pyridinic nitrogens of the heptazine cores and adjacent amine groups and (ii) water molecules and amine groups (Figure 27, d). In contrast, melem crystals obtained *via* sublimation are not aligned in co-planar layers.[142] The refined structure from the single crystal experiment is in good agreement with the PXRD profile of the bulk material (Figure 27, e). Due to the evolution of the second brown phase an additional glassy contribution at 27° 2θ is observed in the PXRD pattern when compared to the simulation of pure crystalline melem hydrate. This contribution is attributed to random stacking of π-conjugated, carbonised fragments that constitute the brown, amorphous phase. The same observation was reported earlier for the condensation of poly(triazine imide) from DCDA in a LiBr/KBr eutectic.[115] As expected, melem hydrate undergoes a phase change to melem during vacuum drying at 200 °C for 24 h (Figure 28).[142]

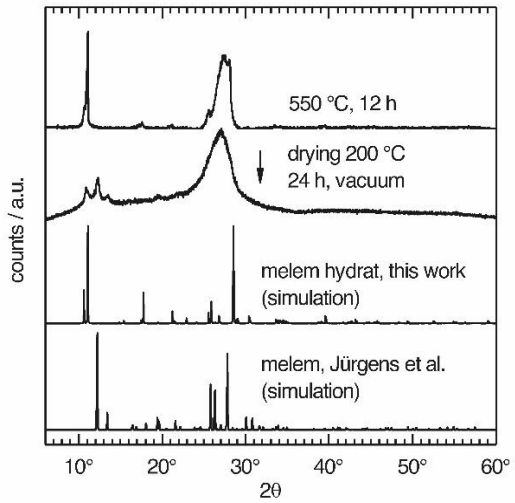

Figure 28. PXRD of condensation product from synthesis at 550 °C, 12 h (first line) compared to PXRD after vacuum drying (second line). The experimentally obtained diffractograms are compared with PXRD simulations of the structural data files of melem hydrate (this work, third line) and the structure of solvent-free melem as obtained by Jürgens et al. (fourth line). (Figure reproduced from Burmeister et al..[116])

Scanning force microscopy (SFM) shows a high degree of order at the surface of melem hydrate single crystals (Figure 29). The observed periodicity is in good agreement with the Connolly surface of a melem hydrate crystal cleaved at the 001 plane. High resolution cryo-transmission electron microscopy (HR-TEM) images show periodic lattice fringes with 0.8 nm distances that correspond to periodic distances on the 001 crystallographic plane of melem hydrate (Figure 30).

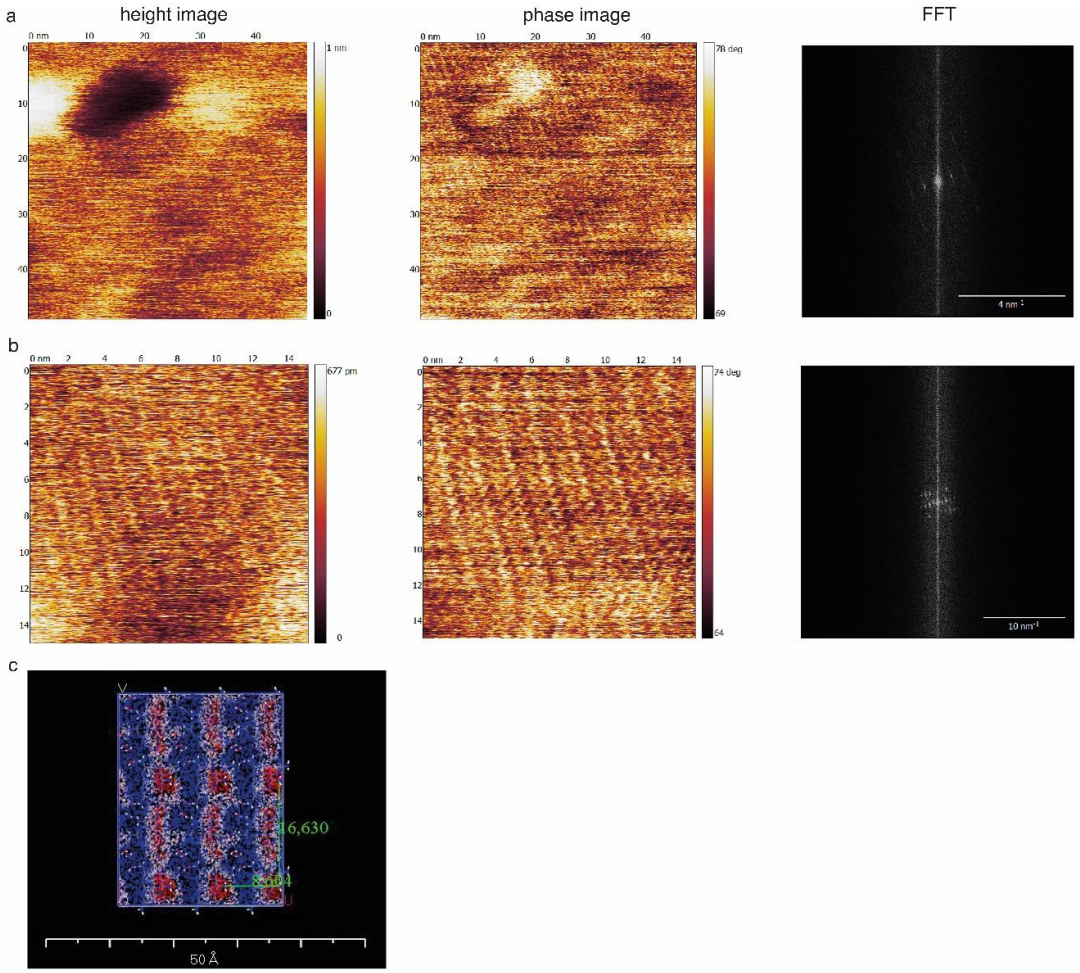

Figure 29. SFM images obtained from melem hydrate crystallite surfaces. Predominantly occurring periodic distances are 0.7 nm and 1.7 nm. a) height and phase image of melem hydrate crystal surface. Fast Fourier transform analysis of the phase images exhibits spots at the spatial frequencies in relation to the image center. b) after decreasing the scan size the periodic distances are still present. c) 001 Connolly surface of melem hydrate crystal structure. The dark-red marked areas contain amine residues pointing out of the surface which are in direct contact with the spheric "Connolly-probe". The distances and angles of the Connolly surface closely resemble the observed patterns. The small deviations can be due to thermal drift of the sample and surface adsorbents. (Figure reproduced from Burmeister et al..[116])

In analogy to PTI-based organic light-emitting diodes (OLEDs),[115] a single layer organic light-emitting device is constructed from the product obtained at 500 °C, 12 h in LiI/KI. The device shows a steep diode-like onset at 4.5 V in forward bias direction. At 13 V one observes a maximum luminance of only 1 cd m^{-2} (Figure 31). The Brunauer–Emmett–Teller (BET) surface area was determined by nitrogen adsorption–desorption isotherms of the 450 °C and 550 °C products, showing no micropores and a low surface area of 57 and 71 m^2 g^{-1} respectively (Figure 32). In addition, the hydrogen evolution reaction (HER) activity of products from 500 °C, 12 h and 550 °C, 12 h with triethanolamine as sacrificial agent under xenon lamp illumination without cutoff filter

and Pt as co catalyst is tested. Unlike PTI and polymeric carbon nitride,[143–146] one does not observe any detectable HER activity for dispersed melem hydrate.

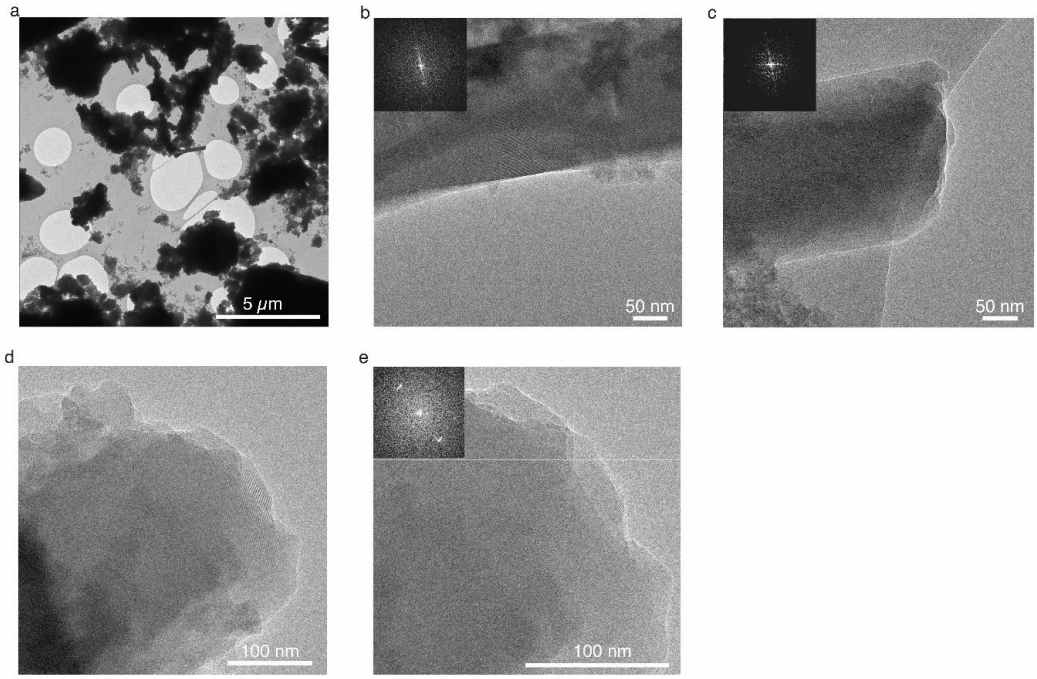

Figure 30. Cryo-HR-TEM (200 kV acceleration voltage) images and fast Fourier transform of an elongated rectangular carbon nitride crystal exhibiting lattice fringes with a periodicity of 0.8 nm. This distance is interpreted as the 100 d-spacing of melem hydrate. (Figure reproduced from Burmeister et al..[116])

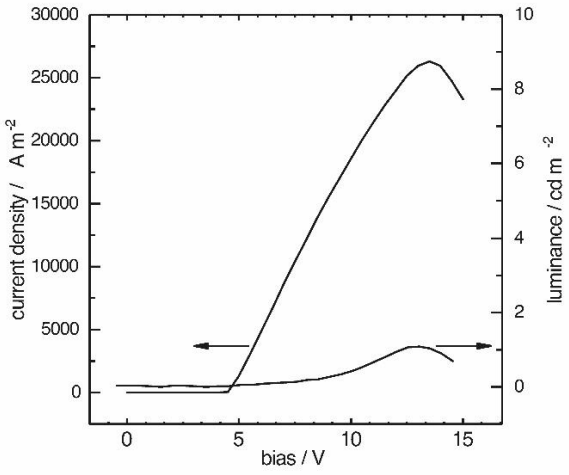

Figure 31. IV characteristics and luminance of OLED constructed from 500 °C condensation product. The device shows a steep diode like onset at 4.5 V in forward bias direction. At 13 V one observes a maximum luminance of 1 cd m^{-2}. Electroluminescence spectra were not obtained since the luminescence was not high enough for the employed set up. (Figure reproduced from Burmeister et al..[116])

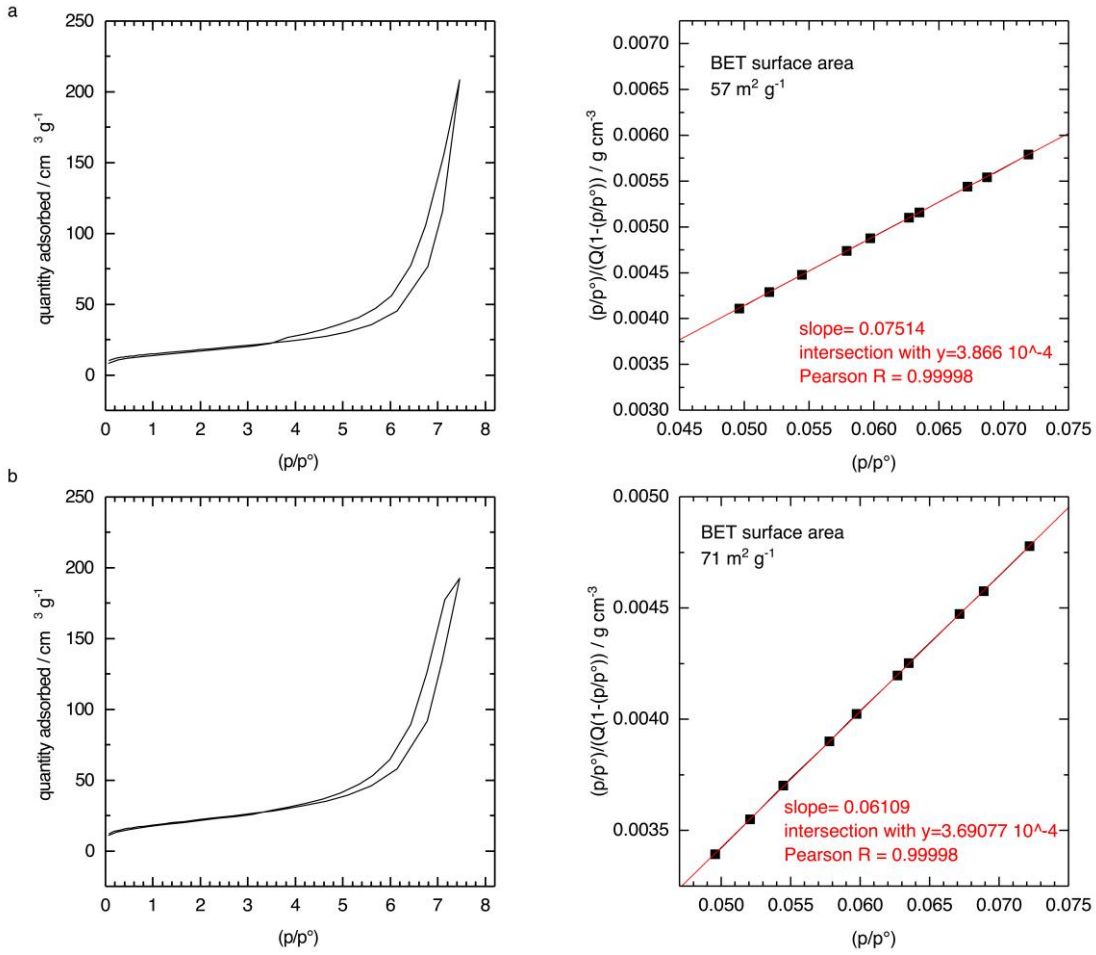

Figure 32. Nitrogen de- and adsorption isotherms from a) 450 °C, 12h and b) 550 °C, 12 h CN condensation products from a LiI/KI eutectic salt melt. (Figure reproduced from Burmeister et al..[116])

Thermodynamic considerations of product stability in dependence on anion size

	Coh. energy, E_{coh} (eV)	Density (g cm^{-3})	Unit-cell volume (Å^3)	Coh. energy per unit vol. (eV Å^{-3})
PTI-LiCl	-8850.712009	1.90543	419.308	-21.10790161
PTI-LiBr	-9005.410554	2.14663	440.875	-20.42622184
PTI-LiI	-9326.962879	2.13797	515.671	-18.0870417
melem hydrate	-18735.83811	1.71677	913.849	-20.5021159

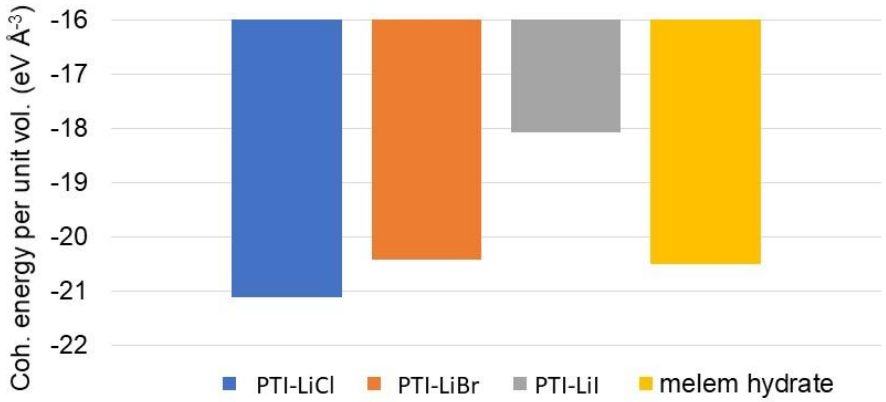

Figure 33. Results of *ab initio* total energy density functional theory (DFT) calculations using a plane wave basis set (CASTEP; energy cut-off 450 eV; exchange correlation PBE-GGA; atomic relaxation until force/atom < 0.02 eV Å^{-1}) for the four periodic carbon nitride materials PTI-LiCl (in blue), PTI-LiBr (in orange), PTI-LiI (in grey), and melem hydrate (in gold). (Figure reproduced from Burmeister et al..[116])

In contrast to the poly(triazine imide) intercalates obtained in LiCl/KCl and LiBr/KBr, one can see that the ionothermal condensation of dicyandiamide in LiI/KI leads to a thermally less stable melem hydrate as the main, crystalline product – and this although the interstitial cavities of the layered PTI framework would be sufficiently large to accommodate LiI in principle (Figure 16). The absence of a poly(triazine imide) analogue is also observed for the condensation of DCDA in a LiI/KI eutectic in an open crucible reaction.[147] This finding indicates that the condensation reaction is halted at melem, the precursor to the formation of poly(triazine imide) in closed ampule as well as open crucible synthesis conditions.[59] A*b initio* total energy density functional theory (DFT) calculations are performed to compare the stabilities of the hitherto known main crystalline products from ionothermal, salt-mediated syntheses – PTI-LiCl and PTI-LiBr – with the stabilities of a hypothetical PTI-LiI crystal and the identified melem hydrate

phase (CASTEP; plane wave basis set; energy cut-off 450 eV; exchange correlation PBE-GGA; atomic relaxation until force/atom < 0.02 eV $Å^{-1}$).[148] Due to the differences in unit-cell volumes and content, the obtained cohesive energies, E_{coh}, are normalized per unit volume and used as a guide for material stability (Figure 33). One finds that in the logical series of lithium halides LiCl → LiBr → LiI, the corresponding poly(triazine imide) intercalation compounds become less stable following a trend in stability of: PTI/Cl > PTI/Br > PTI/I. In the LiI/KI eutectic, melem hydrate is more stable than a hypothetical PTI/I framework, as observed in the experiment.

Based on the initial hypothesis, one can point out the infeasibly large layer-stacking distance between PTI sheets of ≥ 4.12 Å that is needed to accommodate a pillared arrangement of lithium iodide species. The DFT calculations support that the artificially imposed, large gallery height in a PTI-LiI structure chiefly contributes to a loss in cohesive van der Waals interactions between π-aromatic layers and disfavors the formation of a poly(triazine imide) framework. This calculation does not consider conceivable, energetic contributions from ionic stabilisation of triazine-based intermediates along the reaction pathways, but it assists in rationalizing the observed selectivity of experimentally observed products.

4.2. Conclusion

In conclusion, the main, crystalline product obtained from the ionothermal condensation of dicyandiamide in a LiI/KI eutectic salt melt is identified to be melem hydrate ($C_6N_7(NH_2)_3 \cdot H_2O$). This stands in contrast to poly(triazine imide) frameworks with intercalated lithium halides obtained from LiCl/KCl and LiBr/KBr eutectics. Glassy melem is the main product at temperatures below 500 °C, and transparent, monoclinic melem crystals are obtained at 550 °C ($P2_1/c$, a = 8.6040(17) Å, b = 16.630(3) Å, c = 6.8840(14) Å, β = 111.91(3)).

Unlike in LiCl/KCl and LiBr/KBr eutectics, one does not observe selective, stoichiometric intercalation of lithium iodide into a 2D, extended triazine-based framework in the final product. DFT calculations corroborate that the pillared intercalation of lithium halides leads to a loss of stabilizing van der Waals interactions between extended, π-conjugated triazine-based sheets as the size of the intercalate increases (LiCl < LiBr < LiI), and ultimately to the selection of a thermodynamically more favourable, monomeric, heptazine-based product.

An OLED with melem obtained from the synthesis in the eutectic salt melt as the active material shows only low luminance of 1 cd m^{-2}, the products have no detectable activity as a photocatalyst in the hydrogen evolution reaction.

This substudy highlights the importance of anion-size effects in the ionothermal condensation of π-conjugated organic materials, and it showcases a computationally-led methodology for future experiments that (i) use novel, binary and ternary eutectic salt melts, and (ii) aim for thermodynamic selectivity of reaction pathways and products. It also highlights the possibility to obtain single crystallites large enough for single-crystal structure solution from the ionothermal synthesis conditions.

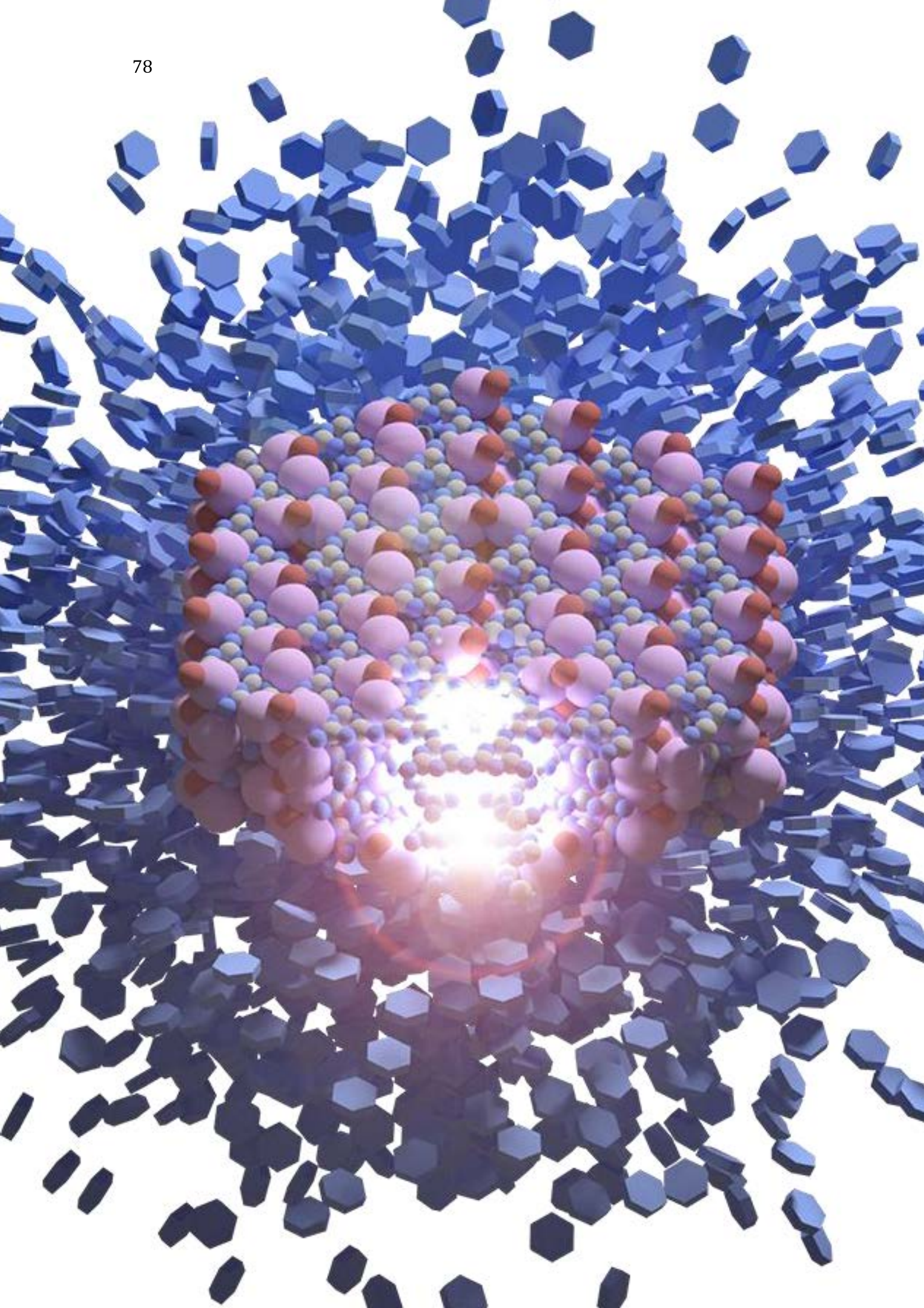

Chapter 5. Poly(triazine imide)-from synthesis to device

Während der ganzen Operation bemerkte man einen starken Geruch nach Blausäure.
(During the whole operation a strong odour of hydrocyanic acid has been noticeable.)
Justus Liebig, 1835, extract from: Über einige Stickstoffverbindungen, translated by David Burmeister.

Results of this chapter were published in:
D. Burmeister, H. A. Tran, J. Müller, M. Guerrini, C. Cocchi, J. Plaickner, Z. Kochovski, E. J. W. List‐Kratochvil, M. J. Bojdys, Angew. Chemie Int. Ed. 2022, 61, 2–10.

Author contributions: D. B. conceived the idea for this project. D. B. designed the experiments and conducted synthesis and experimental characterisation as well as interpretation. H. T. contributed to the OLED construction and synthesis. J. M. and Z. K. contributed electron microscopy results. J. P. contributed UV-Raman results. Theoretical analysis and interpretation was conducted by M. G. and C. C.. D. B.

drafted the article with inputs from all authors. M.J.B. and E. L. K. revised the manuscript.

David Burmeister, Alberto Eljarrat, Michele Guerrini, Eva Röck, Julian Plaickner, Christoph T. Koch, Natalie Banerji, Caterina Cocchi, Emil J. W. List-Kratochvil, Michael J. Bojdys., Chem. Sci. 2023, 14, 6269–6277.

Author contributions: D. B. conceived the idea for this project. D.B. designed the experiments and conducted synthesis and experimental characterisation as well as interpretation. J. M., A. E., Z. K. and T. K. contributed electron microscopy results. A. E. provided the orientation analysis of the nanoparticles. J. P. contributed UV-Raman results. Theoretical analysis and interpretation was conducted by M. G. and C. C.. THz-TDS measurements and interpretation was conducted by E. R. and N. B.. D. B. drafted the article with inputs from all authors. M.J.B. and E. L. K. revised the manuscript.

The following chapter details the first successful integration of a nano-crystalline organic graphitic material into an organic light emitting diode by solution processing. Additionally, comprehensive theoretical analysis and analysis of the electroluminescence reveals a surprising finding: PTI is a lone-pair semiconductor.

5.1. Introduction

As the condensation of DCDA in iodide based eutectic does not yield a graphitic carbon nitride, the synthesis of PTI in a LiBr/KBr eutectic is revisited. PTI-LiBr shows promising features such as high environmental stability due to the high ionisation potential and high electron affinity. Both features are caused by the high nitrogen content. The blue photoluminescence is a promising feature for potential application in OLEDs. Additionally, PTI-IF is prepared and compared to PTI-LiBr to gain information about the effect of the ions on the structure and properties of the material. In this chapter, (i) the impact of different polycondensation conditions on the chemical makeup of PTI and its optical and electronic performance is examined, (ii) the material quality at microscopic and macroscopic scales is monitored, (iii) the electronic structure of the material is elucidated, (iv) the effect of protonation on the optical properties of PTI are discussed, comparing results from theoretical calculations with observed optical spectra, (v) charge carrier properties in the materials are investigated, (vi) a photoconductor, a 2D MoS_2 transistor interfacing PTI-IF and an OLED device based on PTI-LiBr are assembled. The results of this study provide guidelines for improving the optical and electronic properties of organic layered materials; especially ones that incorporate triazine (C_3N_3) subunits and are obtained under polycondensation reaction conditions.

One finds that reduction of the temperature increases the structural order and preserves the desired CN-ratio. This enables us to harness the semiconducting properties in simple prototype devices. To access quality markers for the obtained product PXRD, XPS, FT-IR, UV-Raman, ssNMR, UV-Vis, PL, PLE as well as quantum yield and lifetime measurements are conducted. Furthermore, time domain THz spectroscopy reveals the charge carrier density and mobility in the materials.

The observations of this work also are of explanatory value (i) for the wider organic materials community studying the effects of defects in conjugated polymer semiconductors and (ii) in the context of wide-spread studies into the photocatalytic activity of PTI.[149]

5.2. Results and discussion

Reduction of carbonisation in the synthesis of PTI-LiBr

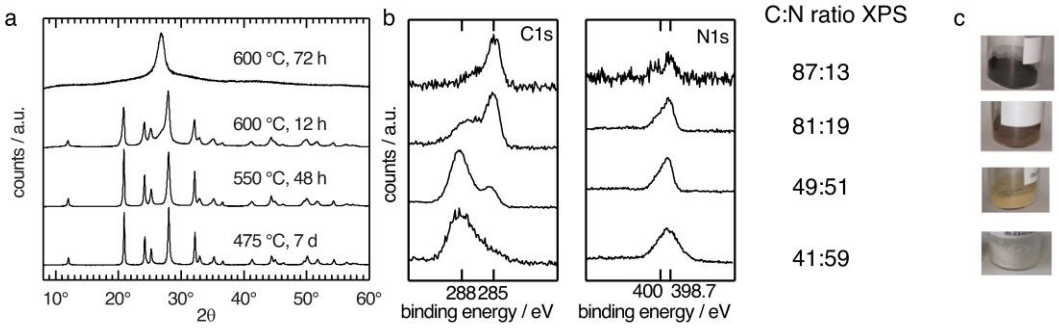

Figure 34. Structural characterisation of PTI-LiBr materials obtained at different temperatures and reaction times. a) Powder x-ray diffraction pattern of product phases. The evolution of a peak at 27° 2Θ for products formed at 600 °C is interpreted as indication of the formation of a disordered carbon-rich material next to PTI-LiBr. b) X-ray photoelectron spectroscopy (XPS) of PTI-LiBr samples. Evaluation of C1s and N1s core regions confirm the presence of carbon-rich product (285 eV) and loss of nitrogen at 600 °C. Quantification by signal integration confirms the carbon-rich nature of the products obtained at 550-600 °C when compared to a theoretical optimal ratio of 40:60 in $C_6N_9H_3$ PTI. c) Images of PTI-LiBr powder in glass vials showing brown discoloration. Figure adapted from Burmeister et al..[115]

The starting point for this work is the ionothermal synthetic protocol for PTI that has not been altered since its first reports.[14,51,150] The significant parameters for polycondensation reactions are the reaction temperature (600 °C) and the reaction time (12 h). The product is characterized in literature as a dark brown powder.[54] The material obtained at 600 °C shows no visible photoluminescence under 375 nm UV-light (Figure 35). Higher luminescence can typically be accessed only by dispersing the material in water/methanol/DMSO.[150] Hence, it is often argued that the emission of the material in its initial graphitic state is quenched by π-π stacking. Instead of excitation and radiative emission, π-π quenching leads to photo-induced electron transfer to a neighboring π-system. This inhibits effective recombination of the electron-hole pair in a radiative process. In this work synthesis at a temperature of 550 °C and extended reaction times of 48 h yields an almost colorless product (Figure 34 a, left) with visible photoluminescence when irradiated with UV-light. The hitherto employed harsh reaction conditions (600 °C, 12 h) are above the onset of carbonisation of the material and introduce carbonaceous contaminants that darken the color of PTI.[53] Qualitative and quantitative XPS analysis of the C1s core region shows an intense peak at 285 eV and confirms the presence of C-C

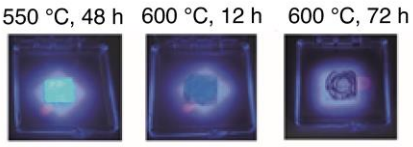

Figure 35. Illumination of PTI-LiBr samples from different reaction conditions with a 375 nm LED. The sample obtained at 550 °C shows visible photoluminescence. Figure adapted from Burmeister et al..[115]

environments (adventitious C1s, C-C peak at 284.8 eV) (Figure 34 b).[151] This contribution is often assigned to adventitious carbon.[14,152,153] However, at 475-550 °C the contribution at 285 eV in the C1s spectrum of PTI-LiBr is greatly reduced. Since the contribution of adventitious carbon should be similar for all samples, one can deduce that part of this contribution comes from a carbon-rich phase that coevolved during the synthesis at 600 °C. Looking at the N1s region, one can observe nitrogen signals from triazine moieties at 398.5 eV and a contribution from the imide-NH bridges between the triazine units at 400 eV with relative intensities of (3:1) for the product from 550 °C (Figure 34 b, right). The product obtained at 475 °C, 7 d approaches the theoretical elemental composition of poly(triazine imide) ($C_6N_9H_3$) of 40:60 C:N most closely (Figure 34 c). Other groups have not reported the presence of this carbon-rich phase under these conditions. Hence, it is likely that it was either overlooked or mistaken for a contribution solely from carbon tape used as substrate or adventitious carbon in XPS experiments. An attempt to study the structure of the phase obtained from synthesis at 600 °C for 72 h was conducted by Suter et al.[154]

The possibility to condense PTI at temperatures at which carbonisation has not yet started is promising since optoelectronic devices require pure, low-defect materials. Mixed phases can lead to energetic disorder which can in turn lead to charge carrier trapping.

Using Soxhlet extraction with water on the improved PTI-LiBr, PTI-IF is obtained.

Elemental composition of PTI-LiBr and PTI-IF

Combustion elemental analysis and inductively coupled plasma-optical emission spectroscopy (ICP-OES) on both PTI derivatives as complementary bulk characterisation methods in regard to XPS are performed. One finds the results to be in good agreement with the theoretical chemical formula (Table 5).

Table 5. Theoretical and experimentally determined elemental analysis of PTI-LiBr and PTI-IF in wt% from combustion analysis and ICP-OES. Table reproduced from Burmeister et al..[111]

	C wt%	N wt%	H wt%	Li wt%	residual wt%
PTI-LiBr experiment	24.67	43.02	0.87	4.47	26.95
$C_6H_3N_9LiBr$ PTI-LiBr in theory	25.02	43.77	1	2.41	27.75
PTI-IF experiment	35.00	61.53	1.73	0	1.74
$C_6H_3N_9$ PTI-IF in theory	35.83	62.67	1.51	0	0

As observed previously in PTI-LiCl, the Li-ion loading in PTI-LiBr is too high to be explained just by intercalation of LiBr. Excess lithium isoelectronically replaces some of the hydrogen atoms at the imide bonds.[155] Overall, one obtains a composition of $[(C_{3.0}N_{3.0})_2(N_{1.0}H_{1-x}Li_x)_3 \cdot Li_{1.2}Br_{1.2}$, x=0.2] for PTI-LiBr (theoretical $C_6H_3N_9LiBr$). Electron energy loss spectra (EELS) confirm the presence of carbon, nitrogen, lithium, and bromine in PTI-LiBr crystals that were identified by the corresponding d-spacings in the HAADF image (Figure 36 a, b). K-edges of additional elements are not observed confirming the high purity of the product on microscopic scale (Figure 36 c, d).

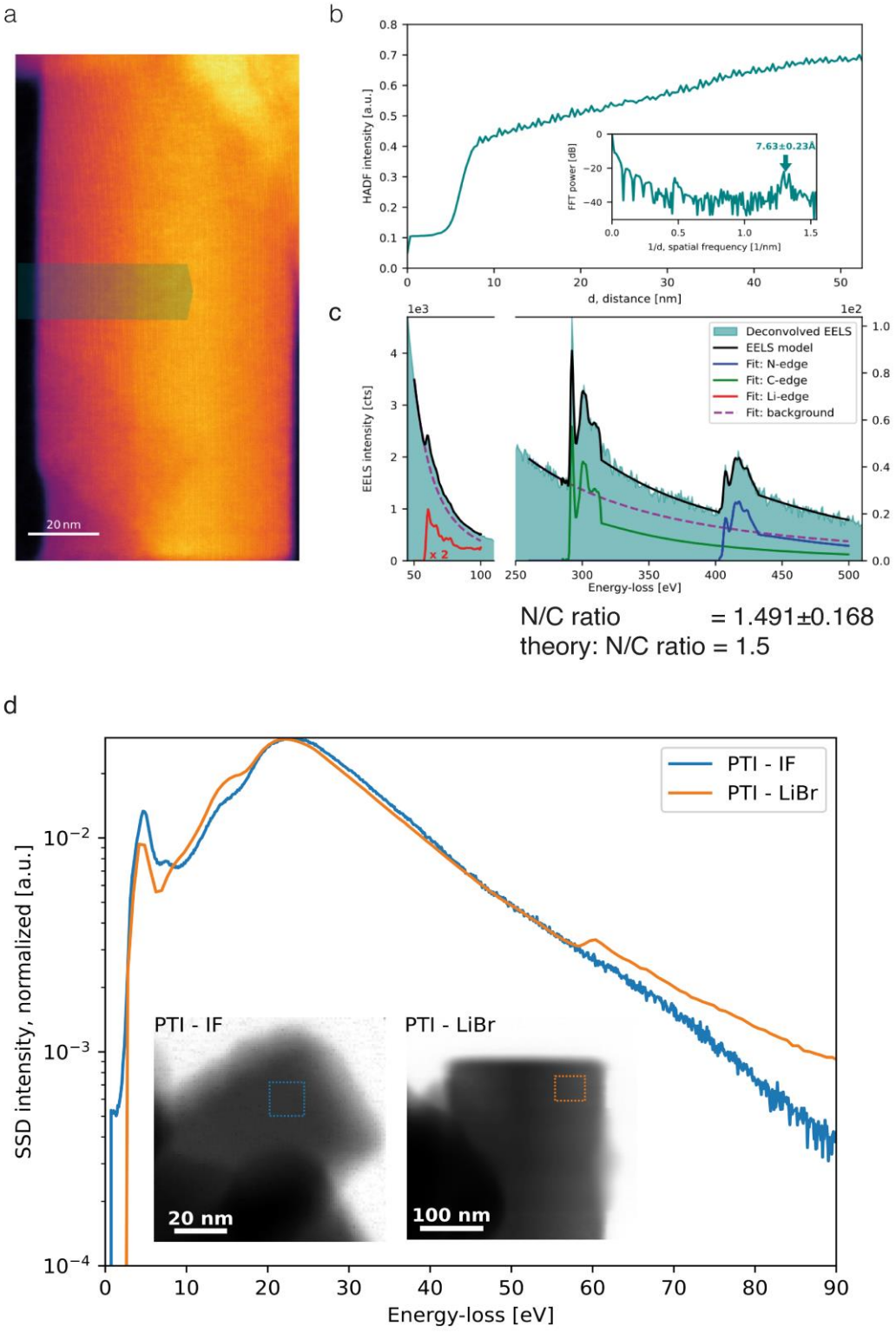

Figure 36. a) High angle annular dark-field (HAADF) image of the PTI-LiBr crystal that was chosen for the EELS experiment. b) Evaluation of lattice plane distance. The c-distance seems to be increased by electron beam irradiation (theory c=7.04 Å) c), d) PTI-LiBr and PTI-IF EELS spectra. Evaluation of the k-edge yields the N/C ratio which is in good agreement with the theoretical expected values of 9N/6C = 1.5. Quantitative analysis of the ion species is not possible due to the overlap of the Br-M4,5 edge at 69 eV with the Li K-edge at around 62 eV. d) EELS spectrum comparison of PTI-LiBr and PTI-IF attesting the absence of Li ions in PTI-IF. Figure reproduced from Burmeister et al..[111]

After de-intercalation by Soxhlet extraction, one detects no Li and no Br ions as rest mass in combustion analysis or Li in ICP-OES. The calculated composition of PTI-IF is $C_{6.0}H_{3.5}N_{9.0}$ (Li wt% << 0.5) (theoretical $C_6H_3N_9$). EELS shows no evidence of intercalated ions in the form of Li/Br K-edges at the microscopic level (Figure 36 c, d). Overall, results of the macroscopic and microscopic composition analysis reflect the theoretically expected elemental composition well.

Having established that the elemental analysis on macro- and microscopic level is meeting the expectations, the effect of de-intercalation on the crystal structure is investigated by x-ray diffraction, electron diffraction and ssNMR.

Effect of de-intercalation on the structure and morphology of PTI crystals

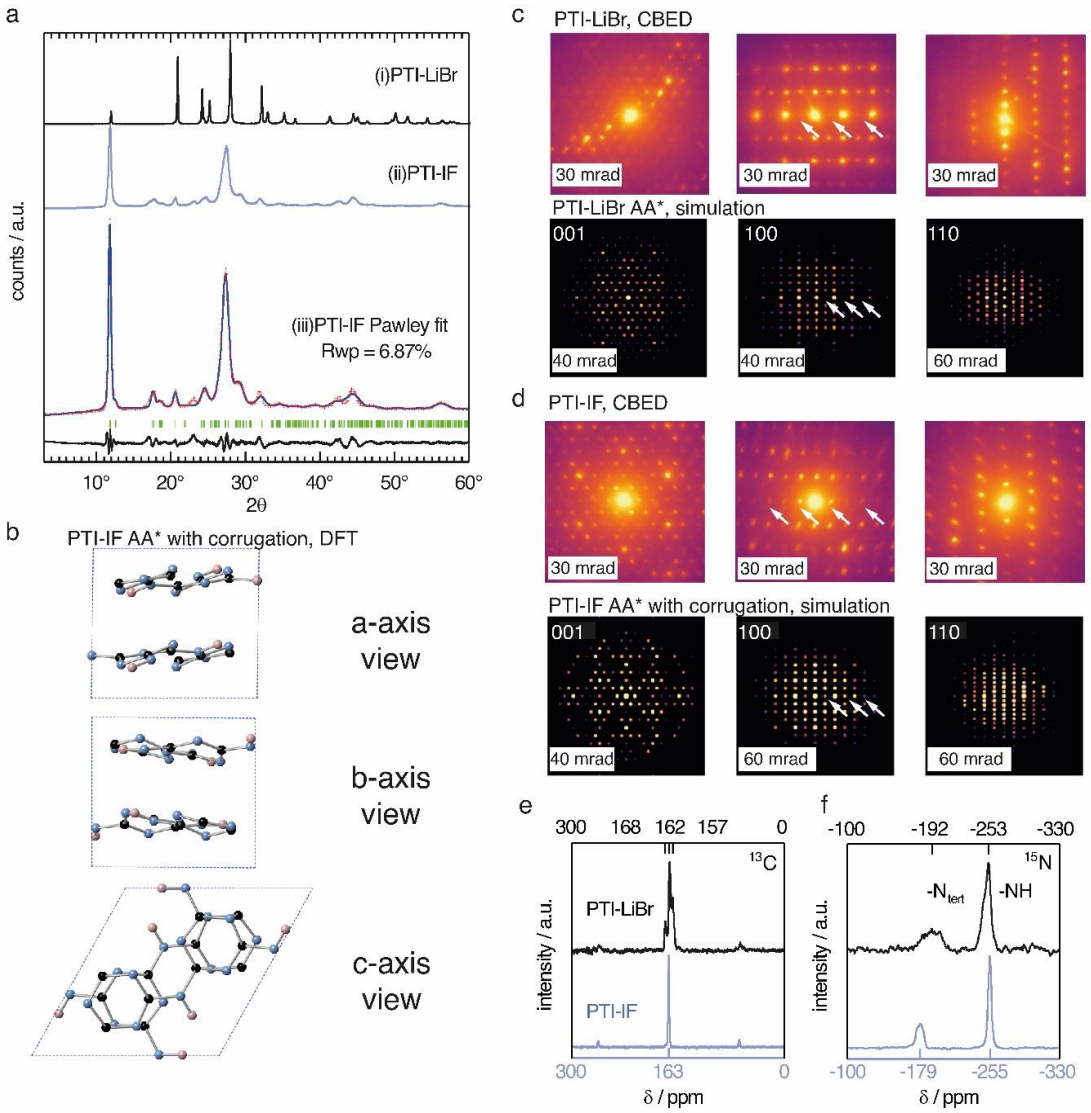

Figure 37. a) Experimentally obtained PXRD patterns of (i) PTI-LiBr and (ii) PTI-IF and (iii) Pawley fit (blue line) of the experimentally obtained pattern (red crosses) to a corrugated AA* stacked PTI-IF cif file, calculated Bragg peak positions (in green), and the difference between the observed and refined pattern (in black). b) Unit-cell of PTI-IF in a corrugated AA* arrangement based on DFT geometry optimisation and Pawley fitting. The unit cell is shown along the three crystal axes with nitrogen atoms as blue spheres, carbon as black spheres, and hydrogen as pink spheres. c) Convergent beam electron diffraction (CBED) patterns of PTI-LiBr and simulated patterns. Systematic absences marked by white arrows. d) Experimental CBED patterns of PTI-IF and simulated patterns. e) ^{13}C referenced to tetramethylsilane and f) ^{15}N referenced to nitromethane solid-state nuclear magnetic resonance (ssNMR) spectra of PTI-LiBr (black line) and PTI-IF (blue line). (Figure reproduced from Burmeister et al..[111])

The unit-cell of PTI-LiBr has been described in great detail,[58,139,155] and it serves as point of reference for the structure refinement and solution of PTI-IF. A unit-cell for PTI-IF is obtained using powder X-ray diffraction (PXRD) (Figure 37, a), convergent beam electron diffraction (CBED) (Figure 37, d), and structural optimisation by density functional theory (DFT) (Figure 37, b). The DFT-optimized and Pawley-

refined unit cell of PTI-IF agrees well with x-ray and electron diffraction data, and it indicates that intercalate-free PTI sheets assume a corrugate arrangement.

Removal of intercalated Br ions from PTI-LiBr – and the accompanying loss of the high-scattering cross section contribution – leads to a broadening of all x-ray diffraction peaks (Table 6). In particular, one can attribute the broadening of diffraction peaks that have 00*l*-components to the exfoliation and the decreasing height of PTI stacks. The median 002 stacking distance between PTI sheets increases from 3.5 Å in PTI-LiBr to 3.6 Å in PTI-IF, either due to corrugation or due to intercalation of water molecules.

Table 6. Peak positions and FWHM of hk0 and 00l peaks of PTI-IF and PTI-LiBr. (Table reproduced from Burmeister et al..[111])

hkl	PTI-IF peak position, FWHM	PTI-LiBr peak position, FWHM
010	11.82 2θ, 0.37 2θ	11.99 2θ, 0.11 2θ
110	20.56 2θ, 0.68 2θ	20.88 2θ, 0.12 2θ
002	24.71 2θ, 0.93 2θ	25.14 2θ, 0.23 2θ

Corrugation of triazine-based 2D networks has been predicted computationally in the past, however, to this date there was experimental evidence to support it.[12,156,157] To corroborate that the removal of intercalated ions is indeed accompanied by corrugation and delamination, the experimentally obtained diffractogram of PTI-IF with the simulated diffraction patterns of corrugated and non-corrugated PTI-structures in three different stacking arrangements are compared: (i) alternating layers with a mirror plane through the triazine units (AA*), (ii) eclipsed orientation (AA), and (iii) staggered orientation (AB). Simulated diffraction patterns based on the corrugated structures match the experimental data better (δRwp = 2-7%), and they correctly describe the peak at 18° 2Θ (assigned as -111) rather than the non-corrugated ones. The best Pawley fit was obtained for the corrugated PTI-IF structure in AA* stacking mode (Figure 37, a-b**,** Table 7). Further evidence for the corrugation of PTI-IF comes from CBED (Figure 37, c-d). In the case of a perfectly planar, intercalated PTI-LiBr structure, one observes no discrepancies between observed and predicted patterns (Figure 37, c).[108]

Table 7. Pawley refinement of cif files with different stacking orders and with and without layer corrugation. (Table reproduced from Burmeister et al..[111])

	Flat Rwp%	Corrugated Rwp%
AA*	17	7
AA	20	13
AB	14	12

For PTI-IF, once again the corrugated structure reproduces the experimental pattern better. In particular, simulated ED patterns based on the corrugated PTI-IF structure account correctly for the missing systematic absences in the 100 zone axis pattern (Figure 37, d). Unfortunately, the AB-stacked structure also accounts for the loss of the systematic absences in the 100 zone axis pattern. A final verdict between an AB-stacked structure and a corrugated AA* one would be only possible by single crystal structure refinement of electron diffraction data which is not obtained in this work.

In conclusion, one arrives at a structural description of PTI-IF as a corrugated or AB-stacked, intercalate-free, triazine-based material coming from various orthogonal methods that encompass microscopic, macroscopic, and *ab initio* structure analysis. As the reason for the corrugation, polar interactions of adjacent PTI-layers are proposed.[158]

Removal of the intercalated ions from PTI-LiBr has a pronounced effect on the local electronic environments of carbon and nitrogen nuclei in PTI-IF that are monitored using solid-state NMR (ssNMR). Carbon environments attributed to the triazine (C_3N_3) ring are split up as ^{13}C (168, 162, 157 ppm) in the PTI-LiBr structure by the heterogeneous distribution of intercalated ions. In comparison, the more homogeneous, intercalate-free PTI-IF structure shows only one carbon signal at 163 ppm (Figure 37, e).[58] Similarly, the ^{15}N signals of PTI-IF appear sharper at -179 (triazine nitrogens) and -255 ppm (imide bridge nitrogen) (Figure 37, f). Bands from the C_3N_3 ring in ^{15}N and ^{13}C ssNMR spectra of PTI-IF are shifted to higher ppm values compared to the PTI-LiBr. This finding indicates that nuclei are de-shielded by the removal of ions; an effect that stems from a reduction of electron density at the carbon and nitrogen nuclei. This experimental observation is corroborated by Bader partial charge analysis based on DFT results (Figure 38). In PTI-LiBr one can observe an increased electron density from the interaction of bromide orbitals with the CN-orbitals.

Presence or absence of intercalated ions has a pronounced effect on the preferred orientation of PTI-IF and PTI-LiBr crystals on substrates such as the carbon net used in CBED experiments. The structural formula of PTI-LiBr and PTI-IF is shown in Figure 40 a). An explanation of the orientation analysis is given in Figure 39.

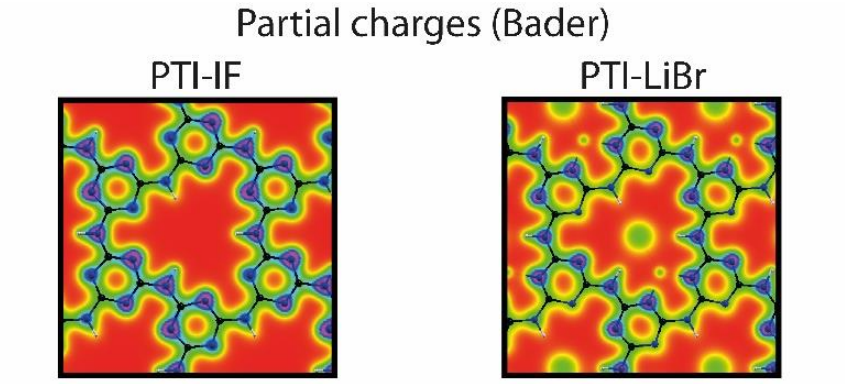

Figure 38. Partial charge analysis (Bader) of PTI-IF and PTI-Br. Electron density at carbon and nitrogen is higher in PTI-LiBr when compared to PTI-IF. Carbon is represented as black sphere, nitrogen as blue spheres and hydrogen as white spheres. Lithium and bromine are not represented as spheres. Bromine is positioned in the center of the pore in PTI-LiBr and Lithium is off-centered. (Figure reproduced from Burmeister et al..[111])

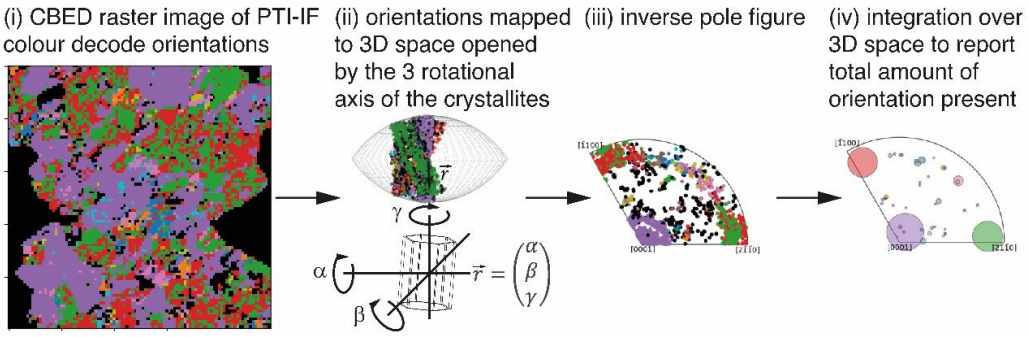

Figure 39. (i) Each individual pixel represents one CBED pattern that was matched to the orientation of the crystal structure. The orientations are mapped into 3D-space utilizing the three rotational axes of the crystal relative to the electron beam that define three integers giving rise to the length and orientation of a vector in the 3D space with the [0001]/[001] zone axis being the center (ii). Each vector is then represented by a point in 3D space (iii). Pixels with similar orientation are then summed up over the 3D space to give a 2D representation (iv). (Figure reproduced from Burmeister et al..[111]).

The majority of 52% of PTI-LiBr crystals is tilted away from the [001] orientation (Figure 40, b). This means that the majority of PTI-LiBr crystals orient themselves with the long side of the pillars in parallel to the substrate and perpendicular to the incident electron beam (denoted with an X in the figure) – as indicated by the wireframe model.

In contrast, for PTI-IF, a major fraction of 34% of CBED patterns is collected from crystals oriented with the [001] zone axis parallel to the beam (Figure 40, c). This means that PTI-IF crystals are oriented with the covalently-bonded basal plane in parallel to the carbon support. The pronounced change in preferred crystal orientations is caused by the removal of ions and the accompanying reduction of cohesive, inter-planar interactions – from a mix of ionic and van der Waals

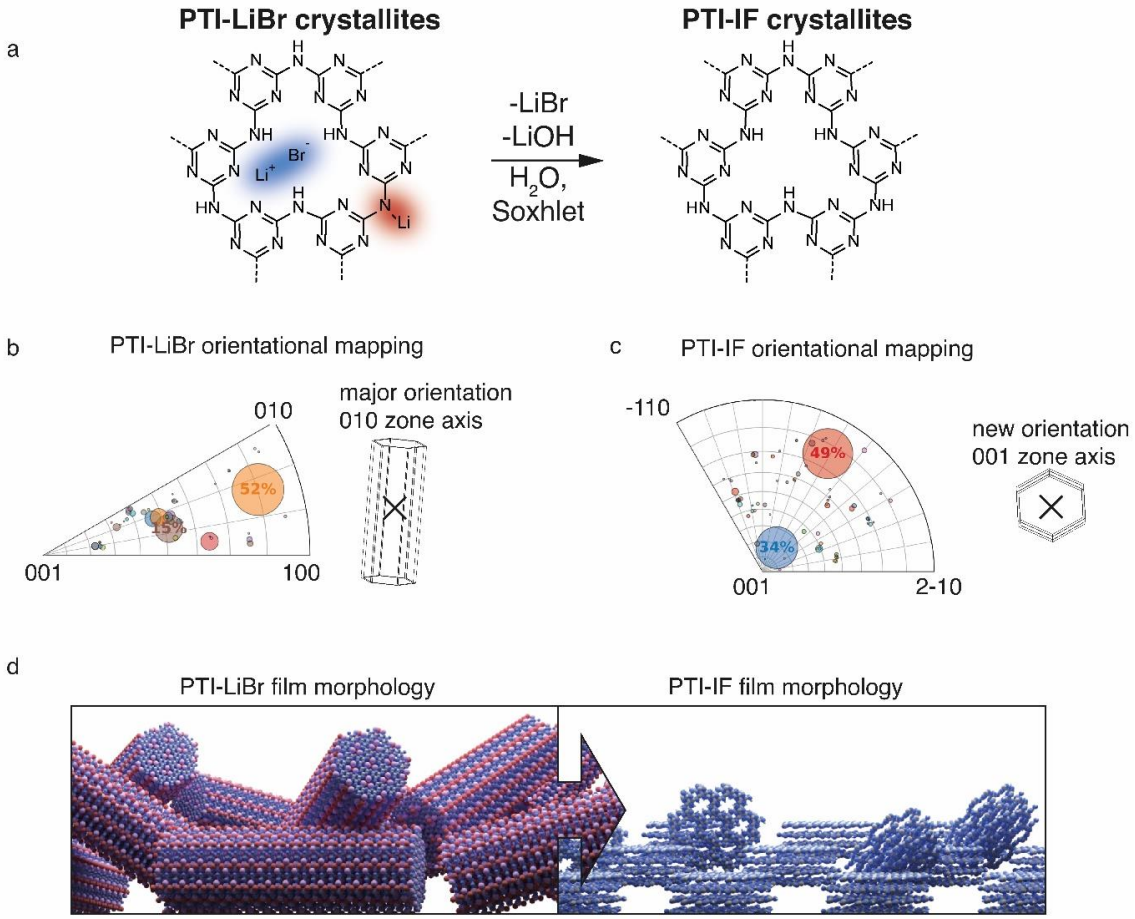

Figure 40. Statistical analysis of the orientations of nano-crystals of PTI-LiBr and PTI-IF based on CBED mapping. a) Structural formula of PTI-LiBr and PTI-IF. b) Integration of the inverse pole figure of PTI-LiBr. c) Integration of the inverse pole figure of PTI-IF. The major observed zone axis in PTI-LiBr is 010/100. In PTI-IF it changes to 001. d) Visualisation of the different morphologies and orientations of PTI-LiBr and PTI-IF in films. (Figure reproduced from Burmeister et al..[111])

interactions in PTI-LiBr to van der Waals interactions only in PTI-IF. As a result, PTI sheets become more easily exfoliated and effectively diminish the stacking height of PTI-IF nano-crystals. The reorientation of PTI-IF nano-crystals with the covalent, planes parallel to a substrate and with pore channels orthogonal to it, is beneficial in device geometries intended for sensing and gating as ions could be moved in these pores away or to the surface of the gate material (Figure 40, d).

Seeing that PTI-IF is exfoliated and pores might be more accessible after de-intercalation, the interaction of CO_2 gas with PTI-IF and PTI-LiBr was studied by

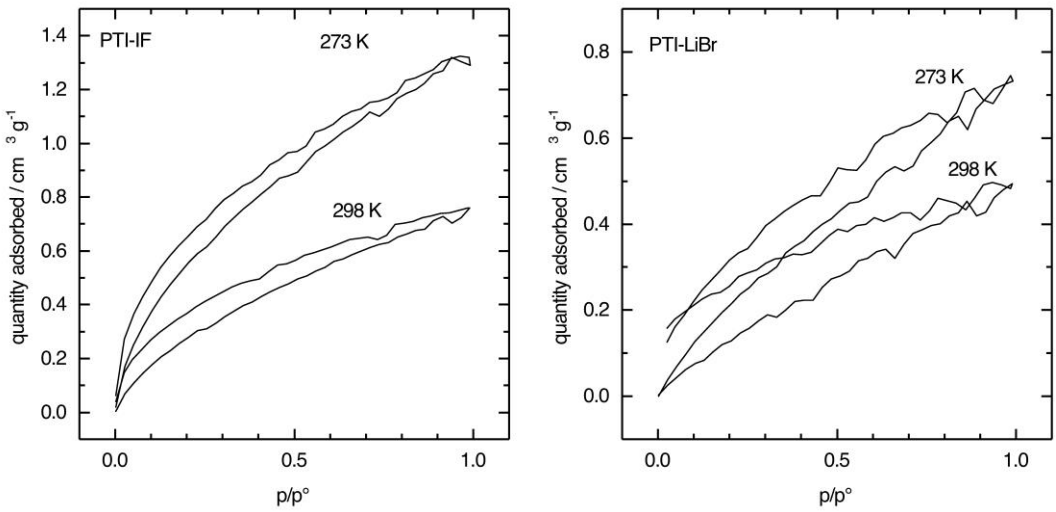

Figure 41. CO_2 adsorption isotherms at 273 and 298 K for PTI-LiBr and PTI-IF used to calculate the heat of adsorption and quantity of adsorption.

collecting gas adsorption isotherms. The de-intercalation nearly doubles the heat of adsorption from 16 to 31 kJ mol^{-1}. However the overall quantity of CO_2 adsorbed is still low with 5 mg g^{-1}.

Microporous covalent triazine polymers obtained by Friedel-Crafts synthesis can reach up to 136 mg g^{-1} uptake and a heat of adsorption up to 40 kJ mol^{-1}.[159] Due to the small pore diameter in the PTI structure the uptake and interaction with CO_2 is hindered.

To consolidate the structural characterisation, vibrational analysis via experimental and theoretical methods is presented in the following section.

Vibrational analysis

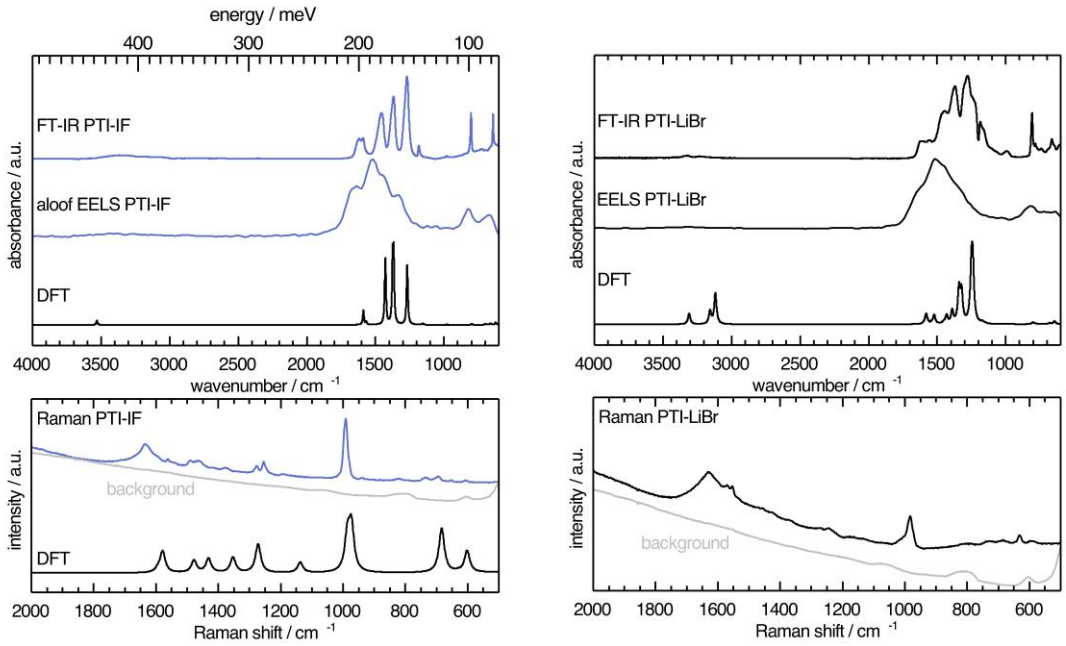

Figure 42. Vibrational modes in PTI-IF and PTI-LiBr determined by FT-IR, aloof-EELS, DFT, and Raman spectroscopy (266 nm). (Figure reproduced from Burmeister et al..[111])

Using a combination of FTIR, UV-Raman microscopy, EELS, and DFT it is possible to assign phonon modes and deformation vectors to PTI-IF (Figure 42, left) and PTI-LiBr (Figure 42, right).

The FT-IR spectra of PTI-LiBr typically have very broad bands (Figure 42, right). One can distinguish between the C_3N_3 ring breathing mode at 808 cm^{-1} and the CN-stretching modes at 1100-1620 cm^{-1}. Further, one observes a split of the weak imide N-H stretch at 3300 cm^{-1} that is caused by heterogeneously intercalated ions that break the symmetry of the material.[108,160]

The UV-Raman spectrum of PTI-LiBr shows only two distinctive features at 1629 and 982 cm^{-1}. The 1629 cm^{-1} band is interpreted as C=N ring-stretching modes, also referred to as G band, while the band at 982 cm^{-1} represents the C_3N_3 breathing mode.[117] The ring mode in PTI-LiBr has a shoulder towards higher wavenumbers. The aloof-EELS phonon spectrum of PTI-LiBr shows a broad feature reminiscent of the CN stretching modes in the FT-IR spectrum. Additionally, the ring mode at around 800 cm^{-1} can be observed with this technique.

The vibrational modes in PTI-IF are better resolved than in PTI-LiBr.[161] DFT calculations predict the main four bands in the aloof-EELS and FT-IR spectra of PTI-

IF observed between 980-1620 cm^{-1} (Figure 42, left). However, the intensity of the ring modes at 642 and 802 cm^{-1} is drastically underestimated in the phonon calculation. The ring mode of PTI-IF at 990 cm^{-1} in the Raman spectrum has a higher intensity and no shoulder compared to PTI-LiBr.

The two triazine ring modes in the FT-IR spectra of PTI-LiBr are observed at 809 and 666 cm^{-1}. In comparison, the ring modes of PTI-IF are observed at 802 and 642 cm^{-1}. The higher energy ring-modes of PTI-LiBr are attributed to structural strain that is induced by the intercalated ions. The observed and calculated energies of the modes and a visual representation of the deformation vectors are presented

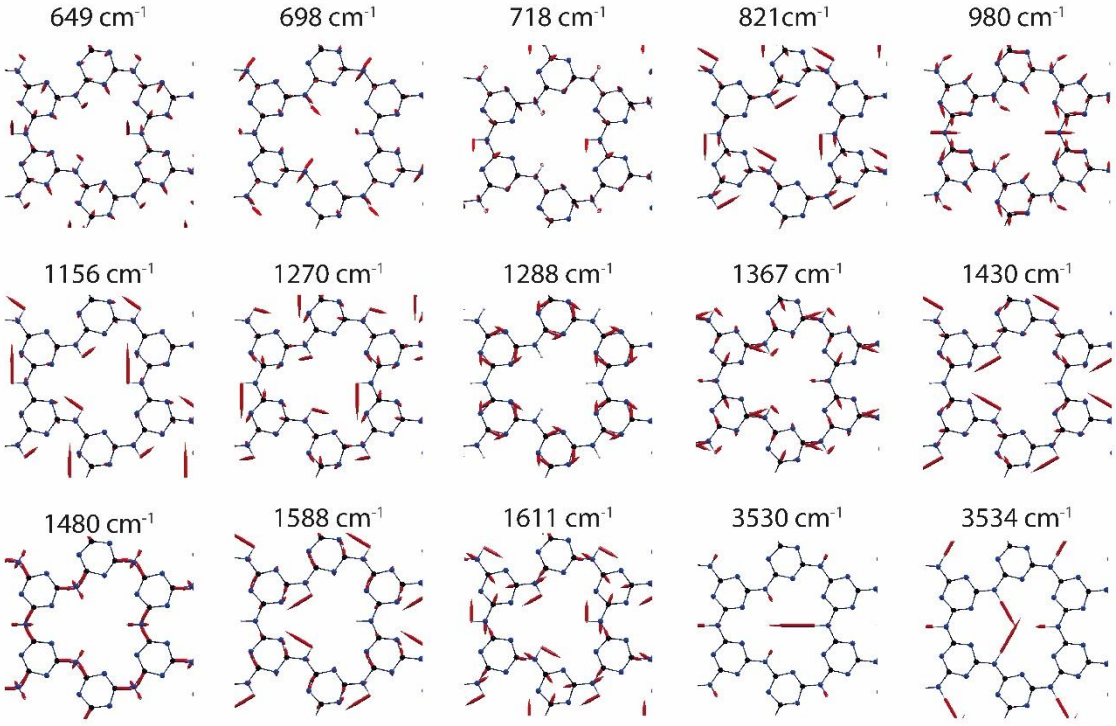

experimentally observed			ν calc.	rel. int.	assignment
IR	Raman	EELS		IR	
			3530, 3534		NH stretching
3360 (b, w)					intercalated water
1620 (m)	1633 (b)	1653 (b)	1611	0.00	NH wagging+ring breathing
1590 (m)	1562 (b)		1588	11.14	quadrant ringstretch
	1490 (w)	1517 (b)	1480	0.07	NH stretching+NC stretching
1455 (m)	1460 (w)	1436 (b)	1430	52.93	NH wagging+ring deformation
1367 (s)	1375 (m)	1333 (b)	1367	95.78	NH wagging+ring deformation
1270 (vs)	1277 (w)		1288	0.11	ring deformation
	1254 (w)		1270	49.74	NH wagging+ring deformation
1182 (w)			1156	1.2	NH wagging+ring deformation
982 (w)	990 (vs)		980	0.21	quadrant ringstretch
802 (s)		820 (b)	821	1.41	NH wagging+ring breathing
	733 (vw)		718	0.03	out of plane def.
	692 (vw)		698	1.44	NH wagging+out of plane ring breathing
642 (s)	650 (vw)	667 (b)	649	0.46	ring deformation

Figure 43. Phonon normal modes of PTI-IF monolayer. Top: phonon frequencies and corresponding eigenmodes represented as red arrows. The normal modes are mainly composed by N-H and C-N stretching. Bottom: summary of DFT vibrational analysis of a monolayer compared to FT-IR, Raman, and EELS results. (Figure reproduced from Burmeister et al..[111])

in an overview figure and table to guide future interpretation of vibrational spectra of triazine-based carbon nitrides (Figure 43).

In general, the inhomogeneous distribution of ions throughout the PTI-LiBr structure causes a significant broadening of the vibrational bands in all spectroscopic methods. Removal of the ions from the structure leads to a more homogeneous chemical environment throughout PTI-IF and, hence, to narrower vibration bands.

Electronic structure of PTI crystals

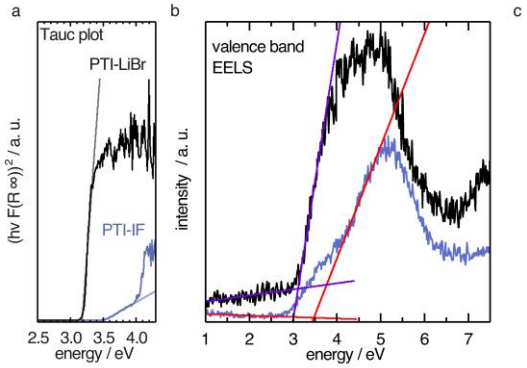

c

	PTI-LiBr	PTI-IF
E_g Tauc	3.2 eV	3.5 eV
E_g EELS	3.1 eV	3.5 eV
DFT results	direct	indirect
E_g bulk crystal	2.29 eV	2.46 eV
E_g Monolayer	2.85 eV	3.19 eV

Figure 44. a) Tauc plot for a direct electronic transition of diffuse reflectance data of PTI-LiBr and PTI-IF. b) valence band EELS c) summary of optical gaps extracted from Tauc plots (E_g Tauc), from valence band EELS (E_g EELS), and band gaps extracted from DFT calculation (see Figure 49).(Figure reproduced from Burmeister et al..[111])

Diffuse reflectance spectroscopy, valence band electron energy loss spectroscopy (VB-EELS) (Figure 44, a), DFT (Figure 46, Figure 49), and UPS (Figure 47) are applied to determine the size (eV), the nature (direct or indirect), and the energetic position of the band gap of PTI-type materials. The optical gap of nano-crystals of PTI-materials is determined using the onset values from the Tauc plot (Figure 44, a),[131,162] and valence-band EELS spectra of the conduction band (Figure 44, b). The DFT calculations show that the valence band of a PTI-IF monolayer is doubly degenerate at the Γ-point, and that it is composed of states that contain mainly contributions from the nitrogen lone-pairs (Figure 46). Group-VI semiconductors with a lone-pair upper-most valence band are referred to as "lone-pair semiconductors".[163] The non-bonding character of the VB has been theoretically predicted also for other graphitic carbon nitride materials.[158]

In contrast to this, in CN-containing molecules like melamine as well as PTI-layer cut-outs (Figure 45), both the highest occupied orbital (HOMO) and the lowest occupied orbital (LUMO) have π-character; thus, the HOMO-LUMO transition is allowed.[164] However, in PTI layers the electronic VB → CB transition is forbidden because there is no orbital overlap between the non-bonding orbitals of the VB and the π*-like orbitals of the conduction band (Figure 46, a). A likely reason for the energetic uplift of the occupied lone-pair band in the periodic structure when compared to the molecular species and pore cut-out above the π-band is the

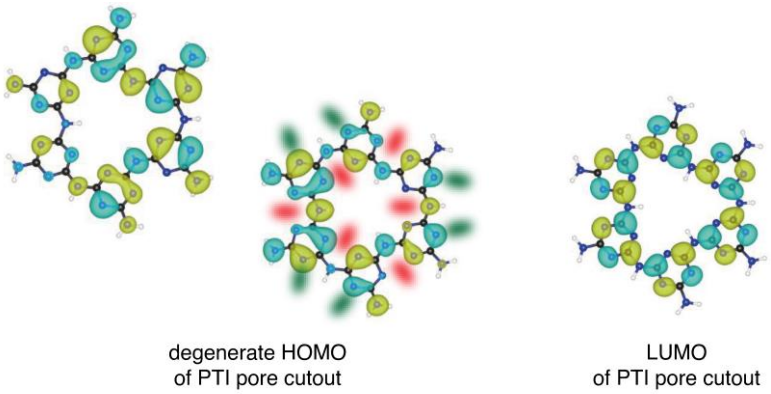

Figure 45. HOMO and LUMO of a "pore cut-out" of a PTI-layer. Similar to melamine the HOMO is not "lone-pair like" with large orbital coefficients on the sp^2-hybridized ring carbon and nitrogen species. Areas with anticipated Pauli repulsion between nitrogen lone-pairs of triazine ring nitrogen atoms are marked red. Positions of ring nitrogen lone-pairs without spatial confinement by other lone-pairs in the pore cut-out are marked green.

presence of Pauli repulsion all around the triazine-ring between the nitrogen lone-pairs. The lone-pair states are observed to be at the top of the valence band in the calculation of all periodic PTI-derivatives. Calculations for pore cut outs such as shown in Figure 45 are hence not a good representations for the electronic structure in PTI crystals. The electronic structure of PTI-IF with corrugated layers exhibits almost identical VB states at the ring-nitrogen as the monolayer with only the degeneracy at the Γ-point being lifted (Figure 49, b).

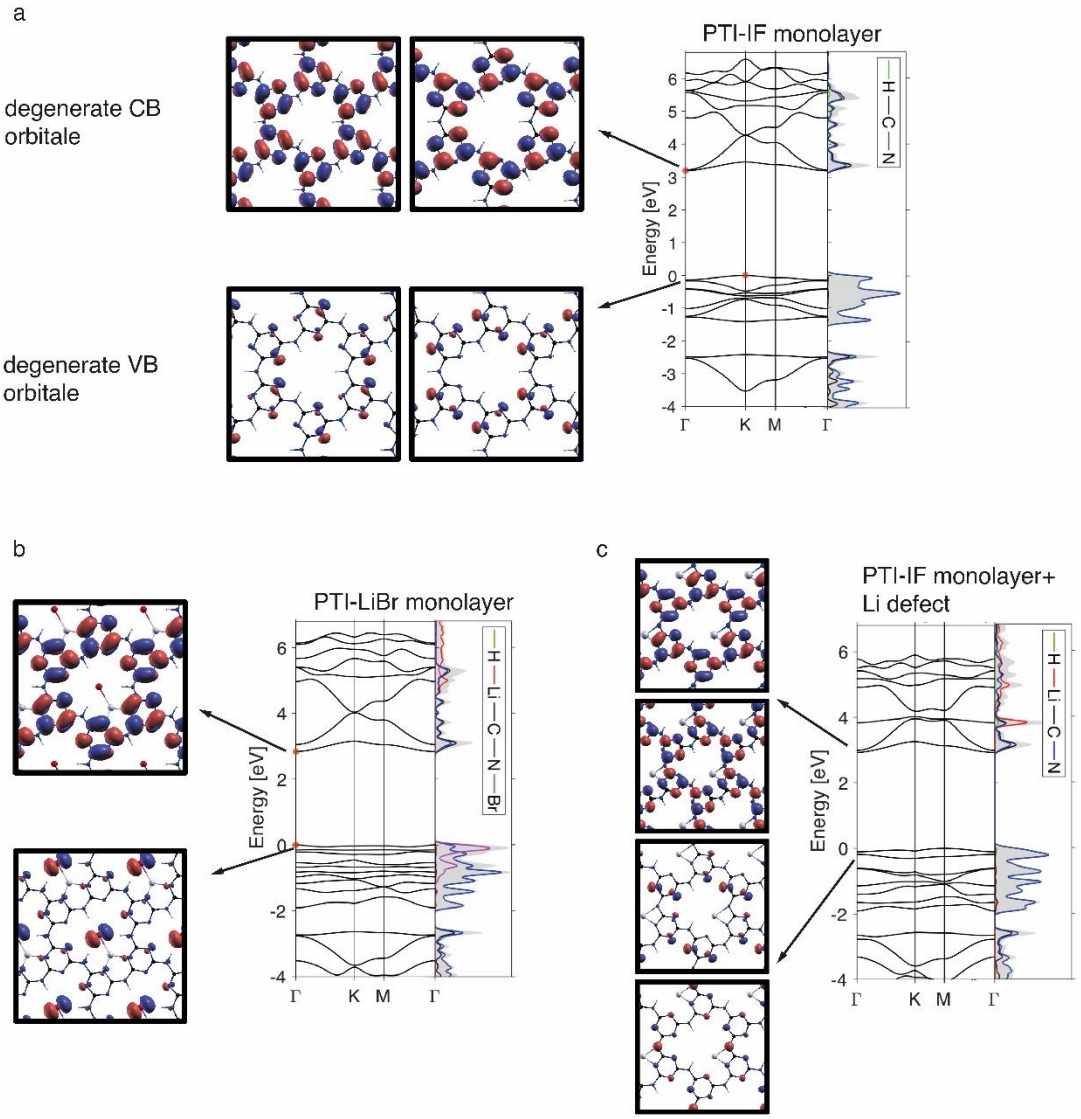

Figure 46. a) PTI-IF pristine monolayer electronic bandstructure and isosurfaces of the double degenerate valence band and conduction band Bloch states at the Γ point (i.e., BZ centre). b) PTI-LiBr monolayer electronic bandstructure and isosurfaces of the valence band and conduction band Bloch states at Γ point. c) Effect of Lithium defect replacing one hydrogen atom at the imide bridge in the PTI-IF monolayer. All upper-most valence bands show significant lone-pair character only revealed using periodic boundary condition DFT calculations. (Figure reproduced from Burmeister et al..[111])

The forbidden VB → CB transition prevents direct estimation of the band gap by optical methods or EELS as the experimentally observed absorption corresponds to the π → π* transition between the VB-2 and the CB. The energetic difference between the forbidden VB → CB and the observed VB-2 → CB transitions is the reason for the significant discrepancy between the DFT band gap and the experimental absorption onset obtained from the Tauc plot and EELS measurements (Figure 44 c). The VB-2 → CB transition is a π → π* transition of

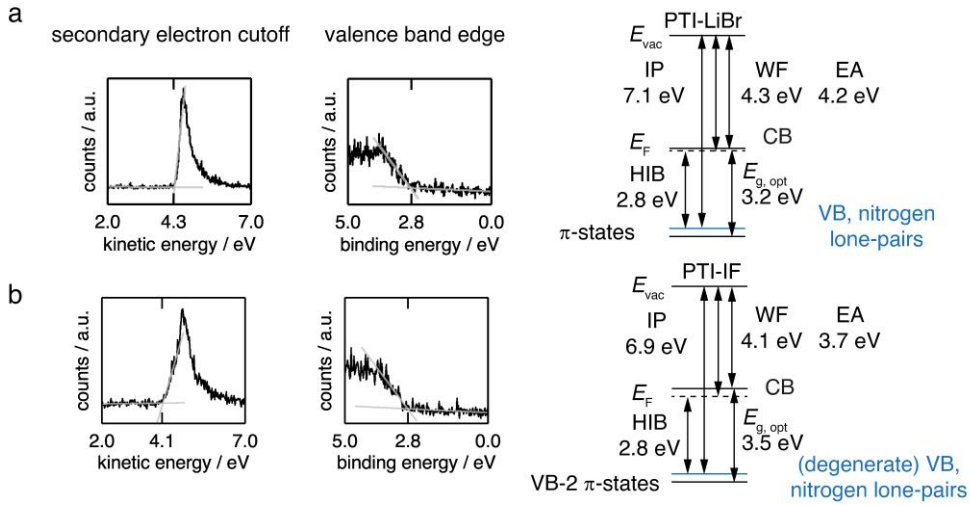

Figure 47. UPS Results and energy level diagrams of a) PTI-LiBr and b) PTI-IF revealing the lone-pair semiconductor property. The work function (WF) is extracted from the onset of the secondary electron cutoff and the hole injection barrier (HIB) is extracted from the onset of the valence band edge scan. (Figure reproduced from Burmeister et al..[111])

3.6 eV that corresponds more closely with the experimentally derived gap by Tauc plot and aloof-EELS (Figure 44, c).

One can observe that the π-band (VB-2) lies below the VB and, as a consequence, the estimated energy of the CB is lowered, i.e. it lies closer to the Fermi level. The energetic distance between VB and VB-2 in the intercalation free monolayer of PTI-IF is approximately 0.3 eV at Γ (Figure 46, a) and the CB position (or electron affinity) is 3.7 eV (Figure 47). Repeating this calculation for PTI-LiBr, one obtains an electron affinity of 4.2 eV; a value that allows environmentally stable n-transport.[74] The results of DFT, EELS, and UPS experiments culminate in the energy level diagrams for PTI-LiBr and PTI-IF in Figure 47.

To estimate the strength of the VB-2 → CB transition, the absorption coefficients of PTI-IF and PTI-LiBr are determined equating a molecular unit with one unit cell. The

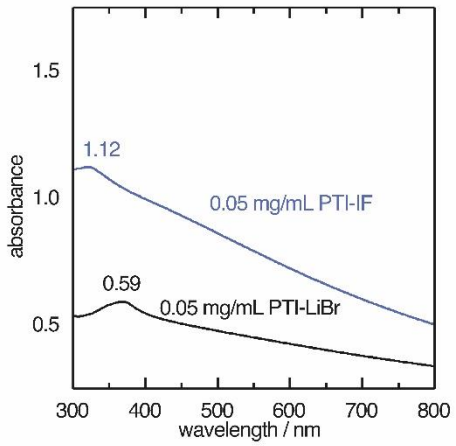

Figure 48. Absorption of PTI-IF (blue) and PTI-LiBr (black) emulsions in a cuvette with 1 cm path length. Molar absorption coefficients: 9032 $M^{-1}cm^{-1}$ PTI-IF, 6860 $M^{-1}cm^{-1}$ PTI-LiBr. (Figure reproduced from Burmeister et al..[111])

obtained absorption coefficients point towards a direct $\pi \rightarrow \pi^*$ (VB-2 → CB) transition in both materials (9032 $M^{-1}cm^{-1}$ for PTI-IF and 6860 $M^{-1}cm^{-1}$ for PTI-LiBr, Figure 48). They are one to two magnitudes lower than the absorption coefficients of molecular species without a forbidden HOMO-LUMO transition.[165,166]

Comparing PTI-LiBr and PTI-IF, removal of intercalated ions induces a significant blue shift of the absorbance onset by 0.3 eV (from 3.2 eV in PTI-LiBr to 3.5 eV in PTI-IF), as seen in the Tauc plot (Figure 44, a). This increase of the optical gap is also present – but less apparent – in the EELS valence band spectra (Figure 44, b). The shoulder appearing below the main EELS band is likely a result of beam damage as it grows in intensity during the measurement. The gap increases from 3.1 eV (PTI-LiBr) to 3.5 eV (PTI-IF) by VB-EELS. The lower optical gap and band gap of PTI-LiBr can be ascribed to two concomitant mechanisms: (1) the formation of ion pairs (*i.e.*

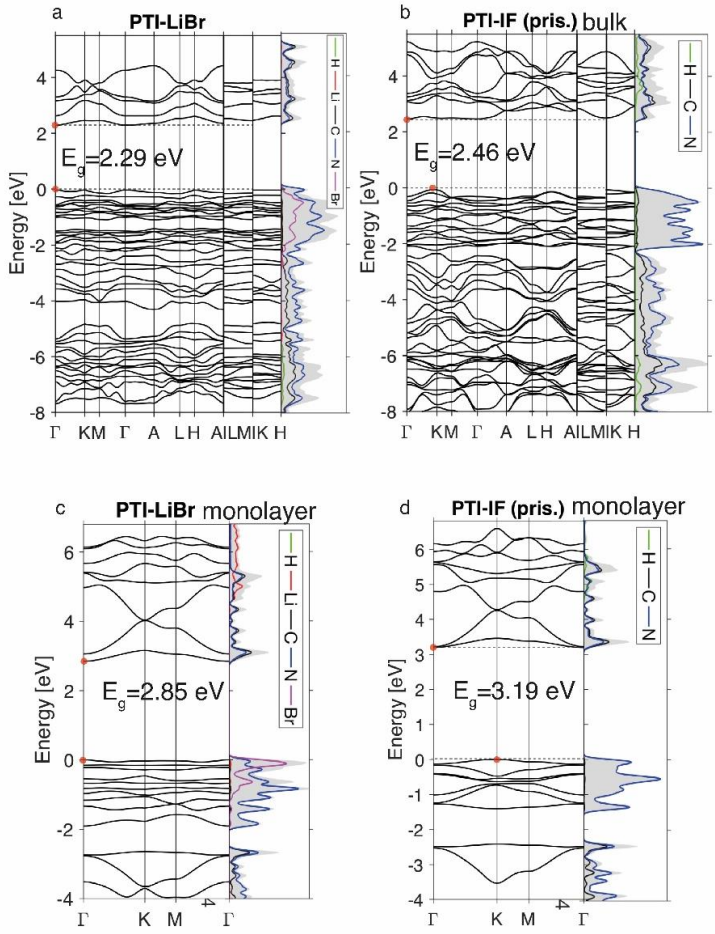

Figure 49. Calculated electronic band structures of a) PTI-LiBr AA* bulk, b) PTI-IF AA* bulk, c) PTI-LiBr monolayer and d) PTI-IF monolayer. (Figure reproduced from Burmeister et al..[111])

static dipoles) within the pores from the intercalated species that break the symmetry of the system. Eventually, this leads to the splitting of the degenerate levels at Γ; (2) the presence of intra- optical-gap defect states associated to the p orbitals of the Br anion (Figure 49, c).

PTI-type intercalation compounds reported hitherto in literature typically show lower optical gaps (2.2-2.7 eV) due to carbonisation.[54]

To complement the understanding of the electronic structure with data characterizing the electronic carriers, time domain-THz spectroscopy is performed. The associated results are presented in the following section.

Charge transport properties of nano-crystalline PTI

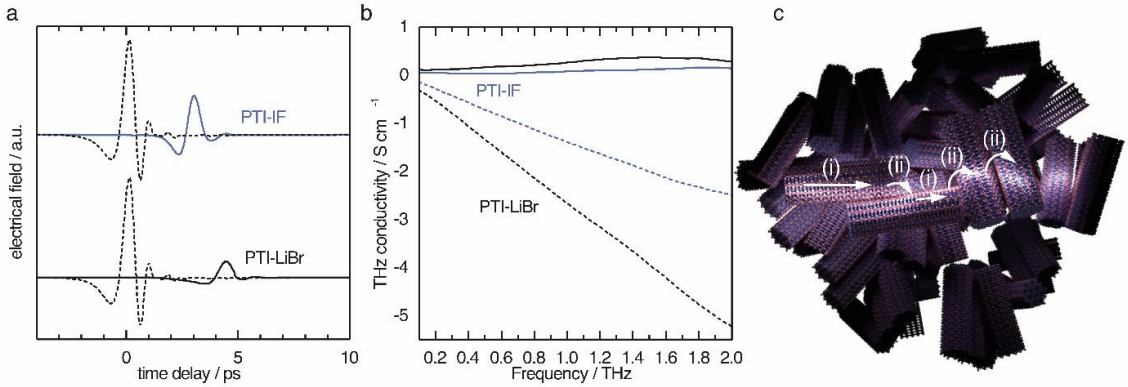

Figure 50. THz-time domain spectroscopy results of PTI-IF and PTI-LiBr as pressed pellets. a) THz reference pulse (dashed lines) transmitted through PTI-IF (blue) and transmitted through PTI-LiBr (black). b) Real (continuous line) and imaginary part (dashed line) of THz conductivity in PTI-IF (blue) and PTI-LiBr (black). c) Schematics of charge transport in PTI thin films. Nanoscale conductivity inside nano-crystals as obtained from THz spectroscopy is up to eight orders of magnitude higher than the electrical conductivity obtained from thin film measurements. The reason is that the charge transport between the nano-crystals (ii) is inefficient compared to the charge transport inside the crystals (i) probed by THz spectroscopy. (Figure reproduced from Burmeister et al..[111])

Intrinsic (*i.e.* undoped) organic semiconductors typically have a charge carrier density of 10^0 cm^{-3} and low mobility, as charge carriers are localized at single molecular units leading to hopping as the dominant transport mechanism. [85]

PTI-IF and PTI-LiBr films formed from nano-crystals typically show low conductivity (PTI-IF 10^{-10} S cm^{-1}, PTI-LiBr 10^{-7} S cm^{-1}) and only small photo-currents in lateral thin-film devices.[115] To answer the question whether the low conductivity of PTI-films is an intrinsic material property or whether it is induced by the nano-crystalline character of the sample, free standing pressed pellets of PTI-LiBr and of PTI-IF are subjected to time-domain terahertz spectroscopy (THz-TDS) experiments.

The obtained time-domain THz pulses after transmission through the sample (Figure 50 a, solid lines) show a significant difference in amplitude and a phase shift when compared to the pulse that did not pass the sample (dashed lines). The observed shifts contain information about the charge carriers inside the nano-crystals. Since the THz pulse is of picosecond duration, it can be translated to the conductivity on the nanoscale by a fast Fourier transform as explained in detail in the appendix.

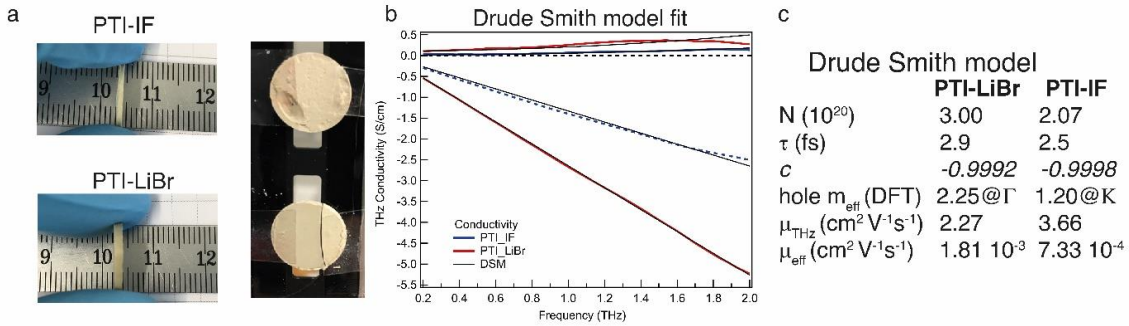

Figure 51. a) Pressed PTI pellets for THz spectroscopy. b) Drude Smith model fit. c) Drude Smith fitting parameters. (Figure reproduced from Burmeister et al..[111])

The THz conductivity at 1 THz is 0.26 S cm^{-1} in PTI-LiBr and 0.07 S cm^{-1} in PTI-IF, exceeding the macroscopic electrical measurements by about six and eight orders of magnitude, respectively (Figure 50 b). Hence, the conductivity inside the single crystals of PTI-LiBr and PTI-IF is much higher (Figure 50 c, (i)) than in the films. This is most likely due to inefficient charge transport between loosely packed PTI crystals (Figure 50 c, (ii)) in the macroscopic films. One can surmise that the reason for the higher THz conductivity in PTI-LiBr compared to PTI-IF lies in the higher orbital coefficients on the lithiated imide bridges and, as a consequence, better charge transport between the triazine units (Figure 46, c).

The obtained complex THz conductivity is analysed using the Drude-Smith model (DSM) that describes Drude-type transport of free charges impeded by spatial confinement with a second term including a localisation parameter (Figure 50, b, Figure 51 b-c).[167] The phenomenological DSM gives an estimation of the density of charge carriers N, the scattering time τ, and the localisation parameter c, which lies between 0 and -1 that describes Drude-type transport and completely immobile charge carriers, respectively.[168] Using the hole effective mass obtained from the DFT calculations (PTI-LiBr m_{eff} = 2.25, PTI-IF m_{eff} = 1.20), the carrier mobility in the nanoscale μ_{THz} and the effective mobility μ_{eff} can be calculated as well, as detailed in the appendix. The fitting parameters reveal a charge scattering time of 2.5 and 2.9 femtoseconds for PTI-LiBr and PTI-IF, respectively, and a localisation parameter of < -0.999 for both (Figure 51 c).

The low scattering time as well as the localisation parameter close to -1 imply a high degree of localisation. The effective mobility of 10^{-3}-10^{-4} cm^2 V^{-1} s^{-1} of PTI-LiBr and

PTI-IF is in the range of the one found in amorphous organic semiconductors.[169] The reasons for the low mobility is the absent conjugation along the imide bridge as well as the highly localized character of the upper most valence band states.

The density of charge carriers contributing to the nanoscale conductivity in PTI-LiBr ($3.00\ 10^{20}$ cm^{-3}) is orders of magnitude higher than what would be expected from an organic semiconductor with a large band gap and no doping.[133] The ion-free PTI-IF has a similar charge carrier density ($2.07\ 10^{20}$ cm^{-3}) revealing that the ions are not responsible for generating electronic carriers in the organic crystals.

The obtained charge carrier density is higher than observed for other layered crystals such as covalent organic frameworks, metal-organic frameworks and transition metal di-chalcogenides, for example MoS_2 (Table 8).

Table 8. Comparison of the THz analysis of PTI to other layered materials in literature. (Table reproduced from Burmeister et al..[111])

Layered material	charge carrier density (298 K)	THz conductivity (S cm^{-1})	mobility (298 K, varying methods) ($cm^2\ V^{-1}s^{-1}$)
graphite[170,171]	$1 \cdot 10^{19}$ cm^{-3}		10^{-4}
MoS_2 bulk crystal[172]	$3.7 \cdot 10^{19}$ cm^{-3}		
CuPc-MIDA-COF[173]	$2.6 \cdot 10^{12}$ cm^{-3}	0.01	13.3 ± 7.5
ZnPc-pz and CuPc-pz COF[135]	10^{12} cm^{-3}	$5 \cdot 10^{-7}$	5
TPB-TFB COF[134]	$3–5 \cdot 10^{16}$ cm^{-3}		165 ± 10
$Fe_3(THT)_2(NH_4)_3$ MOF[174]	10^{16} cm^{-3}	0.8	220
Doped polymer poly(3-hexylthiophene)[175]	10^{21} cm^{-3}		
PTI-LiBr (this work)	$3 \cdot 10^{20}$ cm^{-3}	0.26	$1.81 \cdot 10^{-3}$
PTI-IF (this work)	$2 \cdot 10^{20}$ cm^{-3}	0.07	$7.33 \cdot 10^{-4}$

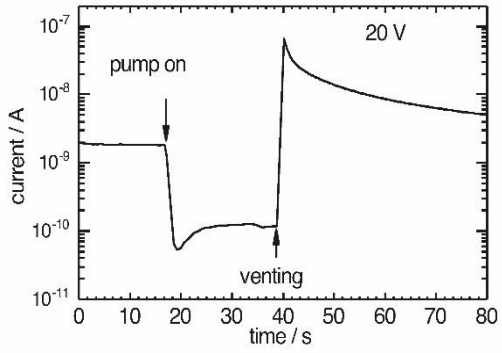

Figure 52. Current- versus time graph of PTI-IF interdigitated device in vacuum chamber. Reduction of pressure leads to drop in current while venting to atmospheric pressure leads to current flow. (Figure reproduced from Burmeister et al..[111])

The carrier densities closest to PTI are those of graphite and MoS_2 bulk crystals ($1\ 10^{19}$ cm^{-3} and $3.7\ 10^{19}$ cm^{-3}, respectively).[170–172] The high carrier concentration

might either be generated by an unknown structural defect or by adsorbed molecules like water, oxygen or CO_2 together with water.[127] Symmetric PTI devices with interdigitated indium-tin oxide electrodes are indeed sensitive to pressure, pointing towards adsorbed species acting as dopants under environmental conditions (Figure 52).

Having detailed the electronic structure in the preceding section, the optical characterisation of PTI-LiBr, PTI-IF and protonated PTI will be discussed in the following section.

Optical properties of PTI-LiBr and PTI-IF films

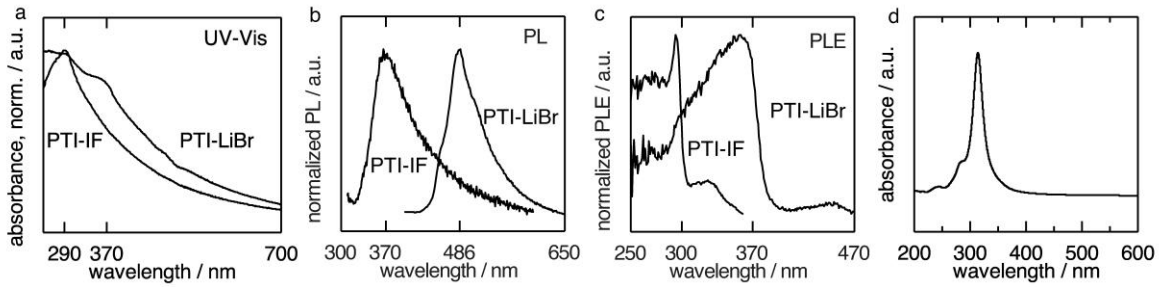

Figure 53. Optical characterisation of PTI-LiBr obtained at 550 °C, 12 h and PTI-IF on quartz substrates. a) UV-Vis (transmission) spectrum b) Photoluminescence spectra show emission maxima at 486 nm for PTI-LiBr and at 370 nm for PTI-IF. c) Photoluminescence excitation spectra of PTI-LiBr (emission collected at 486 nm) and PTI-IF (emission collected at 370 nm). d) Absorption spectrum of a monolayer of PTI-IF computed from time-dependent DFT. Figure adapted from Burmeister et al..[115]

The decreased carbon contamination allows the measurement of UV-Vis spectra of PTI-LiBr and PTI-IF dispersions (Figure 53 a). One finds two broad bands around 370 nm for PTI-LiBr and 290 nm for PTI-IF. The state at 370 nm in PTI-LiBr can be excited yielding the photoluminescence spectrum shown in Figure 53 b (right) with a single maximum at 486 nm. The photoluminescence excitation spectrum shows a single maximum at 370 nm (Figure 53 c). The red shift of this emissive state in respect to the state of PTI-IF with an absorption band at 290 nm and an emission band at 370 nm is a result of the replacement of hydrogen with lithium at triazine-bridging N-H units. This defect reduces the conduction band minimum energy by splitting of unoccupied nitrogen states.[54] Furthermore the ion induced dipoles and the bromide p states that have been mentioned in the discussion of the electronic structure contribute to a band gap contraction. Excitation of PTI-LiBr at around 290 nm does not yield a new emission band and decreases the emission at 486 nm drastically (Figure 54 d). Hence, emission from the state that belongs to the absorption at 290 nm in PTI-LiBr is quenched. An absorption band at lower energy corresponding to the forbidden VB-CB ($n \rightarrow \pi^*$) transition is not observed, neither in experiment nor calculated spectrum (Figure 53 a, d).

The absence of emission from the 290 nm state in PTI-LiBr could be due to the presence of the “Li-defects” acting as a deep trap. Excitons formed in the organic backbone will recombine primarily at these energetically favorable defect sites. A

similar effect can be observed for low concentrations of keto-defects in one-dimensional polyfluorene backbones.[176]

It is not possible to determine the quantum yield of PTI samples obtained at 600 °C because of strong absorption from the accompanying carbon-rich phase. The quantum yield of films cast from the 550 °C product equals 0.4%.

Effect of protonation on the optical states of PTI-LiBr

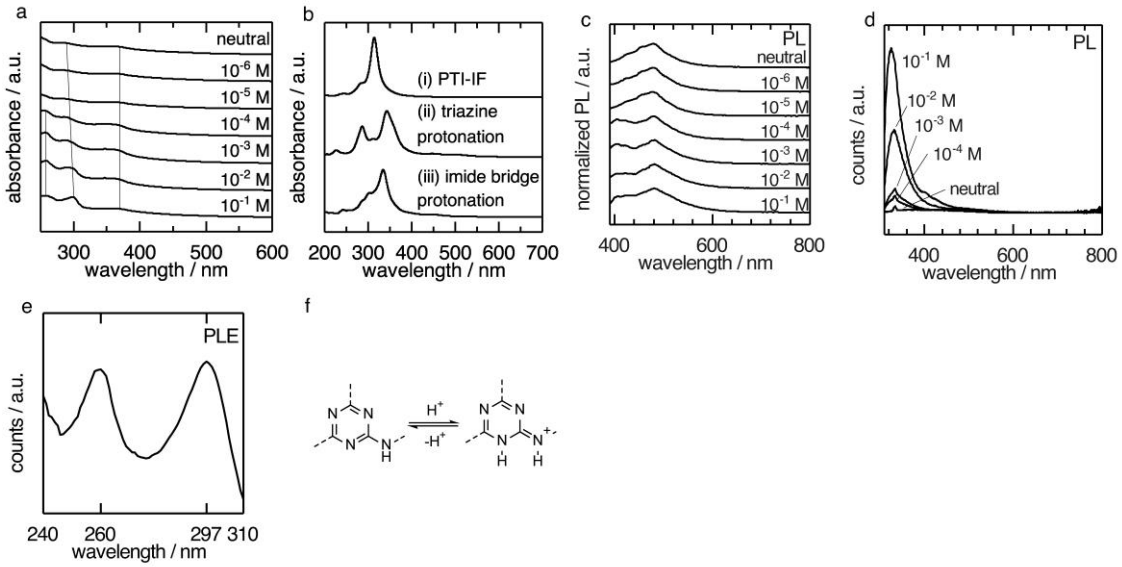

Figure 54. Optical characterisation of PTI-LiBr dispersions in water at different concentrations of HCl. a) UV-Vis (transmission) spectra. b) Time dependent DFT absorption spectrum of (i) a monolayer PTI-IF, (ii) PTI-IF monolayer protonated via HCl at triazine rings and (iii) PTI-IF monolayer protonated via HCl at imide bridges. c) Photoluminescence (PL) spectra excited at 370 nm for PTI-LiBr dispersions with different HCl concentrations. d) Photoluminescence spectra excited at 300 nm for PTI-LiBr dispersions with different HCl concentrations. The Raman band of water can be found at 334 nm. e) Photoluminescence excitation (PLE) spectrum for emission at 330 nm at 10^{-2} M HCl. f) Energetically favored protonation at the triazine ring. Figure reproduced from Burmeister et al..[115]

In a first set of experiments, UV-Vis spectra of PTI-LiBr suspended in water at different concentrations of HCl are collected (Figure 54 a). Without HCl one observes the absorption of the lithium defect states at around 370 nm and the broad absorption of the conjugated PTI-backbone at around 290 nm. By increasing the H_3O^+ concentration, two effects can be identified. First the absorption band of the organic backbone experiences a slight bathochromic shift from 290 to 300 nm. Moreover, a new absorption band at 260 nm arises. There are two possible sites of protonation in the PTI-LiBr structure: (i) at the triazine nitrogen (Figure 54b, ii), and at the imide nitrogen (Figure 54 b, iii). Protonation at the triazine nitrogen compares

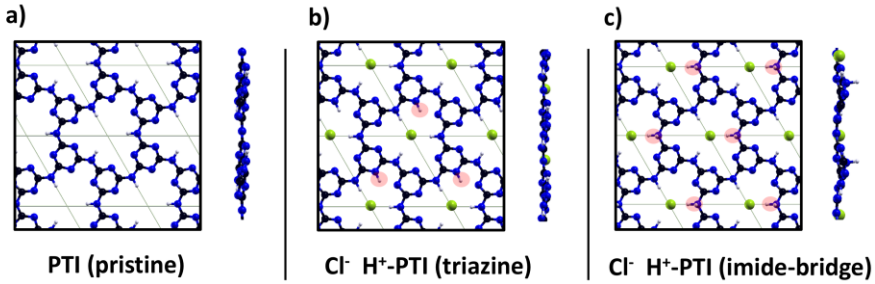

Figure 55. PTI monolayer relaxed structures in-vacuo, relative to PTI-IF (a), the triazine-protonated (b) and the imide-bridge protonated (c) backbones. For protonated structures also the formation energy per unit-cell volume has been evaluated as the difference between the total energy of the protonated system and the sum of the energies of the separated pristine monolayer and HCl subsystems. According to the formation energy the configuration with the protonation at the triazine unit is most stable. Figure reproduced from Burmeister et al..[115]

best with the observed UV-Vis spectra, and accounts for the bathochromic shift and the manifestation of a new band at 260 nm (compare Figure 54 b, i and Figure 54 b, ii). First principles calculations predict that the triazine-protonated structure is more stable than the imide-bridge protonated structure (Figure 55). Based on this finding, one can assume that the triazine protonation is prevalent (Figure 55). The calculated optical absorption spectra of the protonated materials (Figure 54 b) indicate an overall red-shift of the absorption peaks in comparison with PTI-IF. This result is qualitatively in agreement with earlier predictions on analogous model systems.[177] Specifically, the red shift of the main peak in combination with the emergence of a second absorption band in the absorption spectrum of triazine-protonated PTI (Figure 54b, ii) is considered an effect of the symmetry breaking of the backbone structure upon protonation. The presence of two absorption bands in the system is in good agreement with two corresponding PLE maxima at 260 nm and 297 nm of the emission at 330 nm (Figure 54 d and e) present in dispersions with HCl concentrations larger than 10^{-5} M at 260 nm and 300 nm (Figure 54 d and e). The photoluminescence band at 330 nm is assigned to the CN backbone protonated at the triazine moiety which is blue-shifted in respect to the emission of PTI-IF at 370 nm (Figure 54d, b).

It is noteworthy that for excitation at 300 nm in dispersions at 10^{-2} M HCl the quantum yield obtained was 10% and for excitation at 370 nm 9%. The emission of the neutral dispersion at 486 nm is comparatively low with a quantum yield of 1% and no emission for excitation at 300 nm. The increased quantum yield is

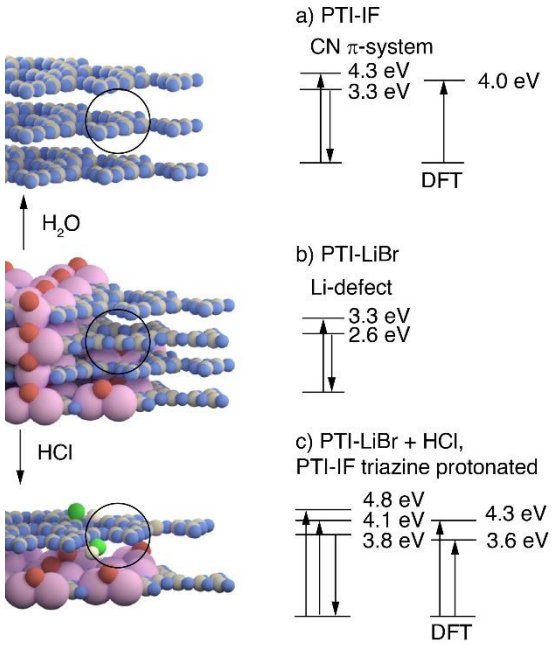

Figure 56. Summary of optical states from DFT, UV-Vis and photoluminescence spectroscopy of dispersions in water of a) PTI-IF obtained from PTI-LiBr by Soxhlet extraction of ions, and optical gap of 2D layer of PTI-IF from DFT calculation, b) partially de-intercalated PTI-LiBr as obtained from ionothermal synthesis, c) effects of HCl at concentrations higher than 10^{-5} M on PTI-LiBr dispersions and optical gaps obtained for 2D layer of triazine-protonated PTI-IF sheet by DFT. Arrows pointing upwards denote an absorption process, arrows pointing downwards denote an emission process. Carbon and nitrogen atoms are represented as grey and blue spheres. Hydrogen atoms at the imide nitrogen are not depicted. Bromine and lithium ions are represented as red and pink spheres. Proton and chloride anion are represented as white and green spheres. Figure reproduced from Burmeister et al..[115]

accompanied by an increase in exciton lifetime (neutral τ_1 = 0.5 ns ±0.03 ns, τ_2 = 3.6 ns ±0.13 ns, pH1 τ_1 = 1 ns ±0.05 ns, τ_2 = 4 ns ±0.10 ns). As typical for CN materials a two-exponential fit was applied.[153] The increase in quantum yield and lifetime is attributed to partial exfoliation of the layered PTI structure and, hence, reduced π- π stacking. Charging of PTI layers by reduction with sodium naphthalide and stabilisation by derivatisation with a C_{12} alkane was described in literature.[178] A route via protonation could be a viable alternative.

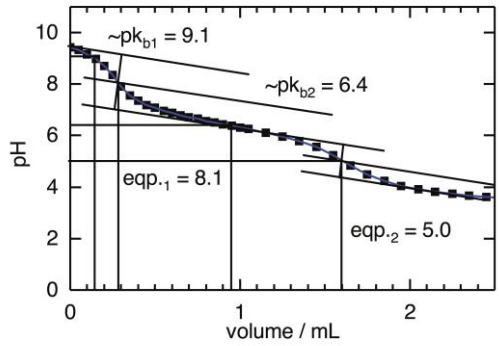

Figure 57. HCl (0.1 M) titration of 26 mg PTI-LiBr (550 °C, 48 h) dispersion. The second equivalence point at pH 5 corresponds to the pH region where also changes in the optical spectra take place (emergence of 330 nm, 420 nm photoluminescence and 260 nm absorption band). Figure reproduced from Burmeister et al..[115]

The changes in the optical spectra coincide with the observation of an equivalence point at pH 5 in the HCl titration of PTI-LiBr dispersions (Figure 57). The pK_b extracted from the titration is pK_b = 6.4. The pK_a value associated with the conjugated acid is 7.6 (pK_a = 14 - pK_b). The conjugated acid is weaker than the conjugated acid of melamin (pK_a = 5.0).[179] This indicates that the protonated PTI-LiBr structure is better stabilized than the triazine-containing monomer, presumably due to conjugation across the PTI-backbone or stabilization by electron density from neighbouring triazine nitrogen lone-pairs (Figure 54 f). The observed optical states are summarised in Figure 56 and compared to the optical gaps predicted by the DFT calculations.

To connect the improved optical and structural properties of the material with better performance in a simple electrical device a photoconductor was assembled. The results are presented in the next section.

Employing PTI-LiBr in a photoconductor

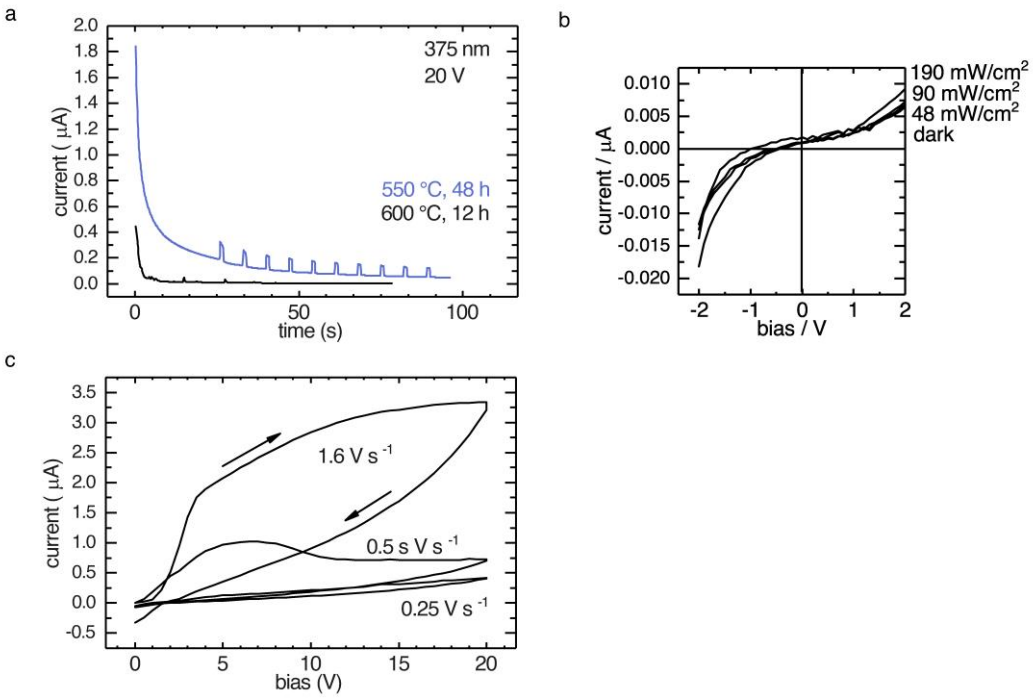

Figure 58. a) Comparison of photoconductors employing PTI-LiBr from 600 °C and 550 °C. Charge transport and photocurrent are absent in the 600 °C material due to the observed partial carbonisation (black line). In the device employing PTI-LiBr from 550 °C current is able to cross the channel of the interdigitated substrate and photocurrent is observed when excited with a 375 nm LED at an irradiance of 46 mW cm^{-2}. b) Irradiance-dependent IV sweep of photoconductor device. Increased irradiance with a 375 nm LED results in increased current flow. The low current is a result of the polycrystalline material property (grain boundaries) and likely energetic disorder at partially intercalation-free layers. b) IV sweeps of an interdigitated device employing 550 °C, 48 h product with different sweep speed. The observed hysteresis is due to migration of Li^+ and Br^- ions. Figure reproduced from Burmeister et al..[115]

A first attempt to connect the increased product quality at lower synthesis temperatures with a performance increase has been conducted in building photoconductors on interdigitated indium tin oxide substrates. Using an LED light and a source measurement unit the photo response for the product from literature synthesis conditions (600 °C, 12 h) and the new synthesis conditions at lower temperature are obtained. The lower carbonisation indeed improved the performance as a photocurrent is measurable (Figure 58, a). However the performance is still low when compared to polymeric or small-molecular semiconductors with photoconductive gains of up to 10^5.[180] The conductivity of the material (550 °C, 48 h) is 4 10^{-10} S cm^{-1} in the dark and 1.0 10^{-9} S cm^{-1} in the illuminated state (at 375 nm and an irradiance of 46 mW cm^{-2}). Photoconductors

using PTI-LiBr undergo changes over the course of the measurement because of the migration of ions. Therefore, the observed hysteresis in IV sweeps is dependent on the scan speed of the sweep (Figure 58 c).

To study the effect of PTI-nanocrystals interfacing directly with a 2D semiconductor, MoS_2 transistors were constructed and characterized. The results are presented in the following chapter.

Hybrid organic/inorganic interface of PTI-IF with a 2D MoS_2 transistor

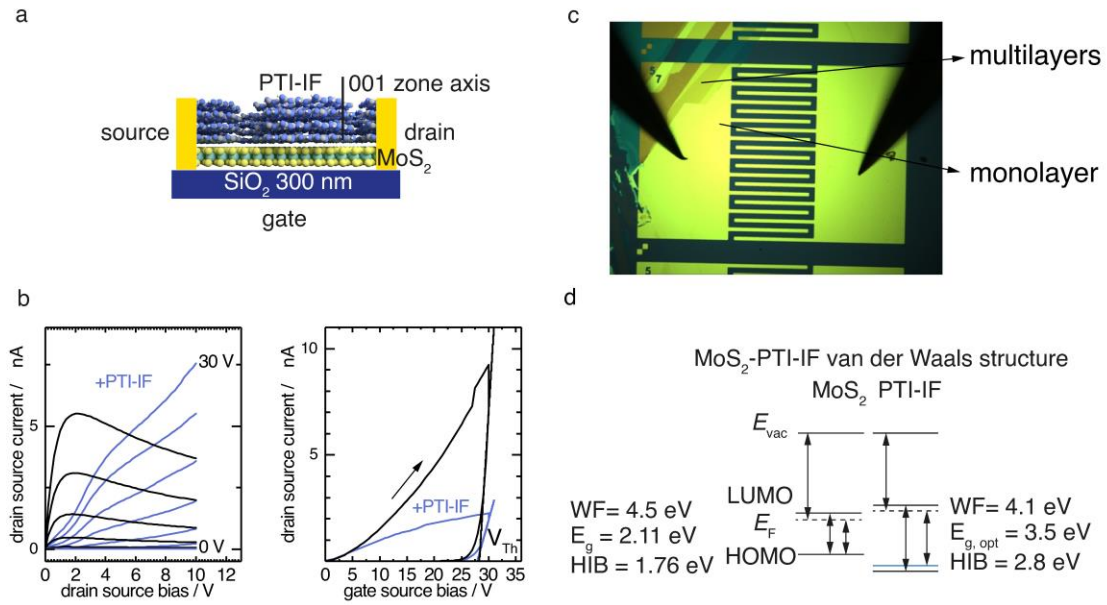

Figure 59. a) Device architecture of MoS_2 transistor interfaced with PTI-IF, b) Transfer and output characteristics of a 2D MoS_2 device in pristine condition and fully covered with PTI-IF. The gate voltage was increased from 0 V in 5 V steps to 30 V for the output curves. c) Microscope image of a interdigitated 2D MoS_2 device on a wafer substrate contacted with tungsten needles. d) Energy levels of PTI-IF and MoS_2.

Since nano-crystalline PTI-IF is not suited as semiconductor in a field effect transistor due to the low mobility as well as structural disorder between the nano-crystallites, the effect of PTI-IF interfacing a 2D MoS_2 transistor is studied (Figure 59, a). MoS_2 monolayers were obtained by a gold-mediated exfoliation and a transfer onto a silicon substrate prepatterned with interdigitated gold electrodes (channel length 15 µm, channel width 4095 µm, 300 nm SiO_2 bottom gate) and PTI-IF was deposited by drop casting from an aqueous dispersion (Figure 59 c).[181] Motivated by the results from Wang et al. utilizing molecular carbon nitride species melamine and cyanuric acid to deposit a co-crystal from water on a MoS_2 monolayer the experiments aim to compare the results with the deposition of a layer of a nano-crystalline covalent carbon nitride (PTI-IF) on a monolayer MoS_2 device.[182] Strong hysteresis in the transfer characteristic and low source drain current are observed already for the pristine MoS_2 device, likely caused by sulfur-vacancies and water at the MoS_2/SiO_2 interface.[183] Application of the PTI-IF film results in a current drop in the transfer characteristic (Figure 59 b, right) and a parasitic resistance in the

output characteristic, which is likely due to a small current passing through the PTI-IF layer (Figure 59 b, left)). Unlike in the deposition of the hydrogen bonded molecular crystals used by Wang et al. strong n-doping was not observed as the threshold voltage interpolated from the linear region of the transfer plot did not change (Figure 59 b, right)). Comparing the energy levels of MoS_2 and PTI-IF, no strong charge transfer is expected as it is a type one (straddling gap) hetero-structure of two n-doped materials (Figure 59 d). This finding was also confirmed by calculating the charge transfer via DFT between a MoS_2-monolayer PTI-IF-monolayer van der Waals hetero-structure. The Bader charge analysis confirms the absence of any charge transfer between the two systems (charge density variation is 0.01 e and of the same order of the numerical error). Future experiments need to be conducted on other gate materials.

Application of PTI-LiBr in an OLED

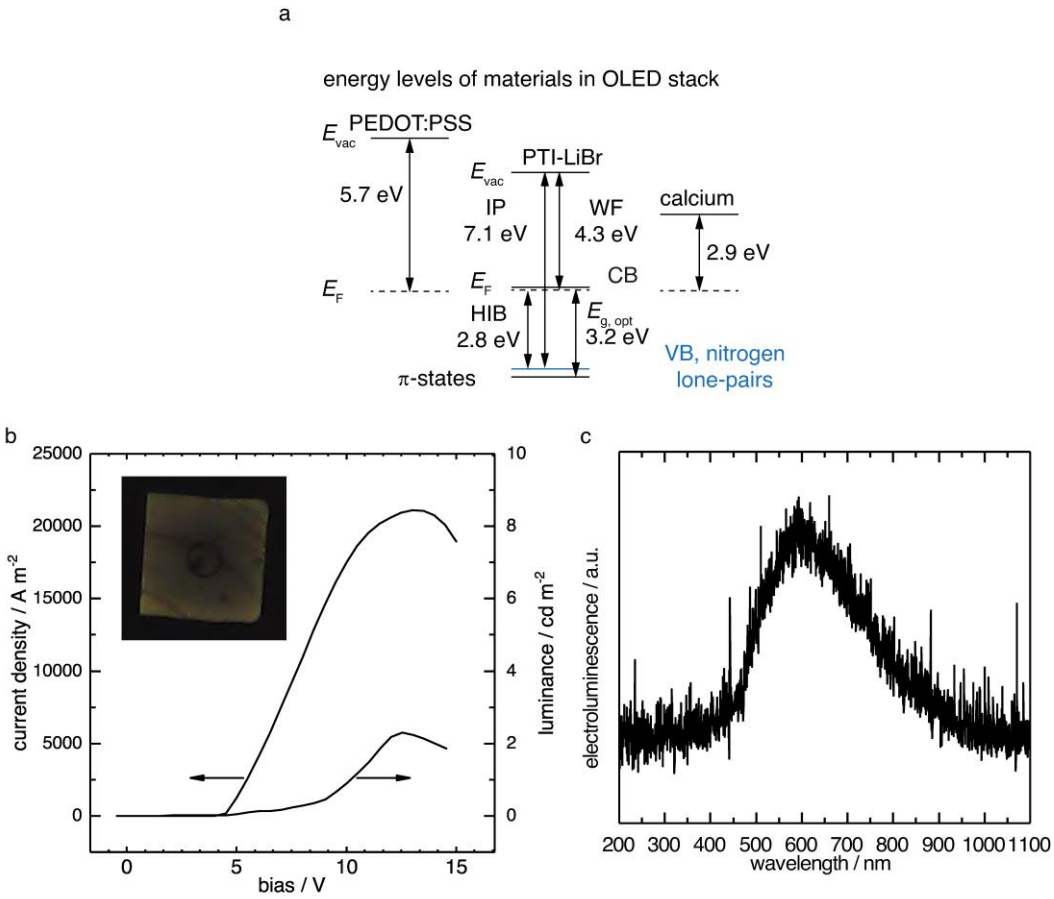

Figure 60. Characterisation of a single layer OLED with Ca/Al as the cathode, PEDOT:PSS/ITO anode, and PTI-LiBr as the active material. a) OLED architecture. b) Current density and luminance versus bias with picture of a PTI-LiBr OLED pixel. c) Electroluminescence of the PTI-LiBr OLED. Figure reproduced from Burmeister et al..[115]

The conclusions so far are that (i) PTI samples obtained at low temperature conditions (550 °C, 48 h) showed enhanced electrical and optical properties and that (ii) it is possible to process PTI-materials from dispersions into thin films. Therefore single layer light emitting device structures with ITO/PEDOT:PSS as anode and Ca/Al as cathode are prepared to investigate PTI-LiBr as electroluminescent active material (Figure 60 a). The OLED stack shows a steep diode-like onset of the device current and electroluminescence emission at ca. 4.5 V in forward bias direction. At 12 V bias one observes a maximum luminance of 2 cd m^{-2}. The device showed a current efficiency of ca. 10^{-4} cd A^{-1} (Figure 60 b). Below onset a high device leakage current is observed which is attributed to film inhomogeneities and pin holes introduced during the drop-casting preparation process of the PTI-LiBr layer. Similar to previous observations for CN-films, the

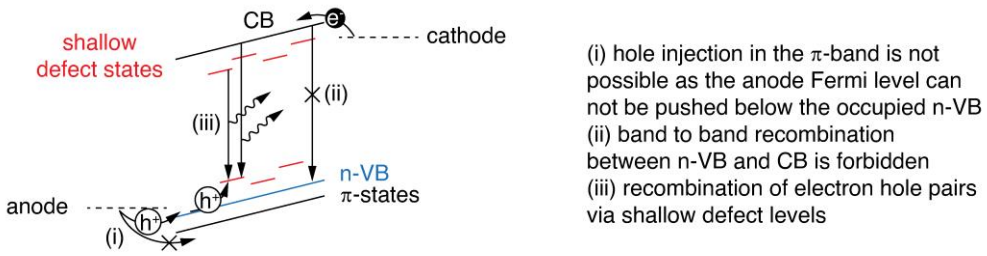

Figure 61. Schematic proposing an explanation for the ineffective hole injection into the lone-pair VB of a PTI emission layer under bias; (i) hole injection into the π-band is not possible as the lone-pair band is the upper most valence band. (ii) n-π*-band to band recombination is forbidden. (iii) The recombination from shallow defect states above the VB and below the CB result in the red- shifted electroluminescence in regard to the photoluminescence.

electroluminescence maximum of PTI-LiBr is red-shifted by 0.5 eV with respect to the PL maximum (Figure 60c).[184] This is explained in literature typically by defect levels. They may arise from small amounts of carbonaceous contaminants still present in the 550 °C PTI-LiBr sample or nitrogen vacancies in the PTI-LiBr crystals. Electrons are preferably injected into defect levels below the conduction band while holes are preferably injected into defect states above the valence band or subsequently relax into these energetically favored states, resulting in a red-shifted emission (Figure 60 c). However, in the case of PTI-derivatives a more fundamental reason can be found. The presence of a non-bonding band above the π-band (Figure 47, Figure 46) is significant as it pins the Fermi level of the cathode and does not allow for effective carrier injection into the π-band. This leads to the absence of the photoluminescence band in the electroluminescence spectrum and, hence, to the defect-dominated electroluminescence spectrum as well as the low luminance of the OLED.[115] Holes injected into the VB will be trapped due to the nature of the highly localized lone-pair orbitals from which recombination is forbidden (Figure 61).

As a consequence of the presence of the lone-pair VB, even envisioning a defect-free PTI-LiBr material, OLEDs cannot yield blue electroluminescence as would be expected from the photoluminescence spectra. While the device performance of this simple single-layer device is rather limited due to the lone-pair semiconductor property of PTI, this nano-crystalline covalent organic frameworks was demonstrated as emissive layer in an OLED.

5.3. Conclusion

Herein an improved synthetic protocol for PTI-LiBr and PTI-IF, respectively was presented highlighting the detrimental effects of high synthesis temperatures (>550 °C) on the optical and electronic properties of the material. One observes that the hitherto reported synthetic conditions that employ temperatures of 600 °C (and above) give rise to partial carbonisation of PTI-LiBr. The formation of these carbonaceous contaminants in PTI-LiBr give rise to low-energy defect states that deteriorate charge transfer pathways and absorb photoluminescence.

One finds that protonation of PTI-LiBr happens preferentially at the nitrogen atoms of the triazine (C_3N_3) moieties. The absorption band of the PTI backbone is split due to the symmetry breaking upon protonation. Protonation also increased the quantum yield of PTI suspensions up to a factor of 9. This indicates a facile route to partial exfoliation of the π-stacked PTI structure in solutions of aqueous acids. UPS results revealed a high ionisation potential (7.1 eV), electron affinity (4.2eV), and hole injection barrier (2.8 eV) for PTI-LiBr, and an ionisation potential (6.9 eV), electron affinity (3.7 eV), and hole injection barrier (2.8 eV) for PTI-IF, respectively. Using time-domain THz spectroscopy, one finds that – despite its covalent character and high crystallinity – PTI exhibits a high charge carrier localisation and low mobility. The low conductivity in macroscopic films is caused by the nano-crystalline morphology. Removal of ions leads to a slightly decreased electron density at the carbon and nitrogen cores of the triazine rings as well as layer corrugation or AB-stacking. Interfacing a MoS_2 2D transistor with PTI-IF resulted in a parasitic current through PTI-IF. Evidence for n-doping as found for molecular carbon nitrides was not observed. Finally, it is possible to produce a simple OLED structure with PTI-LiBr as an active, metal-free material to demonstrate electroluminescence. The maximum of the emission is red shifted by 0.5 eV in regard to the photoluminescence. This observation is assigned to the lone-pair band above the valence band and the presence of defects. Future use of PTI (and analogous, layered CN-materials) in optical and electronic applications is contingent on (i) increasing crystallite size, (ii) development of methods to access its crystal interfaces as well as PTI monolayers on suited substrates, (iii) gaining a thorough understanding of the origin of the charge carriers as well as the charge carrier density and doping/de-doping in this material.

Chapter 6. Summary and conclusion

Men of science have made abundant mistakes of every kind; their knowledge has improved only because of their gradual abandonment of ancient errors, poor approximations, and premature conclusions.

George Sarton, A History of Science, Vol. 2, Hellenistic Science and Culture in the Last Three Centuries B.C., 1959.

The first part of the thesis presented a methodical approach to fundamental characterisation and identification of a single-crystalline carbon nitride phase isolated from a closed system, ionothermal condensation reaction product.
It clearly showed the effect the increased ion size from bromide to iodide has on the product formation. Instead of formation of ion-free graphitic carbon nitride phases or the formation of PTI-LiI, condensation stops at melem with only carbonisation being observed at higher temperatures. The melem phase was identified by single crystal XRD to be melem hydrate ($C_6N_{10}H_6 \cdot H_2O$) and the result was confirmed by elemental analysis, ssNMR, FT-IR, UV-Raman and PXRD spectra. The results are corroborated by DFT calculations showing that PTI-LiI would be the least stable PTI derivative when compared to PTI-LiCl and PTI-LiBr. Application of the product phase in an OLED was possible with very low performance. The product was also tested for photocatalytic water splitting however, there was no activity observed.
The second part of this thesis reports an improved synthesis and characterisation of the graphitic carbon nitrides PTI-LiBr and PTI-IF, utilising the methodical approach presented in part one and expanding it with advanced methods such as CB-ED, THz spectroscopy, UPS, and time-dependent DFT.
To allow application of PTI derivatives in optoelectronic devices, the presence of defects needed to be reduced as the synthesis procedure available resulted in brown discoloured product. The brown discolouration and the absence of conductivity as well as photoconductivity was linked to the presence of significant carbonisation at temperatures above 550 °C. By further reducing the temperature and increasing the reaction time reaction conditions of 475 °C for 7 d yielded a fully condensed product with no carbon-rich sidephase.
Structural solution of PTI-IF via CB-ED PXRD and DFT revealed a corrugated or AB-stacked structure. Comparing the orientation of PTI-LiBr and PTI-IF nanocrystals in films by evaluation of CB-ED maps revealed PTI-LiBr pillars lie with the graphitic layers orthogonally to the surface while PTI-IF crystals lie with the CN-layers parallel to the surface plane. This is due to partial exfoliation of the pillared structures in PTI-LiBr resulting in a change of the largest crystal face and hence the crystal face with the highest crystal-surface interaction. The CO_2 uptake as well as the heat of adsorption is increased after de-intercalation (5 mg g^{-1}, 31 kJ mol^{-1}) but

is still lower in comparison to microporous triazine-containing polymers due to the low pore diameter.

To improve the understanding of phonon modes in PTI derivatives FT-IR, UV-Raman and EELS phonon spectra are presented together with phonon calculations. PTI-LiBr phonon-spectra are affected by the presence of the ions leading to severe peak broadening due to the heterogeneous bond environments. Meanwhile, PTI-IF FT-IR spectra can be readily interpreted with the corresponding calculation. Only the intensity of the ring modes is underestimated in the calculated spectra. UV-Raman spectra still mainly show the triazine breathing mode and the G band. The reason for the low Raman activity of the ring breathing modes when excited with lasers in the visible light range (e.g. 532 nm, 785 nm) instead of UV-light is not yet understood in detail.

The opportunity to obtain phonon spectra of compounds in an electron microscope is extremely beneficial as one can perform structural (CB-ED, SAED, STEM), elemental (EDX, EELS), electronic (valence band EELS) as well as vibrational studies (EELS) on single nano-crystallites. This allows to paint a very clear picture of matter at the nano-scale useful for example in mixed-phase problems and material discovery.

The band structure of the bulk PTI derivatives as well as the monolayers obtained by periodic boundary condition DFT calculations revealed that the valence band states are lone pairs. The occupied π-states are at 0.3 eV lower energy in the VB-2 band. This is most reminiscent of group-VI lone-pair semiconductors. This is a surprising finding as it is the first organic lone-pair semiconductor reported. In organic semiconductors usually the π-orbitals are at the top of the valence band and the optical transition between VB→CB is allowed. In PTI the VB-CB (n→π*) transition is not allowed. Characterisation of the electronic band gap by UV-Vis and EELS is therefore not possible as it probes the allowed π→π* transition. This is the reason for the large difference between the optical gap and the DFT result. In PTI-IF, in addition to the VB-CB (n→π*) transition being forbidden, it is also an indirect transition.

The optical gaps are 3.2 eV and 3.5 eV (Tauc), respectively for PTI-LiBr and PTI-IF, which is higher than reported values due to reduction of defective carbonised side

products that can distort the absorption onset to lower energy. The DFT results imply a direct forbidden VB-CB transition in PTI-LiBr bulk crystals of 2.29 eV and an indirect forbidden VB-CB transition of 2.46 eV in PTI-IF.

UPS results confirmed the anticipated high ionisation potential as well as the high electron affinity of the graphitic carbon nitrides. PTI-LiBr samples showed an ionisation potential of 7.1 eV and an electron affinity of 4.2 eV, potentially allowing environmentally stable n-transport. PTI-IF has a slightly lower ionisation potential of 6.9 eV and an electron affinity of 3.7 eV. Both materials appear to have n-doped characters as their Fermi levels are near to their CB.

Despite the low electrical conductivity of PTI-LiBr as well as PTI-IF of 10^{-7} S cm^{-1} and 10^{-10} S cm^{-1}, respectively, THz-TDS measurements indicate a conductivity of 0.26 S cm^{-1} 0.07 S cm^{-1} respectively at the nanoscale. The loss of conductivity at macroscopic scales can be explained by the nano-crystalline nature of the material. Charge carriers are likely trapped at crystal interfaces in the loosely packed films. The charge carrier density of the PTI derivatives of 10^{20} cm^{-3} is far beyond what would be expected for an intrinsic organic and inorganic semiconductor. Organic and inorganic intrinsic semiconductors are expected to have a charge carrier density of about $\sim10^{0}$ cm^{-3} and $\sim10^{10}$ cm^{-3} respectively.[133] The charge carrier density is not strongly correlated to the ion intercalation and cannot be fully explained at this point.

Likely causes are unknown defects and environmental doping by adsorbents.

THz-TDS revealed the effective nanoscale mobility to lie in the range of amorphous organic semiconductors 10^{-3}-10^{-4} cm^2 V^{-1} s^{-1}. The low mobility in the material is likely caused by the absent conjugation over the imide linkage and the low-dispersion lone-pair VB.

The optical characterisation by UV-Vis of PTI-LiBr and PTI-IF is well reproduced by time-dependent DFT calculations revealing that the forbidden VB-CB ($n\rightarrow\pi^*$) transition is indeed not picked up on and only a single bright state is present in both materials corresponding to the respective $\pi\rightarrow\pi^*$ transitions. Protonation is energetically most favourable at the triazine nitrogen (DFT) and a pK_a value of 7.6 is obtained by titration. Protonation leads to a splitting of the absorption band due to symmetry breaking and an additional emission band at high energy (330 nm).

To find out if the blue photoluminescence band of PTI-LiBr can be used to create a blue organic light emitting diode, a single-layer PTI-LiBr OLED was built. The Electroluminescence maximum was red-shifted by 0.5 eV and emission at the maximum of the photoluminescence band was absent. The reason for the defect-dominated emission is the lone-pair semiconductor character which does not allow injection into the π-VB states and presence of shallow defect states at which recombination is occurring.

A number of profound findings, answering the questions posed in the introduction, yield themselves for abstraction for the future of the field of graphitic carbon nitrides for optoelectronic applications.

(i) Increasing the anion size did not allow condensation of a graphitic carbon nitride. Other eutectic salt mixtures, e.g. ternary mixtures need to be researched while iodide ions could yield themselves as reaction moderator, slowing the stacking process and allowing extended growth of the carbon nitride planes. New eutectic mixtures could also lead to the discovery of new CN-phases.

(ii) The reason for the lack of application of graphitic carbon nitrides in optoelectronic devices is a) the high amount of defects obtained under the previously known synthesis conditions, b) the unusual electronic structure of the condensed organic material revealing itself to be an organic lone-pair semiconductor. By reducing the synthesis temperature to under 500 °C and therefore avoiding carbonisation it is possible to obtain PTI-LiBr without carbon-rich by-products. The properties and origin of charge carriers in the lone-pair band and the n-doped character of PTI have to be better understood to find use cases as it is a hindrance in ordinary optoelectronic devices such as OLEDs, transistors or photoconductors. This finding can be generalized to all graphitic carbon nitrides with lone-pair states at the top of the valence band.

(iii) The intrinsic semiconductor properties of nanocrystalline PTI derivatives are dominated by strong charge-carrier localisation, low mobility, low conductivity, and the presence of strongly localised charge carriers of unknown origin. To achieve better charge-carrier transport

the crystallite size has to be increased as the nano-crystalline character leads to charge-carrier trapping at crystal interfaces. The high ionisation potential as well as the high electron affinity were experimentally confirmed and explain the high thermal and environmental stability of PTI derivatives. The electron affinity of 4.2 eV in PTI-LiBr further confirms the possibility of environmentally stable n-transport in graphitic carbon nitrides without the need for perfluorination.

(iv) The blue photoluminescence is not employable in OLEDs as the lone-pair band at the valence band top does not allow for effective injection into the π-like valence band states in a single-layer OLED.

References

[1] D. J. Wuebbles, A. K. Jain, *Fuel Process. Technol.* **2001**, *71*, 99–119.

[2] J. Li, S. Lai, G. F. Gao, W. Shi, *Nature* **2021**, *600*, 408–418.

[3] U. Hashim, A. A. Ehsan, I. Ahmad, *Chiang Mai J. Sci* **2007**, *34*, 47–53.

[4] C. Liu, H. Chen, S. Wang, Q. Liu, Y. Jiang, D. W. Zhang, M. Liu, P. Zhou, *Nat. Nanotechnol.* **2020**, *15*, 545–557.

[5] R. K. Cavin, P. Lugli, V. V. Zhirnov, *Proc. IEEE* **2012**, *100*, 1720–1749.

[6] J. Shalf, *Philos. Trans. R. Soc.* **2020**, *378*, 1–14.

[7] N. D. Mermin, *Phys. Rev.* **1968**, *176*, 250–254.

[8] K. S. Novoselov, A. K. Geim, S. V. Morozov, D. Jiang, Y. Zhang, S. V. Dubonos, I. V. Grigorieva, A. A. Firsov, *Science* **2004**, *306*, 666–669.

[9] K. S. Novoselov, A. K. Geim, S. V. Morozov, D. Jiang, M. I. Katsnelson, I. V. Grigorieva, S. V. Dubonos, A. A. Firsov, *Nature* **2005**, *438*, 197–200.

[10] J. K. Ellis, M. J. Lucero, G. E. Scuseria, *Appl. Phys. Lett.* **2011**, *99*, 261908.

[11] A. K. Geim, I. V. Grigorieva, *Nature* **2013**, *499*, 419–425.

[12] G. Algara-Siller, N. Severin, S. Y. Chong, T. Björkman, R. G. Palgrave, A. Laybourn, M. Antonietti, Y. Z. Khimyak, A. V. Krasheninnikov, J. P. Rabe, et al., *Angew. Chemie* **2014**, *126*, 7580–7585.

[13] Q. Dong, N. Mohamad Latiff, V. Mazánek, N. F. Rosli, H. L. Chia, Z. Sofer, M. Pumera, *ACS Appl. Nano Mater.* **2018**, *1*, 4442–4449.

[14] T. M. Suter, T. S. Miller, J. K. Cockcroft, A. E. Aliev, M. C. Wilding, A. Sella, F. Corà, C. A. Howard, P. F. McMillan, *Chem. Sci.* **2019**, *10*, 2519–2528.

[15] F. K. Kessler, Y. Zheng, D. Schwarz, C. Merschjann, W. Schnick, X. Wang, M. J. Bojdys, *Nat. Rev. Mater.* **2017**, *2*, 17030.

[16] J. Liebig, *Ann. der Phys. und Chemie* **1835**, *110*, 570–613.

[17] J. R. Partington, *A History of Chemistry*, Macmillan Education UK, London, **1964**.

[18] B. V. Lotsch, M. Döblinger, J. Sehnert, L. Seyfarth, J. Senker, O. Oeckler, W. Schnick, *Chem. - A Eur. J.* **2007**, *13*, 4969–4980.

[19] E. C. Franklin, *J. Am. Chem. Soc.* **1922**, *44*, 486–509.

[20] M. L. Cohen, *Phys. Rev. B* **1985**, *32*, 7988–7991.

[21] C. Niu, Y. Z. Lu, C. M. Lieber, *Science* **1993**, *261*, 334–337.

[22] K. M. Yu, M. L. Cohen, E. E. Haller, W. L. Hansen, A. Y. Liu, I. C. Wu, *Phys. Rev. B* **1994**, *49*, 5034–5037.

[23] J. P. Rivière, D. Texier, J. Delafond, M. Jaouen, E. L. Mathé, J. Chaumont, *Mater. Lett.* **2007**, *61*, 2855–2858.

[24] D. M. Teter, R. J. Hemley, *Science* **1996**, *271*, 53–55.

[25] D. C. Nesting, J. V. Badding, *Chem. Mater.* **1996**, *8*, 1535–1539.

[26] T. Sekine, H. Kanda, Y. Bando, M. Yokoyama, K. Hojou, *J. Mater. Sci. Lett.* **1990**, *9*, 1376–1378.

[27] L. Maya, D. R. Cole, E. W. Hagaman, *J. Am. Ceram. Soc.* **1991**, *74*, 1686–1688.

[28] J. F. D. Chubaci, T. Sakai, T. Yamamoto, K. Ogata, A. Ebe, F. Fujimoto, *Nucl. Inst. Methods Phys. Res. B* **1993**, *80–81*, 463–466.

[29] H. X. Han, B. J. Feldman, *Solid State Commun.* **1988**, *65*, 921–923.

[30] M. R. Wixom, *J. Am. Ceram. Soc.* **1990**, *73*, 1973–1978.

[31] M. Y. Chen, X. Lin, V. P. Dravid, Y. W. Chung, M. S. Wong, W. D. Sproul, *Surf. Coatings Technol.* **1992**, *54–55*, 360–364.

[32] J. J. Cuomo, P. A. Leary, D. Yu, W. Reuter, M. Frisch, *J Vac Sci Technol* **1979**, *16*, 299–302.

[33] R. Hauert, in *Tribol. Diamond-Like Carbon Film.*, Springer US, Boston, MA, **2008**, pp. 494–509.

[34] J. Kouvetakis, A. Bandari, M. Todd, B. Wilkens, N. Cave, *Chem. Mater.* **1994**, *6*, 811–814.

[35] S. Matsumoto, E. Q. Xie, F. Izumi, *Diam. Relat. Mater.* **1999**, *8*, 1175–1182.

[36] T. Malkow, *Mater. Sci. Eng. A* **2000**, *292*, 112–124.

[37] D. M. Teter, *MRS Bull.* **1998**, *23*, 22–27.

[38] R. DeVries, *Mater. Res. Innov.* **1997**, *1*, 161–162.

[39] E. Kroke, M. Schwarz, E. Horath-Bordon, P. Kroll, B. Noll, A. D. Norman, *New J. Chem.* **2002**, *26*, 508–512.

[40] E. Kroke, M. Schwarz, *Coord. Chem. Rev.* **2004**, *248*, 493–532.

[41] B. Yan, Z. Chen, Y. Xu, *Chem. - An Asian J.* **2020**, 1–13.

[42] N. Mansor, T. S. Miller, I. Dedigama, A. B. Jorge, J. Jia, V. Brázdová, C. Mattevi, C. Gibbs, D. Hodgson, P. R. Shearing, et al., *Electrochim. Acta* **2016**, *222*, 44–57.

[43] Q. Han, C. Hu, F. Zhao, Z. Zhang, N. Chen, L. Qu, *J. Mater. Chem. A* **2015**, *3*, 4612–

4619.

[44] G. Liao, Y. Gong, L. Zhang, H. Gao, G.-J. Yang, B. Fang, *Energy Environ. Sci.* **2019**, *12*, 2080–2147.

[45] K. S. Novoselov, Z. Jiang, Y. Zhang, S. V. Morozov, H. L. Stormer, U. Zeitler, J. C. Maan, G. S. Boebinger, P. Kim, A. K. Geim, *Science* **2007**, *315*, 1379.

[46] J. H. Zhan, Z. D. Zhang, X. F. Qian, C. Wang, Y. Xie, Y. T. Qian, *J. Solid State Chem.* **1998**, *141*, 270–273.

[47] Q. Guo, Y. Xie, X. Wang, S. Zhang, T. Hou, S. Lv, *Chem. Commun.* **2004**, *10*, 26–27.

[48] H. Montigaud, S. Courjault, B. Tanguy, G. Demazeau, J. Peyronneau, D. Andrault, M. Jaouen, G. Hug, *High Press. Res.* **2000**, *18*, 213–219.

[49] A. Thomas, A. Fischer, F. Goettmann, M. Antonietti, J. O. Müller, R. Schlögl, J. M. Carlsson, *J. Mater. Chem.* **2008**, *18*, 4893–4908.

[50] E. Horvath-Bordon, R. Riedel, P. F. McMillan, P. Kroll, G. Miehe, P. A. Van Aken, A. Zerr, P. Hoppe, O. Shebanova, I. McLaren, et al., *Angew. Chemie - Int. Ed.* **2007**, *46*, 1476–1480.

[51] M. J. Bojdys, J.-O. Müller, M. Antonietti, A. Thomas, *Chem. - A Eur. J.* **2008**, *14*, 8177–8182.

[52] E. Wirnhier, M. Döblinger, D. Gunzelmann, J. Senker, B. V. Lotsch, W. Schnick, *Chem. - A Eur. J.* **2011**, *17*, 3213–3221.

[53] H. May, *J. Appl. Chem.* **1959**, *9*, 340–344.

[54] E. J. McDermott, E. Wirnhier, W. Schnick, K. S. Virdi, C. Scheu, Y. Kauffmann, W. D. Kaplan, E. Z. Kurmaev, A. Moewes, *J. Phys. Chem. C* **2013**, *117*, 8806–8812.

[55] S. Y. Chong, J. T. A. Jones, Y. Z. Khimyak, A. I. Cooper, A. Thomas, M. Antonietti, M. J. Bojdys, *J. Mater. Chem. A* **2013**, *1*, 1102–1107.

[56] X. Lu, H. Wang, Y. Yang, T. Liu, *J. Mater. Sci. Technol.* **2011**, *27*, 245–251.

[57] T. Suter, V. Brázdová, K. McColl, T. S. Miller, H. Nagashima, E. Salvadori, A. Sella, C. A. Howard, C. W. M. Kay, F. Corà, et al., *J. Phys. Chem. C* **2018**, *122*, 25183–25194.

[58] M. B. Mesch, K. Bärwinkel, Y. Krysiak, C. Martineau, F. Taulelle, R. B. Neder, U. Kolb, J. Senker, *Chem. - A Eur. J.* **2016**, *22*, 16878–16890.

[59] F. K. Kessler, W. Schnick, *Zeitschrift für Anorg. und Allg. Chemie* **2019**, *645*,

857–862.

[60] G. Algara-Siller, N. Severin, S. Y. Chong, T. Björkman, R. G. Palgrave, A. Laybourn, M. Antonietti, Y. Z. Khimyak, A. V. Krasheninnikov, J. P. Rabe, et al., *Angew. Chemie Int. Ed.* **2014**, *53*, 7450–7455.

[61] J. H. Warner, M. H. Rümmeli, L. Ge, T. Gemming, B. Montanari, N. M. Harrison, B. Büchner, G. A. D. Briggs, *Nat. Nanotechnol.* **2009**, *4*, 500–504.

[62] R. Hoffmann, A. A. Kabanov, A. A. Golov, D. M. Proserpio, *Angew. Chemie - Int. Ed.* **2016**, *55*, 10962–10976.

[63] A. Yoshikawa, H. Matsunami, Y. Nanishi, in *Wide Bandgap Semicond.*, Springer Berlin Heidelberg, Berlin, Heidelberg, **2007**, pp. 1–24.

[64] H. Umezawa, *Mater. Sci. Semicond. Process.* **2018**, *78*, 147–156.

[65] W. A. Chalifoux, R. McDonald, M. J. Ferguson, R. R. Tykwinski, *Angew. Chemie Int. Ed.* **2009**, *48*, 7915–7919.

[66] S. Baranovski, *Charge Transport in Disordered Solids with Apllications in Electronics*, Wiley & Sons, Ltd, **2006**.

[67] K. P. Chang, K. I. Ho, M. Boutchich, J. Chaste, H. Arezki, C. S. Lai, *Semicond. Sci. Technol.* **2020**, *35*, 1V.

[68] T. Wu, H. Shen, L. Sun, B. Cheng, B. Liu, J. Shen, *New J. Chem.* **2012**, *36*, 1385.

[69] R. Zbořil, F. Karlický, A. B. Bourlinos, T. A. Steriotis, A. K. Stubos, V. Georgakilas, K. Šafářová, D. Jančík, C. Trapalis, M. Otyepka, *Small* **2010**, *6*, 2885–2891.

[70] F. Karlický, J. Turoň, *Carbon N. Y.* **2018**, *135*, 134–144.

[71] M. Pumera, Z. Sofer, *Chem. Soc. Rev.* **2017**, *46*, 4450–4463.

[72] M. S. Jang, H. Kim, Y. W. Son, H. A. Atwater, W. A. Goddard, *Proc. Natl. Acad. Sci. U. S. A.* **2013**, *110*, 8786–8789.

[73] D. Chen, S. J. Su, Y. Cao, *J. Mater. Chem. C* **2014**, *2*, 9565–9578.

[74] H. Usta, C. Risko, Z. Wang, H. Huang, M. K. Deliomeroglu, A. Zhukhovitskiy, A. Facchetti, T. J. Marks, *J. Am. Chem. Soc.* **2009**, *131*, 5586–5608.

[75] M. Long, L. Tang, D. Wang, Y. Li, Z. Shuai, *ACS Nano* **2011**, *5*, 2593–2600.

[76] S. Thomas, H. Li, C. Zhong, M. Matsumoto, W. R. Dichtel, J. L. Bredas, *Chem. Mater.* **2019**, *31*, 3051–3065.

[77] S. Fratini, D. Mayou, S. Ciuchi, *Adv. Funct. Mater.* **2016**, *26*, 2292–2315.

[78] W. Brutting, *Physics of Organic Semiconductors Handbook*, **2005**.

[79] H. Ibach, H. Luth, *Solid-State Physics, an Introduction to Principles of Material Science.*, **2015**.

[80] T. Sakanoue, H. Sirringhaus, *Nat. Mater.* **2010**, *9*, 736–740.

[81] S. Fratini, M. Nikolka, A. Salleo, G. Schweicher, H. Sirringhaus, *Nat. Mater.* **2020**, *19*, 491–502.

[82] J. Takeya, M. Yamagishi, Y. Tominari, R. Hirahara, Y. Nakazawa, T. Nishikawa, T. Kawase, T. Shimoda, S. Ogawa, *Appl. Phys. Lett.* **2007**, *90*, DOI 10.1063/1.2711393.

[83] J. Lee, A. J. Kalin, T. Yuan, M. Al-Hashimi, L. Fang, *Chem. Sci.* **2017**, *8*, 2503–2521.

[84] D. Burmeister, L. Ahrens, A. Opitz, G. Ligorio, F. Hermerschmidt, D. Jänsch, J. Freudenberg, U. H. F. Bunz, K. Müllen, E. J. W. List-Kratochvil, *J. Mater. Chem. C* **2020**, *8*, 3302–3307.

[85] A. Opitz, *J. Phys. Condens. Matter* **2017**, *29*, 133001.

[86] M. G. Stanford, P. D. Rack, D. Jariwala, *npj 2D Mater. Appl.* **2018**, *2*, 20.

[87] P. M. Fauchet, D. Hulin, R. Vanderhaghen, A. Mourchid, W. L. Nighan, *J. Non. Cryst. Solids* **1992**, *141*, 76–87.

[88] A. R. Moore, *Appl. Phys. Lett.* **1977**, *31*, 762–764.

[89] T. Ma, E. A. Kapustin, S. X. Yin, L. Liang, Z. Zhou, J. Niu, L.-H. Li, Y. Wang, J. Su, J. Li, et al., *Science* **2018**, *361*, 48–52.

[90] S. Thomas, H. Li, R. R. Dasari, A. M. Evans, I. Castano, T. G. Allen, O. G. Reid, G. Rumbles, W. R. Dichtel, N. C. Gianneschi, et al., *Mater. Horizons* **2019**, *6*, 1868–1876.

[91] Y. Noda, C. Merschjann, J. Tarábek, P. Amsalem, N. Koch, M. J. Bojdys, *Angew. Chemie Int. Ed.* **2019**, *58*, 9394–9398.

[92] L.-L. Chua, J. Zaumseil, J.-F. Chang, E. C.-W. Ou, P. K.-H. Ho, H. Sirringhaus, R. H. Friend, *Nature* **2005**, *434*, 194–199.

[93] A. Opitz, M. Horlet, M. Kiwull, J. Wagner, M. Kraus, W. Brütting, *Org. Electron.* **2012**, *13*, 1614–1622.

[94] N. S. Hush, J. A. Pople, *Trans. Faraday Soc.* **1955**, *51*, 600–605.

[95] J. Nitta, K. Miwa, N. Komiya, E. Annese, J. Fujii, S. Ono, K. Sakamoto, *Sci. Rep.* **2019**, *9*, 1–7.

[96] Y. Y. Illarionov, M. Waltl, A. Di Bartolomeo, L. Genovese, Y. Y. Illarionov, G. Rzepa, M. Waltl, T. Knobloch, A. Grill, *2D mater* **2016**, *3*, 1–10.

[97] N. Koch, *ChemPhysChem* **2007**, *8*, 1438–1455.

[98] Y. Xu, Y. Li, S. Li, F. Balestra, G. Ghibaudo, W. Li, Y. F. Lin, H. Sun, J. Wan, X. Wang, et al., *Adv. Funct. Mater.* **2020**, *30*, 1–23.

[99] X.-W. Chen, W. C. H. Choy, C. J. Liang, P. K. A. Wai, S. He, *Appl. Phys. Lett.* **2007**, *91*, 221112.

[100] Y. Liu, C. Li, Z. Ren, S. Yan, M. R. Bryce, *Nat. Rev. Mater.* **2018**, *3*, 18020.

[101] G. Hong, X. Gan, C. Leonhardt, Z. Zhang, J. Seibert, J. M. Busch, S. Bräse, *Adv. Mater.* **2021**, *33*, 2005630.

[102] Y. Miyamoto, M. L. Cohen, S. G. Louie, *Solid State Commun.* **1997**, *102*, 605–608.

[103] M. dos Santos, F. Alvarez, *Phys. Rev. B - Condens. Matter Mater. Phys.* **1998**, *58*, 13918–13924.

[104] G. Algara-Siller, N. Severin, S. Y. Chong, T. Björkman, R. G. Palgrave, A. Laybourn, M. Antonietti, Y. Z. Khimyak, A. V. Krasheninnikov, J. P. Rabe, et al., *Angew. Chemie Int. Ed.* **2014**, *53*, 7450–7455.

[105] E. J. Mele, *J. Phys. D. Appl. Phys.* **2012**, *45*, 154004.

[106] D. Burmeister, M. G. Trunk, M. J. Bojdys, *Chem. Soc. Rev.* **2021**, *50*, 11559–11576.

[107] H. Schlomberg, J. Kröger, G. Savasci, M. W. Terban, S. Bette, I. Moudrakovski, V. Duppel, F. Podjaski, R. Siegel, J. Senker, et al., *Chem. Mater.* **2019**, *31*, 7478–7486.

[108] S. Y. Chong, J. T. A. Jones, Y. Z. Khimyak, A. I. Cooper, A. Thomas, M. Antonietti, M. J. Bojdys, *J. Mater. Chem. A* **2013**, *1*, 1102–1107.

[109] H. R. Karfunkel, T. Dressler, A. Hirsch, *J. Comput. Aided. Mol. Des.* **1992**, *6*, 521–535.

[110] F. Shojaei, H. S. Kang, *RSC Adv.* **2015**, *5*, 10892–10898.

[111] D. Burmeister, A. Eljarrat, M. Guerrini, E. Röck, J. Plaickner, C. T. Koch, N. Banerji, C. Cocchi, E. J. W. List-Kratochvil, M. J. Bojdys, *Chem. Sci.* **2023**, 14, 6269–6277.

[112] E. Wirnhier, M. Döblinger, D. Gunzelmann, J. Senker, B. V. Lotsch, W. Schnick, *Chem. - A Eur. J.* **2011**, *17*, 3213–3221.

[113] Y. B. Zhang, J. Su, H. Furukawa, Y. Yun, F. Gándara, A. Duong, X. Zou, O. M. Yaghi, *J. Am. Chem. Soc.* **2013**, *135*, 16336–16339.

[114] L. Peng, Q. Guo, C. Song, S. Ghosh, H. Xu, L. Wang, D. Hu, L. Shi, L. Zhao, Q. Li, et al., *Nat. Commun.* **2021**, *12*, 5077.

[115] D. Burmeister, H. A. Tran, J. Müller, M. Guerrini, C. Cocchi, J. Plaickner, Z. Kochovski, E. J. W. List-Kratochvil, M. J. Bojdys, *Angew. Chemie Int. Ed.* **2022**, *61*, 2–10.

[116] D. Burmeister, J. Müller, J. Plaickner, Z. Kochovski, E. J. W. List-Kratochvil, M. J. Bojdys, *Chem. – A Eur. J.* **2022**, *28*, e202200705.

[117] A. C. Ferrari, S. E. Rodil, J. Robertson, *Phys. Rev. B* **2003**, *67*, 155306.

[118] N. E. Mircescu, M. Oltean, V. Chiș, N. Leopold, *Vib. Spectrosc.* **2012**, *62*, 165–171.

[119] W. L. Bragg, *Proc. R. Soc. London. Ser. A, Contain. Pap. a Math. Phys. Character* **1913**, *89*, 248–277.

[120] A. L. Patterson, *Phys. Rev.* **1939**, *56*, 978–982.

[121] W. Kabsch, *Acta Crystallogr. Sect. D Biol. Crystallogr.* **2010**, *66*, 125–132.

[122] G. M. Sheldrick, *Acta Crystallogr. Sect. A Found. Crystallogr.* **2015**, *71*, 3–8.

[123] N. Stojilovic, *J. Chem. Educ.* **2012**, *89*, 1331–1332.

[124] J. Huot, T. K. Bose, *J. Chem. Phys.* **1991**, *94*, 3849–3854.

[125] F. R.-R. Matthias Thommes*, Katsumi Kaneko, Alexander V. Neimark, James P. Olivier, J. R. and K. S. W. Sing, *Pure Appl. Chem.* **2013**, *87*, 1051–1069.

[126] K. S. W. Sing, *Pure Appl. Chem.* **1985**, *57*, 603–619.

[127] R. Ben Said, J. M. Kolle, K. Essalah, B. Tangour, A. Sayari, *ACS Omega* **2020**, *5*, 26125–26133.

[128] A. M. MJ, A. S. KA, S. MA, C. DJ, K. MM, *J. Phys. Chem. Biophys.* **2017**, *07*, 1–5.

[129] P. W. Atkins, J. de Paula, *Physikalische Chemie*, Wiley-VCH, Weinheim, **2012**.

[130] P. KUBELKA, *J. Opt. Soc. Am.* **1948**, *38*, 448–457.

[131] J. Tauc, R. Grigorovici, A. Vancu, *Phys. status solidi* **1966**, *15*, 627–637.

[132] D. J. Yun, D. K. Lee, H. K. Jeon, S. W. Rhee, *Org. Electron.* **2007**, *8*, 690–694.

[133] A. Opitz, *J. Phys. Condens. Matter* **2017**, *29*, 133001.

[134] S. Fu, E. Jin, H. Hanayama, W. Zheng, H. Zhang, L. Di Virgilio, M. A. Addicoat, M. Mezger, A. Narita, M. Bonn, et al., *J. Am. Chem. Soc.* **2022**, *144*, 7489–7496.

[135] M. Wang, M. Ballabio, M. Wang, H. Lin, B. P. Biswal, X. Han, S. Paasch, E. Brunner, P. Liu, M. Chen, et al., *J. Am. Chem. Soc.* **2019**, *141*, 16810–16816.

[136] B. Pattengale, J. Neu, A. Tada, G. Hu, C. J. Karpovich, G. W. Brudvig, *Polyhedron* **2021**, *203*, 115182.

[137] S. R. Forrest, *Philos. Trans. R. Soc. A Math. Phys. Eng. Sci.* **2015**, *373*, 20140320.

[138] C. Kittel, *Introduction to Solid State Physics*, Wiley, Hoboken, NJ, **2005**.

[139] E. Wirnhier, M. Döblinger, D. Gunzelmann, J. Senker, B. V. Lotsch, W. Schnick, *Chem. - A Eur. J.* **2011**, *17*, 3213–3221.

[140] S. Y. Chong, J. T. A. Jones, Y. Z. Khimyak, A. I. Cooper, A. Thomas, M. Antonietti, M. J. Bojdys, *J. Mater. Chem. A* **2013**, *1*, 1102–1107.

[141] R. Sridhar, C. E. Johnson, E. J. Cairns, *J. Chem. Eng. Data* **1970**, *15*, 244–245.

[142] B. Jürgens, E. Irran, J. Senker, P. Kroll, H. Müller, W. Schnick, *J. Am. Chem. Soc.* **2003**, *125*, 10288–10300.

[143] L. Heymann, B. Schiller, H. Noei, A. Stierle, C. Klinke, *ACS Omega* **2018**, *3*, 3892–3900.

[144] D. S. Su, J. Zhang, B. Frank, A. Thomas, X. Wang, J. Paraknowitsch, R. Schlögl, *ChemSusChem* **2010**, *3*, 169–180.

[145] L. Lin, C. Wang, W. Ren, H. Ou, Y. Zhang, X. Wang, *Chem. Sci.* **2017**, *8*, 5506–5511.

[146] X. Wang, S. Blechert, M. Antonietti, *ACS Catal.* **2012**, *2*, 1596–1606.

[147] T.-G. Lee, H.-J. Kang, J.-H. Kim, N. Suzuki, A. Fujishima, M. Choi, Y.-S. Jun, *Appl. Catal. B Environ.* **2021**, *294*, 120222.

[148] S. J. Clark, M. D. Segall, C. J. Pickard, P. J. Hasnip, M. I. J. Probert, K. Refson, M. C. Payne, *Zeitschrift fur Krist.* **2005**, *220*, 567–570.

[149] L. Lin, Z. Lin, J. Zhang, X. Cai, W. Lin, Z. Yu, X. Wang, *Nat. Catal.* **2020**, *3*, 649–655.

[150] T. S. Miller, T. M. Suter, A. M. Telford, L. Picco, O. D. Payton, F. Russell-Pavier, P. L. Cullen, A. Sella, M. S. P. Shaffer, J. Nelson, et al., *Nano Lett.* **2017**, *17*, 5891–5896.

[151] S. Evans, *Surf. Interface Anal.* **1997**, *25*, 924–930.

[152] A. P. Dementjev, A. de Graaf, M. C. M. van de Sanden, K. I. Maslakov, A. V. Naumkin, A. A. Serov, *Diam. Relat. Mater.* **2000**, *9*, 1904–1907.

[153] X. Li, G. Hartley, A. J. Ward, P. A. Young, A. F. Masters, T. Maschmeyer, *J. Phys. Chem. C* **2015**, *119*, 14938–14946.

[154] T. Suter, V. Brázdová, K. McColl, T. S. Miller, H. Nagashima, E. Salvadori, A. Sella, C. A. Howard, C. W. M. Kay, F. Corà, et al., *J. Phys. Chem. C* **2018**, *122*, 25183–25194.

[155] M. Pauly, J. Kröger, V. Duppel, C. Murphey, J. Cahoon, B. V. Lotsch, P. A. Maggard, *Chem. Sci.* **2022**, *13*, 3187–3193.

[156] J. Gracia, P. Kroll, *J. Mater. Chem.* **2009**, *19*, 3013–3019.

[157] A. S. Ivanov, E. Miller, A. I. Boldyrev, Y. Kameoka, T. Sato, K. Tanaka, *J. Phys. Chem. C* **2015**, *119*, 12008–12015.

[158] M. Deifallah, P. F. McMillan, F. Corà, *J. Phys. Chem. C* **2008**, *112*, 5447–5453.

[159] M. Senthilkumaran, P. Muthu Mareeswaran, in *Nanomater. CO2 Capture, Storage, Convers. Util.*, Elsevier, **2021**, pp. 31–52.

[160] E. Wirnhier, M. Döblinger, D. Gunzelmann, J. Senker, B. V. Lotsch, W. Schnick, *Chem. – A Eur. J.* **2011**, *17*, 3213–3221.

[161] T. M. Suter, T. S. Miller, J. K. Cockcroft, A. E. Aliev, M. C. Wilding, A. Sella, F. Corà, C. A. Howard, P. F. McMillan, *Chem. Sci.* **2019**, *10*, 2519–2528.

[162] G. Kortüm, D. Oelkrug, *Zeitschrift für Naturforsch. A* **1964**, *19*, 28–37.

[163] M. Kastner, *Phys. Rev. Lett.* **1972**, *28*, 355–357.

[164] J. P. Menzel, H. J. M. De Groot, F. Buda, *J. Phys. Chem. Lett.* **2019**, *10*, 6504–6511.

[165] D. A. R. Barkhouse, O. Gunawan, T. Gokmen, T. K. Todorov, D. B. Mitzi, *Prog. Photovoltaics Res. Appl.* **2015**, *20*, 6–11.

[166] H. Najafov, B. Lee, Q. Zhou, L. C. Feldman, V. Podzorov, *Nat. Mater.* **2010**, *9*, 938–943.

[167] N. Smith, *Phys. Rev. B* **2001**, *64*, 155106.

[168] P. R. Whelan, B. Zhou, O. Bezencenet, A. Shivayogimath, N. Mishra, Q. Shen, B. S. Jessen, I. Pasternak, D. M. A. Mackenzie, J. Ji, et al., *2D Mater.* **2021**, *8*, 022003.

[169] D. R. Evans, H. S. Kwak, D. J. Giesen, A. Goldberg, M. D. Halls, M. Oh-E, *Org. Electron.* **2016**, *29*, 50–56.

[170] D. E. Soule, *Phys. Rev.* **1958**, *112*, 698–707.

[171] K. Sugihara, K. Kawamuma, T. Tsuzuku, *J. Phys. Soc. Japan* **1979**, *47*, 1210–

1215.

[172] N. Kumar, J. He, D. He, Y. Wang, H. Zhao, *J. Appl. Phys.* **2013**, *113*, 1–6.

[173] E. Jin, K. Geng, S. Fu, S. Yang, N. Kanlayakan, M. A. Addicoat, N. Kungwan, J. Geurs, H. Xu, M. Bonn, et al., *Chem* **2021**, *7*, 3309–3324.

[174] R. Dong, P. Han, H. Arora, M. Ballabio, M. Karakus, Z. Zhang, C. Shekhar, P. Adler, P. S. Petkov, A. Erbe, et al., *Nat. Mater.* **2018**, *17*, 1027–1032.

[175] V. I. Arkhipov, P. Heremans, E. V. Emelianova, G. J. Adriaenssens, H. Bässler, *Appl. Phys. Lett.* **2003**, *82*, 3245–3247.

[176] E. J. W. List, R. Guentner, P. S. de Freitas, U. Scherf, *MRS Proc.* **2002**, *734*, B9.11.

[177] M. Guerrini, E. Delgado Aznar, C. Cocchi, *J. Phys. Chem. C* **2020**, *124*, 27801–27810.

[178] J. Jia, E. R. White, A. J. Clancy, N. Rubio, T. Suter, T. S. Miller, K. McColl, P. F. McMillan, V. Brázdová, F. Corà, et al., *Angew. Chemie Int. Ed.* **2018**, *57*, 12656–12660.

[179] Y. H. Jang, S. Hwang, S. B. Chang, J. Ku, D. S. Chung, *J. Phys. Chem. A* **2009**, *113*, 13036–13040.

[180] S. Park, B. T. Lim, B. Kim, H. J. Son, D. S. Chung, *Sci. Rep.* **2014**, *4*, 1–9.

[181] M. Heyl, D. Burmeister, T. Schultz, S. Pallasch, G. Ligorio, N. Koch, E. J. W. List-Kratochvil, *Phys. status solidi – Rapid Res. Lett.* **2020**, *14*, 2000408.

[182] C. Wang, R. Furlan de Oliveira, K. Jiang, Y. Zhao, N. Turetta, C. Ma, B. Han, H. Zhang, D. Tranca, X. Zhuang, et al., *Nat. Commun.* **2022**, *13*, 1–10.

[183] A. Di Bartolomeo, L. Genovese, F. Giubileo, L. Iemmo, G. Luongo, T. Foller, M. Schleberger, *2D Mater.* **2017**, *5*, 015014.

[184] J. Xu, M. Shalom, F. Piersimoni, M. Antonietti, D. Neher, T. J. K. Brenner, *Adv. Opt. Mater.* **2015**, *3*, 913–917.

[185] M. J. Griffith, S. Cottam, J. Stamenkovic, J. A. Posar, M. Petasecca, *Front. Phys.* **2020**, *8*, 1–21.

[186] V. Tozzini, V. Pellegrini, *Phys. Rev. B - Condens. Matter Mater. Phys.* **2010**, *81*, 22–25.

[187] A. K. Bakhshi, A. Kaur, V. Arora, *Indian J. Chem. - Sect. A Inorganic, Phys. Theor. Anal. Chem.* **2012**, *51*, 57–68.

[188] C. J. Shearer, A. D. Slattery, A. J. Stapleton, J. G. Shapter, C. T. Gibson,

Nanotechnology **2016**, *27*, 125704.

[189] K. I. Bolotin, K. J. Sikes, Z. Jiang, M. Klima, G. Fudenberg, J. Hone, P. Kim, H. L. Stormer, *Solid State Commun.* **2008**, *146*, 351–355.

[190] R. Yan, Q. Zhang, W. Li, I. Calizo, T. Shen, C. A. Richter, A. R. Hight-Walker, X. Liang, A. Seabaugh, D. Jena, et al., *Appl. Phys. Lett.* **2012**, *101*, 022105.

[191] S. Wan, F. Gándara, A. Asano, H. Furukawa, A. Saeki, S. K. Dey, L. Liao, M. W. Ambrogio, Y. Y. Botros, X. Duan, et al., *Chem. Mater.* **2011**, *23*, 4094–4097.

[192] J. I. Feldblyum, C. H. McCreery, S. C. Andrews, T. Kurosawa, E. J. G. Santos, V. Duong, L. Fang, A. L. Ayzner, Z. Bao, *Chem. Commun.* **2015**, *51*, 13894–13897.

[193] B. Sun, J. Li, W.-L. Dong, M.-L. Wu, D. Wang, *J. Phys. Chem. C* **2016**, *120*, 14706–14711.

[194] H. Sahabudeen, H. Qi, B. A. Glatz, D. Tranca, R. Dong, Y. Hou, T. Zhang, C. Kuttner, T. Lehnert, G. Seifert, et al., *Nat. Commun.* **2016**, *7*, 13461.

[195] D. D. Medina, M. L. Petrus, A. N. Jumabekov, J. T. Margraf, S. Weinberger, J. M. Rotter, T. Clark, T. Bein, *ACS Nano* **2017**, *11*, 2706–2713.

[196] J. Zhou, Z. Xie, R. Liu, X. Gao, J. Li, Y. Xiong, L. Tong, J. Zhang, Z. Liu, *ACS Appl. Mater. Interfaces* **2019**, *11*, 2632–2637.

[197] D. Zhou, X. Tan, H. Wu, L. Tian, M. Li, *Angew. Chemie Int. Ed.* **2019**, *58*, 1376–1381.

[198] C. Li, Y. Wang, Y. Zou, X. Zhang, H. Dong, W. Hu, *Angew. Chemie* **2020**, *132*, 9489–9493.

Appendix

Chem Soc Rev

REVIEW ARTICLE

View Article Online
View Journal | View Issue

Cite this: *Chem. Soc. Rev.*, 2021, **50**, 11559

Development of metal-free layered semiconductors for 2D organic field-effect transistors

David Burmeister,[ab] Matthias G. Trunk [ab] and Michael J. Bojdys [*abc]

To this day, the active components of integrated circuits consist mostly of (semi-)metals. Concerns for raw material supply and pricing aside, the overreliance on (semi-)metals in electronics limits our abilities (i) to tune the properties and composition of the active components, (ii) to freely process their physical dimensions, and (iii) to expand their deployment to applications that require optical transparency, mechanical flexibility, and permeability. 2D organic semiconductors match these criteria more closely. In this review, we discuss a number of 2D organic materials that can facilitate charge transport across and in-between their π-conjugated layers as well as the challenges that arise from modulation and processing of organic polymer semiconductors in electronic devices such as organic field-effect transistors.

Received 28th June 2021

DOI: 10.1039/d1cs00497b

rsc.li/chem-soc-rev

1. From 0 to 1 to 2D

Silicon transistors are omnipresent in our lives, and they can be thought of as electrically controlled on/off switches. Their integration into circuits and successively smaller-sized logic gates has given rise to an exponential growth of computing power over the last 50 years. While silicon is an abundant material and its processing is one of the most sophisticated technologies ever developed, these processes are also energy-intensive, accounting for 2% of annual consumed energy in the US,[1] and up to 30% of microchip fabrication costs.[2]

Commercial silicon technology can currently mass-produce feature sizes of 5 nm, but short-channel effects,[3] no increase in clock frequency, and extremely costly lithography become increasingly deterrent.[4] According to the International Technology Roadmap for Semiconductors (ITRS), these circumstances render further miniaturization of silicon technologies

[a] *Institut für Chemie, Humboldt-Universität zu Berlin, Brook-Taylor-Str. 2, 12489 Berlin, Germany. E-mail: m.j.bojdys.02@cantab.net*
[b] *Integrative Research Institute for the Sciences Adlershof, Humboldt-Universität zu Berlin, Zum Großen Windkanal 2, 12489 Berlin, Germany*
[c] *Department of Chemistry, King's College London, Britannia House Guy's Campus, 7 Trinity Street, London, SE1 1DB, UK*

David Burmeister

David Burmeister studied chemistry in Berlin. He obtained his Bachelor and Master degree at the Humboldt-Universität zu Berlin in the Hybrid Devices Group under the supervision of Prof. Dr Emil List-Kratochvil. 2019 he joined the Functional Nanomaterials group lead by Prof. Dr Michael Bojdys as PhD student. His current research focus are organic layered materials.

Matthias G. Trunk

Matthias G. Trunk obtained his BSc and MSc from Ludwig-Maximilians-Universität München. In 2017 he obtained his doctorate from Technische Universität Berlin under the supervision of Prof. Dr Arne Thomas. Matthias joined the group of Prof. Dr Seth Cohen at the University of California, San Diego in 2018 where he worked on MOF–polymer composites. Since 2019 he is part of the group of Prof. Dr Michael Bojdys at Humboldt-Universität zu Berlin. His current research interests are porous organic donor–acceptor materials for photocatalytic water-splitting.

economically unfeasible.[5] Additionally, critical raw materials are used in the doping of silicon. The goal is to find new, high-performing semiconductors that are able to adopt the role of silicon at these small scales and are not reliant on critical raw materials. From a materials design perspective, the chemical bias set-up in dense crystalline silicon phases is usually long-lived and stable, but leaves very little scope for chemical modifications of the bulk.[6] Furthermore, silicon lacks flexibility and its high weight, opacity, and low compatibility with biological tissues render it unsuitable for various emerging areas of application such as wearable, breathable electronics.

To find suitable materials that match these criteria, organic molecular (0D) and linear polymeric semiconductors (1D) are widely researched.[7,8] However, these materials often suffer from low structural order, low amounts of charge carriers and high concentrations of defect sites, leading to low mobility and high injection barriers. Some of these shortcomings were resolved by spatially defined doping and attempts at increasing order in these systems by point-anchoring, supramolecular assembly or by liquid crystallinity. However, the inherent free movement of organic molecules and polymer chains in these systems tends to break down the desired chemical bias introduced by dopants and, over time, leads to reduced lifetimes and efficiencies of organic electronic devices.[9] Additionally, ambient conditions can have deteriorating effects on the chemical structures and charge transport properties of the involved organic materials.[10,11] The resulting low performance and possible short-channel effects make miniaturization of devices based on conventional organic (*i.e.* molecular and polymeric) semiconductors challenging.[3,12]

Overcoming the limitations inherent to silicon and conventional organic semiconductors is the prime incentive for the development of two-dimensional (2D) covalent organic semiconducting materials.[13] To reach this ambitious goal, materials need to exhibit (i) a band gap (0.3–3 eV), (ii) structural as well as energetic order (crystallinity), (iii) ambient stability, (iv) 2D morphology and (v) high charge carrier mobility. Material classes with the potential to satisfy these requirements are covalent organic frameworks (COFs) and carbon nitrides. The majority of COFs are crystalline, fully conjugated layered materials synthesized from one or several organic building blocks.[14] This modular makeup allows atomically precise structural engineering on two levels in order to tune the electronic properties of the resulting material.

Firstly, the monomer(s) can be fashioned with specific functional groups. Secondly, the choice of linking chemistry determines the nature of communication between the building blocks of these frameworks. For example, in-plane π-conjugation and layering of aromatic domains determines emerging functionalities such as (semi-)conductivity, optical properties and catalytic activity. Recent approaches based on carbon–carbon couplings have produced highly conjugated structures including materials such as graphdiyne, for which monolayers exhibiting charge carrier mobilities on the order of 10.000 $cm^2 V^{-1} s^{-1}$ and a direct bandgap of 0.46 eV are predicted (see Table 1 at the end of this document).[15] The sizable bandgap of >0.3 eV and high charge carrier mobilities make graphdiyne a promising candidate for high-performance organic 2D transistors.[16] Carbon nitride materials, such as triazine-based graphitic carbon nitride (TGCN), with a high N/C ratio, are expected to exhibit high electron affinity enabling their application as chemically and thermally stable, ambipolar semiconductors.[17] The bandgap of TGCN has been estimated to be <1.6 eV, making it an additional candidate for an organic 2D semiconductor.[18] Both layered COFs and layered carbon nitrides can be potentially exfoliated to covalently bonded layers of atomic thickness, *i.e.* monolayers. Potential organic 2D semiconductors are shown in Fig. 1 and compared to their current competitors. Covalent organic materials are arguably less affected by dopant drift and migration. Depending on pore size and stacking distances the migration of large atomic dopants such as iodine can be sufficiently hindered. This could enable doping at specific sites such as the electrode–semiconductor interface in order to enhance charge injection.[19,20]

Despite the rapid progress in the field of layered organic semiconductors, the anticipated high-performance organic transistor has not been achieved yet. The devices constructed from layered organic materials exhibit mobilities only scarcely exceeding that of amorphous silicon thin film transistors (0.5–1 $cm^2 V^{-1} s^{-1}$).[21] Exploring the present state of the different material classes we notice common challenges, *i.e.* (i) structural and energetic disorder (low crystallinity), (ii) charge carrier anisotropy (intraplane *vs.* interplane charge transport) and (iii) processing of the solids into suitable thin films. In this review we map out the landscape of organic layered semiconductors, the strong points of the individual material types and the challenges the field has to overcome to produce materials applicable in flexible, high-performance, low-cost, low-power electronics.

Michael J. Bojdys

Since 2020 Michael is a Reader in Chemistry at King's College London, UK, a Guest Professor at the Humboldt-Universität zu Berlin, Germany, and a Junior Group Leader at the Integrative Research Institute for the Sciences (IRIS) Adlershof, Berlin, Germany. His research focuses on the design of covalent organic polymers with the aim to study their electric and optical properties and achieve organic transistor devices and light-responsive polymers, and it is funded by the European Research Council.

2. Candidates for 2D organic semiconductors

The "graphene family" as defined by Geim *et al.* in 2013 consists of five members, namely graphene, hexagonal

Table 1 Experimental and theoretical electrical mobility values of covalent organic materials and graphene

Material	Material class	Vertical dimension (method)	Mobility (charge carrier, method)	Ref.
Graphene	2D semimetal	0.4 ± 0.3 nm (peak force tapping AFM)	200 000 $cm^2 V^{-1} s^{-1}$ (electron, suspended, 5 K)	160–162
Graphdiyne	2D semiconductor		10 000 $cm^2 V^{-1} s^{-1}$ (electron, theory)	15
Porphyrin-imine COF	Bulk semiconductor	—	8.1 $cm^2 V^{-1} s^{-1}$ (hole, TOF)	163
Benzodithiophene-imine COF	Bulk semiconductor	1.8 nm (AFM)	3×10^{-6} $cm^2 V^{-1} s^{-1}$ (hole, FET)	113
Porphyrin-imine COF on hBN (COF-366@hBN)	Bulk semiconductor	2.34–4.56 nm (AFM)	0.015×10^{-6} $cm^2 V^{-1} s^{-1}$ (hole, FET)	116
Porphyrin-dihydroxyphenylene COF	Bulk semiconductor	0.7 nm (AFM)	1.3×10^{-6} $cm^2 V^{-1} s^{-1}$; 1.6×10^{-4} $cm^2 V^{-1} s^{-1}$ (I_2-doped)	147
Benzodithiophene-boronate ester COF	Bulk semiconductor	80 nm (cross-section SEM)	3×10^{-7} $cm^2 V^{-1} s^{-1}$ (hole-only device)	144
Graphdiyne	Bulk semiconductor	2.9 nm	6.25 $cm^2 V^{-1} s^{-1}$ (FET)	94
Poly-1,3,5-benzene Suzuki polymer	Bulk semiconductor	—	3.2 $cm^2 V^{-1} s^{-1}$ (FET)	99
Triazatruxene Suzuki polymer	Bulk semiconductor	2.5–46 nm (AFM)	1.37 $cm^2 V^{-1} s^{-1}$ (hole, FET)	100

boronitride (hBN), borocarbonitride (BCN), fluorographene, and graphene oxide.[22] To carve out the necessary steps towards efficient organic 2D semiconductors it is important to understand the advantages as well as the shortcomings of these materials.

Graphene is an inorganic semimetal, hence graphene will only be investigated as a new type of electrode with a variable work function (see Section 3.1). Several derivatives of graphene are insulators, *i.e.* graphane (C_1H_1), fluorographene (C_1F_1), and fluorographane ($C_1H_{0.5}F_{0.5}$).[23] While still intriguing as possible gate insulators or tunnel barriers they cannot be employed as 2D semiconductors.[24–27]

A commonly employed strategy in the semiconductor industry is to alter the electronic properties of homonuclear lattices. In silicon, for example, heteroatoms are incorporated into the bulk lattice, which is typically referred to as "impurity doping".[28–31] Impurity doping of graphene was initially conducted in order to obtain a 2D semiconductor. However, the doping concentration needs to be high and homogeneous enough over the dimensions of the device that no pristine channels of the initial semimetallic material remain. In addition, the introduction of new, polarising elements also introduces new scattering sites for charge carriers. This results in a trade-off between energetic control and deterioration of the extraordinary transport properties of graphene.[32] Doping of graphene with boron and nitrogen defect sites alters the electronic structure, but the surrounding semimetallic domains typically dominate the electronic properties of the B/N doped graphene in device architectures. Hence, the problem of the absence of an off-state – and therefore poor performance of field-effect transistors based on graphene – remains.[33] Tailoring the properties of graphene's electronic structure by nanostructuring increased the performance (on/off

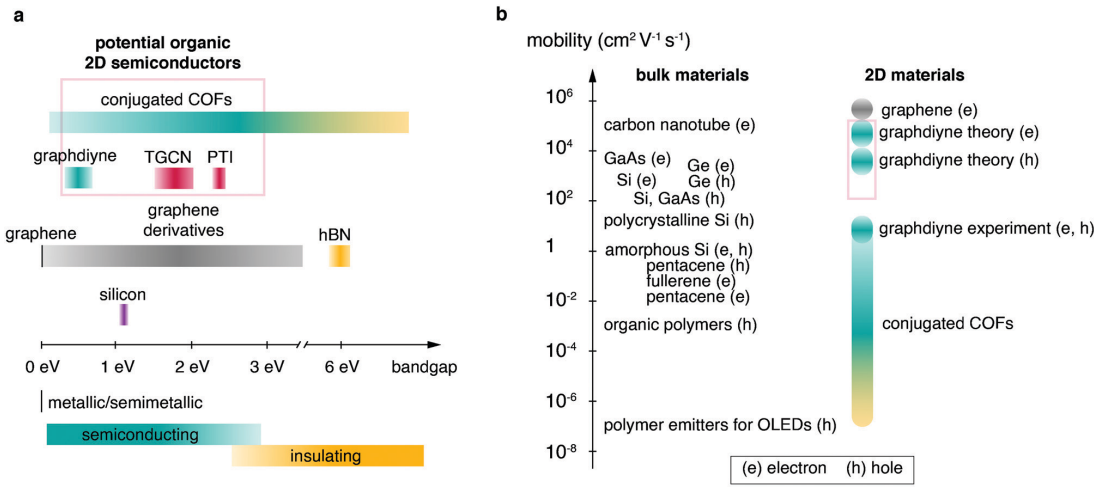

Fig. 1 Overview over semiconducting materials plotted in relation to (a) band gap and (b) mobility (e, electrons; h, holes). Candidates for organic 2D semiconductors are highlighted by red boxes. Fig. 1b was adapted from Tiwari and Greenham[164] with permission from Springer Nature.

ratio up to 10^4) and provided new insights into magnetotransport in graphene, but has not yet reached values to rival existing silicon technology.[34,35]

Graphene oxide has the advantage of being solution-processable, and it is typically viewed as a candidate for metal-free, transparent electrodes. However, the oxidized sites make graphene oxide non-conductive. To regain conductivity, graphene oxide has to be reduced, but reduced graphene oxide films do not yet reach the performance of chemical vapor deposition (CVD) graphene films produced by roll-to-roll processes, or the performance of conventional heavy-metal-based indium tin oxide (ITO) transparent electrodes.[36]

It is evident that the introduction of (few-)site dopants into graphene as a strategy to widen its band gap is highly limited and impractical. An alternative strategy is to synthesize heteroatom-containing structures analogous to graphene in a bottom-up approach.

Hexagonal boron nitride (hBN) – while structurally similar to graphene – is a wide-bandgap semiconductor. In fact, it is one of the most widely employed two-dimensional insulators.[37] It is anticipated that the electronic properties of ternary layered boron carbon nitrides (BCN) can be tuned from insulating to semimetallic with varying composition.[38] The partaking elements B, C, N can form homophilic (C–C) as well as heterophilic (C–N, B–N, C–B) bonds, giving rise to many different polymorphs. Quantum chemical calculations show that semiconducting hexagonal BC_xN alloys could form under non-equilibrium conditions, and that annealing can have a major impact on the electronic structure.[38] An in-depth study of the formation of BCN on a ruthenium catalyst conducted by Lu *et al.* showed the multitude of possible structures and pointed out that the formation of purely two-dimensional BCN alloys is still not well-understood.[39] Many different post-synthetic modifications of BCN materials resulted in various polymorphs and nanostructures. 2D BCN crystallites, however, have yet to be synthesized in a bottom-up approach.[40,41]

Some graphitic semiconducting materials can be found among binary boron carbide (BC_x) polymorphs. Bulk BC_3 was reported to be a metallic material with turbostratically disordered layers, and monolayers were predicted to exhibit an indirect band gap.[42–44] Quantum chemical calculations of boron carbide materials with increasing boron content show that most of these materials exhibit metallic behaviour.[45,46] An experimental study of boron-rich carbon films synthesized by a hot-press method found various polymorphs with local structural disorder.[47] A graphitic, layered boron carbide with a direct bandgap has not been synthesized to date.[48]

Overall, the graphene family consists mostly of semimetal or insulating members and does not yet have a promising candidate for an organic 2D semiconductor.

2.1 Two-dimensional C_3N_4 materials

One field promising the development of new direct-bandgap 2D semiconductors with high environmental stability and intriguing chemically active sites is the field of carbon nitrides.[18,49]

A new synthetic approach entailed the use of solvothermal conditions often applied in inorganic synthesis.[50] Different solvents such as benzene and hydrazine were applied but the products typically displayed residual –NH–/–NH_2 groups as can be deduced from IR bands at 3200–3300 cm^{-1}.[51,52] For complete condensation the absence of reducing agents and elevated temperatures were necessary. Experiments in laser-heated diamond-anvil-cells yielded a crystalline $C_2N_2(NH)$ phase,[53] and a stable, chiral carbon nitride polymorph with space group $P4_32_12$ and mixed sp^2/sp^3 bonding.[54] A synthesis at high temperature under ionothermal conditions using a eutectic salt melt of lithium chloride and potassium chloride for the polycondensation of dicyandiamide was also investigated. The structural analysis of the crystalline product led to the conclusion that the observed product is heptazine-based graphitic carbon nitride (HGCN), but the product was later identified as polytriazine imide (PTI) with intercalated lithium and chloride ions.[55,56] This product constitutes the first truly graphitic carbon nitride for which the structure was fully resolved. Hence, we want to direct our attention to the synthesis, structure, morphology, and recent results regarding this material in more detail.

2.1.1 Polytriazine imide PTI-MX – the first truly graphitic carbon nitride. The in-plane structure of polytriazine imide consists of triazine cores bridged by nitrogen atoms, but the structure is not fully condensed (Fig. 3a). Within each layer, one third of the triazine cores are substituted by metal ions (M^+), which are balanced by halide ions (X^-) intercalated between the layers, hence the nomenclature of PTI-MX. Postsynthetic exchange of the halide and metal ions was investigated to tune the gallery height.[57,58]

Kessler *et al.*[59] published an extensive study on the formation processes of PTI from different precursors and eutectics, suggesting that the first step towards forming the PTI scaffold is always the formation of melem, *i.e.* triaminoheptazine. Depending on the reaction temperature and whether a closed vessel is used or not, melem can either condense under formation of nitrogen-bridged, one-dimensional heptazine chains, *i.e.* melon, or undergo a ring-opening reaction leading to the assembly of nitrogen-bridged, one-dimensional triazine strands. Further condensation of these strands leads to the formation of PTI. This mechanistic insight will be a good foundation for rationally designing new ionothermal synthesis approaches.

A recent study showed that PTI-LiCl produced under ambient conditions has an orthorhombic structure with a $Cmc2_1$ space group,[60] which is a superstructure to the earlier reported hexagonal structure $P6_3cm$.[56] The authors also demonstrate that higher accessibility of the (001) plane increases the photocatalytic activity, indicating that the active sites are not at defect sites or grain boundaries as observed for inorganic materials, but that the planar structures themselves are catalytically active.[60]

The product morphology is characterised as disordered platelets or hollow tubes consisting of hexagonal prisms with single crystallites on the order of 50 nm.[56,57] The layers are stacked in an AA′ manner with ion channels running

orthogonally to the (001) plane of the crystal structure. Due to the high structural order, for the first time it was possible to resolve the triazine breathing modes in a Raman spectrum for a condensed truly graphitic carbon nitride material at 1000 cm^{-1} and 680 cm^{-1}, using a 325 nm laser.[61] This enables to control the quality of microscopic amounts of the material on substrates, which is important for device fabrication. Furthermore, it opened the door to follow-up experiments investigating the vibrations of the material in dependence of temperature or dopants. TEM images of monolayers were first recorded by Villalobos *et al.*[62] This study indicates that PTI indeed is stable as a 2D sheet, opening a door towards experiments with the 2D crystal of PTI. Another complementary approach applying NMR and electron diffraction pinned down the positions of hydrogen atoms and chloride ions.[63] The bandgap of PTI-LiCl was determined to be 2.2 eV, which is 0.5 eV smaller compared to the bandgap of melon, indicating a higher degree of conjugation for PTI-LiCl.[64]

While the existence of PTI proves the possibility of synthesising crystalline, graphitic carbon nitride structures, the presence of –NH– groups and ions inside the structure are unfavourable to achieve a high-mobility organic semiconductor with high energetic order. Hence, the complete condensation to a binary CN material still had to be realised.

2.1.2 The first report of a fully condensed C_3N_4 material – triazine-based graphitic carbon nitride. Siller *et al.* reported the synthesis and characterisation of triazine-based graphitic carbon nitride (TGCN), which remains the only crystalline binary C_3N_4 system to this day.[18,65,66] TGCN comprises two-dimensional networks of triazine units bridged by nitrogen atoms. Infrared spectroscopy and elemental analysis showed that – in contrast to PTI-LiCl – only few –NH groups and salt intercalations remained. Overall, the synthesis conditions are extremely similar to the synthesis of PTI-MX.[55] Dicyandiamide is ground with a eutectic salt mixture and heated to 600 °C in a closed quartz ampule. Further, the high temperature and the presence of decomposition products enable reversible reactions since condensation products such as ammonia remain within the closed system.[67] The differences to the synthesis of PTI-LiBr are the heating program, which for TGCN entails two successive heating steps, and the reaction time, which is increased to three days. These changes were sufficient to observe a new carbon nitride phase evolving at the walls of the quartz ampules as well as at the gas–molten salt interface.

The macroscopic appearance was described as ''shiny flakes'' with colours ranging from transparent red for short reaction times to ''shiny flakes that are optically opaque'' for long reaction times. The structural assignment was conducted by a combination of high-resolution transmission electron microscopy (HRTEM) and powder X-ray diffraction (PXRD) measurements. The observed HRTEM images with hexagonal 2.6 nm periodicity were matched to HRTEM simulations of ABC-stacked TGCN. The synchrotron PXRD measurements further reinforced the PXRD results in showing the (001) reflection (a = 0.504 nm). The best fit for the PXRD data was found to be an AB stacking mode. The conflicting observations of TEM and PXRD were interpreted as weak interplane forces enabling different stacking orders. Hence, locally obtained TEM diffraction data does not necessarily reflect the overall observed PXRD data. Increasing the crystallinity of the material is a future goal since large crystallites and their isolation from amorphous phases has not been reported yet. On the basis of solid-state ultraviolet-visible (UV-Vis) spectra the authors reasoned that the optical gap of the structure is less than 1.6 eV. However, it should be noted that the presented density-functional theory (DFT) calculation of single layer TGCN indicates a bandgap of 2.5 eV, and that DFT typically underestimates the band gap.[68] The discrepancy between DFT and experiment is also reflected by the predicted corrugation of the structure. Geometry-optimized structures by DFT typically show that the triazine cores are not perfectly in-plane (corrugated structure), while structural refinement from diffraction experiments implies a perfectly planar orientation.[18]

In a successive study of the transport characteristics in the as-received films, Noda *et al.* observed that conductivity out-of-plane was higher than in-plane by a factor of 65. The authors concluded that the nitrogen atoms connecting the triazine rings are not fully sp^2-hybridized, which results in a low degree of conjugation for the as-received material. Thus, transport of charge carriers by interplanar hopping is favoured over intra-planar transport.[69] Learning about anisotropic properties is crucial for effective device implementation of newly discovered layered materials.

In an attempt to reproduce the synthesis by Siller *et al.*, Suter *et al.* obtained flakes which did not exhibit the same PXRD reflections.[61] Elemental analysis showed additional amounts of carbon compared to the ideal C_3N_4 composition and the Raman spectrum did not exhibit the characteristic triazine breathing modes. Nevertheless, similar HRTEM images as reported by Siller *et al.* were obtained. Bulk chemical analyses showed that the obtained films contained 2.3–2.5 wt% hydrogen. A neutral hydrogen atom attached to the triazine ring of TGCN was proposed to explain the missing triazine breathing mode in the Raman spectrum, missing NH stretches in the FTIR spectrum, the residual hydrogen in the elemental analysis, and the EPR response. The authors further note that the presence of the neutral hydrogen atoms in the structure could induce conducting domains or localized unpaired spins. The discrepancy to the work conducted by Siller *et al.* is addressed, reasoning that slight differences for example in the geometry of the used ovens can be the reason for different obtained product phases. This observation is important since reproducibility of the synthesis is not only determined by the reaction mixture but also by the heating program and the local temperatures in the oven influenced by the location of the heating elements and temperature sensors.

Truly graphitic carbon nitride materials like PTI-MX and TGCN are first promising steps towards the successful elucidation of structure–property-relationships in 2D carbon nitrides. Next to the previously discussed CN phases the realisation of new CN polymorphs predicted by theory is also a subject of further research.[70]

For the implementation of TGCN into electronic devices, further research must be directed towards increasing the crystalline domain size and isolating the phase-pure material. Current synthetic protocols offer little control of the mixture of co-evolving phases, such as 1D strands, 2D sheets, and predicted tubular structures (Fig. 2, artist's rendition). We adopted the nomenclature recommended by Miller *et al.* for condensed carbon nitride materials and want to recommend it to our quickly growing community, even though we want to stress that in this nomenclature the "g" in "gCN" does not equate to a graphitic material, but to a layered one.[71] Differentiating "graphitic" from "turbostratic" materials has real-world implications. For example, the difference in the electronic system between a defined graphitic stacking motif with strong interlayer coupling and turbostratic (rotationally faulted) structures that are electronically decoupled can be important as observed in multilayer epitaxial graphene.[72] We emphasize the importance of a commonly used language with clearly defined terms in a multidisciplinary research field.

2.2 Metal-free layered semiconductors from designer molecules

Condensed carbon nitride syntheses start from simple precursors such as dicyandiamide. The repeating units are generated *in situ* and then linked *via* a complex series of condensations requiring high temperatures (500–600 °C). Covalent organic frameworks (COFs) on the other hand are generated from *ex situ* synthesized organic monomers. In most cases, the linking of monomers to frameworks entails the elimination of water and the chemical equilibrium of these condensations is reached at much lower temperatures than in the case of pyrolytically generated carbon nitrides. Typically, bulk COF polymerizations can be carried out at 120–150 °C while the synthesis of COF thin films can be performed at or near ambient temperature. A fundamental advantage of COFs over carbon nitrides is the possibility to design monomers with highly specific functions, which translate into the target frameworks. Additional functionality can arise from the electronic interplay between monomers enabled by conjugated linkages as well as from the linkage motif itself.

2.2.1 Covalent organic framework linkages. Various linkages offer π-conjugation and are associated with different combinations of traits, such as reversibility and chemical stability (Fig. 4). These properties can be exploited in different ways to obtain thin films suitable for device fabrication.

2.2.1.1 Imine linkages. The first COFs were connected by boronic acid-based linkages which were rather unstable under ambient conditions. Furthermore, the boronic acid moiety is not conjugated and precludes the formation of fully conjugated materials.[14] The second generation of COFs was based on imine linkages, allowing the formation of fully conjugated sheets. At the same time the imine group provided chemical stability in presence of a wide range of solvents, under acidic pH as well as practically indefinite shelf life under ambient conditions.[73] The addition of hydroxy groups vicinal to the iminogenic aldehyde groups imparts additional hydrolytic stability. The hydroxy group acts as hydrogen bond donor and forms a six-membered ring with the imine group, compelling the system into a more planar geometry than the unsubstituted aldehyde.[74] This should increase the overall conjugation of the framework, however we are not aware of any study examining this effect in detail. When instead of the regularly employed 1,3,5-triformylbenzene the triply hydroxylated 1,3,5-triformyl-2,4,6-trihydroxybenzene (also known as triformylphloroglucinol) is used, the resulting materials do not just experience intramolecular hydrogen bonding but full-fledged tautomerization from enol-imine to β-keto–enamine structures.[75]

This tautomerization is a quasi-irreversible reaction, which is boon and curse at the same time. By effectively removing the imine structure from the chemical equilibrium, the products are rendered resistant even to concentrated acids and bases.[75] Hydrogen bonding serves to guide the emerging structure to grow in plane and thus an appreciable degree of order is inherently present in the growing system. The caveat is that the crystallinity cannot improve due to the strong thermodynamic disadvantage of the reverse reaction. Some success at improving the crystallinity has been achieved by slowing the reaction through acid-modulated protonation of the amine precursors.[76] An elegant approach demonstrated the feasibility of combining

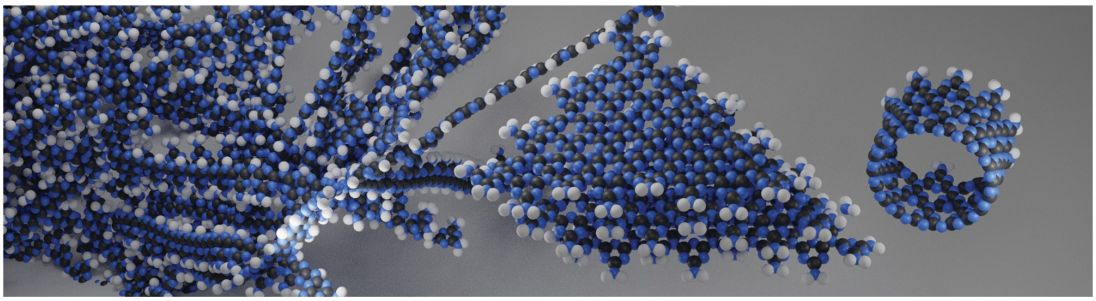

Fig. 2 Artistic depiction of the coevolution of different CN phases in the pyrolytic condensation reaction. From the past into the present towards the future – polymeric CNH as discovered 200 years ago (background), condensed TGCN sheets, discovered in 2014 (middle), and tubular structure predicted in 2015 (right).[70]

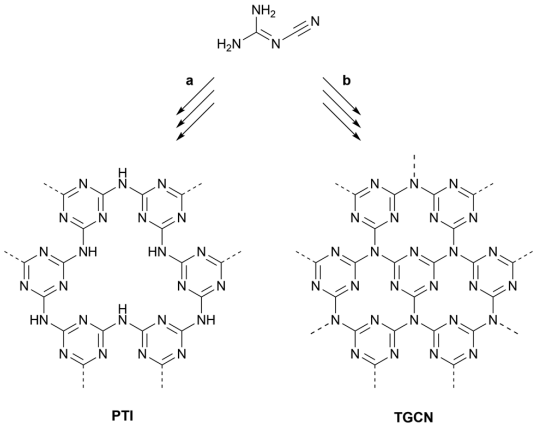

Fig. 3 Ionothermal syntheses of PTI and TGCN from dicyandiamide. (a) 400 °C, 12 h; then 600 °C, 48 h. (b) 400 °C, 4 h; then 600 °C, 60 h.

the high crystallinity of imine frameworks with the exceptional stability of β-keto–enamine frameworks. The 1,3,5-triformylbenzene vertices in a highly crystalline imine framework were postsynthetically exchanged with 1,3,5-triformyl-2,4,6-trihydroxybenzene, but the high degree of crystallinity of the imine material was retained. Following this strategy it is also possible to access keto–enamine frameworks difficult to obtain *via* direct synthesis.[77] The exceptional chemical robustness of β-keto–enamine COFs has already been exploited for real-world applications such as reversible sensing of hydrogen gas,[78] showcasing the suitability of these materials for further applications.

2.2.1.2 Pyrazine linkage. The pyrazine unit is formed by the condensation of two vicinal ketones and two vicinal amines, effectively forming a double-imine.[79] While the first condensation is still reversible, the second condensation locks the structure in place and imparts extra aromatic stabilization, which renders the ring closure an irreversible process. The ring closure also planarizes the system and inherently avoids the formation of defects if symmetric precursors are used exclusively. The resulting materials are fully conjugated and generally display very high bulk electrical conductivity as well as chemical stability.[79–82] In 2019, two studies examining pyrazine-linked COFs synthesized from phthalocyanine and pyrene building blocks were reported.[80,81] In one report, the polycrystalline, layered material exhibited similar electronic properties, such as bandgaps of 1.2 eV, bulk conductivities on the order of 10^{-7} S cm^{-1}, and anisotropic hole mobilities. The out-of-plane hole mobilities were determined to be 4.8 ± 0.7 and 0.9 ± 0.2 cm^2 V^{-1} s^{-1}, whereas in-plane hole mobilities were found to be practically null.[80] Notably, the other report showed significantly higher bulk conductivity of 2.5 × 10^{-5} S cm^{-1} for a material of similar structure, which could be raised by three orders of magnitude by iodine doping.[81]

These reports are still few but show great promise for pyrazine-based materials as active layers in electronic devices,

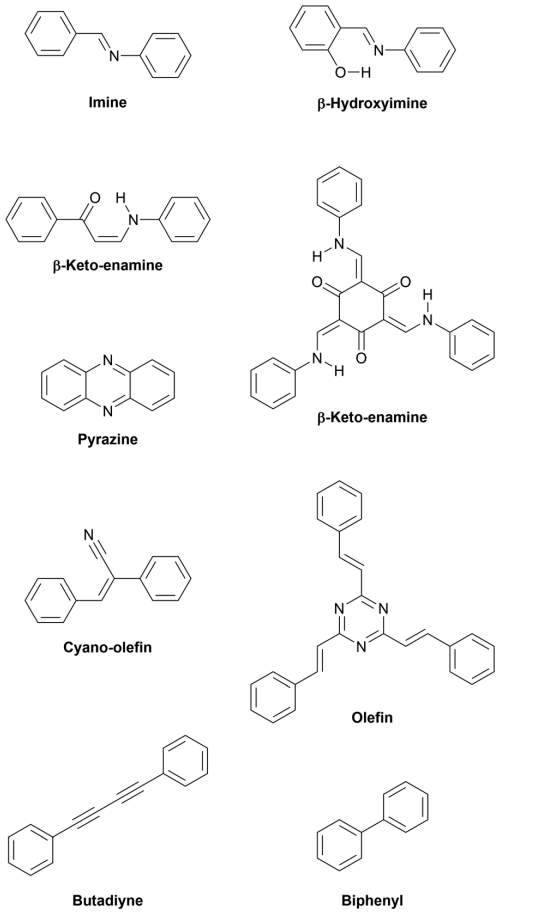

Fig. 4 Various linkages enabling π-conjugation within layers.

but no charge carrier mobilities determined from OFET setups have been reported yet.

2.2.1.3 Olefin linkages. In 2016, the aldol condensation of electron-deficient 1,4-phenylenediacetonitrile with a trialdehyde yielded a crystalline material connected by cyano-substituted olefin units, but in this initial report no use is made of the fully conjugated sp^2-carbon skeleton.[83] This concept was further explored later utilizing pyrene as tecton. The obtained layered material exhibited a bandgap of 1.9 eV as determined by cyclic voltammetry experiments. Upon doping with iodine, its electrical conductivity increased to 7.1 × 10^{-2} S m^{-1}.[84] Building on this work, a series of cyanovinylene frameworks exhibited the expected stability of a pure carbon backbone even in the presence of highly concentrated hydrochloric acid, potassium hydroxide, and aggressive organic solvents. The fully conjugated skeletons are highly emissive in bulk and as exfoliated sheets, showcasing the strong π-conjugation arising from the carbon–carbon linkage.[85]

Since the beginning of 2019, multiple reports of unsubstituted olefin-linked triazine frameworks have appeared,

emphasizing the great interest in these highly conjugated linkages.[86–91] As with their nitrile-substituted predecessors, these materials are formed *via* aldol condensations and are able to withstand even concentrated acidic as well as basic solutions for extended periods of time without apparent loss of crystallinity. The eclipsed olefin bridges in these networks are amenable to photoinduced reversible interlayer dimerization, switching the materials between a fully conjugated, two-dimensional layered structure and a non-conjugated, three-dimensional state. The effect on the electronic structure was observed by diffuse reflectance UV-Vis spectra. Two-dimensional P^2PV and its photodimerization product, P^3PcB, revealed optical bandgaps of 2.52 and 2.95 eV, respectively, demonstrating a significant blueshift due to breaking of the extended π-conjugation upon photodimerization.[90] Analogously, photoinduced ring-closing reactions are employed in molecular switches in order to influence the charge injection at interfaces of multilayer devices.[92] A switchable COF could be switched between insulating and conducting, using light and temperature as external stimuli.

2.2.1.4 COFs from irreversible C–C coupling reactions. Crystalline organic polymers synthesized from irreversible such as C–C coupling reactions are not classically counted among COFs as this term has been mostly reserved for materials synthesized from reversible reactions. Lately, these lines have begun to blur as more examples of ordered structures from irreversible reactions have surfaced. Navigating irreversible C–C coupling reactions in such a way that defects are kept at a minimum is a significant challenge as no error correction can take place in these reactions.

2.2.1.4.1 Graphdiynes. Graphdiynes are synthesized from arylalkynes *via* copper(II)-mediated Glaser-type polymerization reactions, forming lattices of benzene rings connected *via* 1,3-butadiyne – often simply referred to as diyne – groups. A major obstacle associated with terminal alkynes is their inherently high reactivity, therefore alkyne monomers have a tendency to decompose under ambient conditions.[93] During polymerization the decomposition products interfere with the structure reticulation, causing irreparable defects. To remedy this issue, the Hiyama coupling offers an elegant way to cross-couple alkynes directly from the silyl-protected state *via* an *in situ* deprotection-and-coupling cascade. A modified Hiyama coupling has recently been modified to polymerize protected alkynes to ultrathin graphdiyne films suitable for the construction of an OFET device, using graphene as well as hexagonal boron nitride as substrates.[94] An alternative synthetic protocol uses copper foil as a physical template and as the active metal species in the network-forming polymerisation of C_3-symmetric, organic building blocks with terminal alkynes. In theory, growth of the resulting diyne materials should self-terminate once all reactive surface functional groups on the metal support have become covered by the first complete layer(s) of the polymer. In practice, Cu(I) and Cu(II) species coordinate strongly to alkyne functional groups of the organic building blocks and break away from the bulk metal support.[95] Copper species become dislodged from the surface during the polymerisation reaction, and diffuse up to 20 μm away from the surface. Here, these copper species aggregate as nanoparticles (Cu(I) by XPS) and they continue to act as a quasi-homogeneous reagent that promotes further polymer growth away from the surface functional groups. The resulting polymer film is a 2D/3D van der Waals (vdW) heterostructure based on triazine (Tz, C_3N_3) linkers.

The most primitive member of the graphdiyne family is a carbon allotrope that consists of benzene rings in which each of the six carbon atoms is connected to the next benzene ring *via* a diyne group. The calculated bulk material properties were found to depend strongly on the stacking mode, similar to few-layer graphene. For AA stacking a metallic state is predicted, while for some AB stacking modes semiconducting behaviour is predicted. The graphdiyne monolayer is predicted to be semiconducting with a band gap of 0.46 eV and high charge carrier mobility of 10^5 cm^2 V^{-1} s^{-1} (Table 1).[15,96,97] While the high mobility is important for high frequency operation and high on-state current, the sizable band gap allows for low off-state currents and therefore a high on/off ratio. An experimental study indeed found a high off-state current in a transistor setup employing a graphdiyne film synthesized on hexagonal boron nitride. The authors mention that their films might have excessive defect states, hence the relatively low field effect mobility could also be caused by defects instead of the electronic structure of ideal graphdiyne.[94]

C–C coupling reactions catalyzed or mediated by metals can yield highly cross-linked but usually amorphous polymer networks. While slowing polymerization processes down can be advantageous to avoid side reactions,[93] it can also help improve structural order in the resulting system. We obtained an ordered triazine-based graphdiyne polymorph by Glaser coupling, whereas an analogous reaction co-catalyzed by palladium yielded an amorphous material exhibiting inferior semiconducting properties.[98]

2.2.1.4.2 Cross-coupling reactions. If carried out at an interface, in principle any C–C cross-coupling reaction utilizing planar tectons can yield crystalline sheets. Restricting the reaction to a liquid–liquid interface can be accomplished by separating the components necessary to facilitate the coupling into separate phases so that coupling events can only happen where all necessary components meet, *i.e.* at the interface. For instance, the Suzuki coupling is a Pd-catalyzed cross-coupling reaction which couples arylboronic acid derivatives to aryl halides, which makes it attractive as a staging ground for the formation of conjugated materials. Its mechanism requires the presence of stoichiometric amounts of an oxygen base, typically provided by carbonate or hydroxide salts. Deliberately separating the organic precursors from the aqueous base solution provides an interface at which all required components can meet to form two-dimensional materials.[99,100]

2.2.2 Large-area highly crystalline domains. The presence of grain boundaries and defects in crystalline semiconductors are detrimental to charge transport performance, hence large

single-crystalline domains are aspired. We will highlight a number of different strategies to reduce defects, increase domain sizes, and strengthen interlayer interactions to obtain highly crystalline materials.

Next to synthetic approaches, one generally important aspect to consider when synthesizing porous, crystalline materials is the drying process. Two very recent studies demonstrate that the regularly used vacuum evacuation can lead to pore collapse, resulting in lower crystallinity and accessible surface area.[101,102] It is therefore conceivable that feasible reaction conditions, especially shorter reaction times, have been obscured by inadvertent destruction of sensitive frameworks. To avoid pore collapse, a mild activation process based on a simple nitrogen flow process was proposed.[101] Alternatively, a final washing step with low-surface tension solvent such as perfluorohexane can be carried out before vacuum drying to avoid pore collapse.[102]

2.2.2.1 Modulated growth processes. In addition to stoichiometric amounts of building blocks, monodentate modulator molecules such as catechol slow the COF formation process. In one report, the addition of controlled amounts of water to condensation reactions was investigated. The authors found that small amounts of water enhanced the reversibility of the condensation reaction and increased the sizes of the resulting crystalline domains to 40 nm. Consequently, the crystalline domain area increased by a factor of 4 and the BET surface area to about 2000 $m^2 g^{-1}$, approaching the theoretical limit of the material in case.[103] Similarly, addition of 10 mol% of monodentate phenylboronic acid derivatives as modulators in a microwave synthesis yielded COF-5 with an unprecedentedly high BET surface area of 2100 $m^2 g^{-1}$ and a remarkably high degree of crystallinity.[104] Both of these examples are based on the boronate ester linkage, but the modulation strategy is applicable to imine frameworks as well.[105]

2.2.2.2 Interlayer interactions. Studies have shown that the alternating stacking of electron-rich and electron-deficient aromatic systems can be exploited to improve stacking order in COFs. For instance, the synthesis of an imine COF using equimolar amounts of fluorinated and non-fluorinated terephthalic aldehyde gave rise to a highly crystalline framework with alternating electron-rich and electron-deficient layers.[106] The propensity of molecules with dipole moments to align in preferred orientations can be exploited as well. Pyrene-4,5-dione-based building blocks have large dipole moments and preferably assume an antiparallel alignment. This behaviour translates into a COF, with dione units alternatingly protruding from the edges into its pores in a zig-zag fashion. Following this approach, the authors obtained a highly crystalline material with a BET surface area of 1510 $m^2 g^{-1}$, which is almost twice that of the non-oxidized parent pyrene COF, indicating a more highly ordered system.[107]

While intralayer hydrogen bonding has been widely employed in COF synthesis to increase chemical stability, interlayer hydrogen bonding is still relatively unexplored. In a recent example, three amide groups on the sterically encumbered central phenyl ring of a tritopic building block are forced to twist out of plane, enabling the formation of N–H–O contacts between adjacent layers. The hydrogen-bonded COFs exhibit enhanced crystallinity, improved surface area, and increased chemical stability.[108] While the sterically induced twist in the presented system is likely to decrease the conjugation, it is conceivable that this strategy can be applied to different building blocks, preserving the conjugation while enhancing interlayer interactions as well.

Bein and coworkers introduced two concepts for the synthesis of highly crystalline imine frameworks. Both concepts rely on reducing strain within newly emerging layers and allowed the authors to obtain crystalline domains up to 500 nm in diameter.[109,110] Due to steric constraints, molecules such as triphenylamine assume propeller-shapes with their aromatic rings – the propeller blades – tilted in the same rotational direction. If one of these tilted units forms a π-conjugated linkage with another aromatic building block, the same rotational direction is induced in the newly connected unit. If two propeller-shaped molecules are connected *via* a C_2-symmetric unit, such as biphenyls, the same rotational direction is induced in both tectons. These self-repeating units serve as ''molecular docking sites'' for consecutive COF layers. Hence, all the tectons in newly emerging COF islands automatically assume the same rotational direction and are able to coalesce without mismatch, indepenent of their point of origin.[109] Since the peripheral phenyl rings in tetraphenylpyrene are able to rotate independently of each other, they can assume various conformations, *e.g.* ''propeller'' or ''armchair'' conformation. In order to minimize the layer offset and maximize π-stacking of the central pyrene cores between adjacent layers, all peripheral phenyl rings throughout a stack of pyrenes are compelled to face in the same direction (''armchair''). Condensation with rigid π-conjugated units, such as terephthaldehyde, causes the peripheral phenyl rings of all connected pyrene stacks to face in the same direction. This phenomenon was dubbed ''synchronized offset stacking''.[110]

2.2.3 Single crystals. In 2018 the first two instances of single crystals amenable to X-ray diffraction were published in the same issue in Science.[105,111] The two groups facilitated this by different means, however both strategies depended on slowing the COF particle growth. Where the group of Yaghi added a large excess of monodentate modulators (Fig. 5a),[105] the group of Dichtel utilized slow consecutive addition of monomers to preformed particle seeds, which favored the growth of pre-existing particles rather than seeding new crystals (Fig. 5b).[111] While one report focuses on three-dimensional imine COFs comprising tetraphenylmethane building blocks and elaborates on the various crystalline properties of the resulting single crystals,[105] the other report features two-dimensional boronate ester-based materials and highlights their improved superior electronic properties such as (out-of-plane) charge carrier mobility due to the reduced number of defects in the structures.[111]

While both of these reports did not yield a 2D-conjugated semiconductor, they are two of the most important milestones

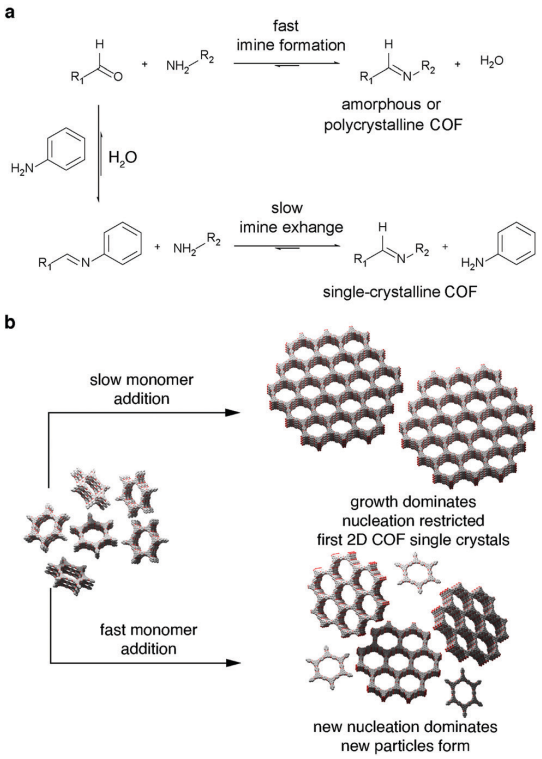

Fig. 5 Strategies to obtain single crystal COFs; (a) slow monomer addition to pre-formed particle seeds to favor seed growth over further nucleation;[111] (b) addition of monodentate modulator to slow growth process in order to avoid the formation of amorphous or polycrystalline phases.[105] Adapted with permission from AAAS.

in the development of the field and provide the necessary tools to produce conjugated, single-crystalline covalent organic frameworks. The application of the modulated imine synthesis approach is a viable route towards a 2D layered semiconductor.

2.2.4 Thin films. COFs are classically obtained as insoluble powders, which are challenging to interface with electrodes.[112] For successful device implementation, the generation of COFs with thin film morphology has to be achieved. Popular techniques to obtain thin films are (i) exfoliation, (ii) synthesis directly on substrate (Fig. 6, top), and (iii) synthesis at gas–liquid or liquid–liquid interfaces (Fig. 6, bottom). The thickness of surface- or interfacially grown films can be varied qualitatively as a function of reaction time and monomer concentrations. Obtaining uniformly thin films with predictable thickness, however, is challenging.[113–117]

2.2.4.1 Exfoliation. Exfoliation can afford sheets for the fabrication of electronic devices. Several exfoliation methods have been reported including sonication of powders in organic solvents,[85,118–122] mechanical exfoliation *via* grinding or ball-milling,[90,123–125] and chemical exfoliation techniques.[126] These methods can yield thicknesses down to the single-layer scale[120]

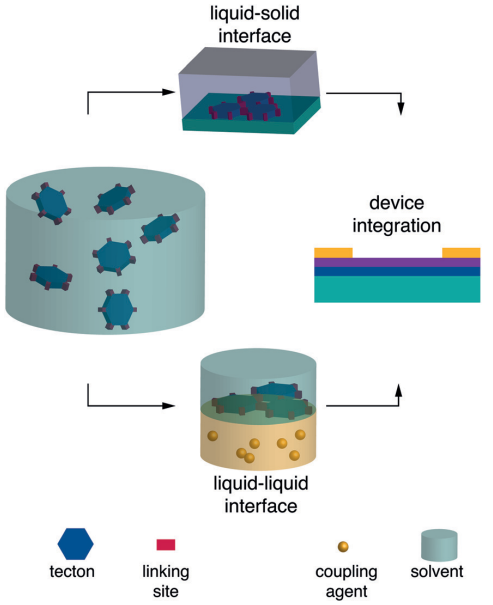

Fig. 6 Top, liquid–solid interfacial synthesis; bottom, liquid–liquid interfacial synthesis.

but typically only produce sheets up to several hundred nanometers in lateral size.

Other chemical[127–129] and charge-induced[130,131] exfoliation techniques have been reported but these methods are not generally applicable to other materials due to their dependence on specifically included functional groups.[127,128,130,131] Imine COFs display copious nitrogen lone pairs amenable to protonation and charge-induced exfoliation[132,133] but many frameworks are susceptible to amorphization at pH values sufficiently low to effect multiple protonation events.[132] The chemical and mechanical stability of recently reported olefine COFs are far superior to imine COFs, enabling exfoliation *via* grinding as well as sonication in pure sulfuric acid to yield continuous sheets of several micrometers.[90]

These reports make it evident that various exfoliation techniques are viable to obtain few-layer materials with lateral sizes of several hundred nanometers. For especially stable materials, exfoliation under harsh conditions can produce crystalline sheets of sufficient size for device integration.[90]

2.2.4.2 Solid–liquid interfaces. Surface-assisted COF syntheses have been carried out by immersion of substrates into reaction mixtures. In this manner, COF can be obtained as a film on the substrate, although the bulk of the product is still obtained as powder. Substrates for surface-assisted COF syntheses include graphene,[94,114,115,134–137] hexagonal boron nitride,[94,116,137] indium tin oxide,[138,139] platinum,[140] glass,[141] highly oriented pyrolytic graphite,[142,143] and molybdenum oxide.[144] It was shown that COFs can grow on various substrates independent of lattice parameters and symmetry.[134]

In most cases the formed COF layers are oriented in parallel to the substrate surface.[94,116,134,137–139,141,144] For conjugated materials, such as imine-linked COFs, a red-shifted UV-vis absorption edge has been observed as a result of the higher degree of conjugation in the oriented films compared to bulk powder.[116]

We have shown that copper surfaces can be used as a template and dual-role catalyst for the one-pot formation of triazine-based van der Waals heterostructures. The copper surface facilitates the cyclotrimerization of alkynes to an ordered film, which is merged with a 3D-amorphous graphdiyne phase whose formation is mediated by copper ions leached from the metal surface.[95]

The surface-assisted synthesis approach has already afforded several materials which were employed for the fabrication of OFET devices (Table 1).[94,115,116]

2.2.4.3 Liquid–liquid and gas–liquid interfaces. Liquid–liquid and gas–liquid interfaces are among the smoothest surfaces known[145] and lend themselves for monomer alignment prior to polymerization, facilitating growth in two dimensions along the interface. To perform a liquid–liquid interfacial polymerization, for example, the monomer(s) can be dissolved in one solvent and the coupling agent in a second, immiscible solvent, and the solutions carefully placed on top of each other. The interfacially grown film can then be transferred to any substrate for the fabrication of a device.

By using surfactants to support the interfacial synthesis of imine COF films, the authors obtained crystalline domains of 100–150 nm.[146] Following the same methodology, imide COF formation was accomplished at room temperature, which is far below conventional imidization temperatures above 100 °C. The crystalline phase was estimated to constitute approximately 60% of the obtained material and contained single-crystalline domains with average sizes of 3.5 μm^2.[117]

Mono- and multilayer porphyrin COF films were synthesized at air–water and liquid–liquid interfaces, respectively. The polycrystalline monolayer material was transferred to a SiO_2/Si substrate for the fabrication of an OFET.[147]

After layering an organic solution containing monomers and palladium catalyst on top of a basic aqueous solution, interfacial Suzuki-type polymerizations yielded films suitable for the fabrication of OFET devices as well.[99,100] The obtained charge carrier mobilities are among the highest values determined in a COF OFET setup.

Dichtel and coworkers were able to control the thickness of imine films obtained from Lewis acid-catalyzed liquid–liquid interfacial reactions. The resulting crystalline films ranged between 2.5 nm and 100 μm in an almost linear dependence on the initial monomer concentration.[148]

Choi and colleagues demonstrated precise control over the number of layers of imine COF films synthesized from an organic precursor solution spread on top of an aqueous phase. This was accomplished by adjusting the composition of the organic phase in order to keep the polarity on a level that precludes precipitation of the organic precursors at the interface between organic and aqueous layer. Film thicknesses between one and eight layers were obtained by varying the loading volume or concentration of the monomer solution. The lateral dimensions of the obtained films were limited by the reaction vessel, which in this case afforded wafer-size films with diameters of four inches.[149] This method was later modified for the synthesis of pyrazine-linked COF films.[82]

3. Organic thin-film transistor

One of the most common organic field effect transistor (OFET) architectures used to characterize the electronic properties and performance of organic semiconductors is the organic thin film transistor (OTFT). The OTFT is a device comprising three terminals, namely source, drain and gate (Fig. 7a). A thin film (20–200 nm) of an organic semiconductor, called the active layer, is either spincoated or evaporated by physical vapour deposition onto what is referred to as the "gate insulator" (typically silicon dioxide). The gate insulator electrically separates the "gate" (typically doped and conductive silicon) from the active layer as well as source and drain electrodes. COF films can either be grown from solution directly on a substrate; alternatively, a thin film can be transferred onto a substrate (see Chapter 2.2.4). For a top contact device the source and drain contacts are evaporated on top of the active layer. Bottom contact devices have the source and drain contacts prefabricated directly on the gate insulator, and the active layer is deposited on top.

Typically, organic semiconducting materials show similar electron and hole mobilities. However, the surface groups of commonly used gate insulator materials – such as silicon dioxide – negatively affect the electron conduction by trapping electrons.[150,151] Ambient water and oxygen have the same effect. For this reason, simple OTFT architectures are most often only used in p-type operation (*i.e.*, hole conduction).

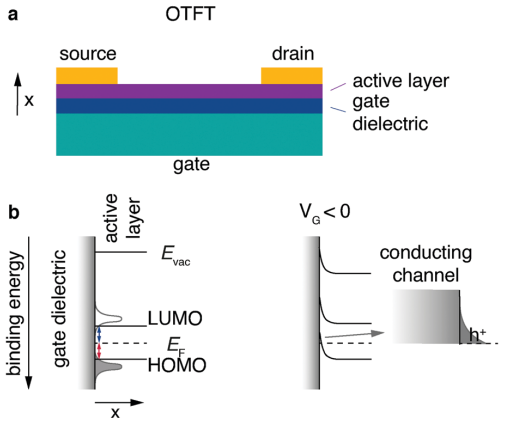

Fig. 7 Architecture and operation of OTFT. (a) Architecture of a top-contact OTFT. (b) Energy level alignment at active layer-insulator interface in off-state and with applied gate voltage in on-state (hole conduction). The arrow marks a magnified area.

To enable stable n-type conduction in an organic semiconductor under ambient conditions, the onset lowest unoccupied molecular orbital energy has to be more negative than −4 eV. To reach this threshold, electron-withdrawing groups or heteroatoms have to be introduced into the structure of the semiconductor.[152,153]

Charge transport in organic small molecules and conjugated one-dimensional polymers is predominantly hopping between adjacent π-orbitals, therefore it is expedient to think of the energy levels as a Gaussian-shaped distribution of localised highest occupied molecular orbital (HOMO) and lowest unoccupied molecular orbital (LUMO) states.[154] Even ''band like'' transport characteristics in small molecule single crystals cannot be equated with band transport in inorganic materials.[155] The energy level alignment of a typical OTFT architecture without applied voltage is depicted (Fig. 7b, left). To simplify the concept, the onsets of the LUMO and HOMO are denoted as lines.

An ideal semiconducting organic material has close to no charge carriers at room temperature, and typically injection barriers are present between the organic active layer and the metal contacts (Fermi level pinning).[154] Hole and electron injection barriers (Fig. 7, red and blue lines, respectively) are the energetic differences between the Fermi level and the onsets of HOMO and LUMO, respectively.

For an applied voltage between drain and source (V_{DS}) the corresponding current (I_{DS}) is therefore low; this is called the ''off-state''. To switch to the ''on-state'', negative gate voltage (V_G) is applied between source and gate electrode resulting in an electric field arising between gate and active layer. The electric field and therefore the field effect can be maximised by decreasing the gate insulator thickness with a 2D insulator, for example with hBN or by using a high-k dielectric. A 2D example is using highly crystalline hBN to increase the performance of 2D transistors by providing a trap-free, thin dielectric.[156] Its main task is, however, to inhibit current flow between gate and active layer and the result is what can be thought of as a capacitor. Positive charge carriers start to accumulate in the active material at the insulator interface (Fig. 7b, right). This local positive ''charging'' of the active material induces a reduction of the local Fermi level of the active layer at the insulator interface, resulting in an alignment of the transport states (HOMO) of the active layer and the electrode Fermi level. The now established energy level alignment constitutes a conductive channel for holes which can be injected from the source electrode. The described effect is synonymous to the ''field effect'' in organic materials and ''switches'' the previously non-conductive active material into a conducting channel for holes. For an applied voltage V_{DS} the corresponding current I_{DS} should be increased by orders of magnitudes compared to the off-state. Due to the necessary accumulation of charges at the interface between insulator and active layer, this mode of operation is known as ''accumulation'' or ''enhancement''.[157] An electron conduction mode can be established if the device architecture (no Si–OH/active layer interface) and the material (no charge traps for electrons) allow it. Transistors that function in electron as well as hole conduction mode are called ambipolar. The extraction of the field-effect mobility from the obtained I–V curves (output characteristics and transfer curves) is discussed in great detail elsewhere.[158]

Replacing the active layer of a field effect transistor with a 2D crystal has two major advantages. 3D materials like silicon stripped down to less than 3 nm thickness are strongly affected by dangling bonds. The dangling bonds constitute scattering sites which decrease the mobility of the material at these small dimensions. 2D crystals on the other hand are atomically thin without dangling bonds, therefore the problem is non-existent for this material class. The second merit of 2D crystals is their electrostatics. In short-channel field effect transistors with 3D active layers current leakage is typically induced due to poorly controllable electrostatics between electrons in the channel and the electric field applied by the gate. Whereas the channel in 3D active layers has a physical extension, in 2D crystals all carriers are confined to the atomically thin channel and the electric field can take effect more evenly. The superior gate coupling also allows to suppress current leakage if a gate voltage is applied. The culmination of these attributes could yield new low-power, highly miniaturizable device architectures like organic thin-tunneling FETs.[16] However, processing of organic layered materials into defect-free organic 2D crystals is still in its infancy. Also, some of the materials showing high crystallinity are not fully conjugated. Employing such a material with higher interplane transport than in-plane transport can, however, still be achieved by using an alternative device architecture, the vertical field-effect transistor (VOFET).

3.1 Graphene-vertical organic field effect transistor (GR-VOFET)

The standard OFET architecture holds two main challenges for covalent organic solids. The first challenge is the processing of covalent organic solids into thin films for electronic device applications (see Chapter 2.2.4). The second challenge is the property of anisotropic transport. Conjugated 2D materials have different intralayer and interlayer transport properties. For instance, for TGCN it was reported that interlayer transport hopping through the stacked layers is energetically favoured compared to intralayer transport.[69] Returning with this knowledge to the OTFT architecture, to have the maximum possible mobility the layers need to be oriented orthogonally to the source–drain axis. For standard OTFT architectures (top/bottom contact), reaching this orientation is not trivial.

For materials exhibiting low intraplane mobility, an intriguing way to solve both of these challenges is to directly grow the crystalline material onto the graphene layer of a graphene-vertical field effect transistor (GR-VOFET, Fig. 8a). In this case the active layer is sandwiched between source and drain electrodes, the source electrode being graphene. To allow efficient hole injection into the active layer, the injection barriers between the graphene source electrode and COF layer have to be minimized (Fig. 8, injection barriers depicted in red (holes) and blue (electrons)). With no gate bias applied, the

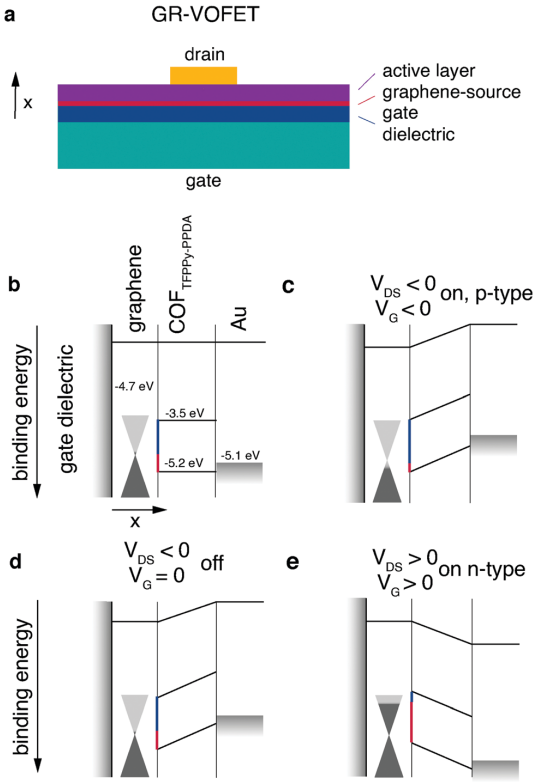

Fig. 8 The first reported COF-GR-VOFET and its modes of operation. (a) Architecture of GR-VOFET, (b) schematic device overview, (c) hole accumulation mode, (d) without gate voltage applied, (e) electron accumulation mode. Adapted with permission from Sun *et al.*, copyright 2021 American Chemical Society.[115]

injection barrier between the source electrode and the active material is high (Fig. 8d). Upon applying a negative gate bias the local work function of graphene is increased (Fig. 8c). This is possible due to graphene's low density of states at the Fermi level as indicated by the cones touching at the tips. The increase in work function results in a decreased injection barrier to the HOMO level of the active layer. Injection of holes into the active layer is possible and the vertical source–drain channel becomes conductive, resulting in a high I_{DS} (Fig. 8c). Switching the gate voltage off leads to an increased hole injection barrier again (Fig. 8d). The application of a positive gate voltage results in a decrease of the work function of graphene and electron injection becomes possible (Fig. 8e). Additional benefits of this architecture are high on-current densities enabled by short channel lengths, ambipolar transport, and high on/off ratios.

The first publication presenting a COF GR-VOFET reported a current density up to 6.8 A cm^{-2} for p-type transport with a channel length of 50 nm and high on/off ratios up to 10^5. For this device both electron and hole-accumulation mode are possible, hence it is an ambipolar transistor. The threshold voltage for the electron accumulation mode was determined to be much higher than that for hole injection. This may be due to the comparatively high electron injection barrier of 1.2 eV that has to be overcome, whereas the hole injection barrier is only 0.5 eV.[115] While the GR-VOFET does not resolve all issues, this study showed the potential of COF materials if applied in device architectures suitable to their properties. The challenges of anisotropic charge transport, low conductivity and insolubility were resolved by a smart choice of device architecture to obtain a functional OFET device. Nevertheless, we would like to point out that the goal – a 2D organic semiconductor – can only be achieved by maximised intralayer charge transport.

4. Conclusion and outlook

The overarching challenge in the synthesis of layered organic materials for electronic devices is to obtain materials of the utmost purity. A similar challenge arose in the early days of semiconducting polymers where catalyst residues proved to be detrimental to device performance. This problem was largely solved by excessive postsynthetic purification of the active materials, which is not an option for covalent layered materials. Unreacted end groups cannot be removed postsynthetically and constitute structural defects deteriorating the energetic order of the materials. The goal of synthetic approaches aiming for "electronic-grade" organic semiconductors is to directly obtain the covalent scaffolds with as few structural and energetic defects as possible. For different synthetic approaches different ways of achieving "electronic-grade" purity are viable.

To obtain highly condensed, layered carbon nitride structures, ionothermal reactions yield the most crystalline and most nitrogen-rich phases to this point. The best-characterised crystalline graphitic carbon nitride material today is PTI-MX. To unlock the full potential of this material, it is now crucial to determine how to enrich and process it. Once crystalline thin films of PTI-MX can be produced reliably, the energy levels of pristine and doped species can be investigated and electrical prototype devices constructed. Due to the intercalated salt and low condensation degree the charge carrier mobility of PTI-MX is not expected to be high, but the polar point group indicates that PTI could be a piezoelectric material as observed in other carbon nitride phases.[159] To study this property, crystalline clean surfaces of PTI have to be produced. The structure of TGCN is not researched to the same extent as the structure of PTI-MX since only nanoscale crystallites have been obtained that are accompanied by amorphous CN phases. Further complementary analysis investigating the crystal structure, elemental composition and vibrational spectra of singular crystallites are key to a better understanding of the first crystalline graphitic C_3N_4 material, TGCN. Theoretically predicted polymorphs such as heptazine based graphitic carbon nitride, fullerene-like as well as tube-like morphologies still have to be discovered experimentally.

Highly crystalline conjugated organic frameworks with crystalline domain sizes on the micron scale and low amounts

of defects have been prepared *via* synthetic strategies that exploit universal monomer properties such as geometry, symmetry, and electron density. COF thin films can be obtained *via* exfoliation or synthesis at various interfaces, and first examples of their application in OFET devices have been presented. Despite this progress, the highest charge carrier mobility of 6.25 $cm^2\ V^{-1}\ s^{-1}$ reported for an OFET with graphdiyne as the active layer falls dramatically short of the predicted mobility of 10 000 $cm^2\ V^{-1}\ s^{-1}$. Generally, the highest charge carrier mobility values as determined in OFET devices are obtained for thin films with carbon–carbon linkages (Table 1). This indicates the superiority of pure carbon–carbon backbones over strongly polarized bonds such as imine linkages despite the superior materials being the products of irreversible coupling reactions and the associated defects.

Organic electronics is an interdisciplinary field requiring expertise from organic synthesis (monomers) to polymer chemistry (covalent layered materials), theory (structural and electronic order), and device fabrication. To facilitate the communication between specialists from different fields, the modes of operation of a standard OFET architecture as well as the recently introduced COF graphene-vertical OFET (GR-VOFET) architecture were elucidated. The latter illustrates how a comprehensive understanding of all aspects involved enables elegant architecture design to exploit material-specific strengths, which is high out-of-plane charge carrier transport in the case at hand.

We hope that this review gives a good perspective on metal-free, layered semiconducting materials for 2D organic devices to facilitate the entry of motivated researchers into this exciting field.

Author contributions

DB and MGT wrote the paper and contributed equally to this work. MJB conceived the project and co-wrote the paper.

Conflicts of interest

There are no conflicts to declare.

Acknowledgements

The authors thank Steffen Rühl, Dr Andreas Opitz and Prof. Dr Emil List-Kratochvil for fruitful discussions. M. J. B. thanks the European Research Council (ERC) for funding under the Starting Grant scheme (BEGMAT-678462) and the Proof of Concept scheme (LiAnMat-957534).

References

1 B. Gopalakrishnan, Y. Mardikar and D. Korakakis, *Energy Eng.*, 2010, **107**, 6–40.
2 S. Chen, A. Gautam and F. Weig, *Bringing energy efficiency to the fab*, 2013.
3 C. Liu, H. Chen, S. Wang, Q. Liu, Y.-G. Jiang, D. W. Zhang, M. Liu and P. Zhou, *Nat. Nanotechnol.*, 2020, **15**, 545–557.
4 R. K. Cavin, P. Lugli and V. V. Zhirnov, *Proc. IEEE*, 2012, **100**, 1720–1749.
5 J. Shalf, *Philos. Trans. R. Soc. A Math. Phys. Eng. Sci.*, 2020, **378**, 20190061.
6 M. Y. Han, B. Özyilmaz, Y. Zhang and P. Kim, *Phys. Rev. Lett.*, 2007, **98**, 1–4.
7 S. E. Root, S. Savagatrup, A. D. Printz, D. Rodriquez and D. J. Lipomi, *Chem. Rev.*, 2017, **117**, 6467–6499.
8 J. Borges-González, C. J. Kousseff and C. B. Nielsen, *J. Mater. Chem. C*, 2019, **7**, 1111–1130.
9 J. Li, C. W. Rochester, I. E. Jacobs, S. Friedrich, P. Stroeve, M. Riede and A. J. Moulé, *ACS Appl. Mater. Interfaces*, 2015, **7**, 28420–28428.
10 R. Di Pietro, D. Fazzi, T. B. Kehoe and H. Sirringhaus, *J. Am. Chem. Soc.*, 2012, **134**, 14877–14889.
11 U. Scherf and E. J. W. List, *Adv. Mater.*, 2002, **14**, 477–487.
12 J. N. Haddock, X. Zhang, S. Zheng, Q. Zhang, S. R. Marder and B. Kippelen, *Org. Electron.*, 2006, **7**, 45–54.
13 M. S. Lohse and T. Bein, *Adv. Funct. Mater.*, 2018, **28**, 1705553.
14 A. P. Cote, A. I. Benin, N. W. Ockwig, M. O'Keeffe, A. J. Matzger and O. M. Yaghi, *Science*, 2005, **310**, 1166–1170.
15 M. Long, L. Tang, D. Wang, Y. Li and Z. Shuai, *ACS Nano*, 2011, **5**, 2593–2600.
16 M. Chhowalla, D. Jena and H. Zhang, *Nat. Rev. Mater.*, 2016, **1**, 16052.
17 S. Yang, W. Li, C. Ye, G. Wang, H. Tian, C. Zhu, P. He, G. Ding, X. Xie, Y. Liu, Y. Lifshitz, S.-T. Lee, Z. Kang and M. Jiang, *Adv. Mater.*, 2017, **29**, 1605625.
18 G. Algara-Siller, N. Severin, S. Y. Chong, T. Björkman, R. G. Palgrave, A. Laybourn, M. Antonietti, Y. Z. Khimyak, A. V. Krasheninnikov, J. P. Rabe, U. Kaiser, A. I. Cooper, A. Thomas and M. J. Bojdys, *Angew. Chem., Int. Ed.*, 2014, **53**, 7450–7455.
19 T. Minari, P. Darmawan, C. Liu, Y. Li, Y. Xu and K. Tsukagoshi, *Appl. Phys. Lett.*, 2012, **100**, 093303.
20 D. Burmeister, L. Ahrens, A. Opitz, G. Ligorio, F. Hermerschmidt, D. Jänsch, J. Freudenberg, U. H. F. Bunz, K. Müllen and E. J. W. List-Kratochvil, *J. Mater. Chem. C*, 2020, **8**, 3302–3307.
21 H. Sirringhaus, *Adv. Mater.*, 2005, **17**, 2411–2425.
22 A. K. Geim and I. V. Grigorieva, *Nature*, 2013, **499**, 419–425.
23 M. Pumera and Z. Sofer, *Chem. Soc. Rev.*, 2017, **46**, 4450–4463.
24 I. V. Antonova, I. A. Kotin, O. M. Orlov and S. F. Devyatova, *Tech. Phys. Lett.*, 2017, **43**, 889–892.
25 K. P. Chang, K. I. Ho, M. Boutchich, J. Chaste, H. Arezki and C. S. Lai, *Semicond. Sci. Technol.*, 2020, **35**, 015005.
26 M. Wall, *The Raman Spectroscopy of Graphene and the Determination of Layer Thickness*, 2011.
27 H. Li, T. Duan, S. Haldar, B. Sanyal, O. Eriksson, H. Jafri, S. Hajjar-Garreau, L. Simon and K. Leifer, *Appl. Phys. Rev.*, 2020, **7**, 011403.

28 L. Ye, S. P. Pujari, H. Zuilhof, T. Kudernac, M. P. de Jong, W. G. van der Wiel and J. Huskens, *ACS Appl. Mater. Interfaces*, 2015, **7**, 3231–3236.
29 J. C. Ho, R. Yerushalmi, Z. A. Jacobson, Z. Fan, R. L. Alley and A. Javey, *Nat. Mater.*, 2008, **7**, 62–67.
30 J. C. Ho, R. Yerushalmi, G. Smith, P. Majhi, J. Bennett, J. Halim, V. N. Faifer and A. Javey, *Nano Lett.*, 2009, **9**, 725–730.
31 N. Kennedy, R. Duffy, L. Eaton, D. O'Connell, S. Monaghan, S. Garvey, J. Connolly, C. Hatem, J. D. Holmes and B. Long, *Beilstein J. Nanotechnol.*, 2018, **9**, 2106–2113.
32 H. Lee, K. Paeng and I. S. Kim, *Synth. Met.*, 2018, **244**, 36–47.
33 T. Wu, H. Shen, L. Sun, B. Cheng, B. Liu and J. Shen, *New J. Chem.*, 2012, **36**, 1385.
34 M. Dragoman, A. Dinescu and D. Dragoman, *Nanotechnology*, 2017, **28**, 015201.
35 B. S. Jessen, L. Gammelgaard, M. R. Thomsen, D. M. A. Mackenzie, J. D. Thomsen, J. M. Caridad, E. Duegaard, K. Watanabe, T. Taniguchi, T. J. Booth, T. G. Pedersen, A.-P. Jauho and P. Bøggild, *Nat. Nanotechnol.*, 2019, **14**, 340–346.
36 A. T. Dideikin and A. Y. Vul', *Front. Phys.*, 2019, **6**, 149.
37 J. D. Caldwell, I. Aharonovich, G. Cassabois, J. H. Edgar, B. Gil and D. N. Basov, *Nat. Rev. Mater.*, 2019, **4**, 552–567.
38 J. da Rocha Martins and H. Chacham, *ACS Nano*, 2011, **5**, 385–393.
39 J. Lu, K. Zhang, X. Feng Liu, H. Zhang, T. Chien Sum, A. H. Castro Neto and K. P. Loh, *Nat. Commun.*, 2013, **4**, 2681.
40 J. Wang, C. Chen, C. Yang, Y. Fan, D. Liu and W. Lei, *Curr. Graphene Sci.*, 2018, **2**, 3–14.
41 W. Lei, D. Portehault, R. Dimova and M. Antonietti, *J. Am. Chem. Soc.*, 2011, **133**, 7121–7127.
42 J. Kouvetakis, R. B. Kaner, M. L. Sattler and N. Bartlett, *J. Chem. Soc., Chem. Commun.*, 1986, 1758–1759.
43 O. O. Kurakevych, T. Chauveau and V. L. Solozhenko, *J. Superhard Mater.*, 2010, **32**, 231–235.
44 D. Tomanek, R. M. Wentzcovitch, S. G. Louie and M. L. Cohen, *Phys. Rev. B: Condens. Matter Mater. Phys.*, 1988, **37**, 3134–3136.
45 Q. Hu, Q. Wu, Y. Ma, L. Zhang, Z. Liu, J. He, H. Sun, H. T. Wang and Y. Tian, *Phys. Rev. B: Condens. Matter Mater. Phys.*, 2006, **73**, 214116.
46 X. Wu, Y. Pei and X. C. Zeng, *Nano Lett.*, 2009, **9**, 1577–1582.
47 K. Y. Xie, V. Domnich, L. Farbaniec, B. Chen, K. Kuwelkar, L. Ma, J. W. McCauley, R. A. Haber, K. T. Ramesh, M. Chen and K. J. Hemker, *Acta Mater.*, 2017, **136**, 202–214.
48 X. Tian, X. Xuan, M. Yu, Y. Mu, H.-G. Lu, Z. Zhang and S.-D. Li, *Nanoscale*, 2019, **11**, 11099–11106.
49 N. Hellgren, N. Lin, E. Broitman, V. Serin, S. E. Grillo, R. Twesten, I. Petrov, C. Colliex, L. Hultman and J.-E. Sundgren, *J. Mater. Res.*, 2001, **16**, 3188–3201.
50 J. H. Zhan, Z. D. Zhang, X. F. Qian, C. Wang, Y. Xie and Y. T. Qian, *J. Solid State Chem.*, 1998, **141**, 270–273.
51 Q. Guo, Y. Xie, X. Wang, S. Zhang, T. Hou and S. Lv, *Chem. Commun.*, 2004, 26.
52 H. Montigaud, S. Courjault, B. Tanguy, G. Demazeau, J. Peyronneau, D. Andrault, M. Jaouen and G. Hug, *High Pressure Res.*, 2000, **18**, 213–219.
53 E. Horvath-Bordon, R. Riedel, P. F. McMillan, P. Kroll, G. Miehe, P. A. van Aken, A. Zerr, P. Hoppe, O. Shebanova, I. McLaren, S. Lauterbach, E. Kroke and R. Boehler, *Angew. Chem., Int. Ed.*, 2007, **46**, 1476–1480.
54 C. J. Pickard, A. Salamat, M. J. Bojdys, R. J. Needs and P. F. McMillan, *Phys. Rev. B*, 2016, **94**, 094104.
55 M. J. Bojdys, J.-O. Müller, M. Antonietti and A. Thomas, *Chem. – Eur. J.*, 2008, **14**, 8177–8182.
56 E. Wirnhier, M. Döblinger, D. Gunzelmann, J. Senker, B. V. Lotsch and W. Schnick, *Chem. – Eur. J.*, 2011, **17**, 3213–3221.
57 S. Y. Chong, J. T. A. Jones, Y. Z. Khimyak, A. I. Cooper, A. Thomas, M. Antonietti and M. J. Bojdys, *J. Mater. Chem. A*, 2013, 1102–1107.
58 X. Lu, H. Wang, Y. Yang and T. Liu, *J. Mater. Sci. Technol.*, 2011, **27**, 245–251.
59 F. K. Kessler and W. Schnick, *Z. Anorg. Allg. Chem.*, 2019, **645**, 857–862.
60 G. Liao, Y. Gong, L. Zhang, H. Gao, G.-J. Yang and B. Fang, *Energy Environ. Sci.*, 2019, **12**, 2080.
61 T. Suter, V. Brázdová, K. McColl, T. S. Miller, H. Nagashima, E. Salvadori, A. Sella, C. A. Howard, C. W. M. Kay, F. Corà and P. F. McMillan, *J. Phys. Chem. C*, 2018, **122**, 25183–25194.
62 L. F. Villalobos, M. T. Vahdat, M. Dakhchoune, Z. Nadizadeh, M. Mensi, E. Oveisi, D. Campi, N. Marzari and K. V. Agrawal, *Sci. Adv.*, 2020, **6**, 1–9.
63 M. B. Mesch, K. Bärwinkel, Y. Krysiak, C. Martineau, F. Taulelle, R. B. Neder, U. Kolb and J. Senker, *Chem. – Eur. J.*, 2016, **22**, 16878–16890.
64 E. J. McDermott, E. Wirnhier, W. Schnick, K. S. Virdi, C. Scheu, Y. Kauffmann, W. D. Kaplan, E. Z. Kurmaev and A. Moewes, *J. Phys. Chem. C*, 2013, **117**, 8806–8812.
65 A. I. Cooper and M. J. Bojdys, *Mater. Today*, 2014, **17**, 468–469.
66 M. J. Bojdys, *Macromol. Chem. Phys.*, 2016, **217**, 232–241.
67 H. May, *J. Appl. Chem.*, 2007, **9**, 340–344.
68 S. N. Steinmann, S. T. A. G. Melissen, T. Le Bahers and P. Sautet, *J. Mater. Chem. A*, 2017, **5**, 5115–5122.
69 Y. Noda, C. Merschjann, J. Tarábek, P. Amsalem, N. Koch and M. J. Bojdys, *Angew. Chem., Int. Ed.*, 2019, **58**, 9394–9398.
70 F. Shojaei and H. S. Kang, *RSC Adv.*, 2015, **5**, 10892–10898.
71 T. S. Miller, A. B. Jorge, T. M. Suter, A. Sella, F. Corà and P. F. McMillan, *Phys. Chem. Chem. Phys.*, 2017, **19**, 15613–15638.
72 M. Ruan, Y. Hu, Z. Guo, R. Dong, J. Palmer, J. Hankinson, C. Berger and W. A. de Heer, *MRS Bull.*, 2012, **37**, 1138–1147.
73 F. J. Uribe-Romo, J. R. Hunt, H. Furukawa, C. Klöck, M. O'Keeffe and O. M. Yaghi, *J. Am. Chem. Soc.*, 2009, **131**, 4570–4571.

74 S. Kandambeth, D. B. Shinde, M. K. Panda, B. Lukose, T. Heine and R. Banerjee, *Angew. Chem., Int. Ed.*, 2013, **52**, 13052–13056.
75 S. Kandambeth, A. Mallick, B. Lukose, M. V. Mane, T. Heine and R. Banerjee, *J. Am. Chem. Soc.*, 2012, **134**, 19524–19527.
76 S. Karak, S. Kumar, P. Pachfule and R. Banerjee, *J. Am. Chem. Soc.*, 2018, **140**, 5138–5145.
77 M. C. Daugherty, E. Vitaku, R. L. Li, A. M. Evans, A. D. Chavez and W. R. Dichtel, *Chem. Commun.*, 2019, **55**, 2680–2683.
78 R. Kulkarni, Y. Noda, D. Kumar Barange, Y. S. Kochergin, P. Lyu, B. Balcarova, P. Nachtigall and M. J. Bojdys, *Nat. Commun.*, 2019, **10**, 3228.
79 J. Guo, Y. Xu, S. Jin, L. Chen, T. Kaji, Y. Honsho, M. A. Addicoat, J. Kim, A. Saeki, H. Ihee, S. Seki, S. Irle, M. Hiramoto, J. Gao and D. Jiang, *Nat. Commun.*, 2013, **4**, 2736.
80 M. M. Wang, M. Ballabio, M. M. Wang, H. Lin, B. P. Biswal, X. Han, S. Paasch, E. Brunner, P. Liu, M. Chen, M. Bonn, T. Heine, S. Zhou, E. Cánovas, R. Dong and X. Feng, *J. Am. Chem. Soc.*, 2019, **141**, 16810–16816.
81 Z. Meng, R. M. Stolz and K. A. Mirica, *J. Am. Chem. Soc.*, 2019, **141**, 11929–11937.
82 S. Kim and H. C. Choi, *Commun. Chem.*, 2019, **2**, 60.
83 X. Zhuang, W. Zhao, F. Zhang, Y. Cao, F. Liu, S. Bi and X. Feng, *Polym. Chem.*, 2016, **7**, 4176–4181.
84 E. Jin, M. Asada, Q. Xu, S. Dalapati, M. A. Addicoat, M. A. Brady, H. Xu, T. Nakamura, T. Heine, Q. Chen and D. Jiang, *Science*, 2017, **357**, 673–676.
85 E. Jin, J. Li, K. Geng, Q. Jiang, H. Xu, Q. Xu and D. Jiang, *Nat. Commun.*, 2018, **9**, 4143.
86 H. Lyu, C. S. Diercks, C. Zhu and O. M. Yaghi, *J. Am. Chem. Soc.*, 2019, **141**, 6848–6852.
87 A. Acharjya, P. Pachfule, J. Roeser, F. Schmitt and A. Thomas, *Angew. Chem., Int. Ed.*, 2019, **58**, 14865–14870.
88 S. Wei, F. Zhang, W. Zhang, P. Qiang, K. Yu, X. Fu, D. Wu, S. Bi and F. Zhang, *J. Am. Chem. Soc.*, 2019, **141**, 14272–14279.
89 J. Xu, Y. He, S. Bi, M. Wang, P. Yang, D. Wu, J. Wang and F. Zhang, *Angew. Chem., Int. Ed.*, 2019, **58**, 12065–12069.
90 T. Jadhav, Y. Fang, C.-H. Liu, A. Dadvand, E. Hamzehpoor, W. Patterson, A. Jonderian, R. S. Stein and D. F. Perepichka, *J. Am. Chem. Soc.*, 2020, **142**, 8862–8870.
91 A. Acharjya, L. Longworth-Dunbar, J. Roeser, P. Pachfule and A. Thomas, *J. Am. Chem. Soc.*, 2020, **142**, 14033–14038.
92 G. Ligorio, G. F. Cotella, A. Bonasera, N. Zorn Morales, G. Carnicella, B. Kobin, Q. Wang, N. Koch, S. Hecht, E. J. W. List-Kratochvil and F. Cacialli, *Nanoscale*, 2020, **12**, 5444–5451.
93 M. Trunk, A. Herrmann, H. Bildirir, A. Yassin, J. Schmidt and A. Thomas, *Chem. – Eur. J.*, 2016, **22**, 7179–7183.
94 J. Zhou, Z. Xie, R. Liu, X. Gao, J. Li, Y. Xiong, L. Tong, J. Zhang and Z. Liu, *ACS Appl. Mater. Interfaces*, 2019, **11**, 2632–2637.
95 D. Schwarz, Y. Noda, J. Klouda, K. Schwarzová-Pecková, J. Tarábek, J. Rybáček, J. Janoušek, F. Simon, M. V. Opanasenko, J. Čejka, A. Acharjya, J. Schmidt, S. Selve, V. Reiter-Scherer, N. Severin, J. P. Rabe, P. Ecorchard, J. He, M. Polozij, P. Nachtigall and M. J. Bojdys, *Adv. Mater.*, 2017, **29**, 1703399.
96 G. Luo, Q. Zheng, W.-N. Mei, J. Lu and S. Nagase, *J. Phys. Chem. C*, 2013, **117**, 13072–13079.
97 Y. Pan, Y. Wang, L. Wang, H. Zhong, R. Quhe, Z. Ni, M. Ye, W.-N. Mei, J. Shi, W. Guo, J. Yang and J. Lu, *Nanoscale*, 2015, **7**, 2116–2127.
98 D. Schwarz, A. Acharjya, A. Ichangi, Y. S. Kochergin, P. Lyu, M. V. Opanasenko, J. Tarábek, J. Vacek Chocholoušová, J. Vacek, J. Schmidt, J. Čejka, P. Nachtigall, A. Thomas and M. J. Bojdys, *ChemSusChem*, 2019, **12**, 194–199.
99 D. Zhou, X. Tan, H. Wu, L. Tian and M. Li, *Angew. Chem., Int. Ed.*, 2019, **58**, 1376–1381.
100 C. Li, Y. Wang, Y. Zou, X. Zhang, H. Dong and W. Hu, *Angew. Chem.*, 2020, **132**, 9489–9493.
101 C. H. Feriante, S. Jhulki, A. M. Evans, R. R. Dasari, K. Slicker, W. R. Dichtel and S. R. Marder, *Adv. Mater.*, 2020, **32**, 1–5.
102 D. Zhu and R. Verduzco, *ACS Appl. Mater. Interfaces*, 2020, **12**, 33121–33127.
103 B. J. Smith and W. R. Dichtel, *J. Am. Chem. Soc.*, 2014, **136**, 8783–8789.
104 M. Calik, T. Sick, M. Dogru, M. Döblinger, S. Datz, H. Budde, A. Hartschuh, F. Auras and T. Bein, *J. Am. Chem. Soc.*, 2016, **138**, 1234–1239.
105 T. Ma, E. A. Kapustin, S. X. Yin, L. Liang, Z. Zhou, J. Niu, L.-H. Li, Y. Wang, J. Su, J. Li, X. Wang, W. D. Wang, W. Wang, J. Sun and O. M. Yaghi, *Science*, 2018, **361**, 48–52.
106 X. Chen, M. Addicoat, S. Irle, A. Nagai and D. Jiang, *J. Am. Chem. Soc.*, 2013, **135**, 546–549.
107 L. M. Salonen, D. D. Medina, E. Carbó-Argibay, M. G. Goesten, L. Mafra, N. Guldris, J. M. Rotter, D. G. Stroppa and C. Rodríguez-Abreu, *Chem. Commun.*, 2016, **52**, 7986–7989.
108 S. B. Alahakoon, K. Tan, H. Pandey, S. D. Diwakara, G. T. McCandless, D. I. Grinffiel, A. Durand-Silva, T. Thonhauser and R. A. Smaldone, *J. Am. Chem. Soc.*, 2020, 0c03409.
109 L. Ascherl, T. Sick, J. T. Margraf, S. H. Lapidus, M. Calik, C. Hettstedt, K. Karaghiosoff, M. Döblinger, T. Clark, K. W. Chapman, F. Auras and T. Bein, *Nat. Chem.*, 2016, **8**, 310–316.
110 F. Auras, L. Ascherl, A. H. Hakimioun, J. T. Margraf, F. C. Hanusch, S. Reuter, D. Bessinger, M. Döblinger, C. Hettstedt, K. Karaghiosoff, S. Herbert, P. Knochel, T. Clark and T. Bein, *J. Am. Chem. Soc.*, 2016, **138**, 16703–16710.
111 A. M. Evans, L. R. Parent, N. C. Flanders, R. P. Bisbey, E. Vitaku, M. S. Kirschner, R. D. Schaller, L. X. Chen, N. C. Gianneschi and W. R. Dichtel, *Science*, 2018, **361**, 52–57.
112 D. D. Medina, T. Sick and T. Bein, *Adv. Energy Mater.*, 2017, **7**, 1700387.
113 J. I. Feldblyum, C. H. McCreery, S. C. Andrews, T. Kurosawa, E. J. G. Santos, V. Duong, L. Fang,

A. L. Ayzner and Z. Bao, *Chem. Commun.*, 2015, **51**, 13894–13897.
114 J. W. Colson, J. A. Mann, C. R. DeBlase and W. R. Dichtel, *J. Polym. Sci., Part A: Polym. Chem.*, 2015, **53**, 378–384.
115 B. Sun, C.-H. Zhu, Y. Liu, C. Wang, L.-J. Wan and D. Wang, *Chem. Mater.*, 2017, **29**, 4367–4374.
116 B. Sun, J. Li, W.-L. Dong, M.-L. Wu and D. Wang, *J. Phys. Chem. C*, 2016, **120**, 14706–14711.
117 K. Liu, H. Qi, R. Dong, R. Shivhare, M. A. Addicoat, T. Zhang, H. Sahabudeen, T. Heine, S. Mannsfeld, U. Kaiser, Z. Zheng and X. Feng, *Nat. Chem.*, 2019, **11**, 994–1000.
118 G. Li, K. Zhang and T. Tsuru, *ACS Appl. Mater. Interfaces*, 2017, **9**, 8433–8436.
119 Y. Peng, Y. Huang, Y. Zhu, B. Chen, L. Wang, Z. Lai, Z. Zhang, M. Zhao, C. Tan, N. Yang, F. Shao, Y. Han and H. Zhang, *J. Am. Chem. Soc.*, 2017, **139**, 8698–8704.
120 D. N. Bunck and W. R. Dichtel, *J. Am. Chem. Soc.*, 2013, **135**, 14952–14955.
121 M. R. Rao, Y. Fang, S. De Feyter and D. F. Perepichka, *J. Am. Chem. Soc.*, 2017, **139**, 2421–2427.
122 M. Heyl, D. Burmeister, T. Schultz, S. Pallasch, G. Ligorio, N. Koch and E. J. W. List-Kratochvil, *Phys. Status Solidi*, 2020, **14**, 2000408.
123 S. Chandra, S. Kandambeth, B. P. Biswal, B. Lukose, S. M. Kunjir, M. Chaudhary, R. Babarao, T. Heine and R. Banerjee, *J. Am. Chem. Soc.*, 2013, **135**, 17853–17861.
124 S. Wang, Q. Wang, P. Shao, Y. Han, X. Gao, L. Ma, S. Yuan, X. Ma, J. Zhou, X. Feng and B. Wang, *J. Am. Chem. Soc.*, 2017, **139**, 4258–4261.
125 Z. Wang, Y. Li, P. Liu, Q. Qi, F. Zhang, G. Lu, X. Zhao and X. Huang, *Nanoscale*, 2019, **11**, 5330–5335.
126 M. J. Bojdys, N. Severin, J. P. Rabe, A. I. Cooper, A. Thomas and M. Antonietti, *Macromol. Rapid Commun.*, 2013, **34**, 850–854.
127 M. A. Khayum, S. Kandambeth, S. Mitra, S. B. Nair, A. Das, S. S. Nagane, R. Mukherjee and R. Banerjee, *Angew. Chem., Int. Ed.*, 2016, **55**, 15604–15608.
128 S. Mitra, H. S. Sasmal, T. Kundu, S. Kandambeth, K. Illath, D. Díaz Díaz and R. Banerjee, *J. Am. Chem. Soc.*, 2017, **139**, 4513–4520.
129 X. Chen, Y. Li, L. Wang, Y. Xu, A. Nie, Q. Li, F. Wu, W. Sun, X. Zhang, R. Vajtai, P. M. Ajayan, L. Chen and Y. Wang, *Adv. Mater.*, 2019, **31**, 1901640.
130 S. Mitra, S. Kandambeth, B. P. Biswal, A. Khayum, M. C. K. Choudhury, M. Mehta, G. Kaur, S. Banerjee, A. Prabhune, S. Verma, S. Roy, U. K. Kharul and R. Banerjee, *J. Am. Chem. Soc.*, 2016, **138**, 2823–2828.
131 L. Wang, C. Zeng, H. Xu, P. Yin, D. Chen, J. Deng, M. Li, N. Zheng, C. Gu and Y. Ma, *Chem. Sci.*, 2019, **10**, 1023–1028.
132 D. W. Burke, C. Sun, I. Castano, N. C. Flanders, A. M. Evans, E. Vitaku, D. C. McLeod, R. H. Lambeth, L. X. Chen, N. C. Gianneschi and W. R. Dichtel, *Angew. Chem., Int. Ed.*, 2020, **59**, 5165–5171.
133 S. A. Ahmed, Q.-B. Liao, Q. Shen, M. M. F. Ashraf Baig, J. Zhou, C.-F. Shi, P. Muhammad, S. Hanif, K. Xi, X.-H. Xia and K. Wang, *Chem. – Eur. J.*, 2020, **26**, 12996–13001.
134 J. W. Colson, A. R. Woll, A. Mukherjee, M. P. Levendorf, E. L. Spitler, V. B. Shields, M. G. Spencer, J. Park and W. R. Dichtel, *Science*, 2011, **332**, 228–231.
135 E. L. Spitler, J. W. Colson, F. J. Uribe-Romo, A. R. Woll, M. R. Giovino, A. Saldivar and W. R. Dichtel, *Angew. Chem.*, 2012, **124**, 2677–2681.
136 X. Feng, L. Chen, Y. Honsho, O. Saengsawang, L. Liu, L. Wang, A. Saeki, S. Irle, S. Seki, Y. Dong and D. Jiang, *Adv. Mater.*, 2012, **24**, 3026–3031.
137 X. Gao, Y. Zhu, D. Yi, J. Zhou, S. Zhang, C. Yin, F. Ding, S. Zhang, X. Yi, J. Wang, L. Tong, Y. Han, Z. Liu and J. Zhang, *Sci. Adv.*, 2018, **4**, eaat6378.
138 M. Dogru, M. Handloser, F. Auras, T. Kunz, D. Medina, A. Hartschuh, P. Knochel and T. Bein, *Angew. Chem., Int. Ed.*, 2013, **52**, 2920–2924.
139 D. D. Medina, V. Werner, F. Auras, R. Tautz, M. Dogru, J. Schuster, S. Linke, M. Döblinger, J. Feldmann, P. Knochel and T. Bein, *ACS Nano*, 2014, **8**, 4042–4052.
140 X. Gou, Q. Zhang, Y. Wu, Y. Zhao, X. Shi, X. Fan, L. Huang and G. Lu, *RSC Adv.*, 2016, **6**, 39198–39203.
141 D. D. Medina, J. M. Rotter, Y. Hu, M. Dogru, V. Werner, F. Auras, J. T. Markiewicz, P. Knochel and T. Bein, *J. Am. Chem. Soc.*, 2015, **137**, 1016–1019.
142 L. Xu, X. Zhou, Y. Yu, W. Q. Tian, J. Ma and S. Lei, *ACS Nano*, 2013, **7**, 8066–8073.
143 C. S. Diercks, S. Lin, N. Kornienko, E. A. Kapustin, E. M. Nichols, C. Zhu, Y. Zhao, C. J. Chang and O. M. Yaghi, *J. Am. Chem. Soc.*, 2018, **140**, 1116–1122.
144 D. D. Medina, M. L. Petrus, A. N. Jumabekov, J. T. Margraf, S. Weinberger, J. M. Rotter, T. Clark and T. Bein, *ACS Nano*, 2017, **11**, 2706–2713.
145 A. Braslau, M. Deutsch, P. S. Pershan, A. H. Weiss, J. Als-Nielsen and J. Bohr, *Phys. Rev. Lett.*, 1985, **54**, 114–117.
146 H. Sahabudeen, H. Qi, M. Ballabio, M. Položij, S. Olthof, R. Shivhare, Y. Jing, S. Park, K. Liu, T. Zhang, J. Ma, B. Rellinghaus, S. Mannsfeld, T. Heine, M. Bonn, E. Cánovas, Z. Zheng, U. Kaiser, R. Dong and X. Feng, *Angew. Chem., Int. Ed.*, 2020, **59**, 6028–6036.
147 H. Sahabudeen, H. Qi, B. A. Glatz, D. Tranca, R. Dong, Y. Hou, T. Zhang, C. Kuttner, T. Lehnert, G. Seifert, U. Kaiser, A. Fery, Z. Zheng and X. Feng, *Nat. Commun.*, 2016, **7**, 13461.
148 M. Matsumoto, L. Valentino, G. M. Stiehl, H. B. Balch, A. R. Corcos, F. Wang, D. C. Ralph, B. J. Mariñas and W. R. Dichtel, *Chem*, 2018, **4**, 308–317.
149 S. Kim, H. Lim, J. Lee and H. C. Choi, *Langmuir*, 2018, **34**, 8731–8738.
150 L.-L. Chua, J. Zaumseil, J.-F. Chang, E. C.-W. Ou, P. K.-H. Ho, H. Sirringhaus and R. H. Friend, *Nature*, 2005, **434**, 194–199.
151 A. Opitz, M. Horlet, M. Kiwull, J. Wagner, M. Kraus and W. Brütting, *Org. Electron.*, 2012, **13**, 1614–1622.
152 N. S. Hush and J. A. Pople, *Trans. Faraday Soc.*, 1955, **51**, 600.
153 H. Usta, C. Risko, Z. Wang, H. Huang, M. K. Deliomeroglu, A. Zhukhovitskiy, A. Facchetti and T. J. Marks, *J. Am. Chem. Soc.*, 2009, **131**, 5586–5608.

154 A. Opitz, *J. Phys.: Condens. Matter*, 2017, **29**, 133001.
155 J. Nitta, K. Miwa, N. Komiya, E. Annese, J. Fujii, S. Ono and K. Sakamoto, *Sci. Rep.*, 2019, **9**, 9645.
156 Y. Y. Illarionov, G. Rzepa, M. Waltl, T. Knobloch, A. Grill, M. M. Furchi, T. Mueller and T. Grasser, *2D Mater.*, 2016, **3**, 035004.
157 N. Koch, *ChemPhysChem*, 2007, **8**, 1438–1455.
158 Y. Xu, Y. Li, S. Li, F. Balestra, G. Ghibaudo, W. Li, Y. F. Lin, H. Sun, J. Wan, X. Wang, Y. Guo, Y. Shi and Y. Y. Noh, *Adv. Funct. Mater.*, 2020, **30**, 1–23.
159 M. Zelisko, Y. Hanlumyuang, S. Yang, Y. Liu, C. Lei, J. Li, P. M. Ajayan and P. Sharma, *Nat. Commun.*, 2014, **5**, 4284.
160 C. J. Shaerer, A. D. Slattery, A. J. Stapleton, J. G. Shapter and C. T. Gibson, *Nanotechnonology*, 2016, **27**, 125704.
161 K. I. Bolotin, K. J. Sikes, Z. Jiang, M. Klima, G. Fudenberg, J. Hone, P. Kim and H. L. Stormer, *Solid State Commun.*, 2008, **146**, 351–355.
162 R. Yan, Q. Zhang, I. Calizo, T. Shen, C. A. Richter, A. R. Hight-Walker, X. Liang, A. Seabaugh, D. Jena, H. G. Xing, D. J. Gundlach and N. V. Nguyen, *Appl. Phys. Lett.*, 2012, **101**, 022105.
163 S. Wan, F. Gándara, A. Asano, H. Furukawa, A. Saeki, S. K. Dey, L. Liao, M. W. Ambrogio, Y. Y. Botros, X. Duan, S. Seki, J. F. Stoddart and O. M. Yaghi, *Chem. Mater.*, 2011, **23**(18), 4094–4097.
164 S. Tiwarni and N. C. Greenham, Charge mobility measurement techniques in organic semiconductors, *Opt. Quantum Electron.*, 2009, **41**, 69–89.

How to cite: *Angew. Chem. Int. Ed.* **2022**, *61*, e202111749
International Edition: doi.org/10.1002/anie.202111749
German Edition: doi.org/10.1002/ange.202111749

Semiconductors

Optimized Synthesis of Solution-Processable Crystalline Poly(Triazine Imide) with Minimized Defects for OLED Application

*David Burmeister, Ha Anh Tran, Johannes Müller, Michele Guerrini, Caterina Cocchi, Julian Plaickner, Zdravko Kochovski, Emil J. W. List-Kratochvil, and Michael J. Bojdys**

Abstract: *Poly(triazine imide) (PTI) is a highly crystalline semiconductor, and though no techniques exist that enable synthesis of macroscopic monolayers of PTI, it is possible to study it in thin layer device applications that are compatible with its polycrystalline, nanoscale morphology. We find that the by-product of conventional PTI synthesis is a C−C carbon-rich phase that is detrimental for charge transport and photoluminescence. An optimized synthetic protocol yields a PTI material with an increased quantum yield, enabled photocurrent and electroluminescence. We report that protonation of the PTI structure happens preferentially at the pyridinic N atoms of the triazine rings, is accompanied by exfoliation of PTI layers, and contributes to increases in quantum yield and exciton lifetimes. This study describes structure–property relationships in PTI that link the nature of defects, their formation, and how to avoid them with the optical and electronic performance of PTI. On the basis of our findings, we create an OLED prototype with PTI as the active, metal-free material.*

Introduction

Interest in atomically thin 2D materials skyrocketed with the isolation of graphene sheets from graphite parent crystals and the realization that these sheets can be exploited in optoelectronic devices.[1] The extraordinarily high charge carrier mobility in graphene of up to 200000 $cm^2 V^{-1} s^{-1}$ is a result of the changed electronic structure of the atomic layer when compared to the bulk material.[2] The high mobility of semimetallic graphene comes at the price of an absent "off state" that has foreclosed its application in transistors.[3,4] Strategies to open up graphene's band gap revolve around the introduction of heteroatoms and structural defects in diffusion-limited or statistical post-processing as well as nanostructuring.[5–7] However, none of these methods are scalable and they do not yield products able to compete with silicon-based devices to date.[8]

Crystalline organic 2D materials that contain predictable "deletions" (i.e. pores) and heteroatoms by design are researched to make up for the missing band gap of graphene. Most notably transition metal dichalcogenides, graphene derivatives and designer covalent organic frameworks (COFs) compete to be the next generation semiconductor.[8–12]

Graphitic carbon nitrides combine two important characteristics: (i) they are overall sp^2-hybridized and covalently bonded, and (ii) they consist of earth abundant, light elements (i.e. they are metal free).[13,14] Poly(triazine imide) (PTI-MX) is a layered intercalation compound obtained from alkali metal halide salt melts and can be exfoliated to monolayers.[15] Even though the material has high environmental stability, crystallinity, blue photoluminescence, and has found application as semiconductor in photo- and electrocatalysts, it has found little to no use in optoelectronic devices up to this point.[16–18] Herein, (i) we elucidate the impact of different polycondensation conditions on the chemical makeup of PTI and its optical and electronic performance, (ii) we monitor the material quality at microscopic and macroscopic scales, (iii) we assemble photoconductor and organic light emitting diode (OLED) devices based on PTI, and (iv) we look at the

[*] Prof. Dr. M. J. Bojdys
Department of Chemistry, Kings College London
Britannia House Guy's Campus, 7 Trinity Street, London, SE1 1DB (United Kingdom)
E-mail: m.j.bojdys.02@cantab.net
D. Burmeister, H. A. Tran, Prof. Dr. E. J. W. List-Kratochvil, Prof. Dr. M. J. Bojdys
Department of Chemistry, Department of Physics
IRIS Adlershof, Humboldt-Universität zu Berlin
Zum Grossen Windkanal 2, 12489 Berlin (Germany)
J. Müller, Prof. Dr. C. Cocchi
Department of Physics, IRIS Adlershof
Humboldt-Universität zu Berlin
Brook-Taylor-Strasse 15, 12489 Berlin (Germany)
Dr. M. Guerrini, Prof. Dr. C. Cocchi
Institute of Physics, Carl von Ossietzky Universität Oldenburg
26129 Oldenburg (Germany)
Dr. J. Plaickner
Helmholtz-Zentrum Berlin für Materialien und Energie GmbH
Hahn-Meitner-Platz 1, 14109 Berlin (Germany),
and
Leibniz-Institut für Analytische Wissenschaften—IAS e.V.
Schwarzschildstrasse 8, 12489 Berlin (Germany)
Dr. Z. Kochovski
Institute of Electrochemical Energy Storage
Helmholtz-Zentrum Berlin für Materialien und Energie
Hahn-Meitner-Platz 1, 14109 Berlin (Germany)
Supporting information and the ORCID identification number(s) for the author(s) of this article can be found under: https://doi.org/10.1002/anie.202111749.

effect of protonation on the electronic structure of PTI comparing results from calculations with observed optical spectra. The results of this study provide guidelines for improving the optical and electronic properties of organic layered materials; especially ones that incorporate triazine (C_3N_3) subunits.

Ionothermal condensation–polymerization of dicyandiamide was first performed by Bojdys et al., and later, Wirnhier et al. solved the structure of the product as poly(triazine imide).[19,20] While the structure of this material was examined in detail, the electronic properties of this system have not been studied thoroughly yet.[19,21–23] We find that the reduction of the temperature increases the structural order and preserves a desired CN-ratio. This enables us to harness the semiconducting properties in simple prototype devices. To access quality markers and properties of the obtained product we applied powder X-ray diffraction (PXRD), scanning electron microscopy (SEM), X-ray photoelectron spectroscopy (XPS), ultraviolet photoelectron spectroscopy (UPS), Fourier-transform infrared spectroscopy (FT-IR), UV–Raman, solid state nuclear magnetic resonance spectroscopy (ssNMR), UV/Vis absorption spectroscopy (UV/Vis), photoluminescence, and photoluminescence excitation spectroscopy (PL, PLE) as well as quantum yield and lifetime measurements.

The observations of this work also are of explanatory value (i) for the wider organic materials community studying the effects of defects in conjugated polymer semiconductors and (ii) in the context of wide-spread studies into the photocatalytic activity of PTI.[24]

Results and Discussion

Structural Characterization of Obtained Products

The starting point for this work is the ionothermal synthetic protocol for PTI that has not been altered since its first reports.[25–27] The significant parameters for polycondensation reactions are the reaction temperature (600 °C) and the reaction time (12 h). The product is characterized as a dark brown powder (Figure 1 a, center).[28] The material shows no visible photoluminescence under 375 nm UV-light (Figure S1). Higher luminescence can typically be accessed only by dispersing the material in water/methanol/DMSO.[27] Hence, it is often argued that the emission of the material in its initial graphitic state is quenched by π–π stacking. Instead of excitation and radiative emission, π–π quenching leads to photo-induced electron transfer to a neighboring π-system. This inhibits effective recombination of the electron hole pair in a radiative process.

We report that synthesis at a temperature of 550 °C and extended reaction times of 48 h yields an almost colorless product (Figure 1 a, left) with visible photoluminescence when irradiated with UV-light. The hitherto employed harsh reaction conditions (600 °C, 12 h) are at the onset of carbonization of the material and introduce carbonaceous contaminants that darken the color of PTI.[29] Qualitative and quantitative XPS analysis of the C1s core region shows an intense peak at 285 eV and confirms the presence of C–C environments (adventitious C1s, C–C peak at 284.8 eV) (Figure 1 b).[30] This contribution is often assigned to adventitious carbon.[25,31,32]

However, at 550 °C the contribution at 285 eV in the C1s spectrum of PTI–LiBr is greatly reduced. Since the contribution of adventitious carbon should be similar for all samples, we deduce that part of this contribution comes from a carbon-

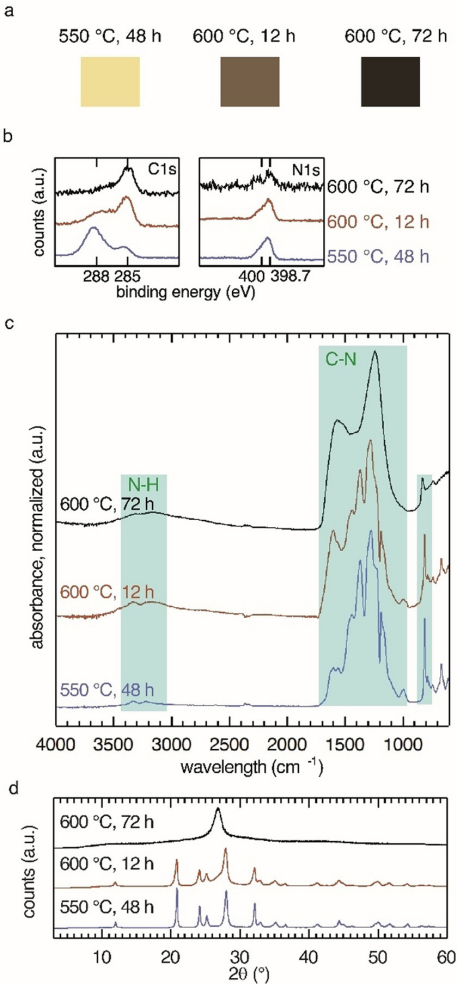

Figure 1. Structural characterization of PTI–LiBr materials obtained at different temperatures and reaction times. a) Discoloration of PTI–LiBr with increasing reaction temperature indicates emergence of carbon-rich phase for products formed at 600 °C. b) X-ray photoelectron spectroscopy (XPS) of PTI–LiBr samples. Evaluation of C1s and N1s core regions confirms the presence of carbon-rich product and loss of nitrogen at 600 °C. c) Fourier-transform infrared (FT-IR) spectra of PTI–LiBr products show decreased band separation for high reaction temperatures, indicating the loss of structural order. d) Powder X-ray diffraction pattern of product phases. The evolution of a peak at 27° 2θ for products formed at 600 °C is interpreted as formation of a disordered carbon-rich material next to PTI–LiBr.

rich phase that coevolved during the synthesis at 600 °C. Looking at the N1s region, we observe nitrogen signals from triazine moieties at 398.5 eV and a contribution from the imide-NH bridges between the triazine units at 400 eV with relative intensities of (3:1) for the product from 550 °C (Figure 1b, right). The product obtained at 550 °C, 48 h approaches the theoretical elemental composition of poly(-triazine imide) ($C_6N_9H_3$) of 40:60 C:N most closely (Table 1).

Table 1: X-ray photoelectron spectroscopy (XPS) analysis of atomic percentage of carbon and nitrogen observed in CN films prepared from different synthetic conditions.[a]

Reaction conditions	C:N at% XPS
600 °C, 72 h	87:13
600 °C, 12 h	81:19
550 °C, 48 h	49:51

[a] The integration of the carbon signal was conducted over all carbon species and not corrected for adventitious carbon.

Other groups have not reported the presence of this carbon-rich phase at these conditions. Hence it is likely that it was either overlooked or mistaken for a contribution solely from carbon tape used as substrate or adventitious carbon in XPS experiments. An attempt to study the structure of the phase obtained from 600 °C for 72 h was conducted by Suter et al.[33]

To access information about the prevalent bond types and therefore the degree of condensation as well as possible defects, we conducted FT-IR spectroscopy on the products (Figure 1c). FT-IR spectra of the high-temperature products at 600 °C show a broad peak around 3300 cm^{-1} in addition to two discernible NH signals (at 3328 and 3217 cm^{-1}). The latter are argued to originate from splitting of the imide N–H bond by partial conversion into N–Li.[19] The broad feature is absent in the product obtained at 550 °C. The sharp band around 810 cm^{-1} is attributed to the out-of-plane bending mode of the six-membered triazine (C_3N_3) ring and is present in all samples.[34–36] Likewise, the material obtained at low temperature has a clearer separation of bands in the CN stretching region 990–1600 cm^{-1}. There are two valid explanations for these observations: (i) the broad feature around 3300 cm^{-1} can be attributed to OH groups attached to the carbonaceous contaminants that are produced at elevated temperatures, and (ii) decreased band separation is indicative of structural disorder in the material obtained at high temperature as a consequence of thermal decomposition. The spectra of samples condensed at 600 °C for 72 h resemble those of amorphous CNH-compounds with the dominant infrared absorption between 1600 and 1300 cm^{-1} from C–N modes and ring species.[37]

PXRD patterns confirm the transition of crystalline PTI–LiBr into a disordered material at long reaction times and 600 °C (Figure 1d). Condensation at 550 °C results in a slight shift in the diffraction pattern towards lower angles corresponding to an increase in plane distances. A conceivable reason is an increased ion loading in the structure obtained at reduced temperature.[38] The same trend of higher product quality at the lower reaction temperature was also found by ssNMR. The C^{13} spectrum shows the three carbon signals also observed in PTI–LiCl at $\delta = 167.0$ ppm, 162.0 ppm and 158.0 ppm (Figure S2). The bands show increased sharpness in the product condensed at 550 °C.[19]

We examined the sample morphologies by SEM (Figure S3a,b). The morphology of PTI-MX is described as hexagonal platelets and prisms with a basal cross-section of 100–500 nm in literature.[20,39] The nanostructure has been elucidated by high resolution transmission electron microscopy (HR-TEM, Figure S3c–e). Fourier transformation of the HR-TEM image reveals the hexagonal periodicity and the characteristic in-plane distance of 0.73 nm corresponding to the 100 reflection at 12° 2θ in the PXRD spectrum (Figure 1d) as indexed by Suter et al.[25]

Further decrease of the reaction temperature to 525 °C resulted in a product with additional PXRD peaks that could not be attributed to a PTI-type material and, hence, the material was not investigated further (Figure S4). We selected the PTI–LiBr sample obtained at 550 °C (48 h) for further optoelectronic experiments based on its structure and composition.

Optical Properties of PTI–LiBr and PTI-IF Films

The decreased carbon contamination allows us to measure UV/Vis of PTI–LiBr dispersions (Figure 2a, blue plot). We find two broad features around 370 and 290 nm. The state at 370 nm can be excited yielding the photoluminescence spectrum shown in Figure 2b (blue plot). The photoluminescence excitation spectrum shows a single maximum at 486 nm

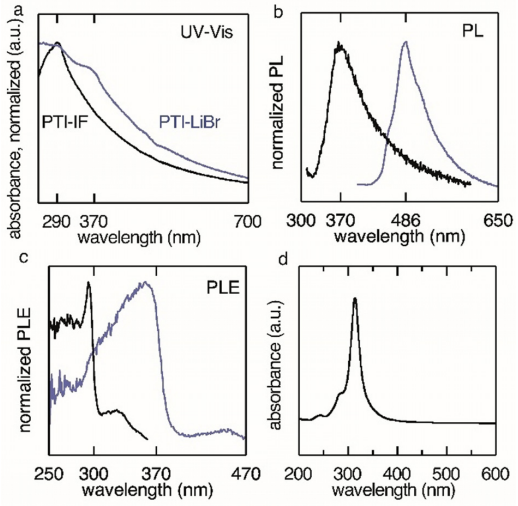

Figure 2. Optical characterization of PTI–LiBr obtained at 550 °C, 12 h (in blue) and intercalation-free poly(triazine imide) (PTI-IF, in black) on quartz substrates. a) UV/Vis (transmission) spectrum. b) Photoluminescence spectra show emission maxima at 486 nm for PTI–LiBr and at 370 nm for PTI-IF. c) Photoluminescence excitation spectra of PTI–LiBr (excited at 370 nm) and PTI-IF (excited at 300 nm). d) Absorption spectrum of a monolayer of PTI-IF computed from time-dependent DFT.

(Figure 2c, blue line). This emissive state is a result of the replacement of hydrogen with lithium at triazine bridging N–H units. This defect reduces the conduction band minimum energy accounting for the contraction of the optical gap of this structure.[28] Exciting PTI–LiBr at around 290 nm does not yield a new emission band and decreases the emission at 486 nm drastically (cf. Figure 3d). Hence, the state that belongs to the absorption at 290 nm in PTI–LiBr is quenched.

To gain a better understanding of these two states, we prepared an intercalation-free PTI (PTI-IF) comprised only of the CN-backbone (SI Experimental). PXRD, FT-IR and UV–Raman of PTI-IF are depicted in Figure S5. Removal of the coordinating lithium and bromine ions leads to disorder as can be found comparing the PXRD spectra of PTI-IF to PTI–LiBr. The width of the reflexes is broadened and some peaks are deleted entirely. Comparing FT-IR spectra of PTI–LiBr and PTI-IF we find better band separation in the ion-free PTI-IF as was observed by Suter et al.[25] UV–Raman spectra

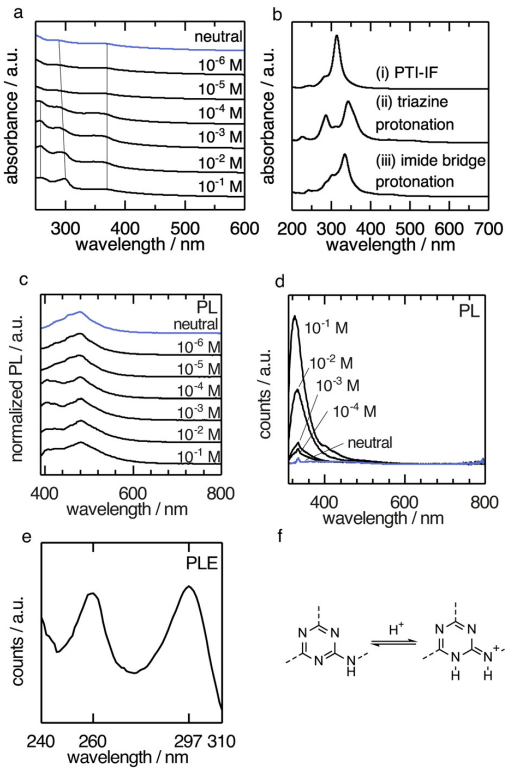

Figure 3. Optical characterization of PTI–LiBr dispersions in water at different concentrations of HCl. a) UV/Vis (transmission) spectra. b) Time-dependent DFT absorption spectrum of (i) a monolayer PTI-IF, (ii) PTI-IF monolayer protonated via HCl at triazine rings and (iii) PTI-IF monolayer protonated via HCl at imide bridges. c) Photoluminescence (PL) spectra excited at 370 nm for PTI–LiBr dispersions with different HCl concentrations. d) Photoluminescence spectra excited at 300 nm for PTI–LiBr dispersions with different HCl concentrations. e) Photoluminescence excitation (PLE) spectrum for emission at 330 nm at 10^{-2} M HCl. f) Energetically favored protonation at the triazine ring.

with a 266 nm excitation source reveal the same trend of sharper bands in PTI-IF. The Raman bands associated with breathing modes of triazine are found at 1002 cm^{-1} (weak) and 685 cm^{-1} (weak) in PTI–LiBr and 983 cm^{-1} (strong) and 685 cm^{-1} (weak) in PTI-IF.[33,40] Broad contributions in both samples at 1300 cm^{-1} (broad, weak) and 1630 cm^{-1} (strong) can be assigned to the so-called D and G bands due to breathing modes in sp^2-bonded rings and CN sp^2 bond stretching in rings and chains, respectively.[37] The presence of a sharp, strong Raman band at 1088 cm^{-1} in PTI–LiBr samples indicates a carbonate species.[41] The lithium defect can undergo hydrolysis to form LiOH in presence of water. This is the known reason for the basic character of PTI-MX in water as reported in literature.[42] LiOH is a known CO_2 absorber.[43] We propose that under environmental conditions (in presence of water and CO_2) LiOH can form at the surface of the crystallites which in turn can absorb CO_2 leading to the presence of lithium carbonate species. Hence, in PTI-IF this Raman band is absent.

Optical characterization by UV/Vis spectroscopy reveals that by removing most of the ions in the structure, we lose the absorption band at 370 nm, as expected, since this state is the result of Li-defects. Absorption at 290 nm is still prevalent and, hence, it is assigned to the PTI-conjugated backbone. This observation matches well with the theoretical predictions for an intercalation-free PTI (see Figure 2d). The result of this calculation shows that PTI-IF layers have a single bright absorption band at around 320 nm, in good agreement with the experimental results, considering the necessary simplifications applied to the model structure adopted in the simulation (see Figure S6, S7) The absence of emission from the 290 nm state in PTI–LiBr could be due to the presence of the Li defects acting as a deep trap. Excitons formed in the organic backbone will recombine primarily at these energetically favorable defect sites. A similar effect can be observed for keto-defects in polyfluorene backbones.[44]

It is not possible to determine the quantum yield of PTI samples obtained at 600 °C because of strong absorption from the accompanying carbon-rich phase. The quantum yield of films cast from the 550 °C product equals 0.4 %. Optical images comparing products obtained at 550 °C and 600 °C illuminated with a 375 nm LED can be accessed in the SI (Figure S1).

Effect of Protonation on the Optical States of PTI–LiBr

In a first set of experiments, we collected UV/Vis spectra of PTI–LiBr suspended in water at different concentrations of HCl (Figure 3a). Without HCl we observe the absorption of the lithium defect states at around 370 nm and the broad absorption of the conjugated PTI-backbone at around 290 nm. By increasing the H_3O^+ concentration, two effects can be identified. First the absorption band of the organic backbone experiences a slight bathochromic shift from 290 to 300 nm. Moreover, a new absorption band at 260 nm arises. There are two possible sites of protonation in the PTI–LiBr structure: at the triazine nitrogen (Figure 3b), or at the imide nitrogen (Figure 3b). Protonation at the triazine nitrogen

compares best with the observed UV/Vis spectra, and accounts for the bathochromic shift and the manifestation of a new band at 260 nm (compare Figure 3b, i and Figure 3b, ii). Our first-principles calculations predict that the triazine-protonated structure is more stable than the imide-bridge-protonated structure. Based on this finding, we assume that the triazine protonation is prevalent. The calculated optical absorption spectra of the protonated materials (Figure 3b) indicate an overall red-shift of the absorption peaks in comparison with PTI-IF. This result is qualitatively in agreement with earlier predictions on analogous model systems.[45] Specifically the red shift of the main peak in combination with the emergence of a second absorption band in the absorption spectrum of triazine-protonated PTI (Figure 3b, ii) is considered an effect of the symmetry breaking of the backbone structure upon protonation. The presence of two absorption bands in the system is in good agreement with two corresponding PLE maxima at 260 nm and 297 nm of the emission at 330 nm (Figure 3d,e) present in dispersions with HCl concentrations larger than 10^{-5} M at 260 nm and 300 nm (Figure 3d,e).

It is noteworthy that for excitation at 300 nm in dispersions at 10^{-2} M HCl the quantum yield obtained was 10% and for excitation at 370 nm 9%. The emission of the neutral dispersion at 486 nm is comparatively low with a quantum yield of 1% and no emission for excitation at 300 nm. The increased quantum yield is accompanied by an increase in lifetime (neutral $\tau_1 = 0.5$ ns ± 0.03 ns, $\tau_2 = 3.6$ ns ± 0.13 ns; pH 1 $\tau_1 = 1$ ns ± 0.05 ns, $\tau_2 = 4$ ns ± 0.10 ns). As typical for CN materials a two exponential fit was applied.[32] The increase in quantum yield and lifetime is attributed to partial exfoliation of the layered PTI structure and, hence, reduced π–π stacking. Charging of PTI layers by reduction with sodium naphthalide and stabilization by derivatization with a C_{12} alkane was described in literature.[46] A route via protonation could be a viable alternative.

The photoluminescence band we assign to the CN backbone protonated at the triazine moiety at 330 nm is blue-shifted with respect to the emission of PTI-IF at 370 nm (Figure 3d, 2b).

The changes in the optical spectra coincide with the observation of an equivalence point at pH 5 in the HCl titration of PTI–LiBr dispersions (Figure S8). The pK_b extracted from the titration is $pK_b = 6.4$. The pK_a value associated with the conjugated acid is 7.6 ($pK_a = 14 - pK_b$). The conjugated acid is weaker than the conjugated acid of melamin ($pK_a = 5.0$).[47] This indicates that the protonated PTI–LiBr structure is better stabilized than the triazine-containing monomer, presumably due to conjugation across the PTI-backbone (Figure 3f). The observed optical states are summarized in Figure 4 and compared to the optical gaps predicted by the DFT calculations.

Photoconductivity experiments using PTI–LiBr were realized on interdigitated indium tin oxide substrates (Figure S9a,b). The conductivity of the material is 4×10^{-10} S cm^{-1} in the dark and 1.0×10^{-9} S cm^{-1} in the illuminated state (at 375 nm and an irradiance of 46 mW cm^{-2}). Photoconductors using PTI–LiBr undergo changes over the course of the measurement because of the migration of ions. Therefore, the

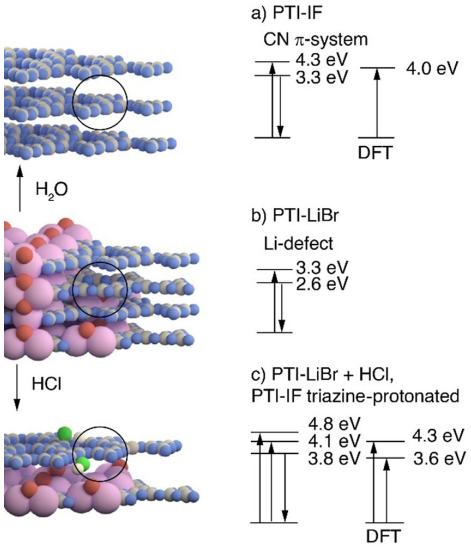

Figure 4. Summary of optical states from DFT, UV/Vis and photoluminescence spectroscopy of dispersions in water of (a) PTI-IF obtained from PTI–LiBr by Soxhlet extraction of ions, and optical gap of 2D layer of PTI-IF from DFT calculation, (b) partially de-intercalated PTI–LiBr as obtained from ionothermal synthesis, (c) effects of HCl at concentrations higher than 10^{-5} M on PTI–LiBr dispersions and optical gaps obtained for 2D layer of triazine-protonated PTI-IF sheet by DFT. Arrows pointing upwards denote an absorption process, arrows pointing downwards denote an emission process. Carbon and nitrogen atoms are represented as gray and blue spheres. Hydrogen atoms at the imide nitrogen are not depicted. Lithium and Bromine ions are represented as red and pink spheres. Proton and chloride anion are represented as white and green spheres.

observed hysteresis in IV-sweeps is dependent on the scan speed of the sweep (Figure S9c). Materials obtained at 600 °C show no photoresponse and can be considered insulating. This is an important observation since it confirms that an increase in structural order and homogeneity in low-temperature PTI samples (as seen in PXRD and FT-IR) and the simultaneous reduction of carbonaceous contaminations translate into better performance of the semiconductor.

We have seen so far that (i) PTI-samples obtained at low temperature conditions (550 °C, 48 h) showed enhanced electrical and optical properties and that (ii) we were able to process PTI-materials from dispersions into thin films. We therefore prepared single-layer light emitting device structures with PEDOT:PSS/ITO as anode and Ca/Al as cathode to investigate PTI–LiBr as electroluminescent active material (Figure 5a). The OLED stack shows a steep diode-like onset of the device current and electroluminescence emission at ca. 4.5 V in forward bias direction. At 12 V bias we observed a maximum luminance of 2 cd m^{-2}. The device showed a current efficiency of ca. 10^{-4} cd A^{-1} (Figure 5b). Below onset we also observed a high device leakage current which is attributed to film inhomogeneities and pin holes introduced during the drop-casting preparation process of the PTI–LiBr layer. Similar to previous observations for CN-films, the

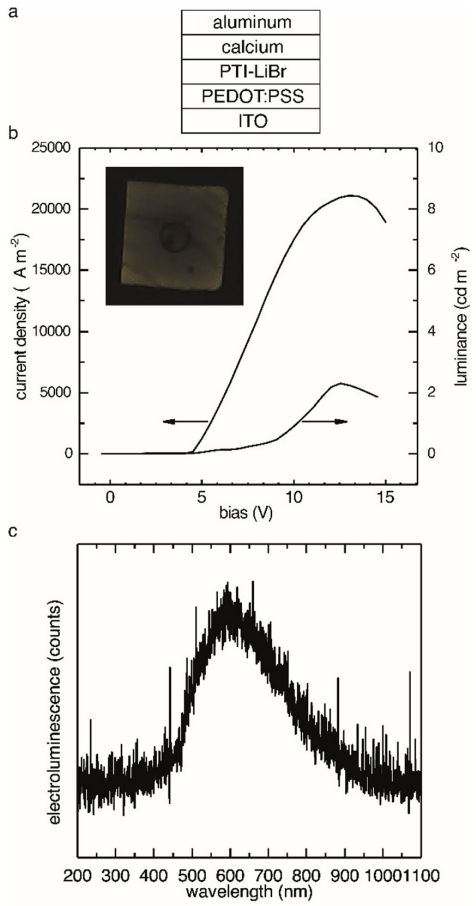

Figure 5. Characterization of a single-layer OLED with Ca/Al as the cathode, PEDOT:PSS/ITO anode, and PTI-LiBr as the active material. a) OLED architecture. b) Current density and luminance versus bias with picture of a PTI–LiBr OLED pixel. c) Electroluminescence of the PTI–LiBr OLED.

electroluminescence maximum of PTI–LiBr has been red-shifted by 0.5 eV with respect to the PL maximum (Figure 5c).[48] Defect levels are a likely explanation for the red-shift. They may arise from small amounts of carbonaceous contaminants still present in the low-temperature PTI–LiBr sample or nitrogen vacancies in the PTI–LiBr crystals. Electrons are preferably injected into defect levels below the conduction band while holes are preferably injected into defect states above the valence band or subsequently relax into these energetically favored states, resulting in a red-shifted emission.[48] The presence of carbonaceous contaminants in the low-temperature PTI–LiBr sample is corroborated in XPS data that show a contribution in the C−C bond region (Figure 1b) as well as the still slightly carbon-rich CN ratio (Table 1). While the device performance of this simple single-layer device is rather limited, we successfully demonstrate that PTI–LiBr can be used as the emissive active layer in OLEDs. In a next step we will introduce hole and electron transport layers and optimize the PTI–LiBr layer preparation to improve the device performance.

Preliminary data from ultraviolet photoelectron spectroscopy (UPS) measurements revealed that PTI–LiBr samples on ITO substrates have a work function (WF) of 4.3 eV and a hole injection barrier (HIB) of 2.8 eV. The ionization potential (IP) equals 7.1 eV (IP = WF + HIB), similar to molecular CN species with high nitrogen content like melem (7 eV).[49] Approximating the conduction band onset using the optical gap extracted from UV/Vis measurements the Fermi level position is near the conduction band and hence pointing towards a n-doped character (Figure S10a). A summary of the electronic levels is depicted in Figure S10b. More studies on the preparation method (inert, environmental conditions) and the influence of the substrate have to be conducted for a more detailed understanding of the electronic structure of poly(triazine imide) and its derivatives.

Conclusion

We present an improved synthetic protocol for PTI–LiBr and highlight the detrimental effects of high synthetic temperatures on the optical and electronic properties of the material. We observe that the hitherto reported synthetic conditions that employ temperatures of 600 °C (and above) give rise to partial carbonization of PTI–LiBr. The formation of these carbonaceous contaminants in PTI–LiBr gives rise to low-energy defect states that deteriorate charge transfer pathways and absorb photoluminescence. We find that protonation of PTI–LiBr happens preferentially at the nitrogen atoms of the triazine (C_3N_3) moieties. The absorption band of the PTI-backbone is split due to the symmetry breaking upon protonation. Protonation also increased the quantum yield of PTI suspensions up to a factor of 9. This indicates a facile route to partial exfoliation of the π-stacked PTI-structure in solutions of aqueous acids. Finally, we are able to produce a simple OLED structure with PTI–LiBr as an active, metal-free material to demonstrate electroluminescence. The maximum of the emission is red-shifted by 0.5 eV in regard to the photoluminescence. This observation is assigned to the presence of defect levels above valence band and below conduction band. UPS results revealed a high ionization potential (7.1 eV) and hole injection barrier (2.8 eV). This finding reveals a possible route towards optimization of the graphitic carbon nitride OLED by introduction of transport layers reducing the injection barriers. Future use of PTI (and analogous, layered CN-materials) in optical and electronic applications is contingent on (i) further reduction of contributions arising from defect states and (ii) development of methods to access its crystal interfaces as well as PTI monolayers on suited substrates.

Acknowledgements

The authors are grateful for the collaboration with Nicolas Zorn Morales, Fabian Gärisch, Vincent Schröder, Dr. Matthias Trunk, Dr. Felix Hermerschmidt, Prof. Christoph T.

Koch, Prof. Norbert Koch, Prof. Nicola Pinna, Prof. Phillip Adelhelm, Prof. Gudrun Scholz, Prof. Norbert Esser and Prof. Hans Börner who provided fruitful discussions, lab space and access to instruments. M.J.B. thanks the European Research Council (ERC) for funding under the Starting Grant Scheme (BEGMAT-678462). M.G. and C.C. acknowledge funding by the German Research Foundation (DFG), project number 182087777-CRC 951, by the German Federal Ministry of Education and Research (Professorinnenprogramm III) as well as from the State of Lower Saxony (Professorinnen für Niedersachsen). Computational resources were provided by HPC cluster CARL at the University of Oldenburg, funded by the DFG (Project No. INST 184/157-1 FUGG) and by the Ministry of Science and Culture of Lower Saxony. J.P. acknowledges funding of the Senatsverwaltung Berlin and European Union within the project EFRE 1.8/07. Open Access funding enabled and organized by Projekt DEAL.

Conflict of Interest

The authors declare no conflict of interest.

Keywords: covalent organic framework · crystalline carbon nitride · ionothermal synthesis · layered materials · metal-free semiconductor

[1] A. Castellanos-Gomez, *Nat. Photonics* **2016**, *10*, 202 – 204.
[2] K. I. Bolotin, K. J. Sikes, Z. Jiang, M. Klima, G. Fudenberg, J. Hone, P. Kim, H. L. Stormer, *Solid State Commun.* **2008**, *146*, 351 – 355.
[3] C. J. Shearer, A. D. Slattery, A. J. Stapleton, J. G. Shapter, C. T. Gibson, *Nanotechnology* **2016**, *27*, 125704.
[4] T. Wu, H. Shen, L. Sun, B. Cheng, B. Liu, J. Shen, *New J. Chem.* **2012**, *36*, 1385.
[5] J. Kotakoski, A. V. Krasheninnikov, U. Kaiser, J. C. Meyer, *Phys. Rev. Lett.* **2011**, *106*, 105505.
[6] M. Pumera, Z. Sofer, *Chem. Soc. Rev.* **2017**, *46*, 4450 – 4463.
[7] B. S. Jessen, L. Gammelgaard, M. R. Thomsen, D. M. A. Mackenzie, J. D. Thomsen, J. M. Caridad, E. Duegaard, K. Watanabe, T. Taniguchi, T. J. Booth, et al., *Nat. Nanotechnol.* **2019**, *14*, 340 – 346.
[8] D. Burmeister, M. G. Trunk, M. J. Bojdys, *Chem. Soc. Rev.* **2021**, *50*, 11559 – 11576.
[9] M. Heyl, D. Burmeister, T. Schultz, S. Pallasch, G. Ligorio, N. Koch, E. J. W. List-Kratochvil, *Phys. Status Solidi RRL* **2020**, *14*, 2000408.
[10] P. Miró, M. Audiffred, T. Heine, *Chem. Soc. Rev.* **2014**, *43*, 6537 – 6554.
[11] A. K. Geim, I. V. Grigorieva, *Nature* **2013**, *499*, 419 – 425.
[12] M. S. Lohse, T. Bein, *Adv. Funct. Mater.* **2018**, *28*, 1705553.
[13] G. Algara-Siller, N. Severin, S. Y. Chong, T. Björkman, R. G. Palgrave, A. Laybourn, M. Antonietti, Y. Z. Khimyak, A. V. Krasheninnikov, J. P. Rabe, et al., *Angew. Chem. Int. Ed.* **2014**, *53*, 7450 – 7455; *Angew. Chem.* **2014**, *126*, 7580 – 7585.
[14] Y. Noda, C. Merschjann, J. Tarábek, P. Amsalem, N. Koch, M. J. Bojdys, *Angew. Chem. Int. Ed.* **2019**, *58*, 9394 – 9398; *Angew. Chem.* **2019**, *131*, 9494 – 9498.
[15] L. F. Villalobos, M. T. Vahdat, M. Dakhchoune, Z. Nadizadeh, M. Mensi, E. Oveisi, D. Campi, N. Marzari, K. V. Agrawal, *Sci. Adv.* **2020**, *6*, 9851.
[16] X. Jia, Q. Guan, Y. Chen, Y. Wang, Q. Zhao, J. Li, *Appl. Surf. Sci.* **2019**, *492*, 879 – 885.
[17] W. R. Lee, Y. S. Jun, J. Park, G. D. Stucky, *J. Mater. Chem. A* **2015**, *3*, 24232 – 24236.
[18] L. Lin, C. Wang, W. Ren, H. Ou, Y. Zhang, X. Wang, *Chem. Sci.* **2017**, *8*, 5506 – 5511.
[19] E. Wirnhier, M. Döblinger, D. Gunzelmann, J. Senker, B. V. Lotsch, W. Schnick, *Chem. Eur. J.* **2011**, *17*, 3213 – 3221.
[20] M. J. Bojdys, J.-O. Müller, M. Antonietti, A. Thomas, *Chem. Eur. J.* **2008**, *14*, 8177 – 8182.
[21] C. Z. Liao, V. W. H. Lau, M. Su, S. Ma, C. Liu, C. K. Chang, H. S. Sheu, J. Zhang, K. Shih, *Inorg. Chem.* **2019**, *58*, 15880 – 15888.
[22] X. Yan, J. Li, H. Zhou, *J. Mater. Sci. Mater. Electron.* **2019**, *30*, 11706 – 11713.
[23] W. Lee, Y.-S. Jun, J. Park, G. D. Stucky, *J. Mater. Chem. A* **2015**, *3*, 24232 – 24236.
[24] L. Lin, Z. Lin, J. Zhang, X. Cai, W. Lin, Z. Yu, X. Wang, *Nat. Catal.* **2020**, *3*, 649 – 655.
[25] T. M. Suter, T. S. Miller, J. K. Cockcroft, A. E. Aliev, M. C. Wilding, A. Sella, F. Corà, C. A. Howard, P. F. McMillan, *Chem. Sci.* **2019**, *10*, 2519 – 2528.
[26] M. J. Bojdys, J.-O. Müller, M. Antonietti, A. Thomas, *Chem. Eur. J.* **2008**, *14*, 8177 – 8182.
[27] T. S. Miller, T. M. Suter, A. M. Telford, L. Picco, O. D. Payton, F. Russell-Pavier, P. L. Cullen, A. Sella, M. S. P. Shaffer, J. Nelson, V. Tileli, P. F. Mc Millan, C. A. Howard, *Nano Lett.* **2017**, *17*, 5891 – 5896.
[28] E. J. McDermott, E. Wirnhier, W. Schnick, K. S. Virdi, C. Scheu, Y. Kauffmann, W. D. Kaplan, E. Z. Kurmaev, A. Moewes, *J. Phys. Chem. C* **2013**, *117*, 8806 – 8812.
[29] H. May, *J. Appl. Chem.* **1959**, *9*, 340 – 344.
[30] S. Evans, *Surf. Interface Anal.* **1997**, *25*, 924 – 930.
[31] A. P. Dementjev, A. de Graaf, M. C. M. van de Sanden, K. I. Maslakov, A. V. Naumkin, A. A. Serov, *Diam. Relat. Mater.* **2000**, *9*, 1904 – 1907.
[32] X. Li, G. Hartley, A. J. Ward, P. A. Young, A. F. Masters, T. Maschmeyer, *J. Phys. Chem. C* **2015**, *119*, 14938 – 14946.
[33] T. Suter, V. Brázdová, K. McColl, T. S. Miller, H. Nagashima, E. Salvadori, A. Sella, C. A. Howard, C. W. M. Kay, F. Corà, et al., *J. Phys. Chem. C* **2018**, *122*, 25183 – 25194.
[34] T. S. Miller, A. B. Jorge, T. M. Suter, A. Sella, F. Corà, P. F. McMillan, *Phys. Chem. Chem. Phys.* **2017**, *19*, 15613 – 15638.
[35] B. V. Lotsch, W. Schnick, *Chem. Eur. J.* **2007**, *13*, 4956 – 4968.
[36] B. Jürgens, E. Irran, J. Senker, P. Kroll, H. Müller, W. Schnick, *J. Am. Chem. Soc.* **2003**, *125*, 10288 – 10300.
[37] A. C. Ferrari, S. E. Rodil, J. Robertson, *Phys. Rev. B* **2003**, *67*, 155306.
[38] S. Y. Chong, J. T. A. Jones, Y. Z. Khimyak, A. I. Cooper, A. Thomas, M. Antonietti, M. J. Bojdys, *J. Mater. Chem. A* **2013**, *1*, 1102 – 1107.
[39] L. Lin, Z. Yu, X. Wang, *Angew. Chem. Int. Ed.* **2019**, *58*, 6164 – 6175; *Angew. Chem.* **2019**, *131*, 6225 – 6236.
[40] N. E. Mircescu, M. Oltean, V. Chiş, N. Leopold, *Vib. Spectrosc.* **2012**, *62*, 165 – 171.
[41] M. H. Brooker, J. Wang, *Spectrochim. Acta Part A* **1992**, *48*, 999 – 1008.
[42] K. Schwinghammer, M. B. Mesch, V. Duppel, C. Ziegler, J. Senker, B. V. Lotsch, *J. Am. Chem. Soc.* **2014**, *136*, 1730 – 1733.
[43] P. Zilberman, *Acta Medica Marisiensis* **2015**, *61*, 4 – 6.
[44] E. J. W. List, R. Guentner, P. S. de Freitas, U. Scherf, *MRS Proc.* **2002**, *734*, B9.11.
[45] M. Guerrini, E. Delgado Aznar, C. Cocchi, *J. Phys. Chem. C* **2020**, *124*, 27801 – 27810.
[46] J. Jia, E. R. White, A. J. Clancy, N. Rubio, T. Suter, T. S. Miller, K. McColl, P. F. McMillan, V. Brázdová, F. Corà, et al., *Angew. Chem. Int. Ed.* **2018**, *57*, 12656 – 12660; *Angew. Chem.* **2018**, *130*, 12838 – 12842.
[47] Y. H. Jang, S. Hwang, S. B. Chang, J. Ku, D. S. Chung, *J. Phys. Chem. A* **2009**, *113*, 13036 – 13040.

[48] J. Xu, M. Shalom, F. Piersimoni, M. Antonietti, D. Neher, T. J. K. Brenner, *Adv. Opt. Mater.* **2015**, *3*, 913 – 917.

[49] K. Akaike, K. Aoyama, S. Dekubo, A. Onishi, K. Kanai, *Chem. Mater.* **2018**, *30*, 2341 – 2352.

Manuscript received: August 30, 2021
Revised manuscript received: September 29, 2021
Accepted manuscript online: October 11, 2021
Version of record online: December 18, 2021

Angewandte Chemie
Eine Zeitschrift der Gesellschaft Deutscher Chemiker

Supporting Information

Optimized Synthesis of Solution-Processable Crystalline Poly(Triazine Imide) with Minimized Defects for OLED Application

*David Burmeister, Ha Anh Tran, Johannes Müller, Michele Guerrini, Caterina Cocchi, Julian Plaickner, Zdravko Kochovski, Emil J. W. List-Kratochvil, and Michael J. Bojdys**

anie_202111749_sm_miscellaneous_information.pdf

SUPPORTING INFORMATION

Experimental

Synthesis of PTI-LiBr: 1 g of precursor dicyandiamide (DCDA, Sigma Aldrich >99%) is ground with a vacuum dried eutectic salt mixture of LiBr and KBr (Sigma Aldrich /Acros Organics >99%) (15 g; 52:48 wt%, m.p. 348°C) in a glovebox. The reaction mixture is filled into a quartz ampule and sealed. The sealed quartz ampule is placed vertically into a furnace (Nabertherm, L 5/11/B180, 2.4 kW) at 400 °C for 4 h. Then the temperature is increased (10 K/min) to the final condensation temperature for the desired timeframe. The ampule is removed at room temperature, opened, and the salt block is dissolved in dest. Water in a 50 mL Falcon. The slurry is centrifuged and the supernatant is decanted. The pellet is re-dispersed in hot water on a shaker and centrifuged again. The supernatant is decanted and the process is repeated for two times with hot water and two times with methanol (>99% for synthesis). The resulting pellet is redispersed in methanol and the methanol is evaporated. The resulting powder is dried under vacuum at 200 °C for 24 h. The furnace geometry and temperature homogeneity play a role for the synthesis of organic materials at temperatures close to carbonization. For repeatable experiments the ampule should be placed at the same spot in the furnace.

PTI-IF was obtained following the procedure proposed by Suter et al. (https://doi.org/10.1039/C8SC05232H) using PTI-LiBr synthesized at 550 °C for 48 h.

First-principle calculations: First-principles calculations are performed on model monolayer structures featuring various protonation conditions – see Figure S6. The unit cell of the PTI monolayer is formed by 18 atoms which comprise the two triazine rings and three imide bridges atoms and the system is assumed to be periodic only in the planar directions. 10 Å of vacuum are included in the directions perpendicular to the layer to avoid unphysical interactions between the replica. Protonation is realized by placing one dissociated HCl molecule per unit cell in proximity to the protonation site (nitrogen at one triazine ring or nitrogen at one imide-bridge, see Figure S6a) and then relaxing the system. The explicit inclusion of the Cl counterion ensures charge neutrality and includes the electrostatic effect of the anion on the protonated system. The equilibrium position of the Cl^- ion, relative to the protonated backbone, is obtained with a further structural optimization of the whole system that places it at the pore centre as shown in Figure S6b-c.

Ground state calculations are performed from spin-restricted DFT [Hohenberg P and Kohn W Phys. Rev. 136 B864 (1964) and Kohn W and Sham L J Phys. Rev. 140 A1133 (1965)] as implemented in the pseudopotential, plane-wave code Quantum Espresso (QE). A uniform 6x6x1 k-mesh is adopted to sample the Brillouin zone, the PBE functional [REF Perdew J P, Burke K and Ernzerhof M Phys. Rev. Lett. 77 3865 (1996)] is used to approximate the exchange-correlation potential, optimized norm conserving pseudopotentials are employed with 50 Ry (200 Ry) plane-wave cut-off to represent the wavefunctions (charge density). The pairwise Tkatchenko-Scheffler scheme [A. Tkatchenko and M. Scheffler, Phys. Rev. Lett. 102, 073005 (2009)] is adopted to include dispersion interactions. The structures are optimized without imposing any symmetry constraint until residual interatomic forces are smaller than 10^{-5} Ry/Bohr. Optical absorption spectra reported are computed from time-dependent DFT [Runge and Gross Physical Review Letters. 52 (12): 997–1000 (1984)] in the linear-response approach. For these calculations the turbo-TDDFT routine of QE is used, implementing the Liouville−Lanczos algorithm. A Lorentzian of 130 meV is applied to each peak.

Preparation of PTI-LiBr dispersions: Sonication of Flakes was conducted with a BANDELIN HD 2200/-U (200 W, HF 20 kHz) sonotrode setup with a MS72 sonotrode with the amplitude set to 10% in continuous mode. 30 mg of PTI-LiBr and 5 mL dist. water are added into a 50 mL falcon tube. The falcon tube is placed in an ice bath and the sonotrode has been immersed about 3-5 mm into the dispersion. Dispersions are sonicated for 3 h, centrifuged at 7690 g for 1 min to reduce large particles and the supernatant was removed from the pellet with a pipet into a falcon. Dispersions with different HCl concentration for optical experiments were prepared by adding 50 µL of the PTI-LiBr dispersion to 3 mL of a corresponding HCl dilution.

Preparation of Photoconductor devices: Ossila “Interdigitated ITO Substrates for OFET and Sensing” S161: $w \times L$: 30 mm × 50 µm were coated with a PTI-LiBr dispersion by drop-casting.

Photoconductor characterisation: Thorlabs LED 375 nm has been controlled by a Keithley 2461 in pulse mode at 3.6 V and a current limit of 1 A. The pulse chain was set to 1 s bias and 5 s off repeating ten times. The interdigitated substrate was contacted by an ossila board “Push-Fit Test Board for Photovoltaic Substrates (8 pixel)” and IV characterisation was conducted with a source measure unit (4200A SCS parameter analyser; Keithley). **For Figure S9a** the LED was focused with a Thorlabs collimator adapter (SM1U25) on the substrate and the irradiance was determined with a thorlabs power meter (PM120VA) to be 458 Wm^{-2}. The current without 375 nm irradiation was determined to be 0.050 µA, with irradiation the current was 0.122 µA at a film thickness of 100 µm and 20 V applied.

$$\sigma = \frac{1}{\rho} = \frac{L}{\frac{U}{I} A} = \frac{L}{\frac{U}{I} w\, t}$$

ρ= electrical resistivity
σ=electrical conductivity
U=bias
I=current
A=surface area
w=channel width
t=film thickness
L=channel length

For **Figure S9b** the LED was not focused with a collimator and the irradiance was determined by calculating it in dependence on the distance between substrate and LED light source.

Film thickness measurements: For extraction of conductivity film thickness values have been obtained with an Olympus LEXT laser scanning microscope.

Fourier transform infrared (FT-IR): Spectra were recorded from solid on a Thermo Scientific Nicolet iS5 spectrometer (Thermo Fisher Scientific, Waltham, MA, USA) in the wavenumber range of 4000-600 cm-1 with resolution of 4 cm-1.

Raman: UV Raman spectra were recorded with a Horiba T64000 spectrometer in single-grating mode. The excitation source was provided by a diode-pumped solid-state laser from CryLas at a wavelength of 266 nm and power of 4 mW. The light was focused on the sample with a Thorlabs LMU-40x-UVB objective (backscattering geometry). A notch filter with cut-off at 220 cm^{-1} was used to filter out the elastically scattered light. The acquired Raman spectra were calibrated by comparison with the spectrum of a Ga_2O_3 crystal by using a quadratic calibration curve. This procedure allows for reduction of the experimental error at approximately 5 cm^{-1}, which is below the spectral resolution of 8 cm^{-1}.

Powder X-ray: Structural analysis of the prepared PTI-MX was performed with a Bruker D2 Phaser X-Ray powder diffractometer (XRD) in Bragg-Brentano geometry. X-rays were generated by a Cu $K_{\alpha 1+2}$ source at 30 kV operating voltage and collected with a LynxEye detector.

Photoluminescence, Photoluminescence excitation, quantum yield, Lifetime: Edinburgh Instruments FLS 980 spectrometer. Photoluminescence, photoluminescence excitation and quantum yield were measured using a Xe lamp. The quantum yield was determined in a direct excitation set up with an integrating sphere. Films were drop-casted from ethanol dispersions on quartz substrates PGO 10x10x0.5 mm. Further, it is important to note that the presented samples were prepared and characterised on the same day. Diffusion of protons in PTI-LiBr has not been studied yet. It is possible that crystals of PTI-LiBr are not fully protonated because the system has had not enough time to equilibrate. This might explain why the luminescence of the basic Li-defect is still present in acidic solutions. Lifetime measurements were conducted with an Edinburgh Instruments 375 nm pulsed laser set to a 50 ns pulse period. Evaluation was conducted with the instrument software choosing a two exponential decay function.

UV-Vis: UV-VIS-measurements were performed in ambient conditions with a PerkinElmer Lambda 950 spectrometer in standard transmission operation, 1 nm step size. Films were measured on 10x10x0.5 mm quartz substrates. Dispersions were measured in a quartz cuvette with 1 cm optical path.

XPS, UPS: JOEL JPS-9030 Photoelectron Spectrometer with an Al kα (1486 eV) excitation source and a monochromator. Quantitative comparison of nitrogen and carbon in single spectra were performed by signal integration after background subtraction of a Shirley function. The samples were prepared by drop-casting PTI dispersions (MeOH) on ITO coated glass substrates to minimize charging and to avoid background carbon signals from e.g. carbon tape as substrate. For UPS experiments, a hydrogen discharge lamp (employing H Lyman-α lamp from Excitech, 10.2 eV) was used.(doi: 10.1016/j.orgel.2016.11.032) For determination of the secondary electron cut off (SECO) a negative bias of 10 V was applied to clear the analyser work function. All measurements were performed at room temperature. The obtained values were rounded to one decimal place. The work function was determined by linear fitting of the background and the linear region of the SECO, and reading of the point of intersection. The hole injection barrier was determined by linear fitting of the background and the valence band onset, and reading of the point of intersection. The error of the measurement is ±0.1 eV. Samples for UPS were prepared by dispersing 6 mg/mL of PTI-LiBr in MeOH (Roth, ≥99%) by sonication for 10 min and subsequently dropcasting 50 µL of the dispersion at 60 °C on ITO coated glas substrates (1x1cm).

SUPPORTING INFORMATION

ssNMR: Cross polarization magic-angle spinning (CP-MAS) solid-state NMR spectra were recorded on a Bruker Avance 400 MHz spectrometer operating at 100.6 MHz (^{13}C).

SEM: The sample was dispersed in Methanol (~0.6 mg/mL) with a micropipette and 0.5-1 µL were dropcast in the middle of a holy carbon TEM grid. SEM images have been recorded with a GeminiSEM 500 electron microscope (Carl Zeiss GmbH, Germany).

Low-dose, high-resolution transmission electron microscopy: The sample was dispersed in Methanol (~0.6 mg/mL) with a micropipette and 0.5-1 µL were dropcast in the middle of a holy carbon TEM grid. The TEM grids were loaded into a cryogenic transfer holder (Gatan 914, Gatan, Munich, Germany) at room temperature and transferred to the TEM. Once in the TEM, the holder was cooled down with liquid nitrogen and imaging was performed with a low dose acquisition scheme using SerialEM (doi: 10.1016/j.jsb.2005.07.007) on JEM-2100 (JEOL GmbH, Eching, Germany) operated at 200 kV and equipped with a 4 k × 4 k CMOS digital camera (TVIPS TemCam-F416). HRTEM images were acquired at a magnification of 500,000×, corresponding to a pixel size of 0.23 Å at the specimen level, while keeping the total electron dose below 20 e $Å^{-2}$. All imaging was carried out at temperatures around 90 K.

PTI-LiBr HCl titration: 26 mg PTI-LiBr were suspended in 30 mL dest. water by sonication. The pH value changed from 5.5 to 9.4 after suspension of PTI-LiBr. A 0.1 M HCl solution was used as titrant and added in 50 µL then 100 µL steps while stirring with a magnet stirrer. The pH was monitored with a pH glas electrode. The experiment was conducted at room temperature.PTI-LiBr dispersion for OLED preparation: 30 mg of PTI-LiBr and 5 mL chlorobenzene (Sigma-Aldrich, anhydrous, 99.8%) are added into a 50 mL falcon tube. The falcon tube is placed in an ice bath and the sonotrode has been immersed about 3-5 mm into the dispersion. Dispersions are sonicated for 3 h, centrifuged at 95 g for 5 min. The supernatant is transferred into a new falcon tube and the procedure is repeated at 857 g for 5 min two times. Sediments were re-dispersed via sonication (10 min) in a sonication bath prior to usage.

OLED preparation: ITO-coated glass substrates (sheet resistance = 20 Ω per square) were cleaned by sequential sonication (10 minutes) in (i) acetone and (ii) isopropanol followed by drying *via* a nitrogen gun. The substrates were then treated *via* O_2 plasma (partial pressure 1.2×10^{-1} mbar) for 15 minutes at 10.2 W. 50 nm PEDOT:PSS (Osilla) films were spin coated as hole injection layer and heated to 220 °C for 10 min. 40 µL PTI-LiBr dispersion were drop cast at 60 C from the chlorobenzene dispersion onto the pixel areas of the PEDOT:PSS covered substrate (ca. 150 mm^2). 5 nm Calcium and 200 nm Aluminium were evaporated in a PVD chamber at 10^{-5} mbar. Finally the OLEDs were encapsulated with UV-curable resin (Osilla) and a glass slide. Current density–voltage–luminance characterization was performed with a Keithley 2612B source meter and a Konica Minolta LS-160 luminance meter in a purpose-built setup. Electroluminescence spectra were taken with a CS2000 spectrometer (Ocean Optics) using OceanView software.

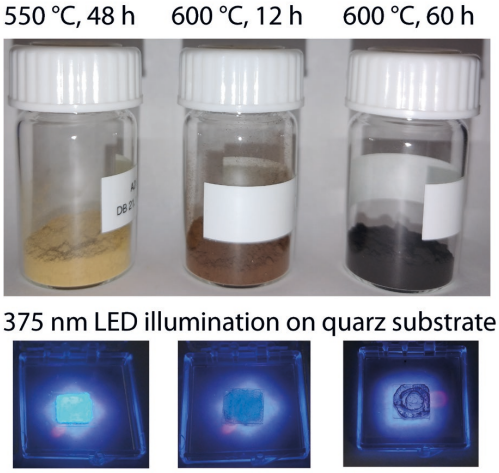

Figure S1. Three vials with the product of the condensation reaction at 550 °C, 48 h, 600 °C, 12h and 600 °C, 72 h are depicted. Underneath are the corresponding films on quartz substrates drop casted from dispersion for the 550 °C 48 h product, 600 °C 12 h and 600 °C 72 h product. The brown color is a result of on setting carbonization and leads to self-absorption and deteriorates charge transport through the polycrystalline material.

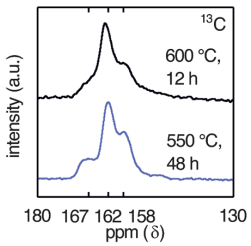

Fig**ure S2**.Solid state NMR (ssNMR) of PTI-LiBr obtained from conditions reported in literature 600 °C 12 h and at lower temperature 550 °C, 48 h. The spectrum obtained from the product synthesized at lower temperature has sharper bands. The three observed bands correspond to three carbon environments present in PTI-LiBr as well as PTI-LiCl at 167.0 ppm 162.0 ppm and 158.0 ppm.

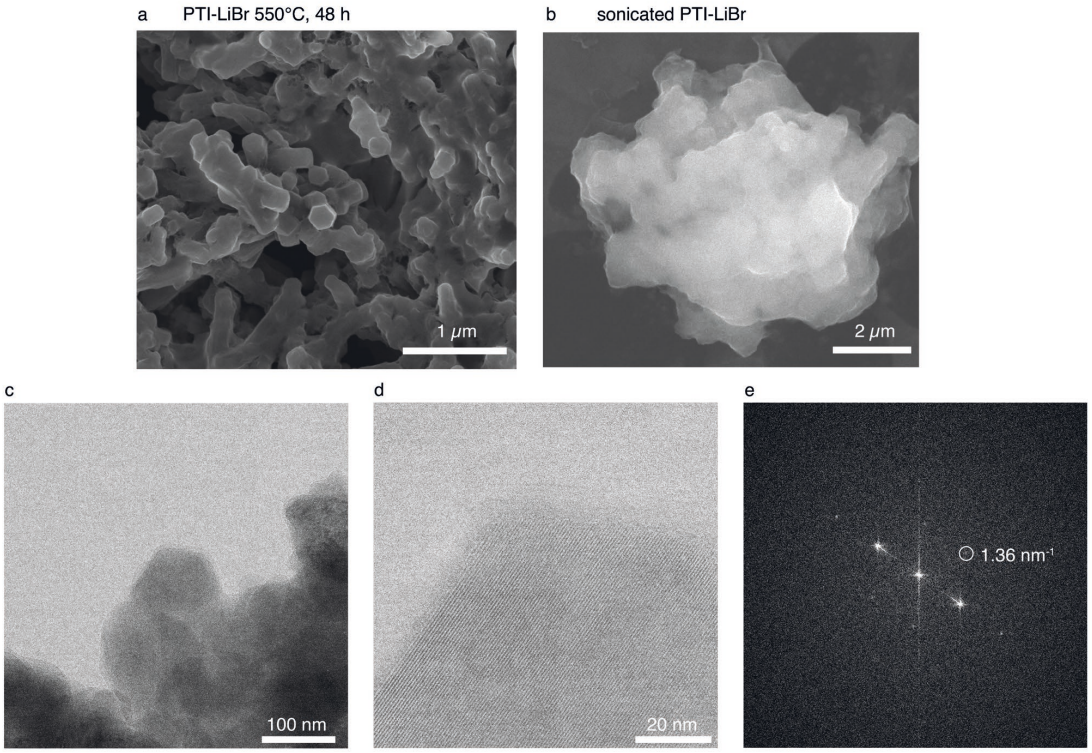

Figure S3. SEM and HR-TEM studies of PTI-LiBr product. a) The anticipated hexagonal platelets of PTI-LiBr (5 kV acceleration voltage). b) PTI-LiBr product after 30 min sonication (20 kV acceleration voltage). SEM pictures after sonication show typically a film of debris covering all structures. HR-TEM at an acceleration Voltage of 200 kV of PTI-LiBr from 550 °C synthesis. c) 100.000x magnification HR-TEM image d) 500.000x magnification HR-TEM image e) Fourier transformation of d) reveals the characteristic 100 reflex at 1.36 nm^{-1} (0.73 nm) and the hexagonal periodicity of PTI-LiBr.

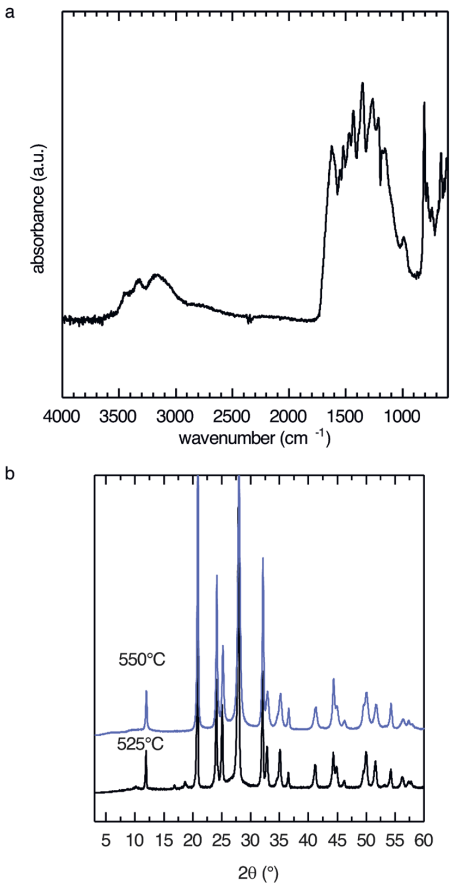

Figure S4. a) FT-IR of PTI-LiBr product from 525 °C for 48 h b) PXRD of PTI-LiBr product from 525 °C for 48 h compared to 550 °C for 48h. Additional contributions in the NH region and additional PXRD peaks indicate incomplete condensation.

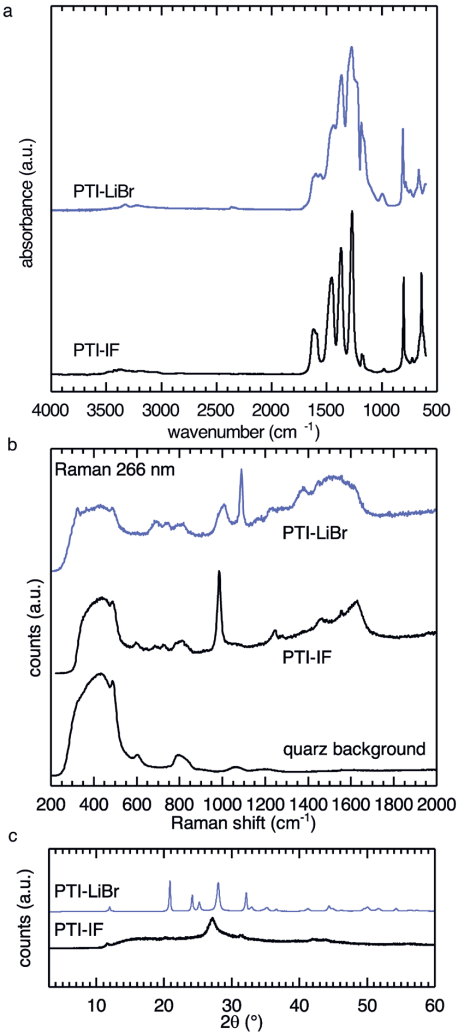

Figure S5. a) FT-IR b) UV-Raman and c) PXRD of PTI-LiBr and PTI-IF. De-intercalation of PTI-LiBr results in more defined IR and Raman bands. PTI-LiBr has an unexpected strong Raman signal at 1088 cm^{-1}. This could be due to formation of small amounts of lithium carbonate in a surface reaction. The lithium defect can undergo hydrolysis in presence of atmospheric water. The reaction of LiOH with atmospheric CO_2 results in lithium carbonate. The PXRD of PTI-IF shows the loss of the graphitic order after removing the structure directing salt ions.

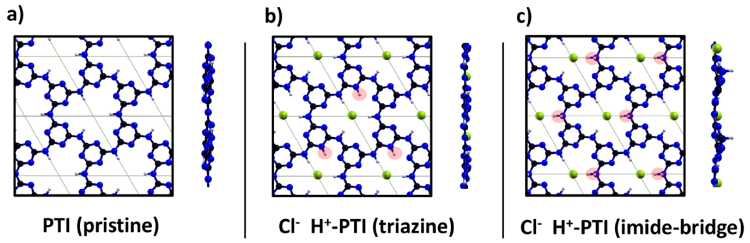

Figure S6. PTI single monolayer relaxed structures in-vacuo, relative to PTI-IF (a), the triazine-protonated (b) and the imide-bridge protonated (c) backbones. In the protonated structures we have also reported the formation energies per unit-cell volume evaluated as the difference between the total energy of the protonated system and the sum of the energies of the separated pristine monolayer and HCl subsystems.

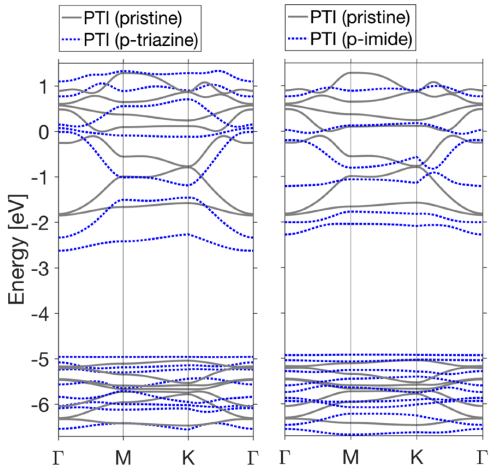

Figure S7. Electronic bandstructures of pristine PTI-IF (gray lines) and triazine / imide-bridge protonated-PTI (blue dashed lines).

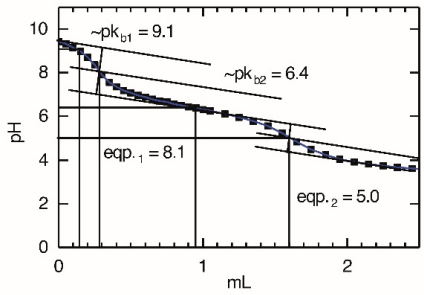

Figure S8. HCl (0.1 M) titration of 26 mg PTI-LiBr (550 °C, 48 h) dispersion. The second equivalence point at pH 5 corresponds to the pH region where also changes in the optical spectra take place (emergence of 330 nm, 420 nm photoluminescence and 260 nm absorption band).

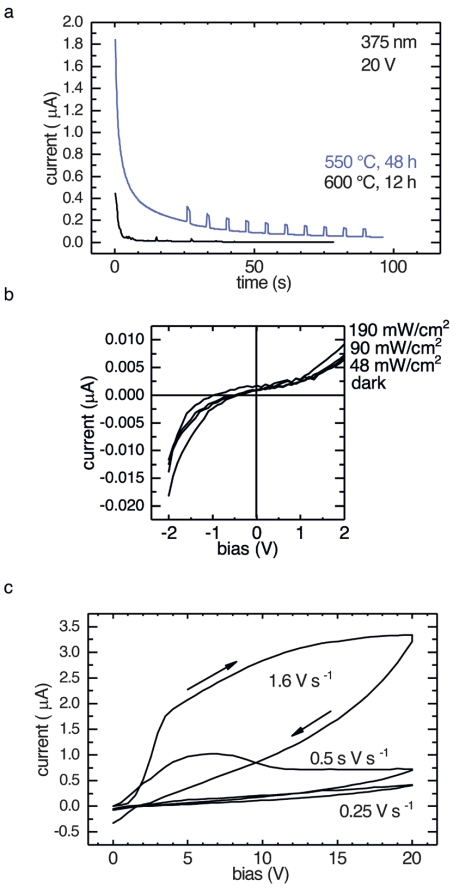

Figure S9. a) Comparison of photoconductor employing PTI-LiBr from 600 °C and 550 °C. Charge transport and photocurrent are absent in the 600 °C material due to the observed partial carbonization (black line). In the device employing PTI-LiBr from 550 °C current is able to cross the channel of the interdigitated substrate and photocurrent is observed when excited with a 375 nm LED at 375 nm at an irradiance of 46 mW cm^{-2}. b) Irradiance dependent IV sweep of photoconductor device. Increased irradiance with a 375 nm LED results in increased current flow. The low current is result of the polycrystalline material property (grain boundaries) and likely energetic disorder at partially intercalation free layers. b) IV sweeps of an interdigitated device employing 550 °C, 48 h product with different sweep speed. The observed hysteresis is due to migration of Li^+ and Br^- ions.

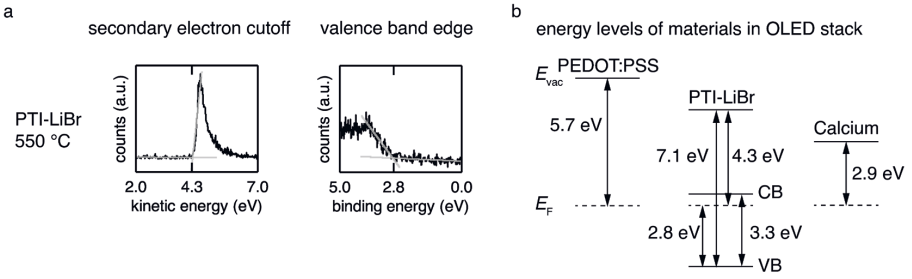

Figure S10. a) Ultraviolet photoelectron spectroscopy (UPS) PTI-LiBr dropcasted on ITO substrates. b) Energy levels of OLED materials. Work functions of PEDOT:PSS and calcium have been extracted from literature (doi: 10.1063/1.2435350, doi: 10.1063/1.32353). The valence band of PTI-LiBr is measured by UPS while the conduction band is estimated combining the latter with the UV-Vis spectroscopy data.

Chemistry–A European Journal
Research Article
doi.org/10.1002/chem.202200705
Chemistry Europe
European Chemical Societies Publishing
www.chemeurj.org

Size Effects of the Anions in the Ionothermal Synthesis of Carbon Nitride Materials

David Burmeister,[a] Johannes Müller,[c] Julian Plaickner,[d] Zdravko Kochovski,[e] Emil J. W. List-Kratochvil,[a] and Michael J. Bojdys*[a, b]

Abstract: Semiconducting carbon nitride polymers are used in metal-free photocatalysts and in opto-electronic devices. Conventionally, they are obtained using thermal and ionothermal syntheses in inscrutable, closed systems and therefore, their condensation behavior is poorly understood. Here, the synthetic protocols and properties are compared for two types of carbon nitride materials – 2D layered poly(triazine imide) (PTI) and hydrogen-bonded melem hydrate – obtained from three low-melting salt eutectics taken from the systematic series of the alkali metal halides: LiCl/KCl, LiBr/KBr, and LiI/KI. The size of the anion plays a significant role in the formation process of the condensed carbon nitride polymers, and it suggests a strong templating effect. The smaller anions (chloride and bromide) become incorporated into triazine (C_3N_3)-based PTI frameworks. The larger iodide does not stabilize the formation of a triazine-based polymer, but instead it leads to the formation of the heptazine (C_6N_7)-based hydrogen-bonded melem hydrate as the main crystalline phase. Melem hydrate, obtained as single-crystalline powders, was compared with PTI in photocatalytic hydrogen evolution from water and in an OLED device. Further, the emergence of each carbon nitride species from its corresponding salt eutectic was rationalized via density functional theory calculations. This study highlights the possibilities to further tailor the properties of eutectic salt melts for ionothermal synthesis of organic functional materials.

Introduction

Carbon nitride materials have emerged as interesting and chemically tunable,[1–10] metal-free semiconductors with applications in heterogenous photocatalysis,[11–15] and most recently as active materials in organic light-emitting diodes.[16–18] Conventional synthetic protocols for carbon nitride materials center on high-pressure decomposition of CNH-containing molecular,[19,20] ion and vapor deposition of nitrogen ions and carbon,[21] plasma decomposition of methane and N_2,[22] shock wave compression,[23] sputtering experiments, pulsed laser ablation of graphite in combination with an atomic nitrogen source, and electrochemical approaches.[24,25] Diffusion-controlled methods do not yield high quality products, as the formation of the crystalline product is impeded by atom displacement and knock-on collisions.[6,26] In contrast, poly(triazine imide) – or PTI for short – is the most well-defined, crystalline form of graphitic carbon nitrides, and it is obtained via ionothermal condensation of dicyandiamide (DCDA, $C_2H_4N_4$) in eutectic salt melts.[1,26] PTI is a 2D material with layers built from covalently-linked triazine (C_3N_3)-units that form triangular pores into which anions (chloride and bromide) and lithium cations from the salt melt become intercalated selectively (Figure 1a, b, d).[26] The snug fit of the halide anions into the pores of layered PTI suggests a strong templating effect. Eutectic salt melts control the structure of the carbon nitride materials formed in ionothermal synthesis as they act as polar solvents with extremely high boiling points for organic mono- and oligomers.[1,26] To-date, however, the role of the anions in the ionothermal formation of carbon nitrides has not been elucidated.

[a] D. Burmeister, Prof. Dr. E. J. W. List-Kratochvil, Prof. Dr. M. J. Bojdys
Department of Chemistry & IRIS Adlershof
Humboldt-Universität zu Berlin
Brook-Taylor-Str. 6, 12489, Berlin(Germany)
E-mail: m.j.bojdys.02@cantab.net

[b] Prof. Dr. M. J. Bojdys
Department of Chemistry
King's College London
Britannia House Guy's Campus, 7 Trinity Street, London, SE1 1DB (UK)

[c] J. Müller
Department of Physics & IRIS Adlershof
Humboldt-Universität zu Berlin
Newtonstraße 15, 12489, Berlin (Germany)

[d] J. Plaickner
Helmholtz-Zentrum Berlin für Materialien und
Energie GmbH Hahn-Meitner-Platz 1
14109 Berlin (Germany)
and
Leibniz-Institut für Analytische Wissenschaften – IAS e.V.
Schwarzschildstrasse 8, 12489 Berlin (Germany)

[e] Dr. Z. Kochovski
Institute of Electrochemical Energy Storage Helmholtz-Zentrum Berlin für Materialien und Energie
Hahn-Meitner-Platz 1, 14109 Berlin (Germany)

Supporting information for this article is available on the WWW under https://doi.org/10.1002/chem.202200705

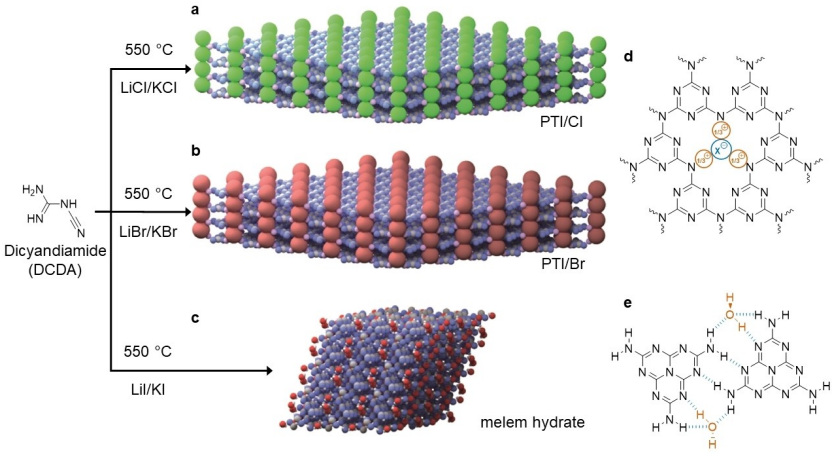

Figure 1. Condensation products of dicyandiamide (DCDA) in different eutectic salt melts: a) poly(triazine imide) with intercalated chloride (PTI/Cl), b) poly(triazine imide) with intercalated bromide (PTI/Br), and c) melem hydrate ($C_6H_6N_{10}\cdot H_2O$). d) The poly(triazine imide) network forms triangular cavities with inclusion of halides (X^-, in blue) counterbalanced by lithium (in orange). e) Melem hydrate forms an extended hydrogen-bonded network (in blue) between melem ($C_6H_6N_{10}$) units and water (in orange) in three-dimensions.

In this study, we investigate systematically the influence of three eutectic salt melts with increasing anion sizes ($Cl^- < Br^- < I^-$) on the formation of carbon nitride materials during ionothermal synthesis, namely: (i) LiCl/KCl (45 wt%/55 wt%, m.p. 352 °C), (ii) LiBr/KBr (52 wt%/48 wt%, m.p. 348 °C), and (iii) LiI/KI (58 wt/42 wt%, m.p. 285 °C).[27]

We consider the known chloride- and bromide-intercalates of poly(triazine imide) and compare them with the hitherto unknown product from the iodide eutectic. The carbon nitride material from the LiI/KI salt melt is obtained as a powder from which we isolate single crystallites for structural analysis using single crystal X-ray diffraction (sc-XRD). The isolated single crystals were identified as melem hydrate (Figure 1c, e). Using the iodide eutectic as the medium for ionothermal synthesis, we did not observe the formation of a crystalline extended polymer with a higher degree of condensation. This finding strongly indicates that the smaller anions (Cl^- and Br^-) are stabilizing the formation of poly(triazine imide) layers and facilitate their π-π stacking, as confirmed by density functional theory calculations (CASTEP).

Results and Discussion

Experimental design

The poly(triazine imide) (PTI) framework provides two types of potentially accessible volumes for lithium halide intercalates: (i) within the pores defined by the in-plane, covalent bonding pattern of covalently linked triazine (C_3N_3)-units (Figure 2, a; blue spheres with radius, r_{pore}), and (ii) in the galleries between π-π stacked PTI layers (Figure 2, a; with distance, $d_{(002)}$). Since the material is overall charge-neutral, we assume intercalation of a lithium halide species with a total, dynamic radius, r_{tot}, that may not exceed the pore diameter, r_{pore} (Figure 2, b). The gallery height for stacked PTI sheets is known to be 3.3751 Å for PTI/Cl and 3.52241 Å for PTI/Br,[1,26] which correlates with the ionic diameters for chloride (3.34 Å) and for bromide (3.64 Å). Hence, for a hypothetical PTI/I we assume that the gallery height does not exceed $d_{(002)} = 4.12$ Å which is the radius of iodide (Figure 2, c). Using standard values from the Computational Chemistry Comparison and Benchmark Data Base (CCCBDB), we obtain dynamic radii of lithium halides as follows: 2.161 Å for LiCl, 2.325 Å for LiBr, and 2.531 Å for LiI (Figure 2, d). These will serve as probe radii for the generation of Connolly surfaces. We further consider the two extreme cases in which (i) the bridging NH-groups are fully deprotonated and become available for isoelectronic replacement by lithium cations (Figure 2, e, f, i, j, m, n) and (ii) the bridging NH-groups remain fully protonated (Figure 2, g, h, k, l, o, p). Examining the Connolly surfaces generated using these constraints (Figure 2, e-p), we observe that lithium halides can in principle be intercalated into the interstitial spaces between the sheets above and below the pores of all PTI structures. In the case that bridging NH-groups are isoelectronically converted to NLi-groups, sufficiently large free volumes exist in the pores of PTI/Cl and PTI/Br to allow in-plane incorporation. However, LiI is too large. In the case that bridging NH-groups remain unchanged, there appears to be no free volume within the pores, but all lithium halides could potentially be situated in the interstitial spaces above and below.

The expected layer-stacking distance for PTI/I of ≥4.12 Å that is needed to accommodate a pillared arrangement of iodide species is exceptionally large for an aromatic, discotic system (cf. graphite 3.35 Å, PTI/Cl 3.38 Å, PTI/Br 3.52 Å).[1] Hence, as a working-hypothesis, we assume that a poly(triazine imide)

Research Article
doi.org/10.1002/chem.202200705
Chemistry Europe
European Chemical Societies Publishing

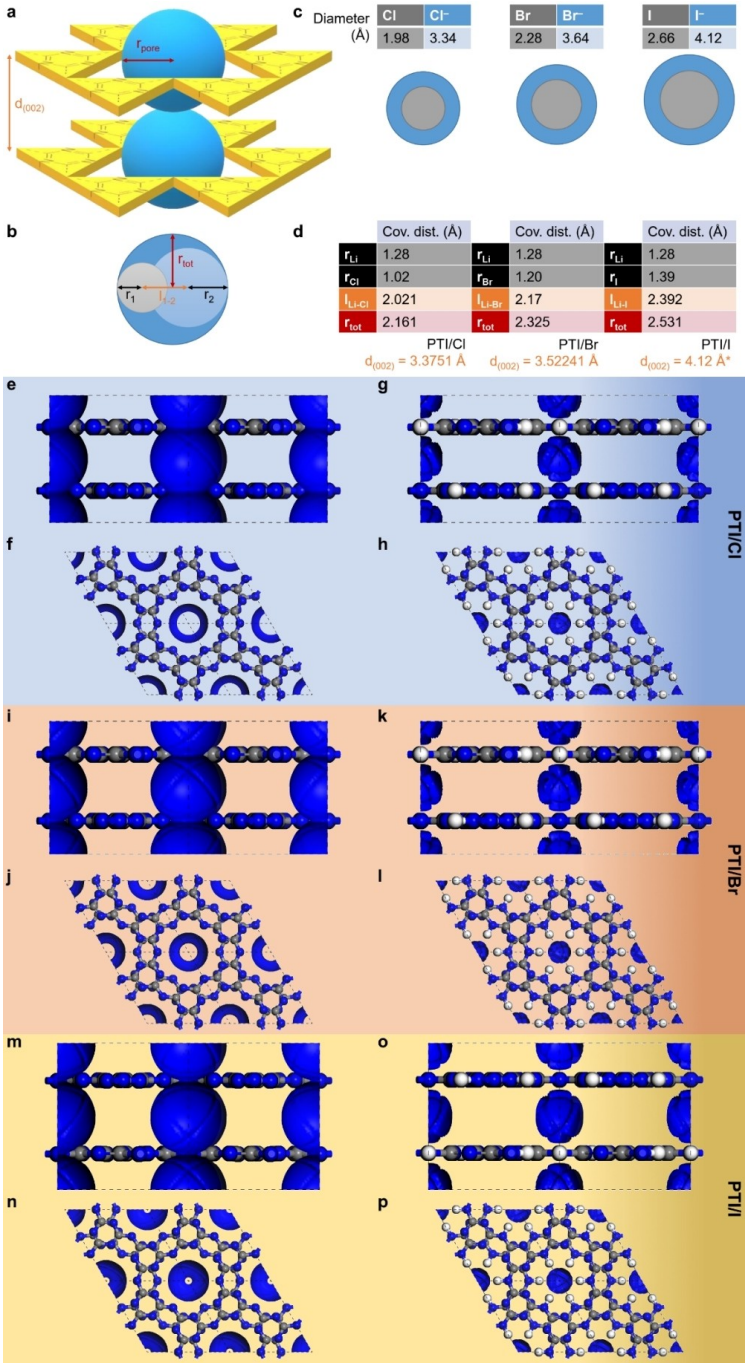

Figure 2. Considerations of available free volume for intercalation of lithium halide species in poly(triazine imide) frameworks. a) Principally available space in a PTI-based framework is confined by the pore diameter, r_{pore}, and the galley height, $d_{(002)}$. b) Representation of the dynamic covalent radius, r_{tot}, of a lithium halide. c) Diameters of halogen atoms and their respective halides. d) Table above, calculation of the dynamic covalent radii of lithium chloride, lithium bromide, and lithium iodide. Below, gallery heights for poly(triazine imide) model structures with intercalated lithium halides, derived from experiment for PTI/Cl and PTI/Br and, and estimated for PTI/I (denoted by *) on the basis of the iodide radius. Connolly surface areas (in blue) generated for PTI frameworks with removed hydrogens (e, f) and without (g, h) using the dynamic covalent radius of LiCl as probe molecule. In analogy, Connolly surface areas generated for PTI frameworks using LiBr (i-l) and LiI (m-p) as probe molecules, respectively.

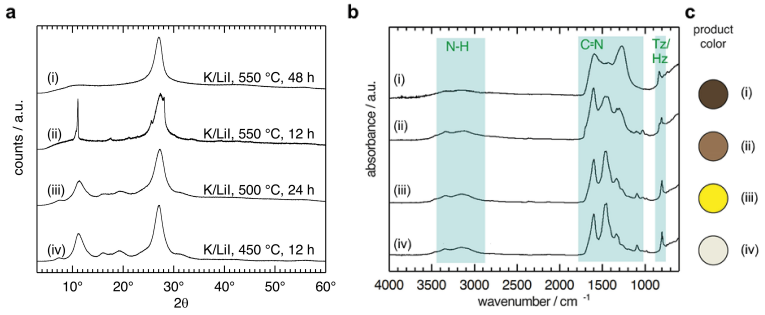

Figure 3. Powder X-ray diffraction (PXRD) data (a), Fourier transform-infrared (FTIR) spectra (b), and product colors (c) of carbon nitride samples obtained at various conditions in a LiI/KI eutectic (i-iv).

with intercalated LiI will not form and that, instead, a synthesis in LiI/KI will conceivably lead to (i) an intercalate-free PTI, (ii) a PTI with a stacking mode other than pore-on-pore, or (iii) a different material entirely.

Characterization and identification of the crystalline product from the iodide eutectic

The ionothermal condensation of DCDA in LiI/KI eutectic was set-up according to literature, in analogy to existing protocols for PTI/Cl and PTI/Br,[16,28] and as outlined in the Supporting Information. We screened reaction conditions with different temperatures between 450 °C and 550 °C and with reaction times from 12 h to 48 h. We present an overview of the powder X-ray diffraction (PXRD) and Fourier transform-infrared spectroscopy (FTIR) data for all additional products obtained at various reaction conditions in the Supporting Information section (Figure S1). Products obtained at temperatures below 550 °C show broad peaks in the diffractogram (Figure 3, a), indicating that the condensation process is still incomplete. The color of the powders obtained in the range from 450–500 °C changes from white to bright yellow as temperature is increasing. FTIR spectra show the presence of NH_2 at 3460 and 3350 cm^{-1} signals and a peak at 796 cm^{-1} attributed to the out-of-plane breathing-mode of triazines (C_3N_3, Tz) and heptazines (C_6N_7, Hz) (Figure 3, b).[29]

The elemental composition of products obtained at temperatures up to 500 °C for 24 h fits with the CN ratio of melem (Table 1, Table S1). Extended reaction times (e.g. 48 h) and higher temperatures (e.g. 550 °C) yield samples with drastically increased carbon content, leading to a darker coloration and an amorphization of the product (Figure 3, a (i)). Compared to crystalline PTI/Br that is obtained as a beige powder after 48 h at 550 °C,[1] the early onset of carbonization in LiI/KI eutectics indicates that the formation of a more temperature stable, crystalline poly(triazine imide) structure is disfavored due to a lack of stabilizing anions of appropriate size. Moreover, instead of the intercalation of alkali iodide and the appearance of a PTI-type diffraction pattern (Figure 3, a), we observe the formation of iodine vapors inside the quartz ampoule at temperatures above 480 °C. This indicates that in the iodide eutectic DCDA reaction mix unidentified redox processes are ongoing at these temperatures (Figure S4). In comparison, using bromine and chlorine eutectics at temperatures up to 600 °C, we observed no formation of halogen gases.

Table 1. Combustion elemental analysis of products obtained from the LiI/KI eutectic at various reaction conditions (i-iv). The CN ratio of the products is compared to the expected CN ratio of melem.

Reaction conditions	C:N
(i) LiI/KI, 550 °C, 48 h	0.55:0.45
(ii) LiI/KI, 550 °C, 12 h	0.46:0.54
(iii) LiI/KI, 500 °C, 24 h	0.38:0.62
(iv) LiI/KI, 450 °C, 12 h	0.38:0.62
melem (theoretical)	0.38:0.62

^{13}C cross-polarization magic-angle-spinning (CP/MAS) solid-state NMR spectra of the products show bands at 154 ppm and 164 ppm in good agreement with the reported values for melem at 155 ppm and 164 ppm (Figure S2).[29] ^{15}N solid-state NMR has two main features at 204 ppm and 280 ppm that we assign to the pyridinic nitrogen and the amine nitrogen environments reported for melem (at 205 ppm and 281 ppm).[29] A weak band at 259 ppm is assigned to amorphous condensation products containing secondary amines that is structurally similar to short chains of condensed melem units (so-called "melon"). When compared to melon, the NH_2 (265 ppm) and NH (245 ppm) nitrogen bands are shifted towards higher ppm values.[30] The photoluminescence (PL) spectrum of the product obtained at 450 °C has a maximum at 385 nm which coincides with the PL data obtained for pure melem (Figure S3.).[29] With increasing temperature, the PL maximum shifts towards higher wavelengths. We interpret this shift as an increasing contribution of the amorphous, brown phase that we believe to be disordered, partially carbonized melon-like structures.[30,31] In summary, samples obtained at temperatures up to 500 °C contain melem as the main phase product. At a temperature of approx. 550 °C, we observe the onset of carbonization of the organic components.

We selected the carbon nitride material with the highest, apparent crystallinity (LiI/KI, 550 °C, 12 h; Figure 3, (ii)) for detailed investigations. Light microscopy reveals two phases: a brown phase with no geometric order and a transparent phase with rectangular crystallites (Figure 4, a). The crystals were imaged by scanning electron microscopy (SEM) (Figure 4, b) showing characteristic, sharp edges, and a rectangular shape.

Energy dispersive X-ray spectroscopy (EDX) of a crystallite corroborates the results of the combustion elemental analysis: the main elements are nitrogen (65 at%) and carbon (35 at%). Contributions from salt residues and carbonization are evident only in the amorphous, brown phase of the product (Figure S5). Notably, we observe no evidence of iodide intercalation in the carbon nitride crystals. To prove that the sample is also free of alkali metals, we performed inductively coupled plasma-optical emission spectroscopy (ICP-OES) and X-ray photoelectron spectroscopy (XPS). The condensation product obtained at 550 °C, 12 h contains 0.38 wt% Lithium and 0.73 wt% potassium. These residual amounts of alkali metals are low and non-stoichiometric. They are most likely inclusions situated in the amorphous, brown phase and cannot be washed out by hot water. XPS results confirm the CN-ratios observed in combustion elemental analysis and in EDX and show no salt contributions (Figure S6). UV-Raman spectra show indicative bands for heptazines at 1661 cm^{-1} (w), 1571 cm^{-1} (w), 1155 cm^{-1} (s) and 545 cm^{-1} (s) in the translucent crystals (Figure S7).[29] Strong bands at 980 cm^{-1} (s), 1401 cm^{-1} (s) and 1310 cm^{-1} (s) are unassigned. Raman bands in the amorphous, brown phase are weaker and broader compared to the spectra obtained for the crystals, as is anticipated for a highly disordered phase.

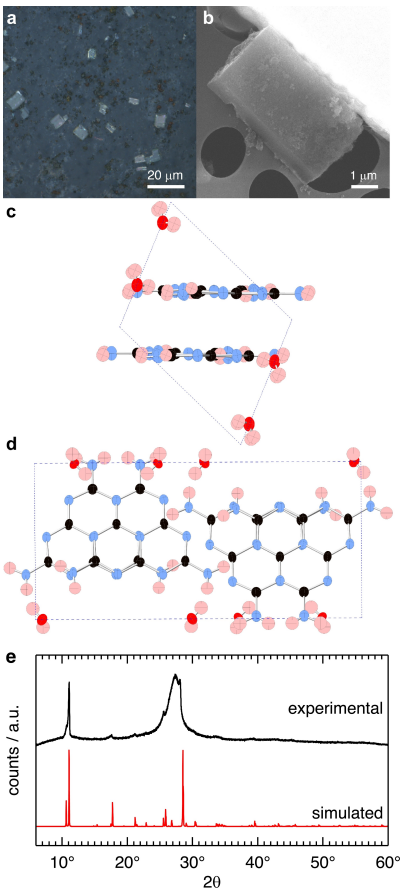

Figure 4. Structural characterization of melem hydrate crystals obtained at 550 °C and 12 h in the LiI/KI eutectic salt melt. a) Light microscopy image of the bulk product on scotch tape shows two morphologies distinguishable as brown, amorphous particles and rectangular crystallites. b) Scanning electron microscopy (SEM) (20 kV accelerating voltage) image of a single crystallite. Ball-and-stick representation of the unit-cell of melem hydrate obtained from single-crystal X-ray diffraction projected along c) the b-axis and d) the c-axis, respectively. Atomic positions are marked as thermal ellipsoids, colored red for oxygen, blue for nitrogen, black for carbon and light red for hydrogen. Hydrogen positions are approximated. e) Comparison of the powder X-ray diffraction (PXRD) pattern of the bulk product (in black) and the simulated diffraction pattern of melem hydrate based on the structural data from single crystal X-ray diffraction data (in red).

We were able to solve the crystal structure of the crystalline phase using single crystal X-ray diffraction. In this experiment, we used a micro actuator to pick up and transfer the micro-sized crystallites (Figure S8). The structure solution revealed the crystallites to be melem hydrate ($C_6N_7(NH_2)_3 \cdot H_2O$) (Table S2). The stacking distance of the melem units is 3.2 Å at slight offset to maximize dipole-dipole interactions (Figure 4, c). Melem hydrate crystals are held together by a three-dimensional network of hydrogen bonds with lengths of ~2.2 Å between (i) pyridinic nitrogen atoms of the heptazine cores and adjacent amine groups and (ii) water molecules and amine groups (Figure 4, d). In contrast, melem crystals obtained via sublimation are not aligned in co-planar layers.[29] The refined structure from the single crystal experiment is in good agreement with the PXRD profile of the bulk material (Figure 4, e). We attribute the additional broad peak at 27° 2θ to the emergence of the glassy, secondary brown phase that is formed because of carbonization of crystalline melem hydrate into randomly stacked, π-conjugated fragments. A similar behavior was reported previously for carbonization products of poly(triazine imide) in a LiBr/KBr eutectic.[16] As expected, melem hydrate undergoes a reversible phase change to melem during vacuum drying at 200 °C for 24 h (Figure S9).[29]

Scanning force microscopy (SFM) shows a high degree of order at the surface of melem hydrate single crystals (Figure S10). The observed periodicity is in good agreement with the Connolly surface of a melem hydrate crystal cleaved at the 001 plane. High resolution cryo-transmission electron microscopy (HR-TEM) images show periodic lattice fringes with 0.8 nm distances that correspond to the 001 crystallographic plane of melem hydrate (Figure S11).

In analogy to PTI-based organic light-emitting diodes (OLEDs),[16] we have constructed a single layer organic light emitting device from the product obtained at 500 °C, 12 h in LiI/KI. The device shows a steep diode like onset at 4.5 V in forward bias direction. At 13 V we observed a maximum luminance of only 1 cd m^{-2} (Figure S12). The Brunauer-Emmett-Teller (BET)

surface area was determined by nitrogen adsorption-desorption isotherms of the 450 °C and 550 °C products showing no micropores and a low surface area of 57 and 71 $m^2 g^{-1}$ respectively (Figure S13). In addition, we tested the hydrogen evolution reaction (HER) activity of products from 500 °C, 12 h and 550 °C, 12 h with triethanolamine as sacrificial agent under xenon lamp illumination without cutoff filter and $PtCl_6$ as co catalyst. Unlike PTI and polymeric carbon nitride,[25,32–34] we did not observe any detectable HER activity for dispersed melem hydrate.

Thermodynamic considerations of product stability in different salt melts

In contrast to the poly(triazine imide) intercalates obtained in LiCl/KCl and LiBr/KBr, we see that the ionothermal condensation of dicyandiamide in LiI/KI leads to a thermally less-stable melem hydrate as the main, crystalline product – and this although the interstitial cavities of the layered PTI framework would be sufficiently large to accommodate LiI in principle (Figure 2). Analogous reactions in an open crucible set-up using DCDA and a LiI/KI eutectic similarly found that no poly(triazine imide) structures are formed.[35] Our work and previous reports indicate that the condensation reaction is halted at melem, the precursor to the formation of poly(triazine imide) – irrespective of whether an open or closed reaction set-up is chosen.[36] We performed ab initio total energy density functional theory (DFT) calculations to compare the stabilities of the hitherto known main crystalline products from ionothermal, salt-mediated syntheses – PTI/Cl and PTI/Br – with the stabilities of a hypothetical PTI/I crystal and the identified melem hydrate phase (CASTEP; plane wave basis set; energy cut-off 450 eV; exchange correlation PBE-GGA; atomic relaxation until force/atom < 0.02 eV $Å^{-1}$) (Figure 5).[37] Due to the differences in unit-cell volumes and content, we have normalized the obtained cohesive energies, E_{coh}, per unit volume and used these values as a guide for material stability. We find that in the logical series of lithium halides LiCl → LiBr → LiI, the corresponding poly(triazine imide) intercalation compounds become less stable following a trend in stability of: PTI/Cl > PTI/Br > PTI/I. In the LiI/KI eutectic, melem hydrate is more stable than a hypothetical PTI/I framework, as observed in the experiment.

Based on our initial hypothesis, we pointed out the infeasibly large layer-stacking distance between PTI-sheets of ≥ 4.12 Å that is needed to accommodate a pillared arrangement of lithium iodide species. Our DFT calculations support that the artificially imposed, large gallery-height in a PTI/I structure chiefly contributes to a loss in cohesive van der Waals interactions between π-aromatic layers and disfavors the formation of a poly(triazine imide) framework. This calculation does not consider conceivable, energetic contributions from ionic stabilization of triazine-based intermediates along the reaction pathways, but it assists in rationalizing the observed selectivity of experimentally observed products.

Conclusion

In summary, we identified the main, crystalline product obtained from the ionothermal condensation of dicyandiamide in a LiI/KI eutectic salt melt as melem hydrate ($C_6N_7(NH_2)_3 \cdot H_2O$). This stands in contrast to poly(triazine imide) frameworks with intercalated lithium halides obtained from LiCl/KCl and LiBr/KBr

	Coh. energy, E_{coh} (eV)	Density (g cm^{-3})	Unit-cell volume ($Å^3$)	Coh. energy per unit vol. (eV $Å^{-3}$)
PTI/Cl	-8850.712009	1.90543	419.308	-21.10790161
PTI/Br	-9005.410554	2.14663	440.875	-20.42622184
PTI/I	-9326.962879	2.13797	515.671	-18.0870417
melem hydrate	-18735.83811	1.71677	913.849	-20.5021159

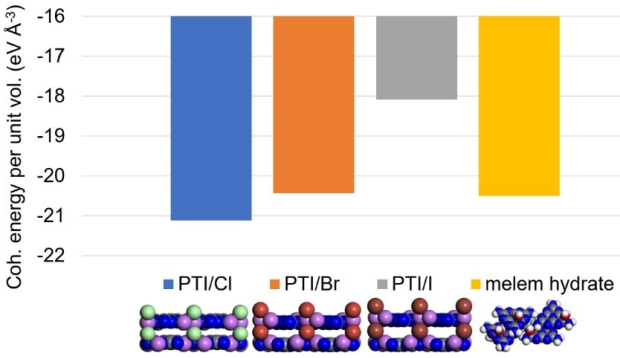

Figure 5. Results of ab initio total energy density functional theory (DFT) calculations using a plane wave basis set (CASTEP; energy cut-off 450 eV; exchange correlation PBE-GGA; atomic relaxation until force/atom < 0.02 eV $Å^{-1}$) for the four periodic carbon nitride materials PTI/Cl (in blue), PTI/Br (in orange), PTI/I (in grey), and melem hydrate (in gold).

eutectics. Glassy melem is the main product at temperatures below 500 °C, and transparent, monoclinic melem crystals are obtained at 550 °C ($P2_1/c$, a = 8.6040(17) Å, b = 16.630(3) Å, c = 6.8840(14) Å, β = 111.91(3)). In contrast to extended carbon nitride polymers, an OLED with melem powders as the active material shows only low luminance of 1 cd m^{-2}, and melem hydrate has no detectable activity as a photocatalyst in the hydrogen evolution reaction.

Unlike in LiCl/KCl and LiBr/KBr eutectics, we observe no selective, stoichiometric intercalation of lithium iodide into a 2D, extended triazine-based framework in the final product. DFT calculations corroborate that the pillared intercalation of lithium halides leads to a loss of stabilizing van der Waals interactions between extended, π-conjugated triazine-based sheets as the size of the intercalate increases (LiCl < LiBr < LiI), and ultimately to the selection of a thermodynamically more favourable, monomeric, heptazine-based product.

This study highlights the importance of anion-size effects in the ionothermal synthesis of π-conjugated organic materials, and it showcases a computationally-assisted methodology for future experiments that (i) use novel, binary and ternary eutectic salt melts, and (ii) aim for thermodynamic selectivity of reaction pathways and products.

Supporting Information

Supporting Information is available from the Wiley Online Library or from the author.

Deposition Number 2095271 contains the supplementary crystallographic data for this paper. These data are provided free of charge by the joint Cambridge Crystallographic Data Centre and Fachinformationszentrum Karlsruhe Access Structures service.

Acknowledgements

The authors are grateful for the collaboration with Ha Anh Tran, Niklas Grabicki, Josefine Sprachmann, Dr. Beatrice Cula, Dr. Christian Feiler and Dr. Manfred Weiss at the beamline sector MX14.2 at BESSY-II, Prof. Dr. Emil List-Kratochvil, Prof. Dr. Christoph Koch, Prof. Dr. Norbert Koch, Prof. Dr. Nicola Pinna, Prof. Dr. Phillip Adelhelm, Prof. Dr. Gudrun Scholz and Prof. Dr. Hans Börner who provided labspace and access to instruments. The research leading to these results has received funding from the European Research Council. Open Access funding enabled and organized by Projekt DEAL.

Conflict of Interest

The authors declare no conflict of interest.

Data Availability Statement

The data that support the findings of this study are openly available in Zenodo at https://doi.org/10.5281/zenodo.6327947, reference number 6327947.

Keywords: covalent organic frameworks · graphitic carbon nitride · ionothermal synthesis · layered materials · metal free semiconductors

[1] S. Y. Chong, J. T. A. Jones, Y. Z. Khimyak, A. I. Cooper, A. Thomas, M. Antonietti, M. J. Bojdys, *J. Mater. Chem. A* **2013**, *1*, 1102–1107.
[2] M. J. Bojdys, N. Severin, J. P. Rabe, A. I. Cooper, A. Thomas, M. Antonietti, *Macromol. Rapid Commun.* **2013**, *34*, 850–854.
[3] M. J. Bojdys, *Macromol. Chem. Phys.* **2016**, *217*, 232–241.
[4] C. J. Pickard, A. Salamat, M. J. Bojdys, R. J. Needs, P. F. McMillan, *Phys. Rev. B* **2016**, *94*, 1–10.
[5] G. M. Veith, L. Baggetto, L. A. Adamczyk, B. Guo, S. S. Brown, X. G. Sun, A. A. Albert, J. R. Humble, C. E. Barnes, M. J. Bojdys, et al., *Chem. Mater.* **2013**, *25*, 503–508.
[6] M. J. Bojdys, J.-O. Müller, M. Antonietti, A. Thomas, *Chem. Eur. J.* **2008**, *14*, 8177–8182.
[7] A. I. Cooper, M. J. Bojdys, *Mater. Today* **2014**, *17*, 468–469.
[8] H. Schlomberg, J. Kröger, G. Savasci, M. W. Terban, S. Bette, I. Moudrakovski, V. Duppel, F. Podjaski, R. Siegel, J. Senker, et al., *Chem. Mater.* **2019**, *31*, 7478–7486.
[9] M. Döblinger, B. V. Lotsch, J. Wack, J. Thun, J. Senker, W. Schnick, *Chem. Commun.* **2009**, 1541–1543.
[10] Y. Noda, C. Merschjann, J. Tarábek, P. Amsalem, N. Koch, M. J. Bojdys, *Angew. Chem. Int. Ed.* **2019**, *131*, 9494–9498.
[11] V. W. H. Lau, I. Moudrakovski, T. Botari, S. Weinberger, M. B. Mesch, V. Duppel, J. Senker, V. Blum, B. V. Lotsch, *Nat. Commun.* **2016**, *7*, 12165.
[12] F. K. Kessler, Y. Zheng, D. Schwarz, C. Merschjann, W. Schnick, X. Wang, M. J. Bojdys, *Nat. Rev. Mater.* **2017**, *2*, 17030.
[13] C. Z. Liao, V. W. H. Lau, M. Su, S. Ma, C. Liu, C. K. Chang, H. S. Sheu, J. Zhang, K. Shih, *Inorg. Chem.* **2019**, *58*, 15880–15888.
[14] L. Lin, Z. Lin, J. Zhang, X. Cai, W. Lin, Z. Yu, X. Wang, *Nat. Catal.* **2020**, *3*, 649–655.
[15] Y. Li, M. Gu, X. Zhang, J. Fan, K. Lv, S. A. C. Carabineiro, F. Dong, *Mater. Today* **2020**, *41*, 270–303.
[16] D. Burmeister, H. A. Tran, J. Müller, M. Guerrini, C. Cocchi, J. Plaickner, Z. Kochovski, E. J. W. List-Kratochvil, M. J. Bojdys, *Angew. Chem. Int. Ed.* **2021**, 2–10.
[17] J. Xu, M. Shalom, F. Piersimoni, M. Antonietti, D. Neher, T. J. K. Brenner, *Adv. Opt. Mater.* **2015**, *3*, 913–917.
[18] L. He, M. Fei, J. Chen, Y. Tian, Y. Jiang, Y. Huang, K. Xu, J. Hu, Z. Zhao, Q. Zhang, et al., *Mater. Today* **2019**, *22*, 76–84.
[19] T. Sekine, H. Kanda, Y. Bando, M. Yokoyama, K. Hojou, *J. Mater. Sci. Lett.* **1990**, *9*, 1376–1378.
[20] L. Maya, D. R. Cole, E. W. Hagaman, *J. Am. Ceram. Soc.* **1991**, *74*, 1686–1688.
[21] J. F. D. Chubaci, T. Sakai, T. Yamamoto, K. Ogata, A. Ebe, F. Fujimoto, *Nucl. Inst. Methods Phys. Res. B* **1993**, *80–81*, 463–466.
[22] H. X. Han, B. J. Feldman, *Solid State Commun.* **1988**, *65*, 921–923.
[23] M. R. Wixom, *J. Am. Ceram. Soc.* **1990**, *73*, 1973–1978.
[24] Q. Lu, J. Deng, Y. Hou, H. Wang, H. Li, Y. Zhang, *Chem. Commun.* **2015**, *51*, 12251–12253.
[25] L. Heymann, B. Schiller, H. Noei, A. Stierle, C. Klinke, *ACS Omega* **2018**, *3*, 3892–3900.
[26] E. Wirnhier, M. Döblinger, D. Gunzelmann, J. Senker, B. V. Lotsch, W. Schnick, *Chem. Eur. J.* **2011**, *17*, 3213–3221.
[27] R. Sridhar, C. E. Johnson, E. J. Cairns, *J. Chem. Eng. Data* **1970**, *15*, 244–245.
[28] G. Algara-Siller, N. Severin, S. Y. Chong, T. Björkman, R. G. Palgrave, A. Laybourn, M. Antonietti, Y. Z. Khimyak, A. V. Krasheninnikov, J. P. Rabe, et al., *Angew. Chem. Int. Ed.* **2014**, *53*, 7450–7455; *Angew. Chem.* **2014**, *126*, 7580–7585.
[29] B. Jürgens, E. Irran, J. Senker, P. Kroll, H. Müller, W. Schnick, *J. Am. Chem. Soc.* **2003**, *125*, 10288–10300.
[30] B. V. Lotsch, M. Döblinger, J. Sehnert, L. Seyfarth, J. Senker, O. Oeckler, W. Schnick, *Chem. Eur. J.* **2007**, *13*, 4969–4980.

[31] A. Thomas, A. Fischer, F. Goettmann, M. Antonietti, J. O. Müller, R. Schlögl, J. M. Carlsson, *J. Mater. Chem.* **2008**, *18*, 4893–4908.
[32] D. S. Su, J. Zhang, B. Frank, A. Thomas, X. Wang, J. Paraknowitsch, R. Schlögl, *ChemSusChem* **2010**, *3*, 169–180.
[33] L. Lin, C. Wang, W. Ren, H. Ou, Y. Zhang, X. Wang, *Chem. Sci.* **2017**, *8*, 5506–5511.
[34] X. Wang, S. Blechert, M. Antonietti, *ACS Catal.* **2012**, *2*, 1596–1606.
[35] T.-G. Lee, H.-J. Kang, J.-H. Kim, N. Suzuki, A. Fujishima, M. Choi, Y.-S. Jun, *Appl. Catal. B* **2021**, *294*, 120222.
[36] F. K. Kessler, W. Schnick, *Z. Anorg. Allg. Chem.* **2019**, *645*, 857–862.
[37] S. J. Clark, M. D. Segall, C. J. Pickard, P. J. Hasnip, M. I. J. Probert, K. Refson, M. C. Payne, *Z. Kristallogr.* **2005**, *220*, 567–570.

Manuscript received: March 4, 2022
Accepted manuscript online: April 11, 2022
Version of record online: May 2, 2022

Chemistry–A European Journal

Supporting Information

Size Effects of the Anions in the Ionothermal Synthesis of Carbon Nitride Materials

David Burmeister, Johannes Müller, Julian Plaickner, Zdravko Kochovski, Emil J. W. List-Kratochvil, and Michael J. Bojdys*

Experimental

Experiments **have to be conducted with caution** since they employ glassware under high pressure and temperature. Furthermore formation of **explosive compounds** like NI_3 can occur.

Dicyandiamide condensation in iodide eutectic salt melts: 1 g of precursor dicyandiamide (DCDA, Sigma Aldrich >99%) is ground together with an eutectic salt mixture of LiI and KI (lithium iodide, anhydrous Sigma Aldrich >99.99%, potassium iodide, anhydrous Sigma Aldrich >99%) (15 g; 58:42 wt%, m.p. 285 °C) in a glovebox. The reaction mixture is filled into a quartz ampule and sealed. The sealed quartz ampule is placed into a furnace (Nabertherm, L 5/11/B180, 2.4 kW) at 400 °C for 4 h. Then the temperature is increased (10 K/min) to 480 °C and held for 2 h. Then the temperature in increased to the final reaction temperature for the time frames stated in the document. At around 450 °C noticeable amounts of Iodine are in the gasphase in the ampule. The furnace is then allowed to cool naturally. The ampule is removed at room temperature, opened, and the salt block is dissolved in Milli-Q water in a 50 mL Falcon. The slurry is centrifuged and the supernatant is decanted. The pellet is resuspended in hot water on a shaker and centrifuged again. The supernatant is decanted and the process is repeated for two times with hot water and two times with methanol (>99% for synthesis). The resulting pellet is resuspended in methanol, transferred into vacuum safe glas ware and the methanol is evaporated. The resulting powder is dried under vacuum at 200 °C for 24 h before combustion analysis. Assuming the product of the synthesis at 450 °C is melem, the yield is 58% (0.5 g).

Preparation of suspensions for TEM, SEM, XPS, Raman sample preparation: For the dispersion 10-20 mg of product are redispersed in 5mL of EtOH. The dispersion is then dropcasted either on a TEM grid (Plano, S147-2, holey carbon) or a wafer for TEM/SEM (1 µL) or a 1x1 cm indium tin oxide coated glas substrate for XPS (10-50 µL).

Sonication of CN suspensions for preparation of OLEDs: Sonication of CN powder was conducted with a BANDELIN HD 2200/-U (200 W, HF 20 kHz) sonotrode setup with a MS72 sonotrode with the amplitude set to 10% in continuous mode. The falcon tube is placed in an ice bath and the sonotrode was immersed about 3-5 mm into the suspension. Suspensions are sonicated for 3 h, centrifuged at 7690 g for 1 min to reduce large particles and the supernatant was removed with a pipet into a falcon.

OLED preparation: ITO-coated glass substrates (sheet resistance = 20 Ω per square) were cleaned by sequential sonication (10 minutes) in (i) acetone and (ii) isopropanol followed by drying *via* a nitrogen gun. The substrates were then treated *via* O_2 plasma (partial pressure 1.2 × 10^{-1} mbar) for 15 minutes at 10.2 W. 50 nm PEDOT:PSS (Osilla) films were spin coated as hole injection layer and heated to 220 °C for 10 min. 40 µL CN dispersion was drop cast at 60 C from the chlorobenzene dispersion onto the pixel areas of the PEDOT:PSS covered substrate (ca. 150 mm^2). 5 nm Calcium and 200 nm Aluminium were evaporated in a PVD chamber at 10^{-5} mbar. Finally the OLEDs were encapsulated with UV-curable resin (Osilla) and a glass slide. Current density–voltage–luminance characterization was performed with a Keithley 2612B source meter and a Konica Minolta LS-160 luminance meter in a purpose-built setup. Electroluminescence spectra were taken with a CS2000 spectrometer (Ocean Optics) using OceanView software.

Fourier transform infrared (FT-IR): Spectra were recorded from solid on a Thermo Scientific Nicolet iS5 spectrometer (Thermo Fisher Scientific, Waltham, MA, USA) in the wavenumber range of 4000-600 cm^{-1} with resolution of 4 cm^{-1}.

Raman: UV Raman spectra were recorded with a Horiba T64000 spectrometer in single-grating mode. The excitation source was provided by a diode-pumped solid-state laser from CryLas at a wavelength of 266 nm and power of 4 mW. The light was focused on the sample

with a Thorlabs LMU-40x-UVB objective (backscattering geometry). A notch filter with cut-off at 220 cm^{-1} was used to filter out the elastically scattered light. The acquired Raman spectra were calibrated by comparison with the spectrum of a Ga_2O_3 crystal by using a quadratic calibration curve. This procedure allows for reduction of the experimental error at approximately 5 cm^{-1}, which is below the spectral resolution of 8 cm^{-1}.

Powder X-ray diffraction (PXRD): Structural analysis of the prepared PTI-MX was performed with a Bruker D2 Phaser X-Ray powder diffractometer (XRD) in Bragg-Brentano geometry. X-rays were generated by a Cu $K_{\alpha 1+2}$ source at 30 kV operating voltage and collected with a LynxEye detector.

Photoluminescence (PL): Edinburgh Instruments FLS 980 spectrometer. Films were dropcasted from ethanol suspensions on quarz substrates PGO 10x10x0.5 mm.

X-ray photoelectron spectroscopy (XPS): JOEL JPS-9030 photoelectron spectrometer with an Al kα (1486 eV) excitation source and a monochromator. Quantitative comparison of nitrogen and carbon in single spectra were performed by signal integration after background subtraction of a Shirley function. The samples were prepared on ITO coated glass substrates to minimize charging.

Scanning electron microscopy and energy-dispersive X-ray spectroscopy: We recorded the SEM images with a GeminiSEM 500 electron microcsope (Carl Zeiss Microscopy GmbH, Germany). The elemental analysis was carried out using an energy-dispersive X-ray spectrometer (EDX, XFlash 6130, Bruker GmbH, Germany) using the same machine. Optical microscopy was performed with an Olympus LEXT laser scanning microscope.

Single-crystal X-ray diffraction (sc-XRD): The data was collected at the beamline MX14.2 of the BESSYII synchrotron and processed using XDS.[25,26] The structure was solved by

intrinsic phasing method (SHELXT-2013)[27] and refined by full matrix least square procedures based on F2 with all measured reflections (SHELXL-2014)[27] in the graphical user interface (OLEX2)[28] with anisotropic temperature factors for all non-hydrogen atoms. If applicable and mentioned, remaining electron density originating from solvent molecules that could not be refined were masked using the solvent mask tool implemented in OLEX2.[29] Deposition Number 2095271 contains the supplementary crystallographic data for this paper. These data are provided free of charge by the joint Cambridge Crystallographic Data Centre and Fachinformationszentrum Karlsruhe Access Structures service.

Scanning force microscopy (SFM): The imaging was performed in amplitude modulation (AM) mode with a Cypher-ES AFM instrument (Asylum research Oxford Instruments Inc.) using photo-thermal excitation of cantilevers. We used qp-fast – long (Nanosensors) cantilever with the nominal fundamental resonance frequency 250 kHz, and spring constant 15 N/m. The cantilever was excited on its third eigenmode at about 5.2 MHz. The setpoint amplitudes were 70 mV. The cantilever was cleaned with air plasma with a Zepto instrument (Diener electronics Inc.) at 50% power for one minute. The sample cell was purged with dry nitrogen (Linde group, 99.999% purity as specified by the manufacturer). Samples were prepared on blue scotch tape (1007R Silicone-Free Blue Adhesive Plastic Film, sps-europe), sonicated in ethanol and glued to a magnetic sample holder with epoxy resin. The images were post processed and plotted in Gwiddyon using the align rows function. The Connolly surface was created in Materials Studio 7.0 with a 001 surface slab of the melem hydrat crystal structure.

Nitrogen (N_2) sorption measurements and BET surface area calculations:
Gas adsorption isotherms were collected using a Micromeritics ASAP 2020 Accelerated Surface Area and Porosity Analyzer. 10-40 mg samples were transferred to dried and tared analysis tubes equipped with filler rods and capped with a seal frit. The samples were heated

to 40 °C at a rate of 1 °C/min and evacuated at 40 °C for 60 min, then heated to 120 °C at a rate of 1 °C/min heat and evacuated at 100°C for 10 h. The tube was weighed again to determine the mass of the activated sample and transferred to the analysis port of the instrument. 99.999% purity N2 was used for all adsorption measurements. N2 isotherms were measured from a relative pressure p/p0 of 0.01 to 1 in a liquid nitrogen (77 K) bath. Brunauer-Emmett-Teller (BET) surface areas were calculated from the N2 isotherm at 77 K within the pressure range p/p0 of 0.05 – 0.07.

$$Q_{monolayer} = \frac{1}{k + d}$$

$$\mathrm{St} = \left(\frac{\mathrm{Q}_{monolayer} \frac{\mathrm{cm}^3}{\mathrm{g}}}{\left(22414 \frac{\mathrm{cm}^3}{\mathrm{mol}} \right)} \right) * \mathrm{NA\ mol^{-1}} * \mathrm{N}_{cs}\ \mathrm{m}^2 = 4.35 * \mathrm{Q}_{monolayer} \frac{\mathrm{m}^2}{\mathrm{g}}$$

St: Surface area in $m^2\ g^{-1}$

$Q_{monolayer}$: quantity of adsorbed nitrogen in $cm^3\ g^{-1}$

k: slope of linear fit of (p/p°)/(Q(1-(p/p°)) plotted versus (p/p°)

d: y axis intersection of linear fit of (p/p°)/(Q(1-(p/p°)) plotted versus (p/p°)

NA: Avogadro constant $6.022\ 10^{23}\ mol^{-1}$

N_{cs}: Nitrogen cross section $1.62\ 10^{-19}\ m^2$

(Peter Klobes, Klaus Meyer Ronald G. Munro, Porosity and specific surface area Measurements for solid materials, 2006, Washington, National Institute of Standards and Technology)

ssNMR: Cross polarization magic-angle spinning (CP-MAS) solid-state NMR spectra were recorded on a Bruker Avance 400 MHz spectrometer operating at 100.6 MHz (^{13}C) and 40.52 MHz (^{15}N).

Low-dose, high-resolution transmission electron microscopy: The sample was dispersed in Methanol (~0.6 mg/mL) with a micropipette and 0.5-1 µL were dropcast in the middle of a

holy carbon TEM grid (Plano S147-2). The TEM grids were loaded into a cryogenic transfer holder (Gatan 914, Gatan, Munich, Germany) at room temperature and transferred to the TEM. Once in the TEM, the holder was cooled down with liquid nitrogen and imaging was performed with a low dose acquisition scheme using SerialEM (doi: 10.1016/j.jsb.2005.07.007) on JEM-2100 (JEOL GmbH, Eching, Germany) operated at 200 kV and equipped with a 4 k × 4 k CMOS digital camera (TVIPS TemCam-F416). HRTEM images were acquired at a magnification of 500,000×, corresponding to a pixel size of 0.23 Å at the specimen level, while keeping the total electron dose below 20 e $Å^{-2}$. All imaging was carried out at temperatures around 90 K.

Hydrogen evolution reaction: 20 mg 500 °C, 12 h iodide eutectic condensation product is added to a 10 vol% 15 ml solution of the sacrificial agent triethanolamine in water. 0.2 ml of a 1 mg/mL H_2PtCl_6 solution is added as co-catalyst and the reaction mixture is argon purged for 10 min while stirring. The reaction mixture is illuminated with a 400 W xenon lamp without cutoff filter and samples of the headspace are extracted through a septum at hourly intervals for five hours. The hydrogen content of the collected samples was determined by gas chromatography. Hydrogen content is under the limit of detection. Please find details about the setup here: doi: 10.33774/chemrxiv-2021-q1b4b.

Table S1. Combustion elemental analysis of of products obtained from the LiI/KI eutectic at various reaction conditions compared to a PTI/Br sample from a LiBr/KBr eutectic.

sample	N wt%	C wt%	H wt%
LiBr/KBr, 550 °C, 48 h	43.118	25.958	1.059
LiI/KI, 550 °C, 48 h	38.100	40.009	2.688
LiI/KI, 550 °C, 12 h	53.294	38.840	2.452
LiI/KI, 500 °C, 24 h	57.393	30.387	3.384
LiI/KI, 450 °C, 12 h	58.287	30.163	3.432

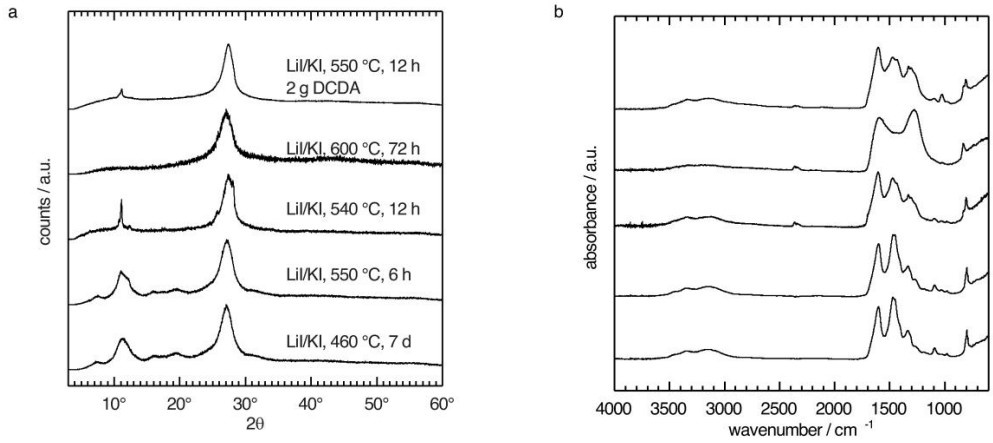

Figure S1. PXRD and FT-IR spectra of additional reaction conditions.

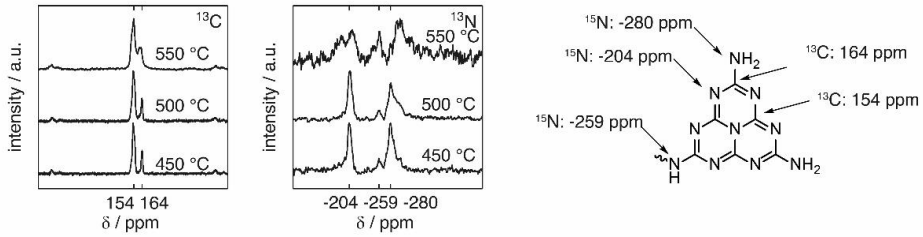

Figure S2. ^{13}C and ^{15}N Solid state NMR of carbon nitride condensation products from 550 °C, 12 h (top line), 500 °C 24 h (middle line) and 450 °C 12 h (bottom line). The bands are assigned to a melem unit in a structural model on the right side of the spectra.

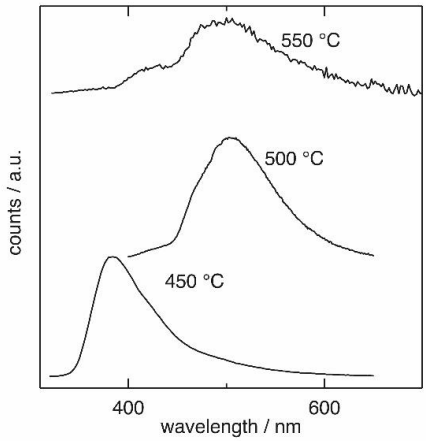

Figure S3. Photoluminescence spectra of CN condensation products from iodide eutectic. Product formed at 450 °C excited at 310 nm closely resembles the emission of melem with a emission maximum at 380 nm (bottom line). The emission of product formed at 500 °C excited at 370 nm is red shifted with an emission maximum at 500 nm (middle line). The product formed at 550 °C excited at 310 nm follows the trend of the broadening emission at 500 nm.

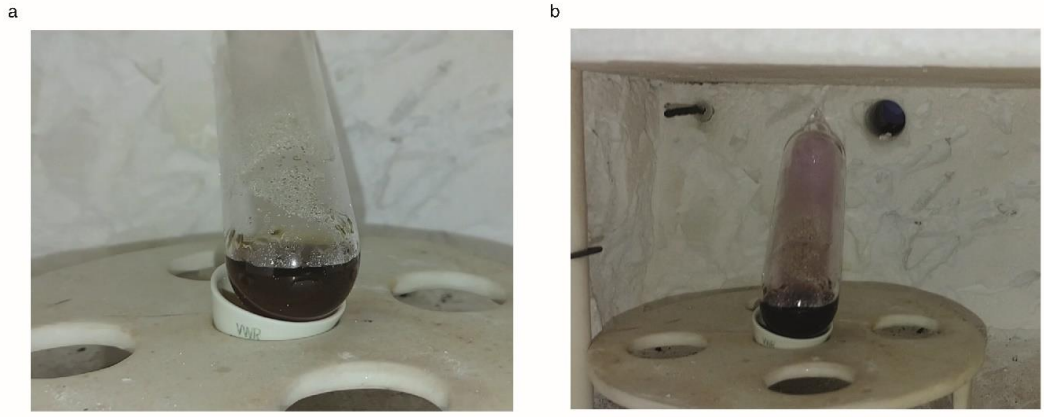

Figure S4. Images of reaction mixtures in a furnace at 400 and 480 °C.

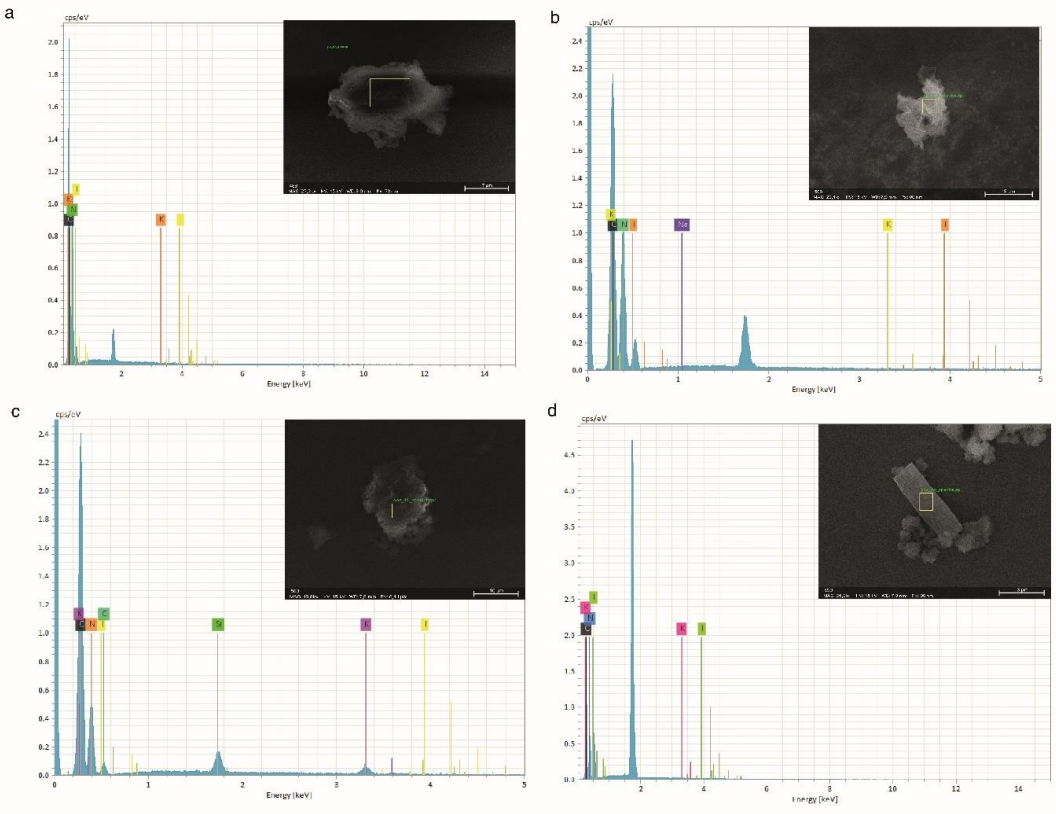

	nitrogen at%	carbon at%	potassium at%	iodine at%
a) 450 °C, 12 h	63±9	37±4	0±0	0±0
b) 500 °C, 12 h	62±8	38±4	0±0	0±0
c) 550 °C, 12 h, amorph	49±7	50±5	0.3±0.1	0±0
d) 550 °C, 12 h, crystal	65±10	35±4	0±0	0±0

Figure S5. Energy dispersive X-ray spectroscopy of condensation products. Atomic percentages of nitrogen and carbon reflect the combustion analysis well. The increased carbon content of the 550 °C, 12 h can be attributed to the brownish amorphous phase.

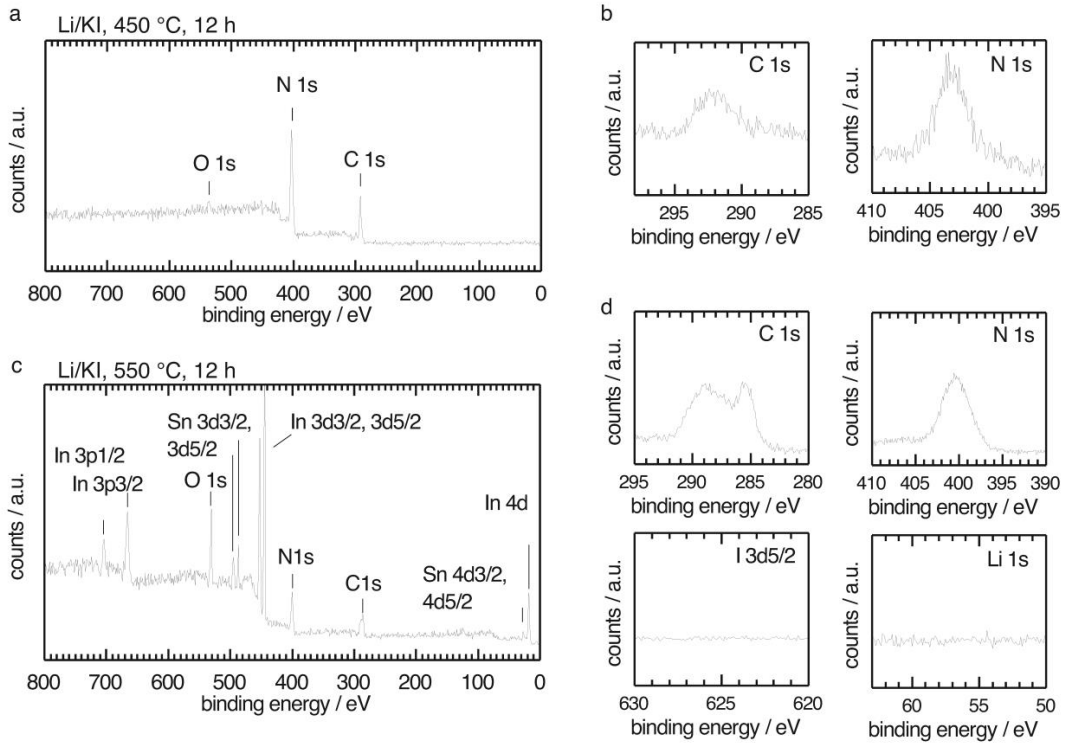

Figure S6. XPS spectra of condensation product from 450 °C and 550 °C. The concentration of the salt melt ions in the sample surface of processed films on indium-tin oxide after workup is under the detection limit. a) XPS survey of CN condensation product from 450 °C. Only carbon nitrogen and oxygen are present. b) XPS spectra of C 1s and N1s. The atomic percentages of carbon and nitrogen are in well accordance with the values found by combustion analysis and EDX nitrogen: 65 at% carbon 35 at%. Due to a film thickness of around 1-10 µm no indium and tin signals are obtained. However the absolute shift is most likely influenced by surface charging (compare e.g. the N 1s spectra). c) The XPS spectrum of the product obtained from 550 °C has as well no ion contributions from the salt melt (LiI/KI). Due to reduced film thickness, in this sample, charging was successful reduced. However, full surface coverage was not achieved and hence contributions of elements of the indium tin oxide substrate are captured in the survey spectrum. d) The C 1s spectrum shows similar trends as observed for carbonization in poly(triazine imide) (doi: 10.1002/anie.202111749). A strong signal at 285 eV arises that can be interpreted as CC environments. The carbon rich property is also reflected by comparison of the atomic percentages of nitrogen: 47 at% and carbon 53 at% to the condensation at lower temperature. Again these values are in good accordance with combustion analysis and EDX.

a

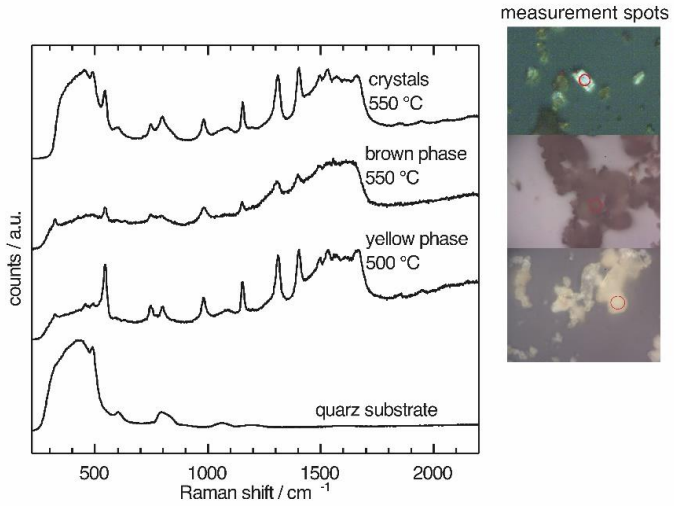

b

ν (observed this work)	ν reference	assignment
1661 (w)	1677 (w)	E′
1571 (w)	1581 (w)	E′
1530 (w)		
1494 (w)		
1401 (s)		
1310 (s)		
1197 (vw)		
1155 (s)	1155 (s)	A1′
980 (s)		
750 (w)		
545 (s)	545 (s)	A1′

Figure S7. UV-Raman spectrum with 255 nm excitation wavelength of DCDA condensation products in LiI/KI eutectics at 500 °C and 550 °C. a) rectangular crystals from 550 °C, 12 h reactions show well resolved Raman bands on a quarz substrate (first line). The band positions of the coevolved brown phase measured on a cleaved mica substrate are closely related to the bands observed in the crystalline phase. Product from 500 °C 12 reaction shows the same dominant Raman bands as the product phases obtained from 550 °C. The observed Raman bands are compared to literature values for melem. (doi: 10.1021/ja0357689). The high similarity of the spectra of the melem crystals obtained from the 550 °C sample and the yellow phase from 500 °C further strengthens the hypothesis that the observed changes in the PXRD are due to phase changes of melem crystals.

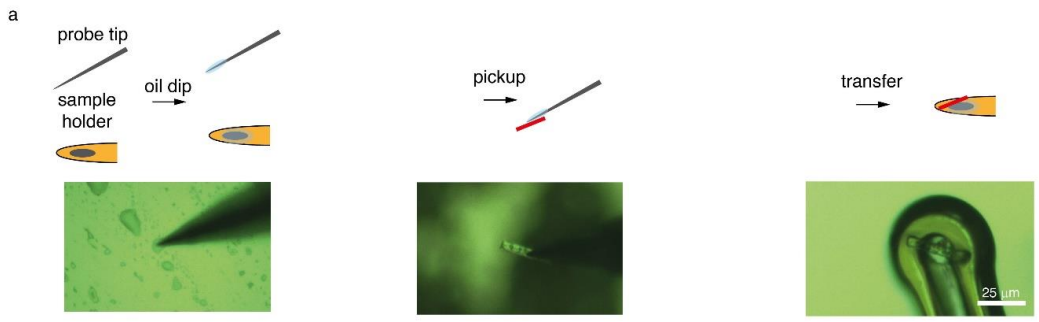

Figure S8. Single crystal X-ray sample preparation. a) pick up transfer of microcrystals in presence of abundant amorphous phase. To be able to mount the crystals even though their small size and the presence of the second brown phase, a pickup transfer with micro-actuators is applied (IMINA technologies). A micro actuator tip is dipped into an oil-drop on a microscopy slide, resulting in better adhesion properties of the tip. The tip with the oil film is used to pick up the micro crystallites. A sample holder with a 10 µm loop is also dip-coated with oil. Then the crystallites were carefully transferred to the sample holder.

Table S2. Crystallographic data for melem hydrate ($C_6N_7(NH_2)_3 \cdot H_2O$) obtained from the ionothermal condensation of dicyandiamide in LiI/KI eutectic salt melt at 550 °C, 12 h.

Identification code	melem hydrate
Empirical formula	$C_6H_8N_{10}O$
Formula weight	236.22
Temperature/K	100 K
Crystal system	monoclinic
Space group	$P2_1/c$
a/Å	8.6040(17)
b/Å	16.630(3)
c/Å	6.8840(14)
α/°	90
β/°	111.91(3)
γ/°	90
Volume/Å^3	913.8(4)
Z	4
ρ_{calc}g/cm^3	1.717
μ/mm^{-1}	0.132
F(000)	488.0
Crystal size/mm^3	0.1 × 0.04 × 0.01
Radiation	synchrotron (λ = 0.799897 Å)
2Θ range for data collection/°	4.898 to 59.504
Index ranges	$-11 \leq h \leq 11$, $-22 \leq k \leq 22$, $-8 \leq l \leq 8$
Reflections collected	15426
Independent reflections	2333 [R_{int} = 0.1298, R_{sigma} = 0.0782]
Data/restraints/parameters	2333/6/175
Goodness-of-fit on F^2	1.024
Final R indexes [I>=2σ (I)]	R_1 = 0.0797, wR_2 = 0.2012
Final R indexes [all data]	R_1 = 0.1656, wR_2 = 0.2574
Largest diff. peak/hole / e Å^{-3}	0.39/-0.37

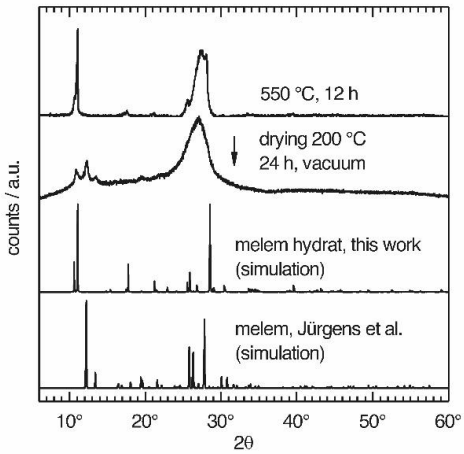

Figure S9. PXRD of condensation product from 550 °C, 12 h (first line) compared to PXRD after vacuum drying (second line). The experimentally obtained diffractograms are compared with PXRD simulations of the structural data files of melem hydrat (this work, third line) and the structure of solvent free melem as obtained by Jürgens et al. (fourth line).

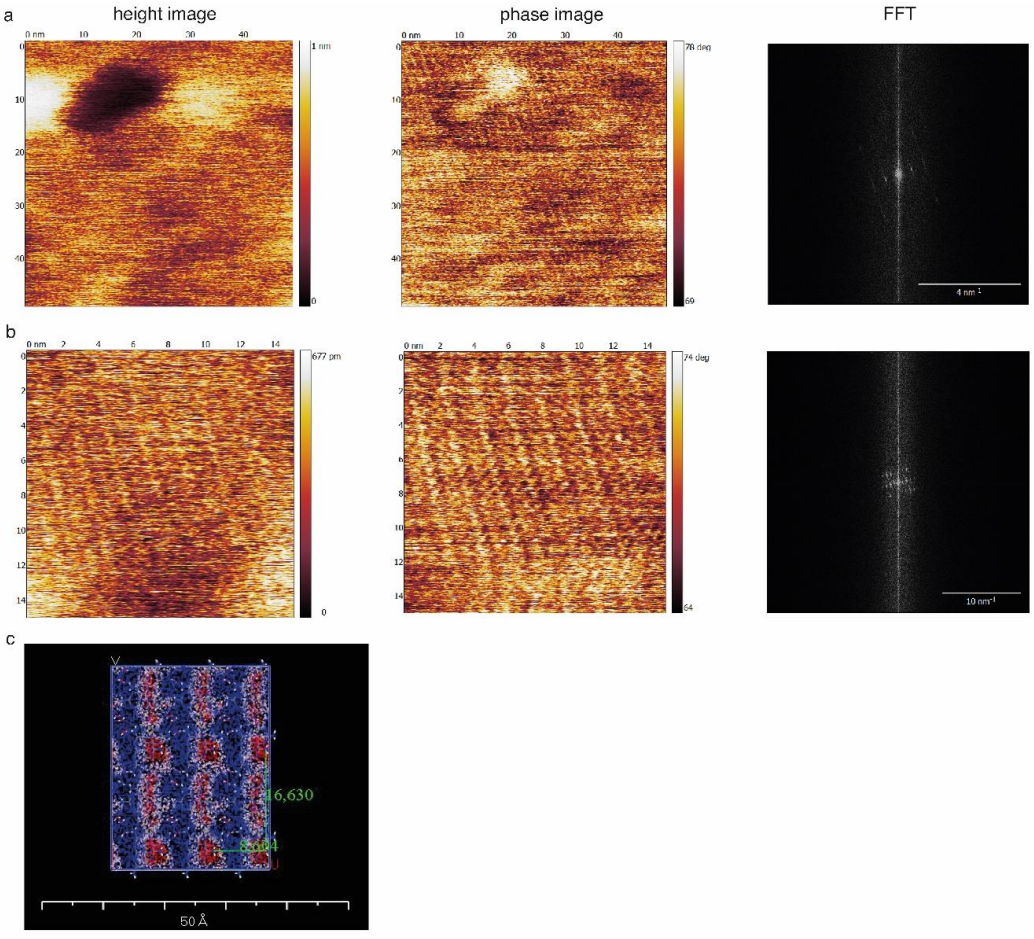

Figure S10. SFM images obtained from melem hydrat crystallite surfaces. Predominantly occurring periodic distances are 0.7 nm and 1.7 nm. a) height and phase image of melem hydrat crystal surface. Fast Fourier transform analysis of the phase images exhibit spots at the spatial frequencies in relation to the image center. b) after decreasing the scan size the periodic distances are still present. c) 001 Connolly surface of melem hydrat crystal structure. The dark-red marked areas contain amine residues pointing out of the surface which are in direct contact with the spheric "connolly-probe". The distances and angles of the Connolly surface closely resemble the observed patterns. The small deviations can be due thermal drift of the sample and surface adsorbents.

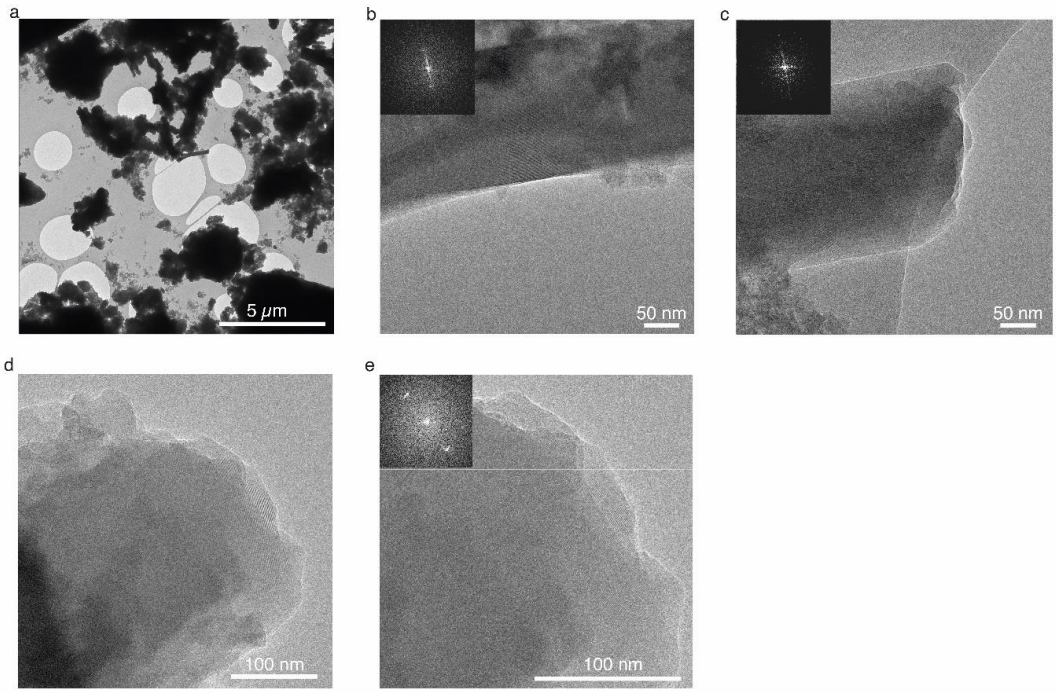

Figure S11. Cryo HR-TEM (200 kV acceleration voltage) images and fast Fourier transform of an elongated rectangular carbon nitride crystal exhibiting lattice fringes with a periodicity of 0.8 nm. This distance is interpreted as the 100 d-spacing of melem hydrat.

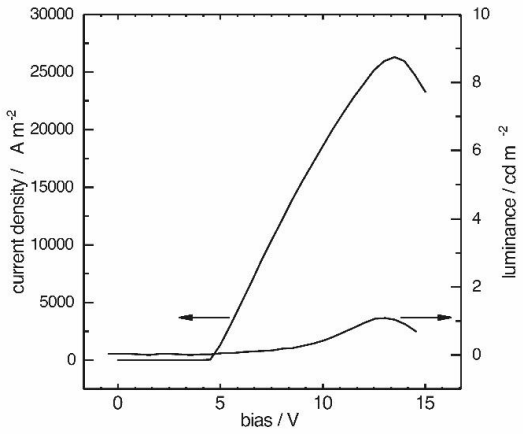

Figure S12. IV characteristics and luminance of OLED constructed from 500 °C condensation product. The device shows a steep diode like onset at 4.5 V in forward bias direction. At 13 V one observes a maximum luminance of 1 cd m^{-2}. Electroluminescence spectra were not obtained since the luminescence was not high enough for the set up that has been employed.

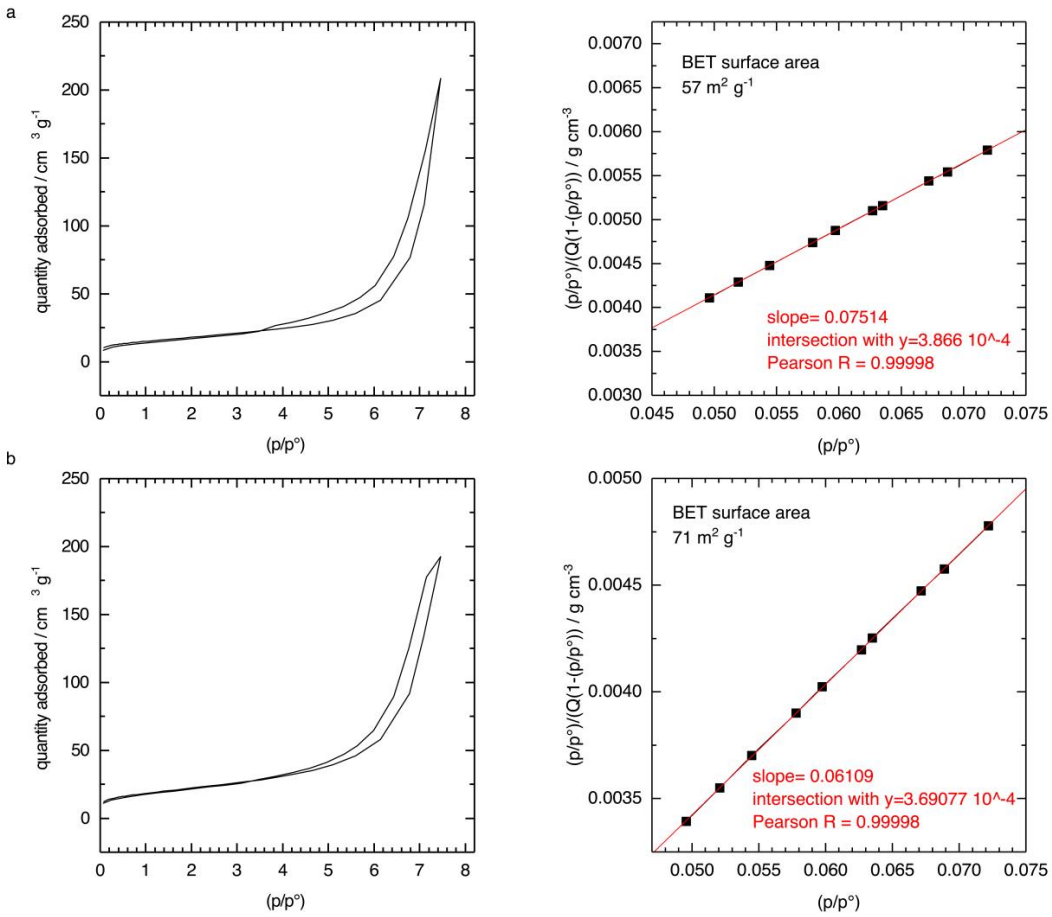

Figure S13. Nitrogen de- and adsorption isotherms from a) 450 °C, 12h and b) 550 °C, 12h CN condensation products from a LiI/KI eutectic salt melt.

On the non-bonding valence band and the electronic properties of poly(triazine imide), a graphitic carbon nitride

David Burmeister, Alberto Eljarrat, Michele Guerrini, Eva Röck, Julian Plaickner, Christoph T. Koch, Natalie Banerji, Caterina Cocchi, Emil J. W. List-Kratochvil, Michael J. Bojdys**

David Burmeister, Prof. Michael Janus Bojdys
Department of Chemistry & IRIS Adlershof, Humboldt-Universität zu Berlin, Brook-Taylor-Str. 6, 12489, Germany

Dr. Alberto Eljarrat, Prof. Christoph T. Koch
Humboldt-Universität zu Berlin, Institut für Physik, IRIS Adlershof,
Zum Großen Windkanal 2, 12489 Berlin, Germany

Prof. Emil J. W. List-Kratochvil
Humboldt-Universität zu Berlin, Institut für Physik, Institut für Chemie, IRIS Adlershof,
Zum Großen Windkanal 2, 12489 Berlin, Germany

Prof. Emil J. W. List-Kratochvil
Helmholtz-Zentrum Berlin für Materialien und Energie GmbH,
Hahn-Meitner-Platz 1, 14109 Berlin, Germany

Dr. Michele Guerrini, Prof. Caterina Cocchi
Institute of Physics, Carl von Ossietzky Universität Oldenburg,
26129 Oldenburg, Germany

Prof. Caterina Cocchi
Humboldt-Universität zu Berlin, Institut für Physik & IRIS Adlershof,
Zum Großen Windkanal 2, 12489 Berlin, Germany

Dr. Julian Plaickner
Helmholtz-Zentrum Berlin für Materialien und Energie GmbH Hahn-Meitner-Platz 1, 14109 Berlin (Germany), and
Leibniz-Institut für Analytische Wissenschaften—IAS e.V. Schwarzschildstrasse 8, 12489 Berlin (Germany)

Prof. Natalie Banerji, Eva Röck
Department for Chemistry and Biochemistry, University of Bern
Freiestrasse 3, 3012 Bern

*E-mail: m.j.bojdys.02@cantab.net

Keywords: graphitic carbon nitride, lone-pair semiconductor, covalent-organic-framework, ionothermal synthesis, THz-time domain spectroscopy

Abstract

Graphitic carbon nitrides are covalently-bonded, layered, and crystalline semiconductors with high thermal and oxidative stability. These properties make graphitic carbon nitrides potentially useful in overcoming the limitations of 0D molecular and 1D polymer semiconductors.

In this contribution, we study structural, vibrational, electronic and transport properties of nano-crystals of poly(triazine-imide) (PTI) derivatives with intercalated Li- and Br-ions and without intercalates. Intercalation-free poly(triazine-imide) (PTI-IF) is corrugated or AB stacked and partially exfoliated. We find that the lowest energy electronic transition in PTI is forbidden due to a non-bonding uppermost valence band and that its electroluminescence from the π-π* transition is quenched which severely limits their use as emission layer in electroluminescent devices.

THz conductivity in nano-crystalline PTI is up to eight orders of magnitude higher than the macroscopic conductivity of PTI films. We find that the charge carrier density of PTI nano-crystals is among the highest of all known intrinsic semiconductors, however, macroscopic charge transport in films of PTI is limited by disorder at crystal-crystal interfaces.

Future device applications of PTI will benefit most from single crystal devices that make use of electron transport in the lowest, π-like conduction band.

1. Introduction

State-of-the-art semiconductor technology is based on rare-earth metal doped silicon that requires a lot of energy and water for its manufacture and reaches its miniaturization limits.[1–3] In comparison, organic semiconductors are flexible, light-weight, cost-effective, and composed of earth-abundant materials. Due to their modularity, organic semiconductor materials can be tailored to have specific properties, including high carrier mobilities, low-cost fabrication, and low environmental impact. Researchers are exploring the use of organic semiconductors in a wide range of applications, from solar cells to transistors to touchscreens. However, the long-term performance of current molecular and polymeric semiconductors is low because of lacking oxidative stability and structural disorder due to the inherent degrees of freedom of their constituents.[4] Charge carrier mobility in organic semiconductors increases as we go from 0D, aromatic molecules (≤ 50 cm^2 V^{-1} s^{-1}) to 1D, linear, conjugated polymers (up to 600 cm^2 V^{-1} s^{-1}).[4] This research logically extends to covalently-bonded, layered 2D-materials often referred to as a subclass of covalent organic frameworks (COFs).[5] In COF-type materials, strong, covalent bonds reduce in-plane disorder and weak, inter-planar van der Waals forces enable exfoliation into (atomically) thin sheets. 2D-materials, most famously graphene, have a different electronic structure than their layered analogues due to the confinement of the electron gas to the 2D-crystal.[6–8] In general, semiconducting 2D materials are expected to suffer less from short channel effects making them uniquely suitable for highly miniaturized field effect transistors.[9]

Graphitic carbon nitrides form a subset of 2D, layered COFs that are semiconductors and can be exfoliated.[10–14] At present, PTI and its intercalated derivatives are the best characterized graphitic carbon nitrides.[15–18] They are composed of triazine (C_3N_3) units that are covalently-linked in-plane by imide-bridges into layered materials with high thermal stability up to 400 °C.[15] Because of their high nitrogen content, PTI has a high ionization potential – that means, a high energetic difference between the vacuum level and the highest valence band –

as well as a high electron affinity – meaning, a high energetic difference between the vacuum level and the lowest conduction band. As a result, PTI has a higher oxidative stability than hydrocarbon based 0D or 1D organic semiconductors.[15,19] High quality PTI materials are typically obtained from ionothermal synthesis in eutectic melts of alkali halides resulting in intercalation of ions like Li^+ and Br^- into the structure.[5,16,20–23] Previously, we were able to reduce the amount of carbonaceous defect sites in poly(triazine imide) (Figure S1).[24] In the following, we combine microscopic and macroscopic characterization methods with *ab initio* calculations to pinpoint the reasons for the surprisingly low electroluminescence and low conductivity (10^{-10} to 10^{-9} S cm^{-1}) of macroscopic films of PTI.[24]

We compare two types of poly(triazine imides): PTI with intercalated LiBr (PTI-LiBr), and an intercalate-free analogue (PTI-IF). Herein, (i) we elucidate the impact of de-intercalation on the structure and electronic properties of PTI using elemental analysis, powder x-ray spectroscopy (PXRD), convergent-beam electron diffraction (CBED), electron energy loss spectroscopy (EELS), ultraviolet photoelectron spectroscopy (UPS) and solid state nuclear magnetic resonance (ssNMR), (ii) we develop a model explaining the observed red-shift of electroluminescence as well as the discrepancy between the optical gap and the band gap using diffuse reflectance spectroscopy, valence band EELS, and *ab initio* computational data, (iii) we propose an energy level diagram on the basis of density-functional theory (DFT) calculations, evaluation of the Tauc plot and UPS, and (iv) from time-domain THz spectroscopy data we find that the nano-crystalline morphology of PTI constitutes the major bottleneck for conductivity. Interestingly, our analysis based on the phenomenological Drude-Smith model reveals an unusually high charge carrier density in both PTI-materials of 10^{20} cm^{-3}. The observed charge carrier concentration is independent of intercalation of ions,

and it is above and beyond that of any known intrinsic inorganic semiconductor (*e.g.* Ge $2.33 \cdot 10^{13}$ cm^{-3}; Si $9.65 \cdot 10^{9}$ cm^{-3}).

To the best of our knowledge, this work establishes PTI as the first reported, organic, lone-pair semiconductor, and it will serve as a guide for even more exciting device applications of 2D, layered organic materials in the near future.

2. Results and discussion

2.1. Elemental composition

We carried out combustion elemental analysis and inductively coupled plasma-optical emission spectroscopy (ICP-OES) on both PTI derivatives to rule out carbonization and presence of residual ions in PTI-IF, and we find the results to be in good agreement with the theoretical chemical formulae (Table S1). As observed previously in PTI-LiCl, the Li-ion loading in PTI-LiBr is too high to be explained just by intercalation of LiBr. Excess lithium isoelectronically replaces some of the hydrogen atoms at the imide bonds.[25] Overall, we obtain a composition of $[(C_{3.0}N_{3.0})_2(N_{1.0}H_{1-x}Li_x)_3 \cdot Li_{1.2}Br_{1.2}$, x=0.2] for PTI-LiBr (theoretical $C_6H_3N_9LiBr$). Electron energy loss spectra (EELS) confirm the presence of carbon, nitrogen, lithium, and bromine in PTI-LiBr. K-edges of additional elements are not observed confirming the high purity of the product on microscopic scale (Figure S2).

After Soxhlet extraction and de-intercalation, we detect no Li- and no Br-ions in combustion analysis and ICP-OES. The calculated composition of PTI-IF is $C_{6.0}H_{3.5}N_{9.0}$ (Li wt% << 0.5) (theoretical $C_6H_3N_9$). EELS shows no evidence of intercalated ions in the form of Li/Br K-edges at the microscopic level (Figure S2). In addition, we performed X-ray photoelectron spectroscopy (XPS) measurements to quantify the C:N ratio at the surface of the PTI-LiBr films. We observe a C:N ratio of 41:59 at% (theoretical 40:60 at%) (Figure S3). Overall, results of the macroscopic and microscopic composition analysis reflect a high material purity.

2.2. Effect of de-intercalation on the structure and morphology of PTI crystals

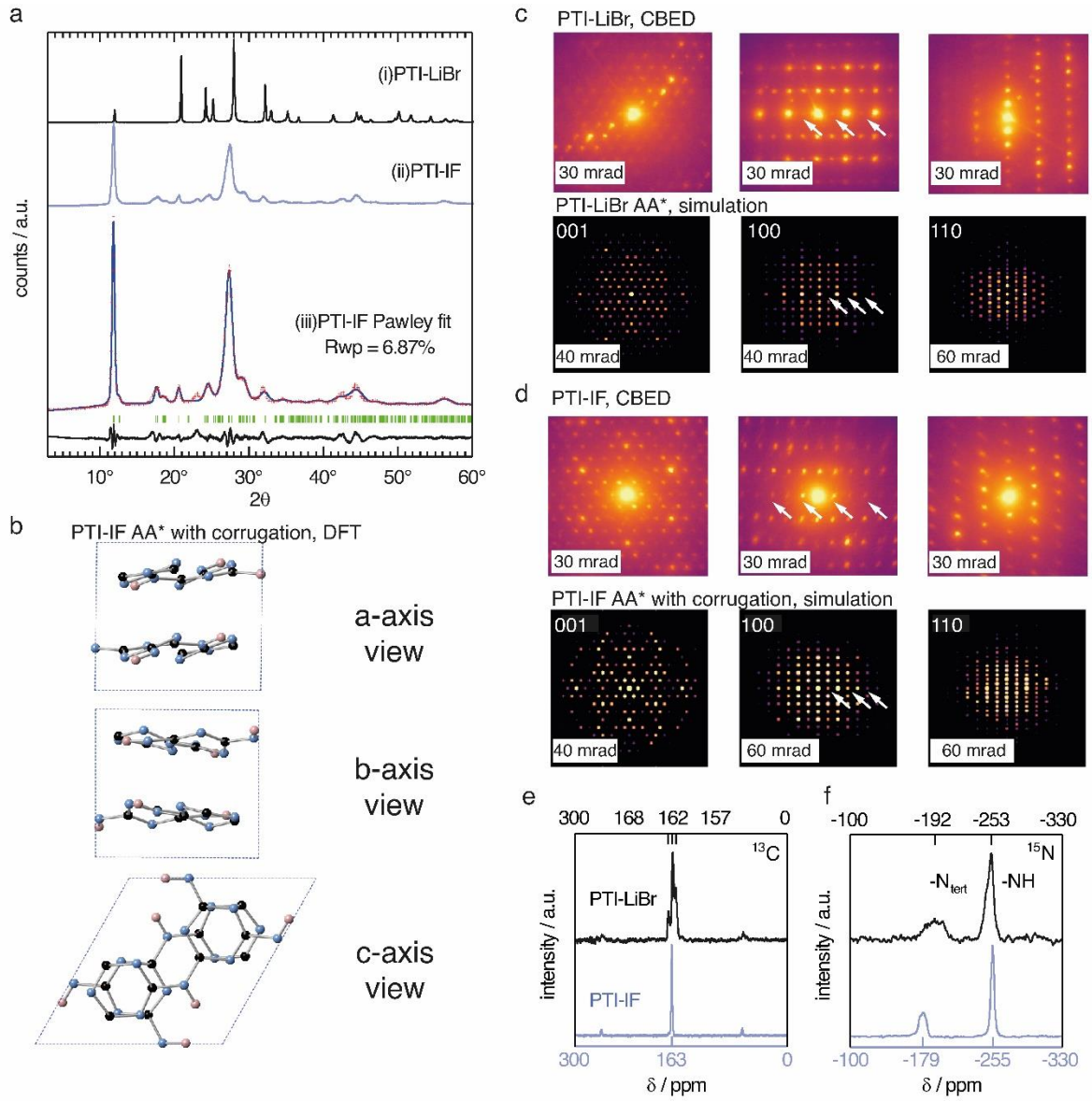

Figure 1. a) Experimentally obtained PXRD patterns of (i) PTI-LiBr and (ii) PTI-IF and (iii) Pawley fit (blue line) of the experimentally obtained pattern (red crosses) to a corrugated AA* stacked PTI-IF cif file, calculated Bragg peak positions (in green), and the difference between the observed and refined pattern (in black). b) Unit-cell of PTI-IF in a corrugated AA* arrangement based on DFT geometry optimization and Pawley fitting. The unit cell is shown along the three crystal axes with nitrogen atoms as blue spheres, carbon as black spheres, and hydrogen as pink spheres. c) Convergent beam electron diffraction (CBED) patterns of PTI-LiBr and simulated patterns. Systematic absences marked by white arrows. d) Experimental CBED patterns of PTI-IF and simulated patterns. e) ^{13}C and f) ^{15}N solid-state nuclear magnetic resonance (ssNMR) spectra of PTI-LiBr (black line) and PTI-IF (blue line).

The unit-cell of PTI-LiBr has been described in great detail,[18,25,26] and it serves as point of reference for the structure refinement and solution of PTI-IF. We obtained a unit-cell for PTI-

IF using powder X-ray diffraction (PXRD) (Figure 1, a), convergent beam electron diffraction (CBED) (Figure 1, d), and structural optimization by density functional theory (DFT) (Figure 1, b). The DFT-optimized unit-cell of PTI-IF agrees well with X-ray and electron diffraction data, and it indicates that intercalate-free PTI-sheets assume a corrugate arrangement. Removal of intercalated Br-ions from PTI-LiBr – and the accompanying loss of the high-scattering cross section contribution – leads to a broadening of all X-ray diffraction peaks (Table S2). In particular, we attribute the broadening of diffraction peaks that have 00*l*-components to the exfoliation and the decreasing height of PTI stacks. The median 002 stacking distance between PTI-sheets increases from 3.5 Å in PTI-LiBr to 3.6 Å in PTI-IF, either due to corrugation or due to intercalation of water molecules.

Corrugation of triazine-based, 2D networks has been predicted computationally in the past, however, to this date there was no experimental evidence to support it.[27–29] To corroborate that the removal of intercalated ions is indeed accompanied by corrugation and delamination, we compared the experimentally obtained diffractogram of PTI-IF with the simulated diffraction patterns of corrugated and non-corrugated PTI-structures in three different stacking arrangements: (i) alternating layers with a mirror plane through the triazine units (AA*), (ii) eclipsed orientation (AA), and (iii) staggered orientation (AB).[27–29] Simulated diffraction patterns based on the corrugated structures match the experimental data better (δRwp = 2-7%), and they correctly describe the peak at 18° 2Θ (assigned as -111) than the non-corrugated ones. The best Pawley fit was obtained for the corrugated PTI-IF structure in AA* stacking mode (Figure 1, a-b**,** Table S3, Figure S4-5). Further evidence for the corrugation of PTI-IF comes from CBED (Figure 1, c-d, Figure S6). In the case of a perfectly planar, intercalated PTI-LiBr structure, we observe no discrepancies between observed and predicted patterns (Figure 1, c).[16] For PTI-IF, once again the corrugated structure reproduces the experimental pattern better. In particular, simulated ED patterns based on the corrugated PTI-IF structure account correctly for the missing systematic absences in the 100 zone axis

pattern (Figure 1, d, Figure S6). We note however, that an AB flat structure also shows a loss of the systematic absences. This means a clear assignment of the effect to corrugation or the presence of other stacking modes is still not possible from the ED patterns.

In conclusion, we arrive at a structural description of PTI-IF as a corrugated, and or AB stacked, intercalate-free, triazine-based material coming from various, orthogonal methods that encompass

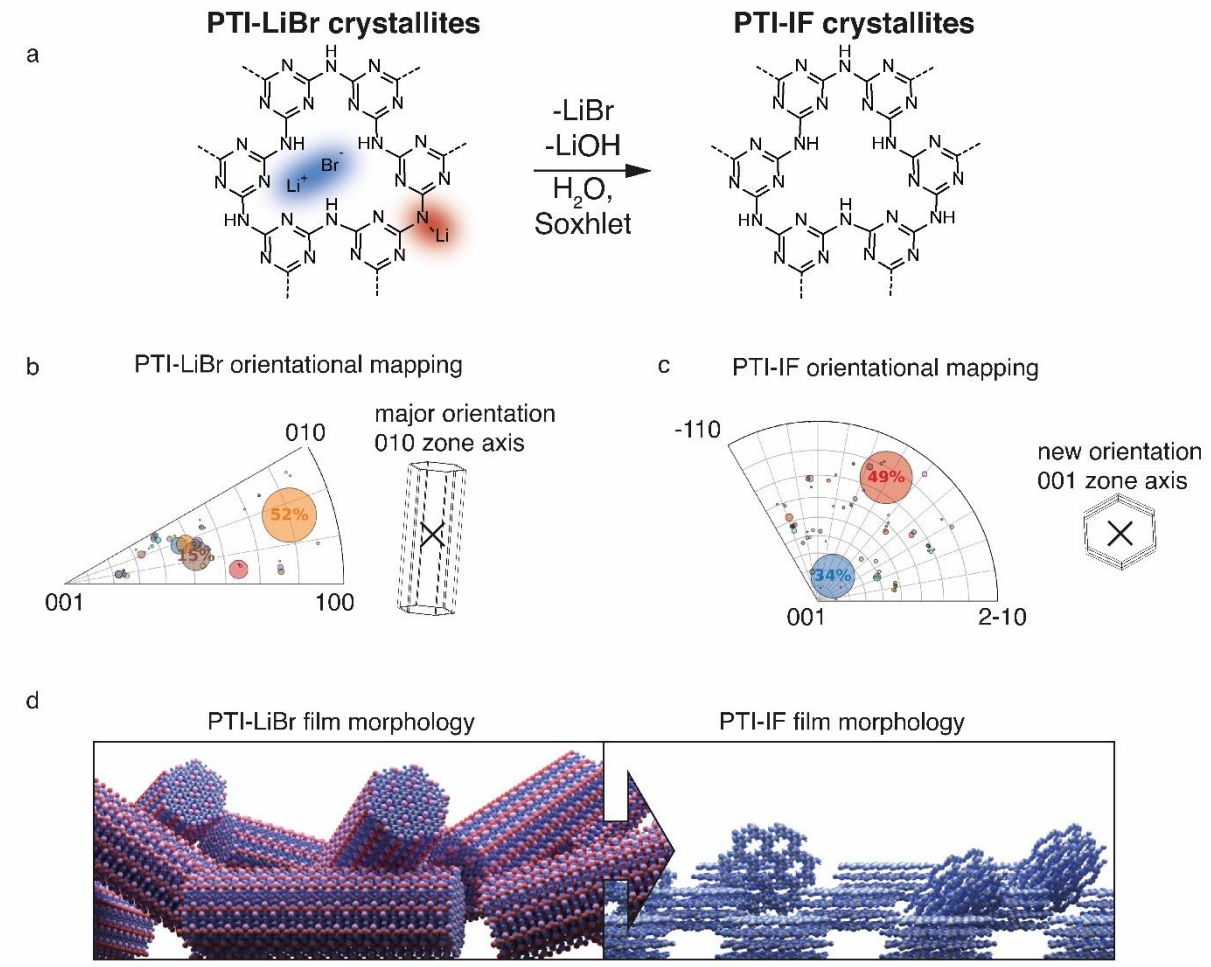

Figure 2. Statistical analysis of the orientations of nano-crystals of PTI-LiBr and PTI-IF based on CBED mapping. a) Structural formula of PTI-LiBr and PTI-IF. b) Integration of the inverse pole figure of PTI-LiBr. c) Integration of the inverse pole figure of PTI-IF. The major observed zone axis in PTI-LiBr is 010/100. In PTI-IF it changes to 001. d) Visualization of the different morphologies and orientations of PTI-LiBr and PTI-IF in films.

microscopic, macroscopic, and *ab initio* structure analysis. As the reason for the corrugation, we propose dipolar interactions of adjacent PTI-layers due to the polar CN-bonds.[30]

Removal of the intercalated ions from PTI-LiBr has a pronounced effect on the local electronic environments of carbon- and nitrogen nuclei in PTI-IF that we monitored using solid-state NMR (ssNMR). Carbon environments attributed to the triazine (C_3N_3) ring are split up as ^{13}C (168, 162, 157 ppm) in the PTI-LiBr structure by the heterogenous distribution of intercalated ions. In comparison, the more homogeneous, intercalate-free PTI-IF structure shows only one carbon signal at 163 ppm (Figure 1, e).[26] Similarly, the ^{15}N signals of PTI-IF appear sharper at -179 (triazine nitrogens) and -255 ppm (imide bridge nitrogen) (Figure 1, f). C_3N_3 ring atoms in ^{15}N and ^{13}C ssNMR spectra of PTI-IF are shifted slightly to higher ppm values compared to the PTI-LiBr. This finding indicates that nuclei are de-shielded by the removal of ions; an effect that stems from a reduction of electron density at the carbon and nitrogen nuclei. We corroborate this experimental observation by Bader partial charge analysis based on DFT results (Figure S7). In PTI-LiBr we observe an increased electron density from the interaction of bromide orbitals with the CN-orbitals.

Presence or absence of intercalated ions has a pronounced effect on the preferred orientation of PTI-IF and PTI-LiBr crystals on substrates such as the carbon net used in CBED experiments. The structural formula of PTI-LiBr and PTI-IF is shown in Figure 2, a. An explanation of the orientation analysis is given in the SI (Figure S8). The majority of 52% of PTI-LiBr crystals is tilted away from the 001 orientation (Figure 2, b). This means that the majority of PTI-LiBr crystals orient themselves with the long side of the pillars in parallel to the substrate and perpendicular to the incident electron beam (X) – as indicated by the wireframe model.

In contrast, for PTI-IF, a major fraction of 34% of CBED patterns is collected from crystals oriented along the 001 zone axis (Figure 2, c). This means that PTI-IF crystals are oriented with the covalently-bonded basal plane in parallel to the carbon support. The pronounced change in preferred crystal orientations is caused by the removal of ions and the accompanying reduction of cohesive, inter-planar interactions – from a mix of ionic and van

der Waals interactions in PTI-LiBr to van der Waals interactions only in PTI-IF. As a result, PTI-sheets become more easily exfoliated and effectively diminish the stacking height of PTI-IF nano-crystals. The reorientation of PTI-IF nano-crystals with the covalent, delocalized planes parallel to a substrate and with pore channels orthogonal to it, is beneficial in device geometries intended for sensing and gating (Figure 2, d).

2.3. Vibrational analysis

We use a combination of Fourier-transform infrared spectroscopy (FTIR), Raman microscopy and electron energy loss spectroscopy (EELS) to assign phonon modes and deformation vectors to PTI-IF (Figure 3) and PTI-LiBr (Figure S9).

The FT-IR spectra of PTI-LiBr have typically very broad bands (Figure S9). We can distinguish between the C_3N_3 ring mode at 808 cm^{-1} and the CN-stretches at 1100-1620 cm^{-1}. Further, we observe a split of the imide N-H stretch at 3300 cm^{-1} that is caused by heterogeneously intercalated ions that break the symmetry of the material.[16,31]

The UV-Raman spectrum of PTI-LiBr shows only two distinctive features at 1629 and 982 cm^{-1}. The 1629 cm^{-1} band is interpreted as C=N ring-stretches, also referred to as G band, while the band at 982 cm^{-1} represents the C_3N_3 breathing mode.[32] The ring mode in PTI-LiBr has a shoulder towards higher wavenumbers. The aloof-EELS phonon spectrum of PTI-LiBr shows a broad feature reminiscent of the CN-stretches in the FT-IR spectrum. Additionally, the ring mode at around 800 cm^{-1} can be picked up with this technique.

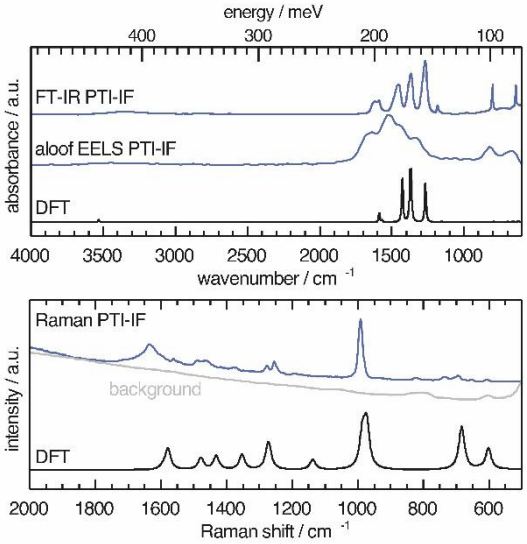

Figure 3. Vibrational modes in PTI-IF determined by FT-IR, aloof-EELS, DFT and Raman spectroscopy (266 nm).

The vibrational modes in PTI-IF are better resolved than in PTI-LiBr (Figure 3, Figure S9).[15] DFT calculations predict the main four bands in the aloof-EELS and FT-IR spectra of PTI-IF observed between 980-1620 cm^{-1} (Figure 3). However, the intensity of the ring modes at 642 and 802 cm^{-1} is drastically underestimated in the phonon calculation. The ring mode of PTI-IF at 990 cm^{-1} in the Raman spectrum has a higher intensity and no shoulder compared to PTI-LiBr.

The two triazine ring modes in the FT-IR spectra of PTI-LiBr are observed at 809 and 666 cm^{-1}. In comparison, the ring modes of PTI-IF are observed at 802 and 642 cm^{-1}. We attribute the higher energy ring-modes of PTI-LiBr to structural strain that is induced by the intercalated ions. We present the observed and calculated energies of the modes and a visual representation of the deformation vectors in an overview figure and table (Figure S10) to guide future interpretation of vibrational spectra of triazine-based carbon nitrides. Generally, the inhomogenous distribution of ions throughout the PTI-LiBr structure causes a significant broadening of the vibrational bands in all spectroscopic methods. Removal of the ions from the structure leads to a more homogenous chemical environment throughout PTI-IF and, hence, to narrower bands.

2.4. Electronic structure of PTI crystals

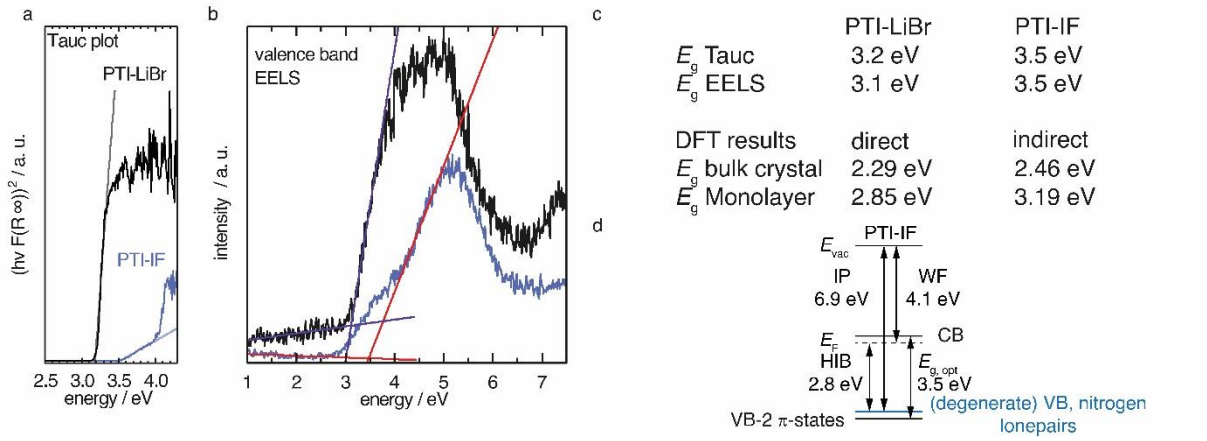

Figure 4. a) Tauc plot for a direct transition of diffuse reflectance data of PTI-LiBr and PTI-IF. b) Valence band EELS c) summary of optical gaps extracted from Tauc plots (E_g Tauc), from valence band EELS (E_g EELS), and from DFT calculations d) Energy level diagram of PTI-IF explaining the difference of the optical gap and the valence band-conduction band gap obtained by DFT. With the work function (WF), ionization potential (IP), the Fermi level (E_F), the optical gap ($E_{g,\,opt}$), the vacuum level (E_{vac}) and the hole injection barrier (HIB).

We applied diffuse reflectance spectroscopy, valence band electron energy loss spectroscopy (VB-EELS) (Figure 4), DFT (Figure S11), and UPS (Figure S12) to determine the size (eV), the nature (direct or indirect), and the energetic position of the bandgap of PTI-type materials. We determined the optical gap of nano-crystals of PTI-materials using the onset values from reflectance spectra (Tauc plot, Figure 4, a),[33,34] and valence band-EELS spectra of the conduction band (Figure 4, b). The DFT calculations show that the valence band of a monolayer is doubly degenerate at the Γ-point, and that it is composed of states that contain contributions from the nitrogen lone-pairs (Figure S11). Group-VI semiconductors with a lone-pair upper most valence band are referred to as "lone-pair semiconductors".[35] The non-bonding character of the VB has been theoretically predicted for other graphitic carbon nitride materials.[30] In CN-containing molecules like melamine, both the highest occupied orbital (HOMO) and the lowest occupied orbital (LUMO) have π-character; thus, the HOMO-LUMO transition is allowed.[36] However, in PTI layers the electronic VB → CB transition is forbidden because there is no orbital overlap between the non-bonding orbitals of the VB and

the π*-like orbitals of the conduction band (Figure S11, a). We observe a similar behavior in the bulk assembly of PTI layers, corrugation only lifts the degeneracy at the Γ-point (Figure S14, b). The forbidden VB → CB transition prevents direct estimation of the band gap by optical methods or EELS as the experimentally observed absorption corresponds to the π → π* transition between the VB-2 and the CB. The energetic difference between the forbidden VB → CB and the observed VB-2 → CB transitions is the reason for the observed discrepancy between the DFT bandgap and the experimental absorption onset obtained from the Tauc plot and EELS measurements (Figure 4, a, b). The VB-2 → CB transition is a π → π* transition of 3.6 eV that corresponds more closely with the experimentally derived gap by Tauc plot and aloof-EELS (Figure 4, c). We summarize the results of DFT, EELS, and UPS considerations in an energy level diagram (Figure 4, d).

We observe that the π-band (VB-2) lies below the VB and, as a consequence, the energy of the CB is lowered, *i.e.* it lies closer to the Fermi level. The energetic distance between VB and VB-2 in the intercalation free monolayer of PTI-IF is approx. 0.3 eV at Γ (Figure S11, a) and the CB position (or electron affinity) is 3.7 eV. Repeating this calculation for PTI-LiBr, we obtain an electron affinity of 4.2 eV; a value that allows environmentally stable n-transport.[37]

To estimate the strength of the VB-2 → CB transition, we determined the absorption coefficients of PTI-IF and PTI-LiBr. The obtained absorption coefficients point towards a direct π → π* (VB-2 → CB)-transition in both materials (9032 $M^{-1}cm^{-1}$ for PTI-IF, and 6860 $M^{-1}cm^{-1}$ for PTI-LiBr, Figure S13), and they are one to two magnitudes lower than the absorption coefficients of molecular species without a forbidden HOMO-LUMO transition.[38,39]

Comparing PTI-LiBr and PTI-IF, removal of intercalated ions induces a significant blue shift of the absorption onset by 0.3 eV (from 3.2 eV in PTI-LiBr to 3.5 eV in PTI-IF), as seen in the Tauc plot (Figure 4, a). This increase of the optical gap is also present – but less apparent – in the EELS valence band spectra (Figure 4, b). The shoulder appearing below the main

EELS band is likely a result of beam damage as it grows in intensity during the measurement. The gap increases from 3.1 eV (PTI-LiBr) to 3.5 eV (PTI-IF) by VB-EELS. The lower optical gap and band gap of PTI-LiBr can be ascribed to two concomitant mechanisms: (1) the formation of ion pairs (*i.e.* static dipoles) within the pores from the intercalated species that break the symmetry of the system. Eventually, this leads to the splitting of the degenerate levels at Γ; (2) the presence of intra- optical-gap defect states associated to the p orbitals of Br anion (Figure S13, a).

PTI-type intercalation compounds reported hitherto in literature typically show lower optical gaps (2.2-2.7 eV) due to carbonization.[17] The presence of a non-bonding band above the π-band (Figure 4, d) is significant as it does not allow for effective carrier injection into the π-band. This leads to the absence of the photoluminescence band in the electroluminescence spectrum and, hence, to the defect dominated electroluminescence spectrum as well as the low luminance of the organic light emitting device (OLED).[24] Holes injected into the VB will be trapped due to the nature of the highly localized lone-pair orbitals and recombination will be forbidden. To complement the understanding of the electronic structure with data characterizing the electronic carriers we performed time domain-THz spectroscopy.

2.5. Charge transport properties of nano-crystalline PTI

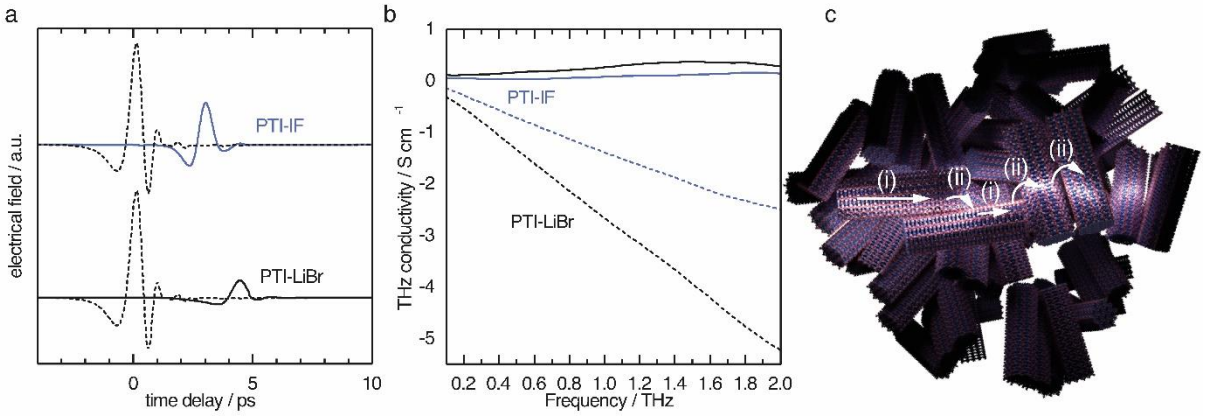

Figure 5. THz-time domain spectroscopy results of PTI-IF and PTI-LiBr as pressed pellets. a) THz reference pulse (dashed lines) transmitted through PTI-IF (blue) and transmitted through PTI-LiBr (black). b) Real (continuous line) and imaginary part (dashed line) of THz conductivity in PTI-IF (blue) and PTI-LiBr (black). c) Schematics of charge transport in PTI thin films. Nanoscale conductivity inside nano-crystals as obtained from THz spectroscopy is up to eight orders of magnitude higher than the electrical conductivity obtained from thin film measurements. The reason is that the charge transport between the nano-crystals (ii) is inefficient compared to the charge transport inside the crystals (i) probed by THz spectroscopy.

Intrinsic (*i.e.* undoped) organic semiconductors typically have a charge carrier density of 10^0 cm^{-3} and low mobility, as charge carriers are localized at single molecular units leading to hopping as dominant transport mechanism.[40]

Nano-crystalline PTI-IF and PTI-LiBr films from nano-crystals typically show low conductivity (PTI-IF 10^{-10} S cm^{-1}, PTI-LiBr 10^{-7} S cm^{-1}) and only small photo-currents in lateral thin-film devices.[24] To answer the question whether the low conductivity of PTI-films is an intrinsic material property or whether it is induced by the nano-crystalline character of the sample, we subjected free standing pressed pellets of PTI-LiBr and of PTI-IF to time domain-terahertz spectroscopy (THz-TDS) experiments.

The obtained time domain THz pulses after transmission through the sample (Figure 5, a) solid lines) show a significant difference in amplitude and a phase shift when compared to the pulse that did not pass the sample (dashed lines). The observed shifts contain information about the charge carriers inside the nano-crystals. Since the THz pulse is of picosecond duration, it can be translated to the conductivity on the nanoscale by a fast Fourier transform as explained in detail in the SI.

The THz conductivity at 1 THz is 0.26 S cm^{-1} in PTI-LiBr and 0.07 S cm^{-1} in PTI-IF, exceeding the macroscopic electrical measurements by about six and eight orders of magnitude, respectively (Figure 5, b). Hence, the conductivity inside the single crystals of PTI-LiBr and PTI-IF is much higher (Figure 5, c) (i)) than in the films. This is most likely due to inefficient charge transport between loosely packed PTI crystals (Figure 5, c) (ii)) in the macroscopic films. We surmise that the reason for the higher THz conductivity in PTI-LiBr compared to PTI-IF lies in the higher orbital coefficients on the lithiated imide bridges and, as a consequence, better charge transport between the triazine units (Figure S11, c).

We analyzed the obtained complex THz conductivity using the Drude-Smith model (DSM) that describes Drude-type transport of free charges impeded by spatial confinement with a second term including a localization parameter (Figure 5, b, Figure S15, b).[41] The phenomenological DSM gives an estimation of the density of charge carriers N, the scattering time τ, and the localization parameter c, which lies between 0 and -1 that describes Drude-type transport and completely immobile charge carriers, respectively.[42] The fitting parameters reveal a charge scattering time of 2.5 and 2.9 femtoseconds for PTI-LiBr and PTI-IF, respectively, and a localization parameter of <-0.999 for both (Figure S15, c). The low scattering time as well as the localization parameter close to -1 imply a high degree of localization. Using the hole effective mass obtained from the DFT calculations (PTI-LiBr bulk m_{eff}=2.25, PTI-IF bulk m_{eff}=1.20), the carrier mobility in the nanoscale μ_{THz} and the effective mobility μ_{eff} can be calculated as described in the SI. The effective mobility of 10^{-3}-10^{-4} cm^2 V^{-1} s^{-1} of PTI-LiBr and PTI-IF is in the range of the one found in amorphous organic semiconductors.[43] The reasons for the low mobility is the absent conjugation along the imide bridge as well as the highly localized character of the valence states.

The density of charge carriers contributing to the nanoscale conductivity in PTI-LiBr (3.00 10^{20} cm^{-3}) is orders of magnitude higher than what would be expected from an organic semiconductor with a large band gap and no doping.[44] The ion free PTI-IF has a similar

charge carrier density (2.07 10^{20} cm^{-3}) revealing that the ions are not responsible for generating electronic carriers in the organic crystals.

The obtained charge carrier density is higher than observed for other layered crystals such as covalent organic frameworks, metal organic frameworks and transition metal di-chalcogenides, for example MoS_2 (Table S4). The carrier densities closest to PTI are those of graphite and MoS_2 bulk crystals (1 10^{19} cm^{-3} and 3.7 10^{19} cm^{-3}, respectively).[45–47] The high carrier concentration might either be generated by an unknown structural defect or by adsorbed molecules like water or oxygen. Symmetric PTI devices with interdigitated indium-tin oxide electrodes are indeed sensitive to pressure, pointing towards water or oxygen acting as adsorbed dopants under environmental conditions (Figure S16).

3. Conclusion

We present an in-depth analysis of the structure, the orientation, and the electronic properties of a graphitic carbon nitride – PTI, with and without intercalated lithium bromide – and we provide a comprehensive energy level diagram for this fascinating material class.

We find that the band gap of the material cannot be assessed directly by optical methods because the VB → CB transition is forbidden. The non-binding upper-most valence band is likely the reason for the previously reported low electroluminescence. As a consequence, we find that PTI is not viable as emission layer in efficient organic light emitting diodes.

Using time-domain THz spectroscopy, we find that – despite its covalent character and high crystallinity – PTI experiences a high charge carrier localization and low mobility. The low conductivity in macroscopic films is caused by the nano-crystalline morphology. Removal of ions leads to a decreased electron density at the carbon and nitrogen cores as well as layer corrugation, and or changed stacking modes.

Future device architectures should exploit the highly stable and porous character of PTI that could be used for ion migration and retention at semiconducting interfaces. Such applications can make use of the preferred orientation effects we observed in this study, as pore-channel entrances of PTI-IF nano-crystals align perpendicular to a flat host-substrate. Further, once PTI single crystals of about 50 μm or larger are available, the extraordinarily stable n-type transport characteristics could be studied in single-crystal devices.

Conflicts of interest
There are no conflicts to declare.

Acknowledgements
The authors are grateful for the collaboration with Dr. Sarah Vogl, Prof. Dr. Norbert Koch, Prof. Dr. Arne Thomas, Prof. Dr. Nicola Pinna, Prof. Dr. Phillip Adelhelm and Prof. Dr. Hans Börner who provided labspace and access to instruments. M.J.B. thanks the European Research Council (ERC) for funding under the Starting Grant Scheme (BEGMAT-678462). C.C. and M.G. acknowledge financial support from the German Research Foundation, Project No. 182087777–CRC 951, by the German Federal Ministry of Education and Research (Professorinnenprogramm III) as well as from the State of Lower Saxony (Professorinnen für Niedersachsen). Computational resources were provided by the cluster CARL at the University of Oldenburg, funded by the German Research Foundation (Project No. INST 184/157-1 FUGG) and by the Ministry of Science and Culture of the State of Lower Saxony. N.B. and E.R. acknowledge the Swiss National Science Foundation (Grant 200020_184819) and the University of Bern for financial support.
The senior lead-author generated the introduction in part with GPT-3, OpenAI's large-scale language-generation model using the prompt "Write a summary paragraph on the state of the art of organic semiconductor research". Upon generating draft language, the lead-author reviewed, edited, and revised the language to their own liking. The lead-author takes ultimate responsibility for the content of this publication.

References

[1] W. Den, C.-H. Chen, Y.-C. Luo, *Water-Energy Nexus* **2018**, *1*, 116–133.

[2] B. Gopalakrishnan, Y. Mardikar, D. Korakakis, *Energy Eng.* **2010**, *107*, 6–40.

[3] T. N. Theis, H. S. Philip Wong, *Comput. Sci. Eng.* **2017**, *19*, 41–50.

[4] S. Fratini, M. Nikolka, A. Salleo, G. Schweicher, H. Sirringhaus, *Nat. Mater.* **2020**, *19*, 491–502.

[5] D. Burmeister, M. G. Trunk, M. J. Bojdys, *Chem. Soc. Rev.* **2021**, *50*, 11559–11576.

[6] A. H. Castro Neto, F. Guinea, N. M. R. Peres, K. S. Novoselov, A. K. Geim, *Rev. Mod. Phys.* **2009**, *81*, 109–162.

[7] K. S. Novoselov, A. K. Geim, S. V. Morozov, D. Jiang, M. I. Katsnelson, I. V. Grigorieva, S. V. Dubonos, A. A. Firsov, *Nature* **2005**, *438*, 197–200.

[8] J. K. Ellis, M. J. Lucero, G. E. Scuseria, *Appl. Phys. Lett.* **2011**, *99*, 261908.

[9] M. G. Stanford, P. D. Rack, D. Jariwala, *npj 2D Mater. Appl.* **2018**, *2*, 20.

[10] P. Miró, M. Audiffred, T. Heine, *Chem. Soc. Rev.* **2014**, *43*, 6537–6554.

[11] A. K. Geim, I. V. Grigorieva, *Nature* **2013**, *499*, 419–425.

[12] D. Burmeister, M. G. Trunk, M. J. Bojdys, *Chem. Soc. Rev.* **2021**, *50*, 11559–11576.

[13] A. I. Cooper, M. J. Bojdys, *Mater. Today* **2014**, *17*, 468–469.

[14] L. F. Villalobos, M. T. Vahdat, M. Dakhchoune, Z. Nadizadeh, M. Mensi, E. Oveisi, D. Campi, N. Marzari, K. V. Agrawal, *Sci. Adv.* **2020**, *6*, 9851.

[15] T. M. Suter, T. S. Miller, J. K. Cockcroft, A. E. Aliev, M. C. Wilding, A. Sella, F. Corà, C. A. Howard, P. F. McMillan, *Chem. Sci.* **2019**, *10*, 2519–2528.

[16] S. Y. Chong, J. T. A. Jones, Y. Z. Khimyak, A. I. Cooper, A. Thomas, M. Antonietti, M. J. Bojdys, *J. Mater. Chem. A* **2013**, *1*, 1102–1107.

[17] E. J. McDermott, E. Wirnhier, W. Schnick, K. S. Virdi, C. Scheu, Y. Kauffmann, W. D. Kaplan, E. Z. Kurmaev, A. Moewes, *J. Phys. Chem. C* **2013**, *117*, 8806–8812.

[18] E. Wirnhier, M. Döblinger, D. Gunzelmann, J. Senker, B. V. Lotsch, W. Schnick, *Chem. - A Eur. J.* **2011**, *17*, 3213–3221.

[19] J. T. E. Quinn, J. Zhu, X. Li, J. Wang, Y. Li, *J. Mater. Chem. C* **2017**, *5*, 8654–8681.

[20] M. J. Bojdys, J.-O. Müller, M. Antonietti, A. Thomas, *Chem. - A Eur. J.* **2008**, *14*, 8177–8182.

[21] M. J. Bojdys, N. Severin, J. P. Rabe, A. I. Cooper, A. Thomas, M. Antonietti, *Macromol. Rapid Commun.* **2013**, *34*, 850–854.

[22] G. Algara-Siller, N. Severin, S. Y. Chong, T. Björkman, R. G. Palgrave, A. Laybourn, M. Antonietti, Y. Z. Khimyak, A. V. Krasheninnikov, J. P. Rabe, et al., *Angew. Chemie Int. Ed.* **2014**, *53*, 7450–7455.

[23] D. Burmeister, J. Müller, J. Plaickner, Z. Kochovski, E. J. W. List-Kratochvil, M. J. Bojdys, *Chem. – A Eur. J.* **2022**, *28*, DOI 10.1002/chem.202200705.

[24] D. Burmeister, H. A. Tran, J. Müller, M. Guerrini, C. Cocchi, J. Plaickner, Z. Kochovski, E. J. W. List-Kratochvil, M. J. Bojdys, *Angew. Chemie Int. Ed.* **2022**, *61*, 2–10.

[25] M. Pauly, J. Kröger, V. Duppel, C. Murphey, J. Cahoon, B. V. Lotsch, P. A. Maggard, *Chem. Sci.* **2022**, *13*, 3187–3193.

[26] M. B. Mesch, K. Bärwinkel, Y. Krysiak, C. Martineau, F. Taulelle, R. B. Neder, U. Kolb, J. Senker, *Chem. - A Eur. J.* **2016**, *22*, 16878–16890.

[27] J. Gracia, P. Kroll, *J. Mater. Chem.* **2009**, *19*, 3013–3019.

[28] A. S. Ivanov, E. Miller, A. I. Boldyrev, Y. Kameoka, T. Sato, K. Tanaka, *J. Phys. Chem. C* **2015**, *119*, 12008–12015.

[29] G. Algara-Siller, N. Severin, S. Y. Chong, T. Björkman, R. G. Palgrave, A. Laybourn, M. Antonietti, Y. Z. Khimyak, A. V. Krasheninnikov, J. P. Rabe, et al., *Angew. Chemie* **2014**, *126*, 7580–7585.

[30] M. Deifallah, P. F. McMillan, F. Corà, *J. Phys. Chem. C* **2008**, *112*, 5447–5453.

[31] E. Wirnhier, M. Döblinger, D. Gunzelmann, J. Senker, B. V. Lotsch, W. Schnick, *Chem. – A Eur. J.* **2011**, *17*, 3213–3221.

[32] A. C. Ferrari, S. E. Rodil, J. Robertson, *Phys. Rev. B* **2003**, *67*, 155306.

[33] J. Tauc, R. Grigorovici, A. Vancu, *Phys. status solidi* **1966**, *15*, 627–637.

[34] G. Kortüm, D. Oelkrug, *Zeitschrift für Naturforsch. A* **1964**, *19*, 28–37.

[35] M. Kastner, *Phys. Rev. Lett.* **1972**, *28*, 355–357.

[36] J. P. Menzel, H. J. M. De Groot, F. Buda, *J. Phys. Chem. Lett.* **2019**, *10*, 6504–6511.

[37] H. Usta, C. Risko, Z. Wang, H. Huang, M. K. Deliomeroglu, A. Zhukhovitskiy, A. Facchetti, T. J. Marks, *J. Am. Chem. Soc.* **2009**, *131*, 5586–5608.

[38] D. A. R. Barkhouse, O. Gunawan, T. Gokmen, T. K. Todorov, D. B. Mitzi, *Prog. Photovoltaics Res. Appl.* **2015**, *20*, 6–11.

[39] H. Najafov, B. Lee, Q. Zhou, L. C. Feldman, V. Podzorov, *Nat. Mater.* **2010**, *9*, 938–943.

[40] A. Opitz, *J. Phys. Condens. Matter* **2017**, *29*, 133001.

[41] N. Smith, *Phys. Rev. B* **2001**, *64*, 155106.

[42] P. R. Whelan, B. Zhou, O. Bezencenet, A. Shivayogimath, N. Mishra, Q. Shen, B. S. Jessen, I. Pasternak, D. M. A. Mackenzie, J. Ji, et al., *2D Mater.* **2021**, *8*, 022003.

[43] D. R. Evans, H. S. Kwak, D. J. Giesen, A. Goldberg, M. D. Halls, M. Oh-E, *Org. Electron.* **2016**, *29*, 50–56.

[44] A. Opitz, *J. Phys. Condens. Matter* **2017**, *29*, 133001.

[45] N. Kumar, J. He, D. He, Y. Wang, H. Zhao, *J. Appl. Phys.* **2013**, *113*, 1–6.

[46] D. E. Soule, *Phys. Rev.* **1958**, *112*, 698–707.

[47] K. Sugihara, K. Kawamuma, T. Tsuzuku, *J. Phys. Soc. Japan* **1979**, *47*, 1210–1215.

Supporting Information

On the non-bonding valence band and the electronic properties of poly(triazine imide), a graphitic carbon nitride

David Burmeister, Alberto Eljarrat, Michele Guerrini, Eva Röck, Julian Plaickner, Christoph T. Koch, Natalie Banerji, Caterina Cocchi, Emil J. W. List-Kratochvil, Michael J. Bojdys**

Experimental

Experiments **have to be conducted with caution** since they employ glassware under high pressure and temperature.

Preparation of PTI-LiBr: 1 g of precursor dicyandiamide (DCDA, Sigma Aldrich >99%) is ground together with an eutectic salt mixture of LiBr and KBr (Sigma Aldrich /Acros Organics >99%) (15 g; 58:42 wt%, m.p. 348 °C) in a glovebox. The reaction mixture is filled into a quartz ampule and sealed. The sealed quartz ampule is placed into a furnace (Nabertherm, L 5/11/B180, 2.4 kW) at 400 °C for 4 h. Then the temperature is increased (10 K/min) to 475 °C for 7 days. The furnace is then allowed to cool naturally. The ampule is removed at room temperature, opened, and the salt block is dissolved in Milli-Q water in a 50 mL Falcon. The slurry is centrifuged and the supernatant is decanted. The pellet is dispersed in hot water on a shaker and centrifuged again. The supernatant is decanted and the process is repeated for two times with hot water and two times with methanol (>99% for synthesis). The resulting pellet is re-dispersed in methanol, transferred into vacuum safe glas ware and the methanol is evaporated. The resulting powder is dried under vacuum at 200 °C for 24 h before combustion analysis. The yield is 82% (0.93 g).

Preparation of PTI-IF: 0.7206 g PTI-LiBr is filled into a Soxhlet thimble and extracted for 20 days with water. To retain crystallinity the product is only dried at 60 °C at ambient pressure

for 24 h. Drying at 200 °C in reduced pressure reduces crystallinity. The yield is 0.4699 g, 94%.

Preparation of suspensions for TEM, SEM, Raman sample preparation: For the dispersion 10-20 mg of product are re-dispersed in 5 mL of EtOH. The dispersion is then dropcast either on a TEM grid (Plano, S147-2, holey carbon) or a wafer (1 µL) or a 1x1 cm quarz glas substrate for Raman (10-50 µL).

PTI suspensions: 6 mg PTI are suspended in 1 mL methanol and pipetted up and down.

Fourier transform infrared (FT-IR): Spectra were recorded from solid on a Thermo Scientific Nicolet iS5 spectrometer (Thermo Fisher Scientific, Waltham, MA, USA) in the wavenumber range of 4000-600 cm^{-1} with resolution of 4 cm^{-1}.

DFT calculations: The PTI-IF (bulk and monolayer) structure was taken from Ref. [DOI: 10.1039/c2ta01068b] removing the Li and Br ions and adding hydrogen to the imide bridges. The structure was subsequently optimized using the PBE exchange-correlation functional with the Tkatchenko-Sheffler pairwise correction scheme for van der Waals dispersions, a plane wave cut-off of 50 Ry, norm-conserving pseudo-potentials, and a 6x6(x6) Monkhorst-Pack k-mesh to ensure convergence of the electronic band structure.[1–3] The PTI-LiBr (bulk and monolayer) has been obtained from the structural relaxation of the geometry taken from Ref.[DOI: 10.1039/c2ta01068b] using the same computational parameters as specified above. Both the PTI-IF and PTI-LiBr 2D structures (monolayers), on which phonon calculations have been performed, have been obtained from the bulk structures by taking out one single layer (and associated LiBr intercalants) and adding 20 Å of vacuum in the normal direction with respect to the monolayer plane in order to avoid spurious interaction between the replicas upon the application of periodic boundary conditions. All calculations were performed with the ab initio package- Quantum Espresso.[4]

To study the effect of lithium replacing hydrogen at the imide bridges, one third of the hydrogens in the PTI-IF monolayer was replaced by lithium and the structure was further

Unit cell data of DFT optimized AA* stacked PTI-IF.

```
# CRYSTAL DATA

#------------------------------------------------------------------------

data_VESTA_phase_1


_chemical_name_common                  'XCrySDen XSF file'
_cell_length_a                         8.02801
_cell_length_b                         8.16505
_cell_length_c                         6.34309
_cell_angle_alpha                      90.70694
_cell_angle_beta                       89.98965
_cell_angle_gamma                      119.43531
_space_group_name_H-M_alt              'P 1'
_space_group_IT_number                 1

loop_
_space_group_symop_operation_xyz
   'x, y, z'

loop_
   _atom_site_label
   _atom_site_occupancy
   _atom_site_fract_x
   _atom_site_fract_y
   _atom_site_fract_z
   _atom_site_adp_type
   _atom_site_B_iso_or_equiv
   _atom_site_type_symbol
   C1        1.0     0.683936     0.167584     0.301117     Biso  1.000000 C
   N1        1.0     0.525734     0.176754     0.345431     Biso  1.000000 N
   N2        1.0     0.676592    -0.001833     0.285344     Biso  1.000000 N
   C2        1.0     0.856113     0.473902     0.249480     Biso  1.000000 C
   C3        1.0     0.542938     0.339775     0.283267     Biso  1.000000 C
   C4        1.0     0.315150     0.837415     0.767967     Biso  1.000000 C
   C5        1.0     0.142820     0.530788     0.817544     Biso  1.000000 C
   C6        1.0     0.456007     0.665016     0.784318     Biso  1.000000 C
   C7        1.0     0.797478     0.348459     0.783968     Biso  1.000000 C
   C8        1.0     0.484186     0.176262     0.800347     Biso  1.000000 C
   C9        1.0     0.618433     0.482406     0.748672     Biso  1.000000 C
   C10       1.0     0.201349     0.656444     0.284051     Biso  1.000000 C
   C11       1.0     0.514689     0.828717     0.268841     Biso  1.000000 C
   C12       1.0     0.380228     0.522179     0.318190     Biso  1.000000 C
   N3        1.0     0.856118     0.313057     0.273851     Biso  1.000000 N
   N4        1.0     0.699926     0.487003     0.208312     Biso  1.000000 N
   N5        1.0     0.473614     0.828629     0.723998     Biso  1.000000 N
   N6        1.0     0.142778     0.691626     0.793109     Biso  1.000000 N
   N7        1.0     0.298910     0.517521     0.858772     Biso  1.000000 N
   N8        1.0     0.787934     0.495709     0.708747     Biso  1.000000 N
   N9        1.0     0.651355     0.185625     0.846087     Biso  1.000000 N
   N10       1.0     0.457333     0.321456     0.771033     Biso  1.000000 N
   N11       1.0     0.210778     0.508883     0.358521     Biso  1.000000 N
   N12       1.0     0.347607     0.819841     0.223661     Biso  1.000000 N
   N13       1.0     0.541403     0.683169     0.296046     Biso  1.000000 N
   N14       1.0     0.024512     0.639716     0.256722     Biso  1.000000 N
   N15       1.0     0.382394     0.356168     0.308374     Biso  1.000000 N
   N16       1.0     0.322304     0.006640     0.785932     Biso  1.000000 N
   N17       1.0    -0.025646     0.365030     0.810382     Biso  1.000000 N
   N18       1.0     0.616222     0.648351     0.757874     Biso  1.000000 N
   H1        1.0     0.020485     0.754709     0.205959     Biso  1.000000 H
   H2        1.0     0.802548    -0.001731     0.285475     Biso  1.000000 H
   H3        1.0     0.196334     0.006487     0.784564     Biso  1.000000 H
   H4        1.0    -0.021608     0.250153     0.861591     Biso  1.000000 H
   H5        1.0     0.263399     0.241162     0.359132     Biso  1.000000 H
   H6        1.0     0.735521     0.763467     0.707939     Biso  1.000000 H
```

optimized.

IR absorption spectra and phonon normal modes for the PTI-IF and PTI-LiBr monolayers have been calculated in the framework of density functional perturbation theory with the *PHonon* package of Quantum Espresso using a 6x6 q-mesh.

Calculated Raman spectra were obtained using CASTEP as embedded in the Materials Studio 7.0 suite after a geometry optimization and vibrational analysis using the PBE as exchange-correlation functional, a plane-wave basis set cut-off of 700 eV, and choosing an excitation source with wavelength 266 nm.[5]

Raman: UV Raman spectra were recorded with a Horiba T64000 spectrometer in single-grating mode. The excitation source was provided by a diode-pumped solid-state laser from CryLas at a wavelength of 266 nm and power of 4 mW. The light was focused on the sample with a Thorlabs LMU-40x-UVB objective (backscattering geometry). A notch filter with cut-off at 220 cm^{-1} was used to filter out the elastically scattered light. The acquired Raman spectra were calibrated by comparison with the spectrum of a Ga_2O_3 crystal by using a quadratic calibration curve. This procedure allows for reduction of the experimental error at approximately 5 cm^{-1}, which is below the spectral resolution of 8 cm^{-1}.

Powder X-ray diffraction (PXRD): Structural analysis of the prepared PTI-MX was performed with a Bruker D2 Phaser X-Ray powder diffractometer (XRD) in Bragg-Brentano geometry. X-rays were generated by a Cu $K_{\alpha 1+2}$ source at 30 kV operating voltage and collected with a LynxEye detector.

Optical microscopy: Film thickness measurements for determination of conductivity were performed with an Olympus LEXT laser scanning microscope.

ssNMR: Cross polarization magic-angle spinning (CP-MAS) solid-state NMR spectra were recorded on a Bruker Avance 400 MHz spectrometer operating at 100.6 MHz (^{13}C) and 40.52 MHz (^{15}N).

EELS, CBED: Scanning transmission electron microscopy (STEM) studies were performed for the intercalation-free PTI-IF and LiBr intercalated PTI-LiBr samples. Scanning electron energy-loss spectroscopy (EELS) and convergent beam electron diffraction (CBED) experiments were carried out. All data was acquired using a Nion HERMES microscope equipped with an aberration corrector, a cold-field-emission-gun (cFEG), a monochromator at ground potential, and a hybrid-pixel direct-detection camera (Dectris ELA). The accelerating voltage was 60 kV and other experimental conditions were adjusted to each case as detailed below.

For EELS experiments, medium STEM convergence and collection angles (20 mrad) were matched in order to have good spatial resolution (130 pm) and discard the scattered beams from entering the EELS detector. This probe is rastered over the sample collecting an EELS spectrum for each position. Aloof and transmission EELS was carried out to assess induced damage to the beam sensitive sample.

In CBED mode, a relatively small convergence angle (0.5 mrad) of the STEM probe was used in order to form smaller, point-like diffraction disks. This probe is rastered over the sample collecting a CBED pattern for each position. In order to obtain CBED signal, the beam needs to transmit through the sample, cancelling the possibility of an aloof acquisition mode.

The acquired CBED datasets are large (several Gb), since the diffraction pattern dimensions are 512x512 pixel and the raster dimensions are 100x100 pixel. In order to analyze them, the open-source Python library `pyxem` in combination with `hyperspy` were employed.[6–8] Distortion of the experimental diffraction data was corrected by measuring the elliptical shapes of rings in position averaged CBED and house-developed software.

Pawley refinement: Pawley refinement of the unit cell was performed using the Reflex tools in the Materials Studio 7.0 suit.

UV-Vis of dispersions: UV-VIS measurements were performed in ambient conditions with a PerkinElmer Lambda 950 spectrometer in standard transmission operation with 1 nm step size. Dispersions were obtained by dispersing a known quantity of PTI powder in DI water and sonicating it for 60 min with a benchtop sonication bath. Dispersions were measured in a quartz cuvette with 1 cm optical path. Molar absorption coefficients were obtained equating the mass of one unit cell with one molecule, using Lambert-Beer law.

$$A = \varepsilon\, c\, d \tag{1}$$

A: absorbance

c: concentration

d: length of the optical path in cuvette

ε: molar absorption coefficient

Solid state UV-Vis: A Edinburgh Instruments FLS 980 spectrometer was used. Reflectance spectra were collected with a Xe lamp in an Ulbricht sphere. The reflectance spectra were converted using the Kubelka-Munk relation and plotted via the Tauc expression.

Kubelka Munk equation:

$$F(R\infty) = \frac{(1 - R(\infty))^2}{2\, R(\infty)} \tag{2}$$

F(R∞): Kubelka Munk function

R(∞): reflectance of infinite thick material

Relation proposed by Tauc Mott and Davis for direct band gaps:

$$C(hv - E_g) = (F(R\infty)\, hv)^2 \tag{3}$$

C: proportionality constant

h: plank constant

v: frequency

E_g: band gap energy

Preparation of thin film devices for conductivity determination: Ossila "Interdigitated ITO Substrates for OFET and Sensing" S161: w × L: 30 mm × 50 µm were coated with a PTI-LiBr and PTI-IF dispersion by drop-casting. Samples were placed in an Ossila low density OFET test board and IV characterisation was conducted with a source measure unit (4200A SCS parameter analyser; Keithley).

$$\sigma = \frac{1}{\rho} = \frac{L}{\frac{U}{I} A} = \frac{L}{\frac{U}{I} w t} \quad (4)$$

ρ = electrical resistivity
σ=electrical conductivity
U=bias
I=current
A=surface area
w=channel width
t=film thickness
L=channel length

Devices for pressure sensitivity measurements were placed in a vacuum chamber and the pressure was reduced with a laboratory vacuum oil pump.

THz-spectroscopy: The THz time domain spectroscopy (THz-TDS) setup is based on the output of a regeneratively-amplified Ti:sapphire laser system (Coherent Astrella). Part of the 800 nm output with an average power of 6.5 W and ~35 fs pulse duration at 1 kHz repetition rate is split to a 30 µW beam to generate the probe beam. The THz probe pulses are generated via optical rectification in a 2 mm [110] ZnTe crystal. The THz probe pulse is detected by electro-optic sampling in another 1 mm [110] ZnTe crystal. The setup from the

ZnTe generation crystal, sample holder, to the detector camera is enclosed in a chamber in nitrogen atmosphere to exclude THz absorption by air humidity. The immediate response of the THz electric field to the charges in the investigated material yields the ground state conductivity. It is obtained from the Fourier transform of the THz probe response to the pressed pellets and the Fourier transform of the transmitted THz pulses through air.

To get information about the charge carrier mobility, the conductivity spectra are fit using the modified Drude–Smith Model (DSM). The experimental real and imaginary conductivity σ as a function of THz frequency ω are fitted well using the DSM and give a valuable estimation of the number of charge carriers per unit volume N, the average undisturbed travelling time τ and the localization parameter c.

$$\sigma(\omega) = \frac{Ne^2\tau/m^*}{1 - i\omega\tau}\left(1 + \frac{c}{1 - i\omega\tau}\right) \tag{5}$$

Hereby, the effective mass m^* of the holes is used from density functional theory calculations of PTI-LiBr and PTI-IF. The localization parameter c can vary between 0 and -1, where the charge transport is Drude-like and completely suppressed, respectively. The localization parameter c stems from factors such as structural disorder, coupling to nuclear modes and interactions with ions and/or between the charge carriers. It is important to highlight that the localization parameter describes the overall localization of charges but does not distinguish between the aforementioned factors.

We use τ and c to calculate the effective THz mobility μ_{eff}, which includes the localization parameter, for the pressed pellets of PTI-LiBr and PTI-IF. It corresponds to the mobility over distances probed by THz measurements, i.e. few nanometers.

$$\mu_{eff} = \mu_{THz}(1 + c) = \frac{e\tau}{m^*}(1 + c) \ , \tag{6}$$

where the effective mass m^* of the holes is determined by DFT calculations. The THz mobility μ_{THz} describes mainly the coherent charge motion in a nano-crystal. We find the effective mobility in PTI-LiBr ($1.81 \cdot 10^{-3}$ $cm^2V^{-1}s^{-1}$) to be significantly higher than in PTI-IF ($7.33 \cdot 10^{-4}$ $cm^2V^{-1}s^{-1}$).

XPS, UPS: The samples were prepared by drop-casting PTI dispersions (MeOH) on ITO coated glass substrates to minimize charging and to avoid background carbon signals from e.g. carbon tape as substrate. For UPS experiments, a hydrogen discharge lamp (employing H Lyman-α lamp from Excitech, 10.2 eV) in a JOEL JPS-9030 Photoelectron Spectrometer was used.(doi: 10.1016/j.orgel.2016.11.032) For determination of the secondary electron cut off (SECO) a negative bias of 10 V was applied to clear the analyzer work function. All measurements were performed at room temperature. The obtained values were rounded to one decimal place. The work function was determined by linear fitting of the background and the linear region of the SECO, and reading of the point of intersection. The hole injection barrier was determined by linear fitting of the background and the valence band onset, and reading of the point of intersection. The error of the measurement is ±0.1 eV.

For XPS the JOEL JPS-9030 Photoelectron Spectrometer with an Al kα (1486 eV) excitation source and a monochromator was utilized. Quantitative comparison of nitrogen and carbon in single spectra were performed by signal integration after background subtraction of a Shirley function.

Table S1. Theoretical and experimentally determined elemental analysis of PTI-LiBr and PTI-IF in wt% from combustion analysis and ICP-OES.

	C	N	H	Li	residual wt%
PTI-LiBr	24.67	43.02	0.87	4.47	26.95
$C_6H_3N_9LiBr$ PTI-LiBr in theory	25.02	43.77	1	2.41	27.75
PTI-IF	35.00	61.53	1.73	0	1.74
$C_6H_3N_9$ PTI-IF in theory	35.83	62.67	1.51	0	0

Table S2. Peak positions and FWHM of hk0 and 00l peaks of PTI-IF and PTI-LiBr.

hkl.	PTI-IF peak position, FWHM	PTI-LiBr peak position, FWHM
010	11.82 2θ, 0.37 2θ	11.99 2θ, 0.11 2θ
110	20.56 2θ, 0.68 2θ	20.88 2θ, 0.12 2θ
002	24.71 2θ, 0.93 2θ	25.14 2θ, 0.23 2θ

Table S3. Pawley refinement of cif files with different stacking orders and with and without layer corrugation.

	Flat Rwp%	Corrugated Rwp%
AA*	17	7
AA	20	13
AB	14	12

Table S4. Comparison of the THz analysis of PTI to other layered materials in literature.

Layered material	charge carrier density (298 K)	THz conductivity (S cm^{-1})	mobility (298 K, varying methods) (cm^2 $V^{-1}s^{-1}$)
graphite[9,10]	$1\cdot10^{19}$ cm^{-3}		10^{-4}
MoS_2 bulk crystal[11]	$3.7\cdot10^{19}$ cm^{-3}		
CuPc-MIDA-COF[12]	$2.6\cdot10^{12}$ cm^{-3}	0.01	13.3 ± 7.5
ZnPc-pz and CuPc-pz COF[13]	10^{12} cm^{-3}	$5\cdot10^{-7}$	5
TPB-TFB COF[14]	$3–5 \cdot 10^{16}$ cm^{-3}		165 ± 10
$Fe_3(THT)_2(NH_4)_3$ MOF [15]	10^{16} cm^{-3}	0.8	220
Doped polymer poly(3-hexylthiophene)[16]	10^{21} cm^{-3}		
PTI-LiBr (this work)	$3\cdot10^{20}$ cm^{-3}	0.26	$1.81\cdot10^{-3}$
PTI-IF (this work)	$2\cdot10^{20}$ cm^{-3}	0.07	$7.33\cdot10^{-4}$

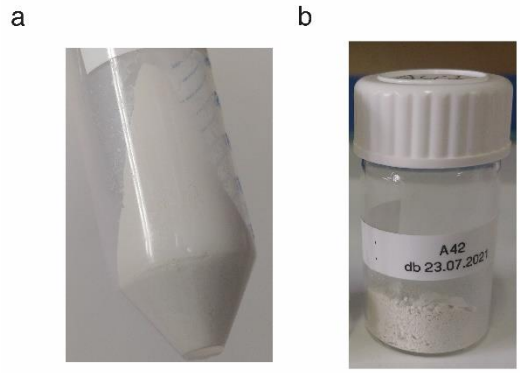

Figure S 1. Images of PTI-LiBr synthesized at 475 °C, 7 d. a) pellet after centrifugation in water. b) powder after drying.

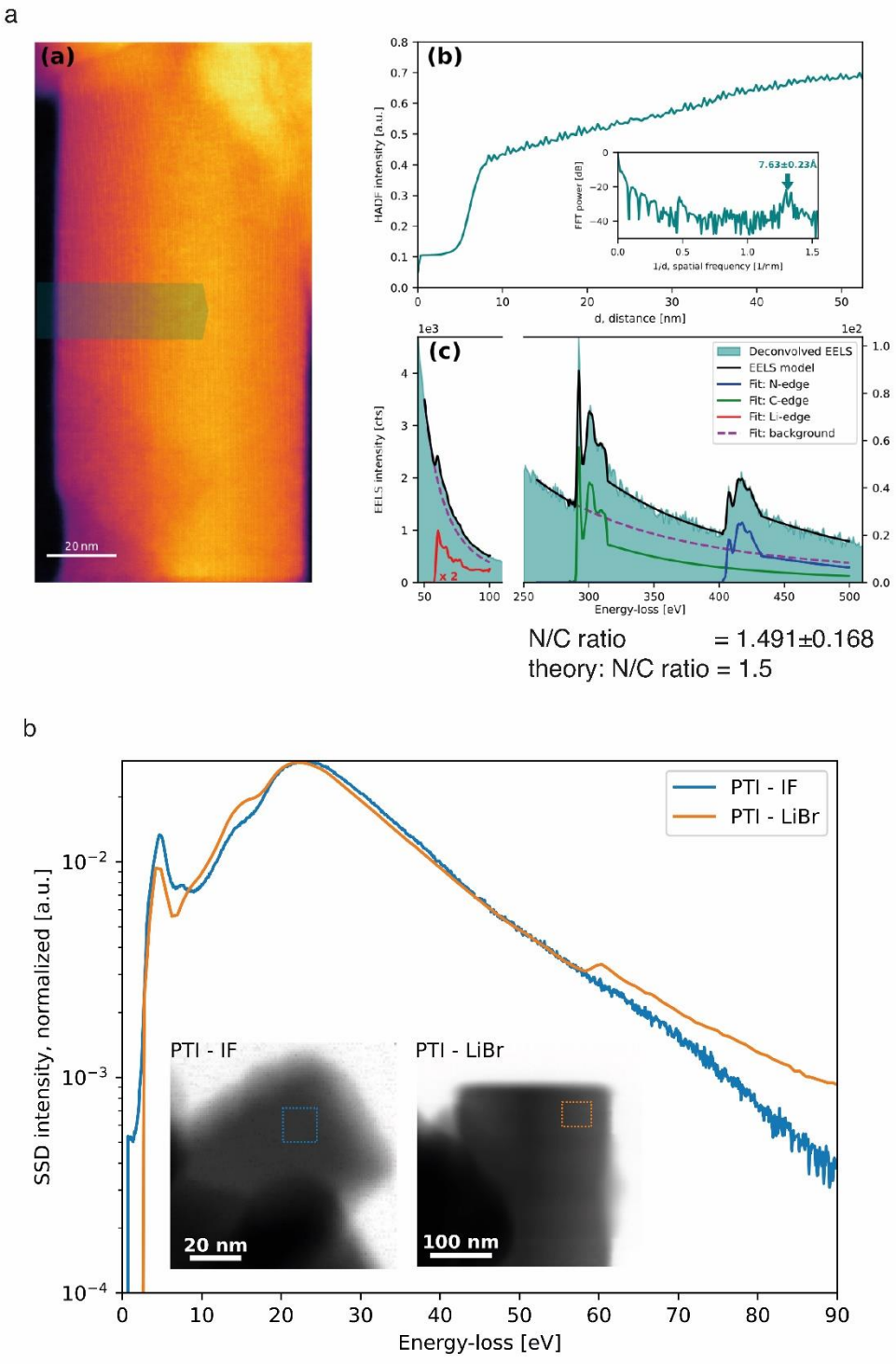

Figure S 2. a) (a) High angle annular dark-field (HAADF) image of the PTI-LiBr crystal that was chosen for the EELS experiment. (b) Evaluation of lattice plane distance. The c-distance seems to be increased by electron beam irradiation (theory c=7.04 Å) a) (c), b) PTI-LiBr and PTI-IF EELS spectra. Evaluation of the k-edge yields the N/C ratio are in good agreement with the theoretical expected values of 9N/6C = 1.5. Quantitative analysis of the ion species is not

possible due to the overlap of the Br-M4,5 edge at 69 eV with the Li k-edge at around 62 eV. b) EELS spectrum comparison of PTI-LiBr and PTI-IF attesting absence of Li ions in PTI-IF.

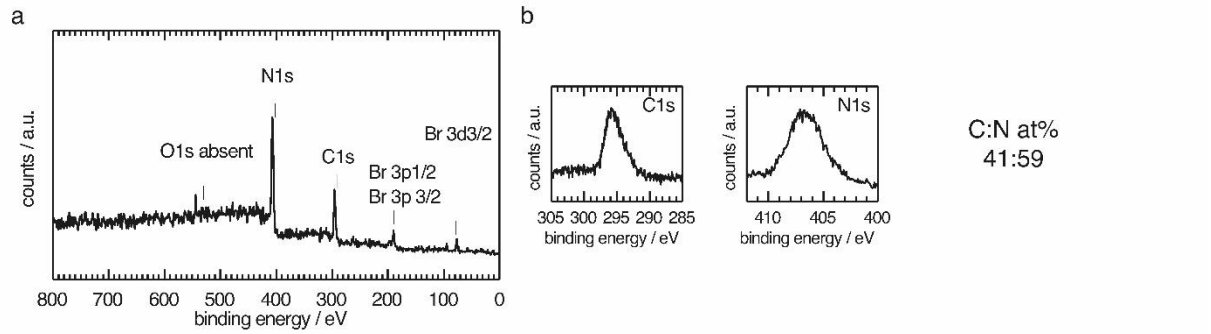

Figure S 3. XPS spectra of PTI-LiBr from new synthesis conditions reveal a further decrease in carbonization when compared to our last work. a) Survey spectra show presence of carbon nitrogen and bromine. b) Quantification of carbon and nitrogen single element spectra reveal a C:N ratio of 41:59 at%.

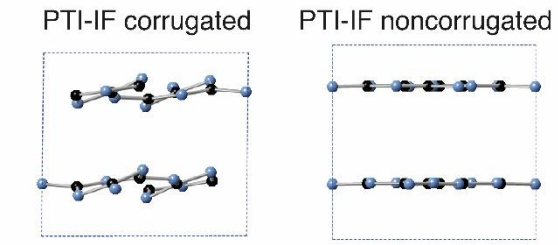

Figure S 4. Comparison of corrugated and non corrugated b-achsis view of PTI AA* stacked cif files used for Pawley refinement.

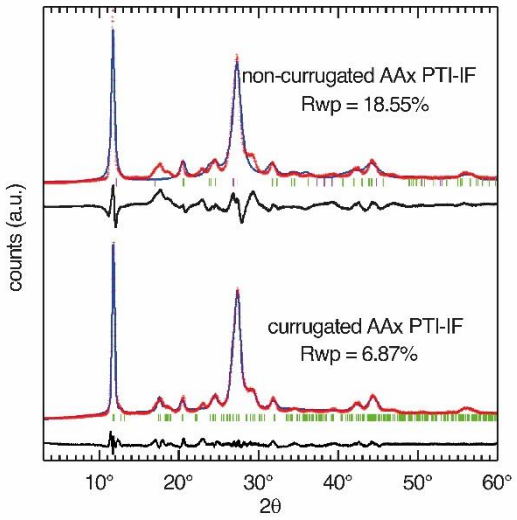

Figure S 5. Comparison of Pawley refinement of PTI-IF AA* stacked unit cells with and without layer corrugation. Red crosses indicate the experimental spectrum, the blue line is the result of the Pawley fit, green markers show markers for observed reflections and violet markers show positions of symmetry forbidden reflections. Pawley refinement of the diffractogram of the "flat" non corrugated unit cell reveals several symmetry forbidden reflections (violet markers) due to the high symmetry of the unit cell (P63CM, Spacegroup 185). The relaxation of the system via DFT induces layer corrugation which in turn reduces the symmetry of the system to P1, hence no symmetry forbidden reflections are observed in the calculation result. Intensities at positions with prior absences are indeed observed for example at 12.2° and 17.1°. Additionally the peaks at 18.5° and 29.0° are better represented. A peak that is not accounted for in any structure we used for Pawley refinement is at 23.0°. The Pawley refinement with the corrugated unit cell overall better fits the observed spectrum as is also reflected by the lower weighted profile R-value (Rwp).

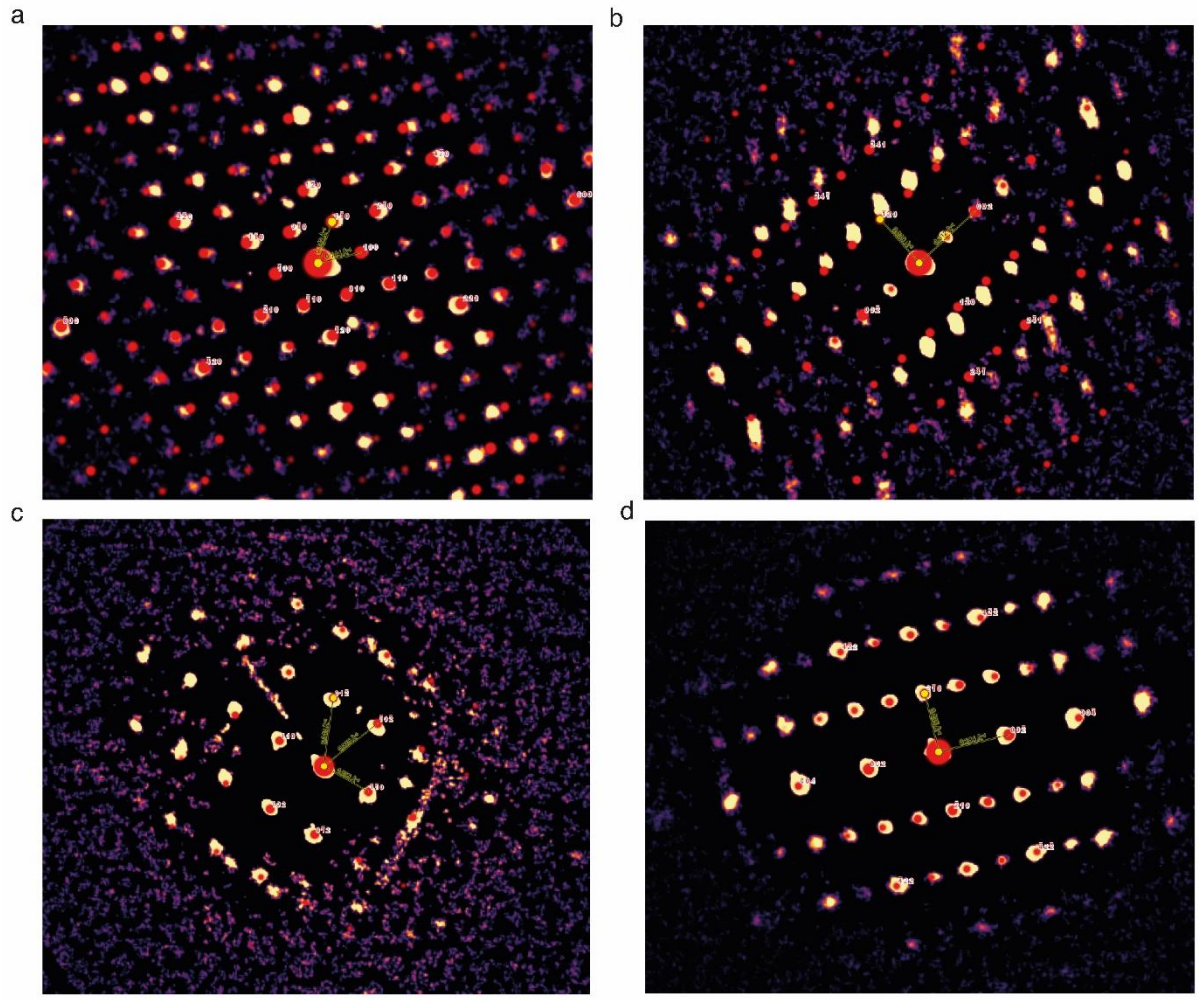

Figure S 6. Overlay of CBED diffractograms of PTI-IF (a 001, b 100) and PTI-LiBr (c 001, d 100) with calculated patterns (red dots). Systematic absences are absent in the 100 pattern of PTI-IF.

Partial charges (Bader)

PTI-IF

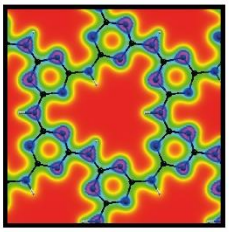

species	charge
Triazine 1 / 2	+2.32e / +2.05e
bridge 1 / 2 / 3	-1.42e / -1.57e / -1.39e

PTI-LiBr

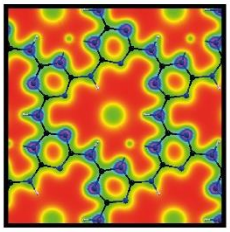

species	charge
Triazine 1 / 2	+1.61e / +1.09e
bridge 1 / 2 / 3	-0.77e / -0.69e / -1.34e
Li	+0.87e
Br	-0.77e

Figure S 7. Partial charge analysis (Bader) of PTI-IF and PTI-Br. Electron density at carbon and nitrogen is higher in PTI-LiBr when compared to PTI-IF. Carbon is represented as black sphere, nitrogen blue sphere and hydrogen white sphere. Lithium and bromine are not represented as spheres. Bromine is positioned in the center of the pore in PTI-LiBr and Lithium is off centered.

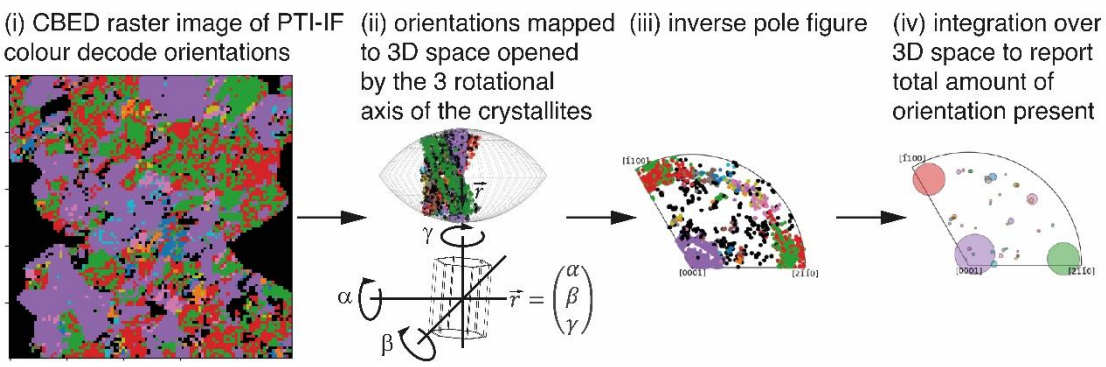

Figure S 8. (i) Each individual pixel represents one CBED pattern that was matched to the orientation of the crystal structure. The orientations are mapped into 3D-space utilizing the three rotational axis of the crystal relative to the electron beam that define three integers giving rise to the length and orientation of a vector in the 3D space with the 0001/001 zone axis being the center (ii). Each vector is then represented by a point in 3D space (iii). Pixels with similar orientation are then summed over the 3D space to give a 2D representation (iv).

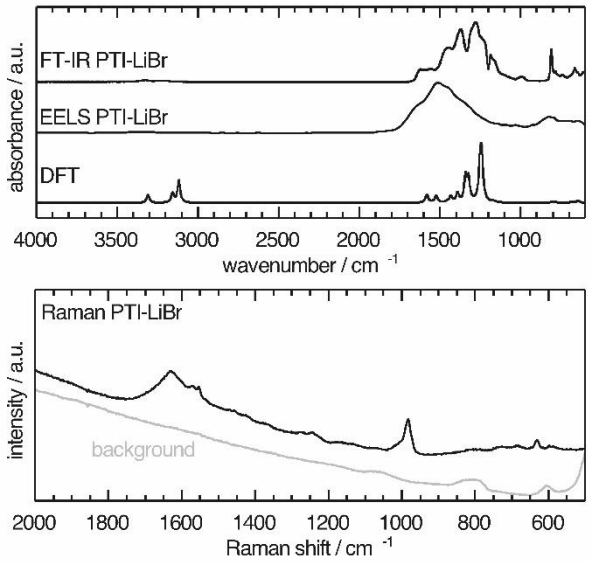

Figure S 9. Vibrational modes in PTI-LiBr determined by FT-IR, DFT, Raman (266 nm) and EELS.

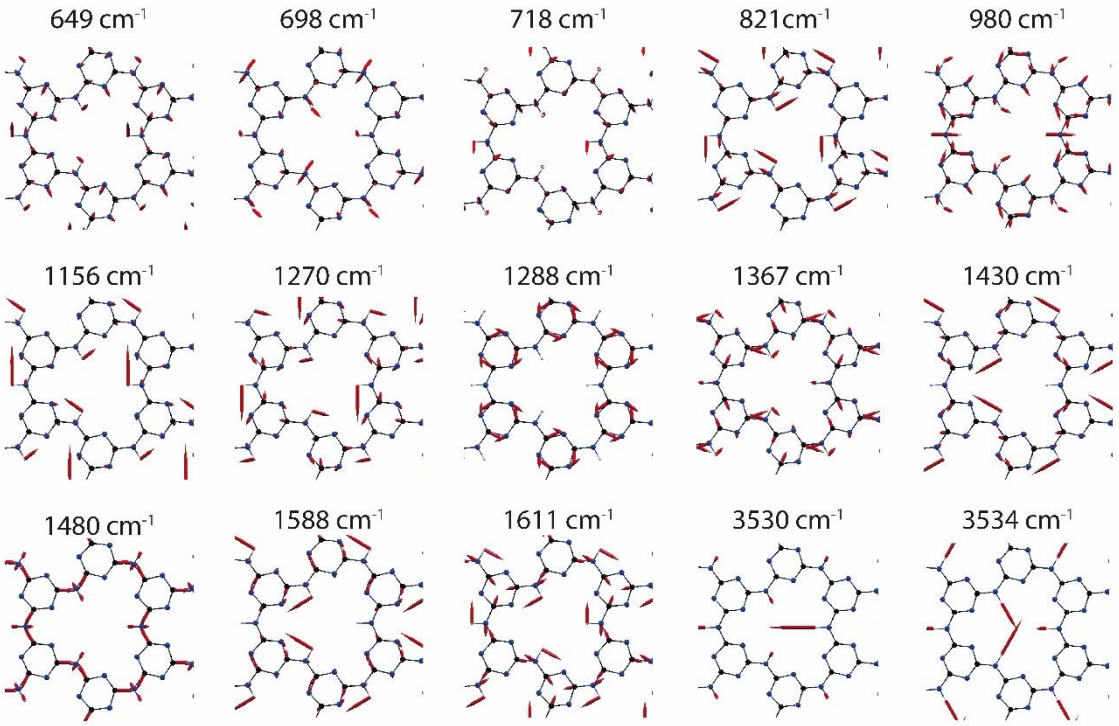

experimentally observed IR	Raman	EELS	ν calc.	rel. int. IR	assignment
			3530, 3534		NH stretching
3360 (b, w)					intercalated water
1620 (m)	1633 (b)	1653 (b)	1611	0.00	NH wagging+ring breathing
1590 (m)	1562 (b)		1588	11.14	quadrant ringstretch
	1490 (w)	1517 (b)	1480	0.07	NH stretching+NC stretching
1455 (m)	1460 (w)	1436 (b)	1430	52.93	NH wagging+ring deformation
1367 (s)	1375 (m)	1333 (b)	1367	95.78	NH wagging+ring deformation
1270 (vs)	1277 (w)		1288	0.11	ring deformation
	1254 (w)		1270	49.74	NH wagging+ring deformation
1182 (w)			1156	1.2	NH wagging+ring deformation
982 (w)	990 (vs)		980	0.21	quadrant ringstretch
802 (s)		820 (b)	821	1.41	NH wagging+ring breathing
	733 (vw)		718	0.03	out of plane def.
	692 (vw)		698	1.44	NH wagging+out of plane ring breathing
642 (s)	650 (vw)	667 (b)	649	0.46	ring deformation

Figure S 10. Phonon normal modes of PTI-IF monolayer. Top: phonon frequencies and corresponding eigenmodes represented as red arrows. The normal modes are mainly composed by N-H and C-N stretching. Bottom: summary of DFT vibrational analysis of a monolayer compared to FT-IR, Raman, and EELS results.

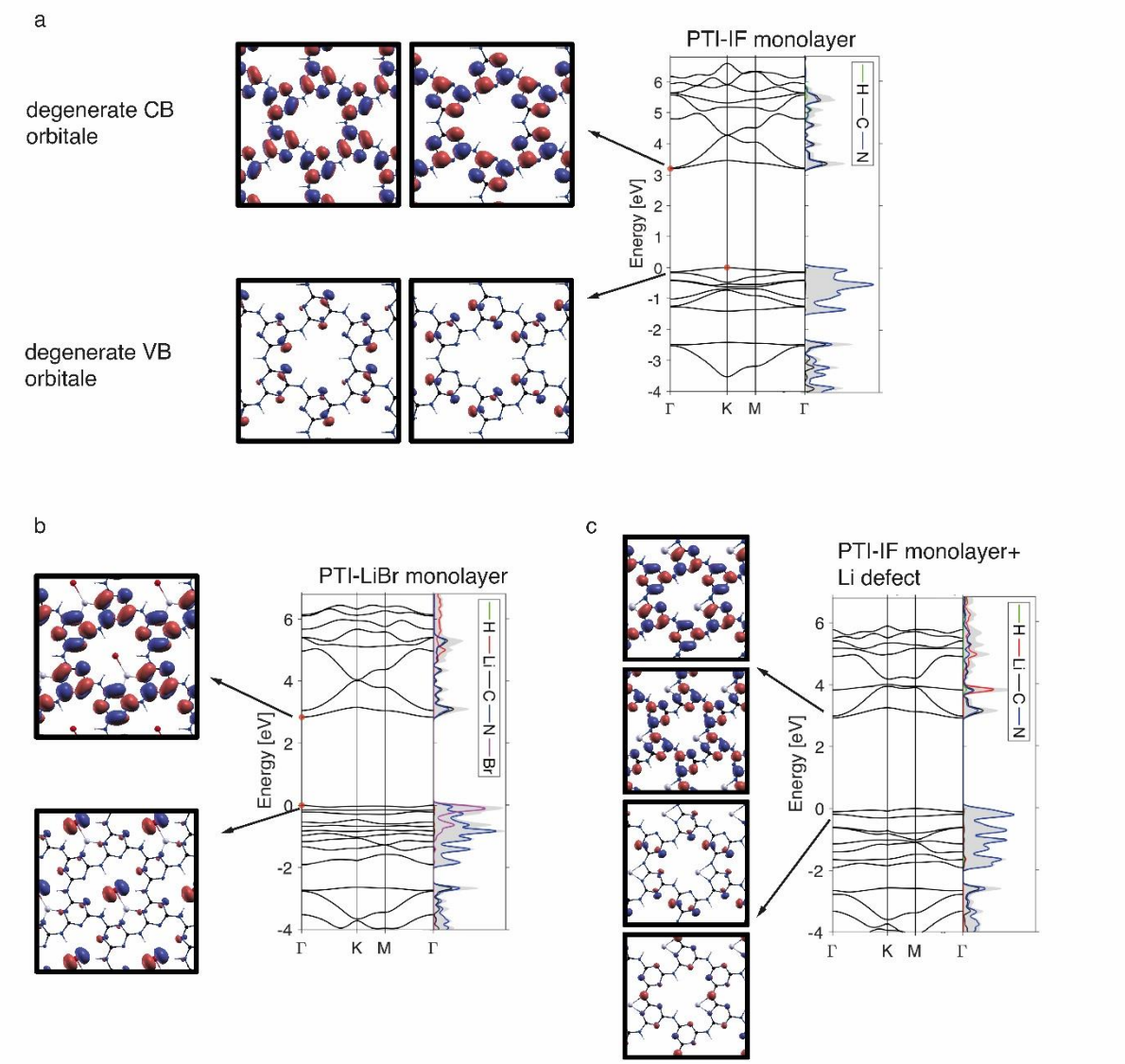

Figure S 11. a) PTI-IF pristine monolayer electronic bandstructure and isosurfaces of the double degenerate valence band and conduction band Bloch states at Γ point (i.e., BZ centre). b) PTI-LiBr monolayer electronic bandstructure and isosurfaces of the valence band and conduction band Bloch states at Γ point. c) Effect of Lithium defect replacing one Hydrogen at the imide bridge in the PTI-IF monolayer.

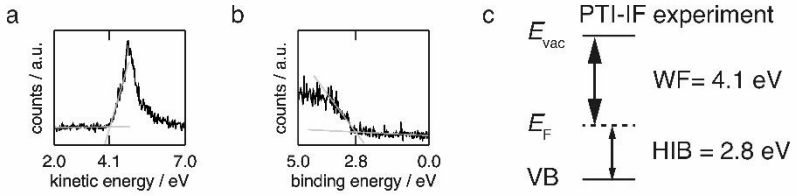

Figure S 12. Ultraviolet photoelectron spectroscopy (UPS) results for PTI-IF layer on indium tin oxide. a) Secondary electron cut-off. b) Valence band scan. c) Energy levels of PTI-IF obtained from UPS. The ionization potential (IP) is equal to IP=WF+HIB=6.9 eV. With work function denoted by WF and hole injection barrier by HIB.

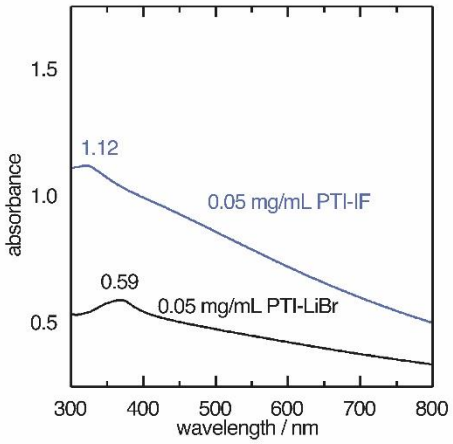

Figure S 13. Absorption of PTI-IF (blue) and PTI-LiBr (black) emulsions. Molar absorption coefficients: 9032 $M^{-1}cm^{-1}$ PTI-IF, 6860 $M^{-1}cm^{-1}$ PTI-LiBr.

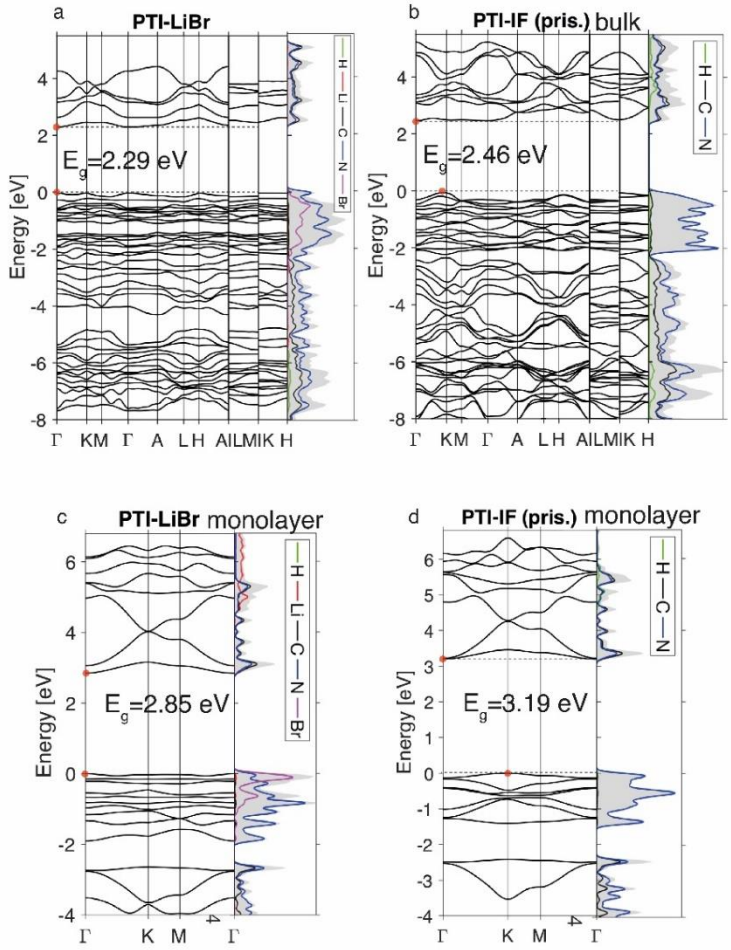

Figure S 14. Calculated band structures of a) PTI-LiBr AA* bulk, b) PTI-IF AA* bulk, c) PTI-LiBr monolayer and d) PTI-IF monolayer.

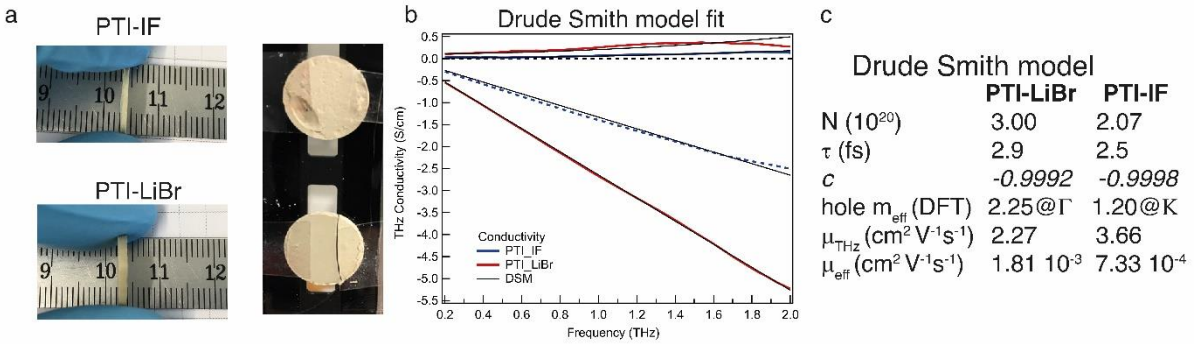

Figure S 15. a) Pressed PTI pellets for THz spectroscopy. b) Drude Smith model fit. c) Drude smith fitting parameters.

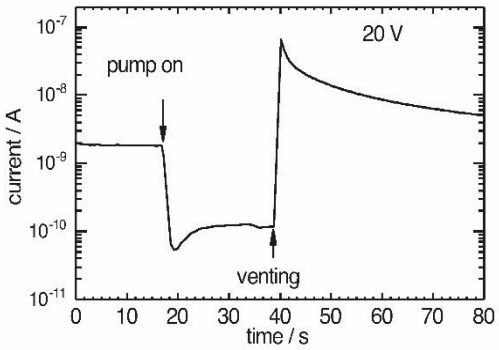

Figure S 16. Current versus time graph of PTI-IF interdigitated device in vacuum chamber. Reduction of pressure leads to drop in current while venting to atmospheric pressure leads to current flow.

References

[1] A. Tkatchenko, R. A. Distasio, R. Car, M. Scheffler, *Phys. Rev. Lett.* **2012**, *108*, 1.

[2] J. P. Perdew, K. Burke, M. Ernzerhof, *Phys. Rev. Lett.* **1996**, *77*, 3865.

[3] A. Tkatchenko, M. Scheffler, *Phys. Rev. Lett.* **2009**, *102*, 6.

[4] P. Giannozzi, S. Baroni, N. Bonini, M. Calandra, R. Car, C. Cavazzoni, D. Ceresoli, G. L. Chiarotti, M. Cococcioni, I. Dabo, A. Dal Corso, S. De Gironcoli, S. Fabris, G. Fratesi, R. Gebauer, U. Gerstmann, C. Gougoussis, A. Kokalj, M. Lazzeri, L. Martin-Samos, N. Marzari, F. Mauri, R. Mazzarello, S. Paolini, A. Pasquarello, L. Paulatto, C. Sbraccia, S. Scandolo, G. Sclauzero, A. P. Seitsonen, A. Smogunov, P. Umari, R. M. Wentzcovitch, *J. Phys. Condens. Matter* **2009**, *21*.

[5] S. J. Clark, M. D. Segall, C. J. Pickard, P. J. Hasnip, M. I. J. Probert, K. Refson, M. C. Payne, *Zeitschrift fur Krist.* **2005**, *220*, 567.

[6] D. Johnstone, P. Crout, Pyxem https://doi.org/10.5281/zenodo.2649351.

[7] F. de la Peña, V. Tonaas Fauske, Hyperspy https://doi.org/10.5281/zenodo.5608741.

[8] D. N. Johnstone, B. H. Martineau, P. Crout, P. A. Midgley, A. S. Eggeman, *J. Appl. Crystallogr.* **2020**, *53*, 1293.

[9] D. E. Soule, *Phys. Rev.* **1958**, *112*, 698.

[10] K. Sugihara, K. Kawamuma, T. Tsuzuku, *J. Phys. Soc. Japan* **1979**, *47*, 1210.

[11] N. Kumar, J. He, D. He, Y. Wang, H. Zhao, *J. Appl. Phys.* **2013**, *113*, 1.

[12] E. Jin, K. Geng, S. Fu, S. Yang, N. Kanlayakan, M. A. Addicoat, N. Kungwan, J. Geurs, H. Xu, M. Bonn, H. I. Wang, J. Smet, T. Kowalczyk, D. Jiang, *Chem* **2021**, *7*, 3309.

[13] M. Wang, M. Ballabio, M. Wang, H. Lin, B. P. Biswal, X. Han, S. Paasch, E. Brunner, P. Liu, M. Chen, M. Bonn, T. Heine, S. Zhou, E. Cánovas, R. Dong, X. Feng, *J. Am. Chem. Soc.* **2019**, *141*, 16810.

[14] S. Fu, E. Jin, H. Hanayama, W. Zheng, H. Zhang, L. Di Virgilio, M. A. Addicoat, M. Mezger, A. Narita, M. Bonn, K. Müllen, H. I. Wang, *J. Am. Chem. Soc.* **2022**, *144*, 7489.

[15] R. Dong, P. Han, H. Arora, M. Ballabio, M. Karakus, Z. Zhang, C. Shekhar, P. Adler, P. S. Petkov, A. Erbe, S. C. B. Mannsfeld, C. Felser, T. Heine, M. Bonn, X. Feng, E. Cánovas, *Nat. Mater.* **2018**, *17*, 1027.

[16] V. I. Arkhipov, P. Heremans, E. V. Emelianova, G. J. Adriaenssens, H. Bässler, *Appl. Phys. Lett.* **2003**, *82*, 3245.